

Experimental Characterization and Material Modeling of Photopolymers in Additive Manufacturing

Thomas Rasmus Rainer Rehbein

Vollständiger Abdruck der bei der Fakultät für Luft- und Raumfahrttechnik der
Universität der Bundeswehr München zur Erlangung des akademischen Grades
eines

Doktor-Ingenieurs (Dr.-Ing.)

genehmigten Dissertation.

Gutachter:

Univ.-Prof. Dr.-Ing. habil. Alexander Lion

Univ.-Prof. Dr. habil. Andrei Constantinescu

Die Dissertation wurde am 25.05.2022 bei der Universität der Bundeswehr München
eingereicht und durch die Fakultät für Luft- und Raumfahrttechnik am 12.11.2022
angenommen. Die mündliche Prüfung fand am 13.12.2022 statt.

Acknowledgements

The research project "Constitutive modeling of UV-curing printed polymer composites" associated with the present dissertation was funded by the Deutsche Forschungsgemeinschaft (DFG, German Research Foundation, project number 406819523). Therefore, I express my gratitude to the Deutsche Forschungsgemeinschaft for the financial support.

First of all, I thank Univ.-Prof. Dr.-Ing. habil. Alexander Lion for having given me the opportunity to work at his institute and serving as examiner of this dissertation. His outstanding knowledge regarding continuum mechanics and its application in solving engineering problems has always been an inspiration. He always provided me with the necessary freedom to find the right direction, and assisted to overcome arising obstacles in the daily work of a researcher.

The project was carried out together with research partners from the Laboratoire de Mécanique des Solides of the École Polytechnique. Thus, I express my gratitude to Univ.-Prof. Dr. habil. Andrei Constantinescu for serving as co-examiner of this dissertation and consistently having given me valuable feedback during the project duration. Additionally, I appreciate the cooperation with Kübra Sekmen.

Furthermore, I thank Prof. Dr.-Ing. habil. Michael Johlitz for his perseverance in terms of the procurement of laboratory equipment and intermediate financing of fixed-term positions. He always found a solution even when the bureaucratic obstacles seemed insurmountable.

Finishing this dissertation would not have been possible without the support of my former colleagues. Among all the various people that contributed with their expertise, I would like to highlight the following: Dr.-Ing. Christoph Mittermeier for the fruitful discussions about calorimetric and rheometric measurements, Tomáš Gejguš for his deep engineering knowledge, and Michaela Lochbihler for her pragmatic mindset in terms of problem solving.

Last but not least, special thanks go to the people that accompanied and supported me throughout my academic studies: Dr.-Ing. Alexander Nelson, Dr.-Ing. Robert Fiedler, Dr.-Ing. Ulrich Kroll, and Dr.-Ing. Marvin Nahrman.

Kurzfassung

In der vorliegenden Arbeit wird ein Materialmodell für die Beschreibung der Aushärtung und der damit einhergehenden Phänomene von Photopolymeren in additiven Fertigungsprozessen mit Hilfe von kontinuumsmechanischen Methoden entwickelt. Die darin enthaltenen Gleichungen werden anhand von experimentellen Untersuchungen motiviert, die an einem kommerziell verfügbaren Photopolymer durchgeführt werden. Das Materialmodell ist in der Lage, die viskoelastischen und viskoplastischen Eigenschaften des Photopolymers in Abhängigkeit des Aushärtegrads und der Temperatur abzubilden. Zunächst werden in einer Diskussion des aktuellen Stands der Forschung und Technik der additiven Fertigung von Photopolymeren etablierte Verfahren vorgestellt. Das DLPTM-Verfahren wird aufgrund des einfachen Geräteaufbaus und der erhöhten Druckgeschwindigkeit im Vergleich zu anderen Verfahren zur Fertigung der Proben ausgewählt.

Die daran anschließenden Experimente untersuchen den Übergang des Photopolymers vom flüssigen in den festen Zustand und die damit verbundenen Änderung der Materialeigenschaften. Hierzu werden vorhandene Messgeräte (DSC, Rheometer) mit einer Lichtquelle erweitert, um die für den Start der Aushärtungsreaktion notwendige Bestrahlung im Messaufbau zu ermöglichen. Die maßgeblichen Parameter des DLPTM-Verfahrens können mit den modifizierten Messaufbauten variabel eingestellt werden. Dynamisch-mechanische Analysen werden zur Charakterisierung der temperaturabhängigen viskoelastischen Eigenschaften von gedruckten Proben mit verschiedenen Aushärtegraden durchgeführt, wohingegen die viskoplastischen Eigenschaften anhand von Zugversuchen mit verschiedenen Temperaturen, Aushärtegraden und Dehnraten untersucht werden.

Das Materialmodell wird für die Implementierung in das Finite-Elemente-Programm LS-DYNA[®] numerisch aufbereitet, um dreidimensionale Berechnungen durchzuführen. Die Parameter des Materialmodells werden mit innovativen Optimierungsalgorithmen identifiziert und liefern zusammen mit dem Modell eine gute Übereinstimmung mit den Versuchsdaten. Die Validierung der entwickelten Modellgleichungen und identifizierten Parametersätze wird anhand von simulierten Zugversuchen unter zyklischer Be- und Entlastung durchgeführt, um die Prognosefähigkeit des Materialmodells zu zeigen.

Abstract

In the present thesis, a material model is developed to describe the crosslinking progress and the associated phenomena of photopolymers in additive manufacturing processes. The model equations therein are motivated by experimental investigations conducted on a commercial photopolymer and formulated by means of the methods of continuum mechanics. The material model can represent the viscoelastic and viscoplastic properties of the photopolymer depending on the degree of cure and temperature.

First, established additive manufacturing processes for photopolymers are presented, and their benefits and limitations are discussed. Digital Light Processing™ is selected for the fabrication of the specimens due to its simple design and increased printing speed compared to other processes.

The subsequent experiments investigate the transition of the photopolymer from the liquid to the solid state and the associated change in the material properties. For this purpose, existing experimental setups (DSC, rheometer) are modified with a light source enabling the irradiation necessary to start the crosslinking reaction in the photopolymer. The decisive parameters in Digital Light Processing™ can be variably adjusted with the modified measurement setup. Dynamic mechanical analyses are performed to characterize the temperature-dependent viscoelastic properties of printed specimens with different degrees of cure, whereas the viscoplastic properties are investigated using tensile tests with different temperatures, degrees of cure, and strain rates. The material model is numerically discretized for the implementation into the finite element program LS-DYNA® to perform three-dimensional simulations. The parameters of the material model are identified using innovative optimization algorithms, and provide, in combination with the model, a good agreement with the experimental data. The validation of the developed model equations and identified parameter sets is performed using simulated tensile tests subjected to cyclic loading and unloading in order to demonstrate the predictive quality of the material model.

Contents

Nomenclature	i
1 Introduction and State of the Art	1
1.1 Motivation	1
1.2 Additive manufacturing processes for photopolymers: state of the art and current research activities	4
1.3 Objectives and structure of work	11
2 Experimental Characterization	13
2.1 Investigated material and employed DLP printer	13
2.2 Differential Scanning Calorimetry (DSC)	14
2.2.1 Experimental setup and governing equations	15
2.2.2 Extension with the OmniCure® S2000 curing system for photo- DSC measurements	17
2.2.3 Crosslinking	20
2.2.4 Glass transition temperature	28
2.2.5 Isobaric specific heat capacity	30
2.3 Rheometric measurements during crosslinking	32
2.3.1 Mechanical properties	36
2.3.2 A new method to determine temperature-dependent working curves	41
2.3.3 Chemical shrinkage	45
2.4 Dynamic-mechanical analysis of printed specimens	49
2.4.1 Specimen fabrication	51
2.4.2 Determination of the degree of cure	52
2.4.3 Results of the torsional DMA tests	54
2.5 Tensile tests	60
2.5.1 Monotonic loading	63
2.5.2 Cyclic loading and unloading	65

3	Material Modeling	71
3.1	Degree of cure	72
3.1.1	Internal variable	72
3.1.2	Modified working curve model	75
3.2	Kinematic and kinetic quantities	76
3.3	Multiplicative decomposition of the deformation gradient	78
3.4	Representation by rheological elements	88
3.5	Viscoelasticity	90
3.6	Plasticity	95
3.6.1	Consideration of viscoplastic effects	97
3.6.2	Consistent discretization	98
4	Parameter Identification and Validation	109
4.1	Crosslinking	109
4.2	Viscoelastic properties	112
4.2.1	Viscoelastic properties of printed specimens	112
4.2.2	Viscoelastic properties during crosslinking	116
4.3	Tensile properties	121
4.3.1	Finite element model of the tensile specimen	121
4.3.2	Temperature- and degree of cure-dependent bulk modulus	122
4.3.3	Parameters of the viscoplastic part of the material model	126
4.4	Validation by means of tensile specimens subjected to cyclic loading and unloading	132
5	Conclusion and Outlook	137
A	Identified values of the shear moduli and relaxation times	139
	Bibliography	141
	List of Tables	151
	List of Figures	153

Nomenclature

Acronyms

AM	Additive manufacturing
APF	ARBURG Plastic Freeforming
CAD	Computer aided desing
cf.	Compare
ch.	Chapter
CLIP TM	Continuous Liquid Interface Production TM
DLP TM	Digital Light Processing TM
DLS TM	Digital Light Synthesis TM
DMA	Dynamic-mechanical analysis
DMD TM	Digital Micromirror Device TM
DSC	Differential Scanning Calorimetry
e.g.	For example
EHP	Electrically heated plates
eq.	Equation
eqs.	Equations
et al.	And others
ETC	Environmental test chamber
FDM	Fused Deposition Modeling
FFF	Fused Filament Fabrication
fig.	Figure
figs.	Figures
GCA	Gas cooling accessory
i.e.	That is
MDSC [®]	Modulated DSC
MJF	Multi Jet Fusion
MPa	Megapascal
MSE	Mean squared error
MSLE	Mean squared logarithmic error
Nd:YVO ₄	Neodymium-doped yttrium orthovanadate
OECD	Organisation for Economic Co-operation and Development
sec.	Section
SiO ₂	Silicon dioxide
SLA	Stereolithography
SLS	Selective Laser Sintering
SRSM	Sequential Response Surface Methodology
subsec.	Subsection
UV	Ultraviolet

Fourth order tensors

\mathcal{C}	Consistent tangent modulus
\mathcal{C}_{el}	Elasticity tensor
\mathcal{I}	Fourth order identity tensor

Operators

$\bar{(\cdot)}$	Isochoric part of the quantity (\cdot)
$\frac{\partial (\cdot)}{\partial (\circ)}$	Partial derivative of the quantity (\cdot) with respect to (\circ)
$\dot{(\cdot)}$	Material time derivative of the quantity (\cdot)
$\hat{(\cdot)}$	Volumetric part of the quantity (\cdot)
$(\cdot) \cdot (\circ)$	Double contraction between two tensors (\cdot) and (\circ)
$(\cdot) (\circ)$	Tensor product of two second order tensors (\cdot) and (\circ)
$(\cdot) \otimes (\circ)$	Dyadic product of two second order tensors (\cdot) and (\circ)
$\ \cdot\ $	FROBENIUS norm of the quantity (\cdot)
$\text{tr}(\cdot)$	Trace of the second order tensor (\cdot)
$\det(\cdot)$	Determinant of the quantity (\cdot)
$\text{Grad}(\cdot)$	Gradient of the quantity (\cdot) in the reference configuration

Scalars

α	Attenuation factor
α_{ch}	Chemical shrinkage constant
α_{th}	Coefficient of thermal expansion
δ	Phase shift, layer thickness
$\dot{\epsilon}_{\text{global}}$	Global strain rate
\dot{Q}	Differential rate of heat flow
\dot{q}	Specific differential rate of heat flow
$\dot{Q}_{\text{s}}, \dot{Q}_{\text{r}}$	Rates of heat flow at the sample and reference platforms
η_k	Viscosity of the MAXWELL element k
γ	Shear strain
γ^*	Complex shear strain
γ_0	Shear strain amplitude
$\kappa_0(\theta, c), \kappa_1(\theta, c)$	Parameters of the isotropic hardening function
λ	Wavelength, plastic multiplier
\mathcal{B}	Material body
\mathcal{B}_0	Material body in the initial configuration
\mathcal{B}_t	Material body in the current configuration
\mathcal{I}	Irradiance, $[\mathcal{I}] = \text{mW}/\text{cm}^2$
\mathcal{I}_0	Incident irradiance
\mathcal{I}_{ref}	Reference irradiance
dV	Volume element in the reference configuration
dv	Volume element in the current configuration

ω	Angular frequency
\overline{m}	Length-specific mass
τ	Shear stress
τ^*	Complex shear stress
τ_0	Shear stress amplitude
$\tau_{vp}(\theta, c)$	Normal of the yield surface
$\tau_k(\theta, c)$	Relaxation time of the MAXWELL element k
$\tau_{vp0}, \tau_{vp1}, \tau_{vp2}$	Parameters of the function $\log_{10}(\tau_{vp}(\theta, c))$
τ_{kR}	Reference relaxation time of the MAXWELL element k
θ	Temperature
θ_0	Temperature of the DSC furnace, reference temperature
θ_g	Glass-transition temperature
θ_R	Reference temperature
θ_s, θ_r	Temperatures at the sample and reference platforms
ε_{ch}	One-dimensional chemical shrinkage strain
$\varepsilon_{true, global}$	True global strain
φ	Twist
φ_0	Twist amplitude
φ_{ch}	Function describing the chemical shrinkage
φ_{th}	Function describing the thermal expansion
ζ	Accumulated plastic strain
a	Aspect ratio
A_1, A_2	Pre-exponential factors
c	Degree of cure
c_0	Parameter of the model equation $c_{max}(T)$
C_d	Curing depth
c_{eff}	Effective degree of cure
c_{gel}	Degree of cure at the gel point
c_{max}	Maximum attainable degree of cure
c_p	Isobaric specific heat capacity
c_R	Reference degree of cure
C_s, C_r	Heat capacities of the sample and reference platforms
d	Diameter
D_p	Penetration depth
D_{p0}, D_{p1}	Parameters of the model equation $D_p(\theta)$
E_0	Incident exposure dose, $[E_0] = \text{mJ}/\text{cm}^2$
E_1, E_2	Activation energies
E_c	Critical exposure dose
E_{c0}, E_{c1}	Parameters of the model equation $E_c(\theta)$
f	Yield function
f_0	Constant parameter of the viscoplastic flow rule
f_D	Diffusion factor
G'	Shear storage modulus
G''	Shear loss modulus
G^*	Complex shear modulus
$G_\infty(c)$	Equilibrium shear modulus

G_k	Shear modulus of the MAXWELL element k
$G_{\infty 1}, G_{\infty 2}$	Parameters of the function $G_{\infty}(c)$
H	Layer thickness
h	Height
$H(\zeta, \theta, c)$	Isotropic hardening function
$H_0(\theta, c)$	Hardening modulus
h_{res}	Residual heat of reaction
h_{tot}	Total specific heat of reaction
H_{01}, H_{02}, H_{03}	Parameters of the function $H_0(\theta, c)$
i	Imaginary number
I_1	First invariant of the CAUCHY stress
J	Jacobian
J_2	Second invariant of the isochoric part of the CAUCHY stress
$K(\theta, c)$	Bulk modulus
K_0, K_1, K_2	Parameters of the function $K(\theta, c)$
k_1, k_2	ARRHENIUS factors
l	Length
l_0	Initial distance between the clamps in the tensile tests
M	Torque
m	Mass
m_{vp}	Parameter of the viscoplastic flow rule
n, p	Exponents of the model equation describing the degree of cure
R	Radius, universal gas constant
R_s, R_r	Thermal resistances of the sample and reference platforms
$s_{\theta}(\theta)$	Shift function for the time-temperature superposition
$s_c(c)$	Shift function for the time-cure superposition
$s_{\theta 0}, s_{\theta 1}$	Parameters of the function $\log_{10}(s_{\theta}(\theta))$
$s_{c, \text{bulk}}(c)$	Shift function of the bulk modulus
$s_{c, \text{relax}}(c)$	Shift function of the viscoplastic relaxation time
$s_{c, \text{yield}}(c)$	Shift function of the initial yield stress
$s_{c1}, s_{c2}, s_{c3}, s_{c4}$	Parameters of the function $\log_{10}(s_c(c))$
$s_{c, \text{gel}}$	Shift factor for the time-cure superposition at the gel point
T	Absolute temperature
t	Thickness
t	Time
$T_{c, \text{max}}$	Parameter of the model equation $c_{\text{max}}(T)$
w	Width
x, y, z	Coordinates
$Y_0(\theta, c)$	Initial yield stress
Y_{01}, Y_{02}, Y_{03}	Parameters of the function $Y_0(\theta, c)$

Second order tensors

χ	Total strain
$\dot{\mathbf{T}}$	Material time derivative of the CAUCHY stress

$\mathbf{1}$	Second order identity tensor
\mathbf{d}	Strain rate tensor
\mathbf{F}	Deformation gradient
\mathbf{H}	Displacement gradient
\mathbf{L}	Spatial velocity gradient
\mathbf{N}	Normal of the yield surface
\mathbf{T}	CAUCHY stress
\mathbf{T}^∇	JAUMANN rate of the CAUCHY stress
\mathbf{T}_R	First PIOLA-KIRCHHOFF stress
\mathbf{w}	Spin tensor
$\mathring{\mathbf{T}}$	Arbitrary objective rate of the CAUCHY stress

Sub- and superscripts

$(\cdot)_{\text{ch}}$	Chemical part of the quantity (\cdot)
$(\cdot)_{\text{el}}$	Elastic part of the quantity (\cdot)
$(\cdot)_{\text{in}}$	Inelastic part of the quantity (\cdot)
$(\cdot)_{\text{m}}$	Mechanical part of the quantity (\cdot)
$(\cdot)_{\text{th}}$	Thermal part of the quantity (\cdot)
$(\cdot)_{\text{tr}}$	Trial state of the quantity (\cdot)
$(\cdot)_{\text{ve}}$	Viscoelastic part of the quantity (\cdot)
$(\cdot)_{\text{vp}}$	Viscoplastic part of the quantity (\cdot)
$^{n+1}(\cdot)$	Quantity (\cdot) at time ^{n+1}t
$^n(\cdot)$	Quantity (\cdot) at time nt
$^{j+1}(\cdot)$	Quantity (\cdot) at the iteration step $j + 1$
$_j(\cdot)$	Quantity (\cdot) at the iteration step j

Vectors

ϕ	Motion of the material body
τ_R	Vector of the reference relaxation times τ_k
$\mathbf{e}_1, \mathbf{e}_2, \mathbf{e}_3$	Basis unit vectors
\mathbf{G}	Vector of the shear moduli G_k
\mathbf{n}	Normal vector of the surface element in the current configuration
\mathbf{t}	Traction vector
\mathbf{u}	Displacement field
\mathbf{v}	Velocity field
\mathbf{X}	Position of the material point in the reference configuration
\mathbf{x}	Position of the material point in the current configuration
$d\mathbf{X}$	Line element in the reference configuration
$d\mathbf{x}$	Line element in the current configuration

1 Introduction and State of the Art

1.1 Motivation

In 2016, the Organisation for Economic Co-operation and Development (OECD) classified additive manufacturing (AM) as one of the 40 key and emerging technologies for the future [OECD, 2016]. Unlike conventional manufacturing based on subtractive or formative technologies, additive manufacturing is principally characterized by the layerwise generation of three-dimensional structures. This innovative manufacturing paradigm allows for novel designs that cannot be achieved through conventional manufacturing processes. For example, unexploited lightweight potentials can be achieved by lattice structures generated by additive manufacturing [Plocher and Panesar, 2019].

Nowadays, several material types can be processed as feedstock in different additive manufacturing processes. Among others, polymers and metals are most commonly processed. The complementary technologies have rapidly developed from prototyping to small and medium-sized production, especially for polymers. Since the development of the first additive manufacturing technology for polymers in the 1980s, various additive manufacturing processes have found their way into commercialization. In general, these processes can be divided into three categories depending on the state of the feedstock [Gibson et al., 2015]:

- processes for the fusion of materials in the **powdery** state,
- processes for the fusion of materials in the **solid** state, and
- processes for the polymerization of materials in the **liquid** state.

The first mentioned can be divided into Selective Laser Sintering (SLS) and the proprietary Multi Jet Fusion (MJF) technology provided by HP Inc. The thermoplastic powder is selectively melted in both processes. Considering SLS, a laser beam directly fuses the polymer particles. Different from that, a heat-sensitive binding agent is jetted on the powder bed in the MJF process. Subsequently, the built-in infrared lamp activates the binding agent, and the wetted polymer particles melt

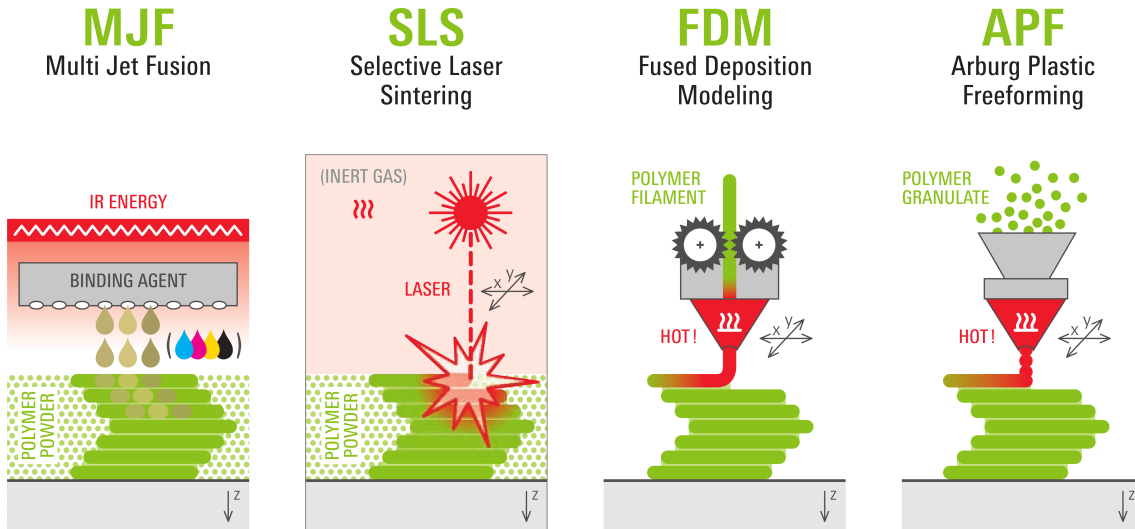


Figure 1.1. Additive manufacturing processes for the fusion of polymers in the powdery and solid state [Mesago Messe Frankfurt GmbH, 2021]

together.

Thermoplastic materials in the solid state are melted by means of a heated extruder head in the fused filament fabrication (FFF/FDM¹) process. Therein, the thermoplastic filament is pulled into the extruder head and deposited on the build plate in the melted state. Additionally, the ARBURG Plastic Freeforming (APF) utilizes a similar approach. Compared to the filament-based process, the thermoplastic material is in granular shape and melted by a screw extruder. Then, tiny droplets are deposited on the build plate. Thereby, a piezoelectric actor controls the drip rate. Fig. 1.1 shows an overview of the additive manufacturing processes for polymers in the powdery and solid states.

Photoreactive resins, also denoted as photopolymers, are principally used in additive manufacturing processes for polymers in the liquid state². Photopolymerization is the radiation-induced process of crosslinking reactive monomers and oligomers to form a solid polymer network. Moreover, this type of polymerization is subdivided into free-radical and cationic photopolymerization [Pappas, 1992; Nakamura, 2015]. Considering free-radical photopolymerization, the incident radiation decomposes the photoinitiator in the photopolymer resin. Then, the resulting free radicals connect with the monomers and oligomers [Scranton et al., 1997]. Comparatively, considering cationic photopolymerization, the reaction is started by carbenium ions [Kaiser,

¹Fused deposition modeling (FDM) is a trademark owned by Stratasys, Ltd.

²Additionally, the Liquid Additive Manufacturing (LAM) technology provided by innovatiQ GmbH & Co. KG processes a two-component liquid silicone rubber (LSR) whose polymerization is started by heat.

2006].

According to [Pappas, 1992], several advantages and limitations arise from photopolymerization in additive manufacturing processes. Among others, the rapid formation of the polymeric network represents an excellent property for being processed in additive manufacturing because a typical print job consists of several hundreds of layers, and every layer must be crosslinked. The most significant drawback results from the limitation of the glass transition temperature if the curing temperature is too low.

XU et al. stated that additive manufacturing processes employing photopolymerization have the fastest build speed and allow for the best surface quality among all other additive manufacturing processes for polymers [Xu et al., 2020]. Additionally, GIBSON et al. emphasize the accuracy of additively manufactured parts using photopolymers [Gibson et al., 2015]. However, the final mechanical properties of printed parts turn out to be a disadvantage compared to MJF and SLS. In 2019, systems based on photopolymerization served for $\approx 25\%$ of 97000 installed additive manufacturing systems for polymers in total. Furthermore, a compound annual growth rate of 10 % is expected through 2024 in terms of sales of additive manufacturing machines using photopolymerization [Xu et al., 2020].

If the number of worldwide installed AM machines using photopolymers continuously increases, the demand for novel materials increases as well. Additionally, these novel materials must be qualified for the desired application. The resulting qualification process is usually accompanied by extensive testing procedures that provide insight into the suitability of the material. Thus, existing devices for standardized experiments may have to be extended.

In order to predict the material properties of printed parts, one has to develop suitable model equations to describe the material behavior based on the experimental investigations mentioned above. Considering the photopolymerization process, describing the transition from the liquid state to the solid state is of great interest. As a result, optimized printing parameters deducted from model-based simulations can serve for the reduction of the tedious trial and error process that goes along with the identification of the correct printing parameters. Moreover, analyzing the capability of novel photopolymeric materials is facilitated for printing existing parts.

1.2 Additive manufacturing processes for photopolymers: state of the art and current research activities

Until now (2022), several processes exist for the additive manufacturing of photopolymers exhibiting different characteristics. However, all of them have one thing in common. The generated CAD file of the structure to be fabricated must be sliced into the resulting layers in a preprocessing step. Additionally, support structures are potentially added to the CAD file in order to stabilize the printing process. Usually, this procedure is automatically conducted through optimization algorithms by the supplied print job preparation software.

The first additive manufacturing technology using photopolymers was developed by 3D Systems in the 1980s and denoted as stereolithography (SLA). Therein, the photopolymer is filled into the vat of the machine and selectively cured by radiation emitted by a laser. Principally, the laser operates at wavelengths in the ultraviolet spectrum. For example, the printer Form 3L provided by Formlabs operates at 405 nm, whereas the ProX 950 provided by 3D Systems uses an Nd:YVO₄ laser operating at 354.7 nm [3D Systems, Inc., 2017; Formlabs, 2021]. The wavelength of the radiation emitted by the laser must always be chosen accordingly to the absorption spectrum of the employed photopolymer resin. Otherwise, the photoinitiators may not react to the incident radiation. Generally, the layer thickness can be adjusted down to several microns. However, reducing the layer thickness increases the print job duration. Thus, choosing the right layer thickness is always subject to the tradeoff between a sufficient vertical resolution and a reasonable print job duration. Comparatively, the horizontal resolution mainly depends on the spot size of the laser. The irradiance \mathcal{I} of the laser ($[\mathcal{I}] = \text{mW}/\text{cm}^2$) is attenuated while passing through the photopolymer layer and follows the BEER-LAMBERT law:

$$\mathcal{I}(z) = \mathcal{I}_0 \exp(-\alpha z) . \quad (1.1)$$

Herein, \mathcal{I}_0 is the incident irradiance at the surface of the photopolymer layer, and α is denoted as the attenuation factor. Hence, if the layer thickness is too large, the irradiance at the bottom of the layer may not be sufficient to cure the photopolymer at this depth. Once the laser has finished the trajectory in the present layer, the build plate is lowered by the layer thickness. Then, the cured layer is wetted with fresh resin by means of a wiper. Fig. 1.2 (right) shows a schematic of the SLA process using a top-down configuration. The laser is positioned above the photopolymer

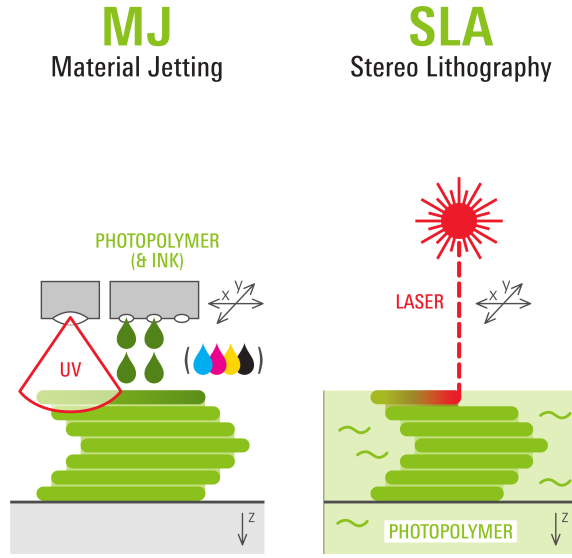


Figure 1.2. Schematics of material jetting and stereolithography [Mesago Messe Frankfurt GmbH, 2021]

vat in this configuration. Comparatively, using the bottom-up approach, the laser is positioned below the vat and irradiates the photopolymer through a transparent window. After finishing the print job, the printed structure is in the green state and cleaned in an ultrasonic bath filled with isopropanol to remove the excessive resin. Afterward, the printed structure is post-cured in a UV light chamber to achieve the final material properties.

PolyJet is a proprietary additive manufacturing technology using material jetting provided by the company Stratasys and primarily used for rapid prototyping. Therein, the photopolymer is jetted on the build plate layer by layer and simultaneously cured by a UV lamp, see fig. 1.2 (left). In order to achieve the necessary viscosity of the photopolymer, the print heads are heated to a specific temperature above ambient temperature. The combination of differently colored resins allows for multicolor printing. Additionally, photopolymers with different hardnesses can be combined to achieve a broad spectrum of material properties in the final printed object. Unfortunately, the photopolymeric material is contained in sealed cartridges. Thus, no third-party resins can be used, and the amount of possible applications is restricted by the provided photopolymers.

Reconsidering the SLA process, following a trajectory in the photopolymer layer through a laser is a significant drawback. This procedure is highly time-consuming because every layer has its trajectory to be irradiated. Therefore, irradiating the whole photopolymer layer at once can tremendously reduce the print job duration.

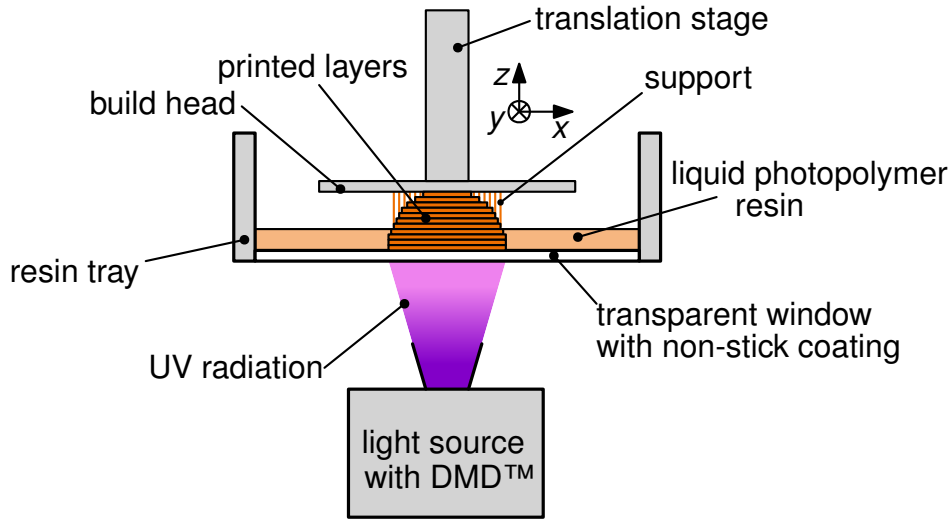


Figure 1.3. Cross-sectional schematic of a DLP™ additive manufacturing device

The Digital Light Processing (DLP™) technology, originally developed by Texas Instruments, enables the simultaneous irradiation of the photopolymer layer. Fig. 1.3 shows a cross-sectional schematic of the corresponding additive manufacturing device. Following the bottom-up approach, the light source and the Digital Micromirror Device™ (DMD™) are positioned below the resin tray. The light source emits the necessary radiation, which is reflected by the DMD™ and directed to the transparent window of the resin tray. The DMD™ consists of many tiny quadratic mirrors that can be tilted by $\pm 12^\circ$ in order to redirect or deflect the incident radiation [Brennesholtz and Stupp, 2008]. Most commonly, the light source is a LED, which is doped in the desired wavelength. Typical wavelengths are 405 nm (atum3D DLP Station 5-405) or 385 nm (Stratasys Origin® One) [atum3D, 2022; Stratasys, Ltd., 2021].

The slicing process results in monochrome images of the cross-sections of the CAD model perpendicular to the z -axis. Then, the light source projects the first image on the transparent window of the resin tray for a predefined exposure time. The radiation passes through the window and irradiates the photopolymer layer. It crosslinks and adheres to the build plate and the non-stick coating. Subsequently, the translation stage moves upwards and peels off the crosslinked photopolymer layer from the coating. New resin flows into the resulting gap and wets the coating. Following this, the translation stage moves downwards and adjusts the gap to the desired layer thickness. Afterward, the light source projects the following image on the transparent window, and the process continues until the print job has finished. Principally, the exposure times of the first layers are higher than those of the following layers in order to maintain sufficient adhesion between the printed part and the build plate.

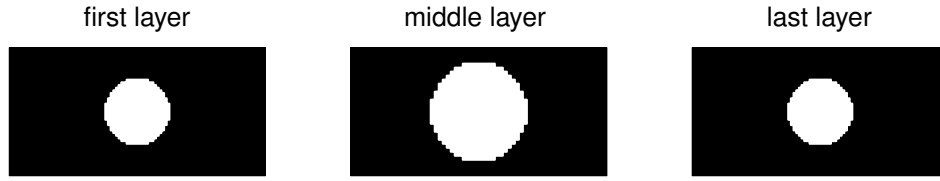


Figure 1.4. Images of selected slices of the printed sphere in fig. 1.3 (support structures are neglected). The stair-like approximation of the edges is caused by the resolution of the DMD™.

After finishing the print job, the printed structure is in the so-called green state. Hence, the printed part is additionally irradiated in a curing chamber to achieve the final material properties.

As mentioned above, the slicing process results in rectangles, which approximate the curvature of the sphere's surface. Considering the printed sphere in fig. 1.3, the surface quality of the sphere significantly depends on the chosen layer thickness. If the layer thickness decreases, the quality of the approximation increases, but the print job duration increases tremendously.

Fig. 1.4 shows selected monochrome images resulting from the slicing process for the printed sphere in fig. 1.3. The projected cross-section is indicated by white pixels, and the unexposed pixels remain black. The first layer is identical to the last one, whereas the middle layer exhibits a larger diameter.

The cross-sections of the printed sphere are circles. Since each mirror of the DMD™ represents one pixel of the projected image, the reproduction of arbitrary-shaped edges is limited by the number of arrays. Hence, the curvature is approximated by the pixels of the DMD™. Principally, all images with edges that are not parallel to the x - and y -axis are approximated. The resulting dimension of the image, i.e., the printing dimension in the x - y -plane, is calculated by multiplying the size of the mirrors with the number of employed mirrors. For example, the atum3D DLP Station 5-405 utilizes 1920 mirrors in the x -direction and 1080 mirrors in the y -direction with an edge length of 100 μm . Thus, the printing dimension in the x - y -plane is 192 mm x 108 mm. Comparatively, the Stratasys Origin® One provides a resolution of 3840 x 2160 pixels with the same printing dimension. Hence, the edge length of the mirrors is 50 μm .

Compared to SLA, the print job duration is strongly reduced by irradiating the whole layer at once. However, since the exposure time of each layer is only several seconds, the print job duration mainly depends on the repetitive movement of the translation stage. In order to eliminate this drawback, Carbon® developed the

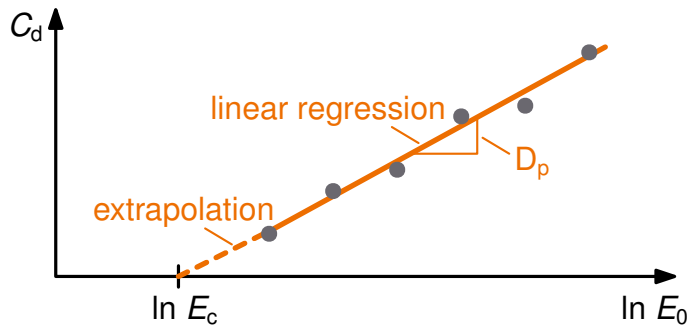


Figure 1.5. Schematic diagram of the working curve equation

Continuous Liquid Interface ProductionTM technology (CLIPTM) [Tumbleston et al., 2015]. Therein, the transparent window is made of TeflonTM AF 2400, which enables the permission of oxygen. Oxygen inhibits the crosslinking reaction of photopolymers [Ligon et al., 2014]. Consequently, a dead zone forms up between the TeflonTM window and the crosslinked photopolymer. Hence, the crosslinked photopolymer does not adhere to the transparent window, and the printed structure can be continuously elevated out of the resin tray. The CLIPTM technology allows for print speeds greater than 1000 mm/h. However, increasing the print speed deteriorates the vertical resolution of the printed structure.

Furthermore, efficiency gains can be achieved by increasing the temperature of the photopolymer resin during the manufacturing process. Elevating the temperature of the resin yields a higher reactivity of its constituents [Dall’Argine et al., 2020]. Thus, the conversion of the photopolymer can be accelerated. For example, the double bond conversion of dimethylacrylates can be increased by 21 percentage points if the temperature of the photopolymer is increased from 23 °C to 70 °C [Steyrer et al., 2018]. Additionally, the viscosity of the photopolymer decreases. This behavior enables the processing of resins exhibiting a high viscosity at room temperature [Dall’Argine et al., 2020]. The Austrian-based company Cubicure GmbH developed the hot lithography technology to process high viscosity photopolymers at operating temperatures up to 120 °C [Pfaffinger, 2018]. Thereby, a heated coating unit applies the photopolymer layer to the resin tray.

Since the research activities in terms of additive manufacturing of photopolymers continuously increase along with the general market growth, the experimental characterization, the modeling of the accompanying phenomena, and the simulation of the processes and fabricated parts are of particular interest.

One of the most established methods to predict the crosslinking progress in the photopolymer layer is the working curve model, which was developed by JACOBS

at the beginning of the commercialization of 3D System's Stereolithography process [Jacobs, 1992]. Precisely, the relationship between the cured depth C_d of the photopolymer layer and the exposure dose $E_0 = \mathcal{I}_0 \cdot t$ is derived from the BEER-LAMBERT law in eq. (1.1) and described by

$$C_d = D_p \ln \left(\frac{E_0}{E_c} \right) . \quad (1.2)$$

The penetration depth D_p is the slope of the working curve in a semi-logarithmic C_d - E_0 plot. The critical exposure dose E_c represents the necessary amount of irradiation to solidify an infinitesimally thin photopolymer layer ($C_d \rightarrow 0$). Thus, E_c corresponds to the gel-point of the photopolymer [Jacobs, 1992].

In order to generate the required data points for identifying the working curve parameters D_p and E_c , several exposure doses E_{0i} are chosen to create photopolymer layers with different thicknesses. Then, the thicknesses C_{di} of the layers are measured through calipers, profilometers, or confocal microscopes [Bennett, 2017]. Subsequently, the resulting data points, indicated as gray dots in fig. 1.5, are visualized in the semi-logarithmic C_d - E_0 plot. Next, D_p and E_c are identified by applying linear regression to the data set. Since the data points are created for finite layer thicknesses, the critical exposure dose E_c is the intersection of the extrapolated working curve with the abscissa.

Furthermore, calorimetric measurements conducted by a Differential Scanning Calorimetry (DSC) device provide a deep insight into the crosslinking progress of photopolymers. Therefore, the DSC device must be modified to allow for the consideration of radiation-induced crosslinking reactions (photo-DSC). Since the crosslinking reaction is an exothermic process, heat is generated and measured by the DSC as the rate of heat flow. As a result, the exothermic rate of heat flow corresponds to the rate of the degree of cure. During the last four decades, photo-DSC measurements have been extensively applied for the experimental characterization of photopolymers [Tryson and Shultz, 1979; Maffezzoli and Terzi, 1998; Rusu et al., 2012]. Most recently, this experimental method is also applied to characterize photopolymer resins processed in additive manufacturing [Kim et al., 2017; Obst et al., 2020; Rehbein et al., 2020; Bachmann et al., 2021]. Moreover, the crosslinking progress of photopolymers can also be measured by Raman spectroscopy [Martin et al., 2018].

The progressing crosslinks in the photopolymer layer go along with the reduction of the volume of the photopolymer, which is denoted as chemical shrinkage. The chemical shrinkage can lead to undesired warpage and residual stresses of the printed



Figure 1.6. Adidas® 4DFWD running shoe with additively manufactured midsole [Carbon, Inc., 2021]

structure. In order to record the chemical shrinkage depending on the progressing crosslinks, KOSEKI et al. developed an in situ measuring system based on a confocal displacement meter [Koseki et al., 2013]. Comparatively, the axial strain of the photopolymer layer resulting from the shrinkage can be measured by a linometer [Park et al., 2016]. Unfortunately, density measurements only allow for the determination of the chemical shrinkage at selected conversion states.

In order to predict the chemical shrinkage, the residual stresses, and the material properties of photopolymers in additive manufacturing through simulations based on the finite element method, BARTOLO, WU et al., and WESTBEEK et al. developed material models capturing these phenomena [da Silva Bartolo, 2007; Wu et al., 2018; Westbeek et al., 2020, 2021]. Additionally, they set up simulation frameworks considering the incident radiation as a spatially distributed boundary condition. Moreover, the simulation of the macroscopic material response of printed photopolymeric parts using the methods of continuum mechanics is the subject of the investigations in [Weeger et al., 2019; Hossain and Liao, 2020; Hossain et al., 2020].

Additive manufacturing of photopolymers has found its way into several applications. Among others, Adidas® has collaborated with Carbon® in order to develop an additively manufactured midsole with an anisotropic lattice structure using Carbon®'s proprietary Digital Light Synthesis® (DLS®) technology and an elastomeric photopolymer resin, see fig. 1.6. In order to achieve the desired macroscopic mechanical properties, the design of lattice structures is subject to solving an optimization problem [Nika and Constantinescu, 2019; Agnelli et al., 2020, 2021]. Principally, the resulting polymeric lattice structure exhibits viscoelastic behavior on the macroscopic scale [Krödel et al., 2017].

Furthermore, clear orthodontic aligners are increasingly fabricated using additive manufacturing technologies for photopolymers [Tartaglia et al., 2021]. Photopolymers also serve as matrix material for the fabrication of short fiber reinforced composites using additive manufacturing processes [Cheah et al., 1999; Schlotthauer et al., 2021]. Naturally, these applications do not represent the full spectrum of possibilities of photopolymers processed in additive manufacturing and are only mentioned as illustrative examples.

1.3 Objectives and structure of work

The main objective of the present doctoral thesis is the continuum-mechanical modeling of photopolymers in additive manufacturing processes based on experiments conducted with a representative and commercially available photopolymer. Precisely, DLP is chosen as the underlying process due to its benefits compared to SLA, PolyJet, or other additive manufacturing processes for photopolymers. The material model is intended to describe the phenomena that occur during the crosslinking of the photopolymer depending on the process parameters, namely irradiance, the temperature of the photopolymer, and exposure time.

The results of the conducted experiments serve as basis for the development of the constitutive model. In detail, the experiments comprise the measurement of the crosslinking progress and its effects on the material properties of the photopolymer depending on the process parameters mentioned above. Therefore, the existing experimental devices (DSC, rheometer) must be extended in order to implement the radiation. Most of the experimental investigations in the references discussed in the preceding section do not consider the spectral power distribution of the employed light source. Hence, appropriate filters must be selected in accordance with the wavelength of the utilized DLP device. Additionally, the description of the experimental methods is supposed to serve as a guidance for researchers in order to characterize novel photopolymers efficiently.

Finally, the developed model equations and the associated parameters are validated by comparing three-dimensional finite element simulations with the experimental data.

In order to conduct the investigations in terms of the objectives mentioned above, this thesis is split into three parts. First, the experimental characterization of a pre-selected photopolymer is conducted in ch. 2. Therein, the material properties of the photopolymer are determined in the liquid and solid state by means of sophisticated experimental methods. Additionally, special attention is paid to the transition from

the liquid to the solid state.

Following this, the material model is developed and numerically discretized in ch. 3 using a continuum-mechanical framework for the reproduction of the experimental phenomena. The associated model parameters are identified in ch. 4 by means of established optimization techniques. Moreover, the proposed material model and the identified parameters are validated by simulations of cyclic tension tests.

Last but not least, the thesis concludes with a summary of the most important findings of the conducted investigations and a presentation of open questions for future considerations in ch. 5.

2 Experimental Characterization

This chapter comprises the experimental characterization of photopolymer resins using several experimental methods. Therefore, the general applicability of the presented experimental methods is shown using a commercial photopolymer resin. The findings of this chapter serve as a basis for the material modeling following after.

2.1 Investigated material and employed DLP printer

Due to the rapid increase of different additive manufacturing processes that use photopolymer resins as the feedstock, many companies extended their product portfolio with suitable resin formulations aiming towards various areas of application.

The following reasons mainly drive the selection of an appropriate resin for the subsequent investigations:

- The resin should distinctly exhibit elastic-plastic behavior at small deformations in the tensile tests. According to sec. 3.3, this behavior can be represented by hypoelastic material models, which are also suitable for modeling curing processes.
- The glass transition temperature θ_g of the resin should be significantly above room temperature but also below $\theta = 100^\circ\text{C}$ for the fully cured state. At lower degrees of cure, the glass transition temperature is smaller. Consequently, tensile tests of printed specimens will show a completely different behavior compared to the fully cured state if the temperature of the specimen is slightly changed.
- The resin should be acquirable in small containers ($< 1000\text{ ml}$) with resealable closures. Comparatively, the cartridges for the proprietary PolyJet[®] process are sealed and cannot be opened without damaging the container. Therefore, proprietary resins are not suitable for the investigations in this thesis.

A suitable resin according to the requirements mentioned above is the Loctite[®] 3D 3818 photopolymer resin, which is selected for the investigations in this thesis

[Henkel Corp., 2019]. This photopolymer is an acrylic resin primarily used for prototyping applications. Furthermore, pigments are added to the resin for a black appearance. The findings of this thesis can also be transferred to other additive manufacturing systems using the same photopolymer resin.

The Loctite® EQ PR10.1 DLP 3D printer is used to fabricate the specimens for the DMA and tensile tests following later¹. Its print dimension is 192 mm x 108 mm x 250 mm. Moreover, the projector emits radiation with a resolution of 1920 x 1080 pixels at 405 nm. The maximum irradiance can be set to 15 mW/cm². The open system allows for the processing of all third-party photopolymer resins that cure at a wavelength of 405 nm. All relevant printing parameters (layer thickness, irradiance, and exposure time) can be adjusted. However, the minimum layer thickness is 6 μ m. Unfortunately, the temperature of the resin tray cannot be controlled during the printing process.

Furthermore, the EQ CL36 LED cure chamber provided by Loctite® is employed to post-cure the specimens and to achieve their fully cured state. The LEDs of the device also operate at 405 nm and can provide a maximum irradiance of 205 mW/cm². Furthermore, the table on which the printed parts are placed can be rotated while the printed parts are irradiated.

2.2 Differential Scanning Calorimetry (DSC)

Caloric measurements using a differential scanning calorimetry (DSC) device provide insight into the different characteristics of polymers. In particular, these include

- the glass transition temperature,
- the melting,
- the crystallization,
- the isobaric specific heat capacity, and
- the crosslinking of polymers [Menczel and Prime, 2009].

The characteristics mentioned above are derived from the DSC signal, the mass-specific differential heat flow² \dot{q} calculated between the investigated specimen stored in the specimen crucible and an empty reference crucible. Both crucibles are then exposed to a predefined temperature program in a controlled atmosphere [Höhne et al., 2003]. Several inert gases can be used to maintain this atmosphere. Gaseous

¹This device is identical to the DLP STATION 5-405 provided by atum3D.

²Precisely, \dot{q} actually denotes the specific heat flow rate.

nitrogen is frequently used due to its lower costs compared to argon or helium [Frick and Stern, 2013].

In the following, the TA[®] Instruments Q2000 DSC is employed to investigate the calorimetric properties of the selected photopolymer. Special attention is paid to the crosslinking behavior of the photopolymer.

2.2.1 Experimental setup and governing equations

Different from disk-type or cylinder-type heat flux DSC measuring systems, turret-type systems provide several benefits. Principally, higher sensitivity and larger heating and cooling rates can be achieved. Moreover, only a small sample volume is necessary to achieve satisfactory results [Höhne et al., 2003]. In order to account for these benefits, DANLEY developed the Tzero[™] sensor with turret-type platforms. Therefore, the following considerations are motivated and inspired by [Danley, 2003].

Fig. 2.1 shows the cross-sectional view of the Tzero[™] sensor. The reference and sample platforms have the shape of thin-walled circular turrets and are made of constantan. Chromel disks are welded to the bottom of each platform. Additionally, chromel wires are connected to the disks. Two wires made of constantan and chromel are located in the middle of the constantan base. Likewise, they are also welded to the constantan base.

A pair of chromel and constantan wires form a thermocouple. Therefore, the temperature at the reference platform θ_r is measured between the chromel wire located at the reference platform and the constantan wire located in the middle of the constantan base. Similarly, the temperature at the sample platform θ_s is measured between the chromel wire located at the sample form and the constantan wire located in the middle of the constantan base. The temperature θ_0 controls the temperature program of the measurement and is measured between the chromel and constantan wires located in the middle of the constantan base.

Employing the lumped capacitance method³, the sample and reference specific heat flows are expressed by

$$\dot{Q}_s = \frac{\theta_0 - \theta_s}{R_s} - C_s \dot{\theta}_s \quad (2.1)$$

$$\dot{Q}_r = \frac{\theta_0 - \theta_r}{R_r} - C_r \dot{\theta}_r . \quad (2.2)$$

³See [Holman, 2010; Bergman and Lavine, 2017] for detailed explanations.

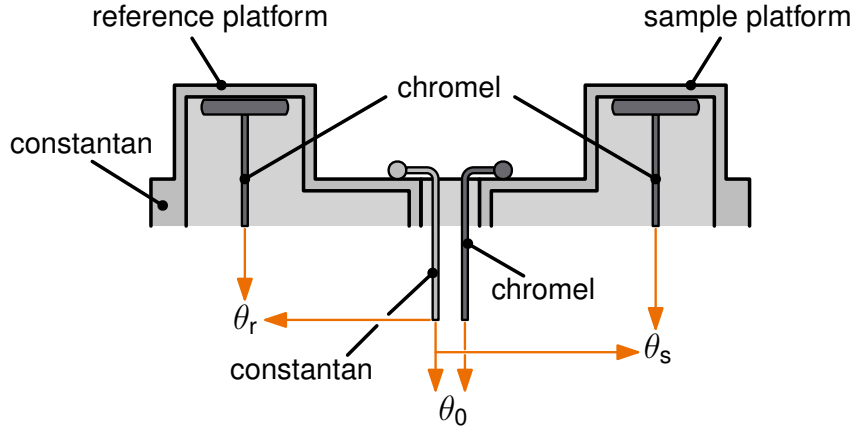


Figure 2.1. Cross-sectional view of the Tzero™ sensor of the TA® Instruments Q2000 DSC (derived from and inspired by [Danley, 2003])

Therein, R_r and R_s are the thermal resistances of the reference and sample platforms. C_r and C_s are the reference and sample heat capacities, respectively. Consequently, the differential heat flow \dot{Q} calculated between the heat flows at the sample and reference platforms reads as

$$\begin{aligned} \dot{Q} &= \dot{Q}_s - \dot{Q}_r \\ &= -\frac{\theta_s - \theta_r}{R_r} + (\theta_0 - \theta_s) \left(\frac{1}{R_s} - \frac{1}{R_r} \right) + (C_r - C_s) \dot{\theta}_s - C_r (\dot{\theta}_s - \dot{\theta}_r) , \end{aligned} \quad (2.3)$$

which is also denoted as the T4 heat flow equation. The first summand represents the general DSC heat flow signal, which is also measured by conventional disk-type measuring systems. The second summand accounts for imbalances between the thermal resistances of the sample and reference platforms, which improves the baseline signal. Furthermore, the third summand considers imbalances between the reference and sample heat capacities, which also improves the baseline signal. In contrast, the fourth summand takes into account differences between the measured sample and reference heating or cooling rates, enhancing the overall measurement resolution. The latter one goes along with transitions of the sample (e.g., glass transition, melting, crystallization, and crosslinking). The measured differential heat flow in eq. (2.3) is divided by the specimen mass in order to obtain mass-specific quantities:

$$\dot{q} = \frac{\dot{Q}}{m_{\text{specimen}}} . \quad (2.4)$$

In order to determine the constants R_r , R_s , C_r , and C_s , a two-step calibration procedure must be conducted for the desired temperature range before starting the

measurement. First, considering an empty cell, the heat flows \dot{Q}_s and \dot{Q}_r in the eqs. (2.1) and (2.2) are zero. Hence, the products $C_s R_s$ and $C_r R_r$ can be calculated by means of the measured temperatures. Next, sapphire disks are placed on the sample and reference platforms. Since sapphire melts at temperatures above 2000 °C and its temperature-dependent specific heat capacity is known over a broad temperature range, the sample and reference heat flows in the eqs. (2.1) and (2.2) can be calculated by the products of the individual sapphire disk mass, specific heat capacity, and the sample and reference heating rates. Thus, the four necessary equations are determined to calculate the four constants. Additionally, the measurement inaccuracy of the temperature is taken into account by comparing the theoretical and actual melting temperatures of standard materials (e.g., indium, tin, and zinc).

The explanations mentioned above are limited to standard analyses of calorimetric properties of substances. In order to investigate the crosslinking properties of photopolymer, the DSC must be extended to convey the radiation into the measuring cell.

2.2.2 Extension with the OmniCure® S2000 curing system for photo-DSC measurements

Fig. 2.2 shows the experimental setup of the TA® Instruments Q2000 DSC extended by the photocalorimetric accessory. In order to generate the necessary radiation in the desired wavelength range, the OmniCure® S2000 curing system provided by Excelitas Technologies® Corp. is connected to the DSC via a serial cable. The OmniCure® S2000 curing system contains a high-pressure mercury-vapor lamp, which emits the radiation required to start the crosslinking reaction of the photopolymer.

Fig. 2.3 shows the spectral flux diagram of the high-pressure mercury-vapor lamp (gray). Therein, the wavelength-specific power of the lamp is plotted versus the wavelength. Three distinct peaks are visible at 365 nm, 405 nm, and 435 nm, which are typical for this type of gas-discharge lamp. Additionally, the OmniCure® S2000 curing system is equipped with an internal bandpass filter that restricts the emitted radiation to the wavelength range 320...500 nm. Hence, the smaller peaks at wavelengths below 320 nm or above 500 nm are omitted.

In order to investigate the crosslinking properties of photopolymers that are processed by DLP printers operating at $\lambda = 405$ nm, the spectrum of the mercury-vapor

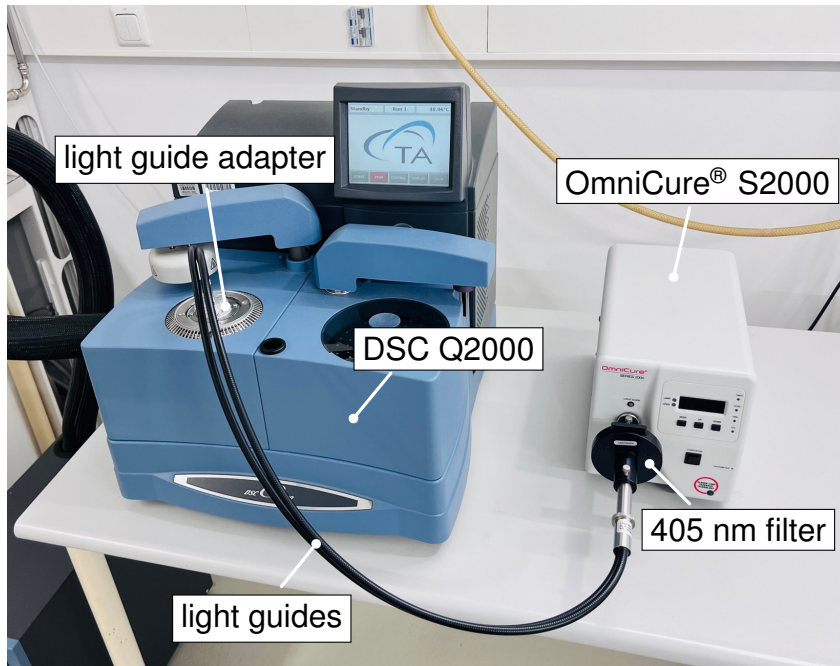


Figure 2.2. Experimental setup of the photo-DSC

lamp must be further restricted. Hence, a filter adapter in conjunction with a band-pass filter operating at $\lambda = 405 \pm 20$ nm is plugged into the output socket of the OmniCure® S2000 curing system, as depicted in fig. 2.2. The relative transmittance of the additional bandpass filter is depicted in fig. 2.3 (orange). Eventually, multiplying the spectral flux diagram of the mercury-vapor lamp with the relative transmittance of the additional bandpass filter yields the resulting spectral flux diagram, which is visualized in fig. 2.4. Depending on the employed semiconductor material, standard LEDs operating in the wavelength range of UV Light typically have a half-power bandwidth ranging from 6 nm to 20 nm [Pedrotti et al., 2005; Dr. Hönle AG, 2020]. Thus, the resulting spectral flux in fig. 2.4 can be considered equivalent to the spectrum of the UV led in the DLP printer. If the bandpass filter is not used, the crosslinking reaction may be accelerated because some constituents of the photopolymer react on irradiation operating at wavelengths below or above 405 nm. This scenario would influence the measurement.

Two glass fiber light guides transport the emitted radiation into the DSC measuring cell. They are held in position by the light guide adapter base, mounted on top of the DSC measuring cell. A schematic cross-sectional view of the DSC measuring cell with the installed photo-DSC extension is depicted in fig. 2.5 with the light guides, the quartz glass plate, and the inner and outer silver lids.

The calibration of the constants in the eqs. (2.1) and (2.2) is conducted with two

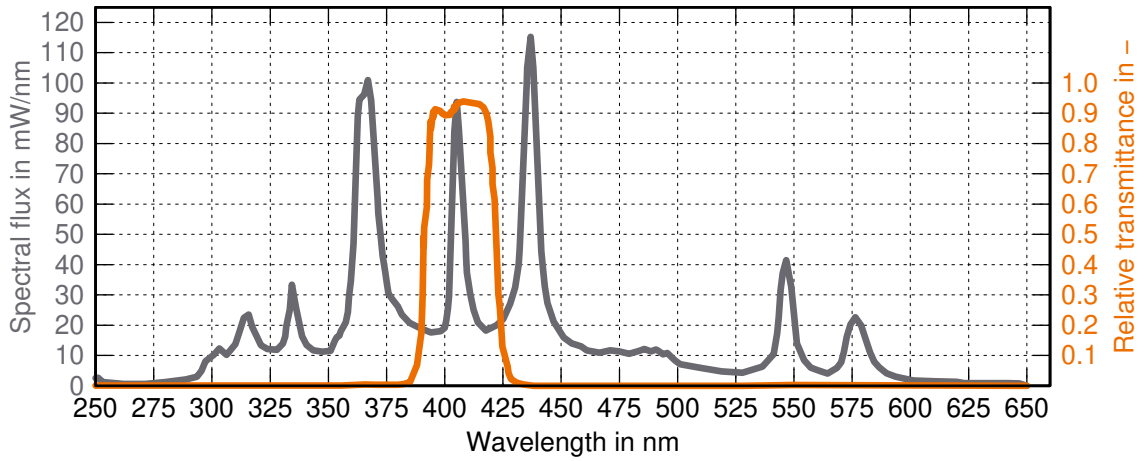


Figure 2.3. Diagram of the spectral flux (grey) of the high pressure mercury vapor lamp of the OmniCure® S2000 curing system without the internal 320 - 500 nm bandpass filter (derived from [Excelitas Technology Corp., 2014b]) and relative transmittance of the additional 405 ± 10 nm bandpass filter (orange)

closed silver lids. Thus, the perforated silver lids and the quartz glass plate in fig. 2.5 are employed so that the experimental setup is most consistent with the calibration constants while passing the incident radiation. Neutral density filters are placed at the end of the light guides in order to reduce the irradiance of the incident radiation. Since the absolute power of the mercury-vapor lamp causes a comparatively high irradiance on the platform surfaces of the DSC sensor⁴, the neutral density filters reduce the incident radiation to 1 % of its initial value. It should be noted that the irradiance is further reduced due to the air gaps between the neutral density filter and the quartz glass plate, as well as between the inner silver lid and the crucibles in the measurement cell. Furthermore, the iris of the shutter of the OmniCure® S2000 curing system can be opened in relative steps of 1 %. Thus, the irradiance can be adjusted to reasonable values concerning the DLP printing process.

According to [Pedrotti et al., 2005], optical radiation can be measured by means of the following two detector types:

- thermal detectors and
- quantum detectors.

The first mentioned include thermocouples and thermopiles, whereas the latter ones comprise photodiodes, among others. Principally, thermal detectors are insensitive to the wavelength of the emitted radiation. Comparatively, quantum detectors are

⁴The platforms have a diameter of ≈ 5 mm.

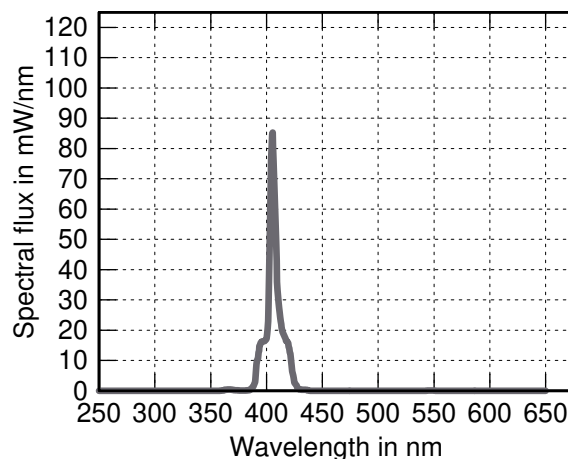


Figure 2.4. Resulting diagram of the spectral flux of the high pressure mercury vapor lamp of the OmniCure[®] S2000 curing system using the additional 405 ± 20 nm bandpass filter

limited to a narrow wavelength range and must be selected with respect to the wavelength of the source of the emitted radiation.

Before conducting the crosslinking measurement, one must calibrate the irradiance at the sample and reference platforms. The reference and sample platforms each form a thermocouple with the chromel disks and wires welded to the bottom of each platform. As a consequence, the incident radiation is absorbed by the platforms and causes a rise in the temperatures of the platforms θ_s and θ_r . Then, the eqs. (2.1) and (2.2) determine the resulting heat flows by means of the previously calibrated constants. The heat flows are divided by the surface area of the platforms leading to the irradiances \mathcal{I} at each platform ($[\mathcal{I}] = \text{mW}/\text{cm}^2$) [TA[®] Instruments, 2019]. One should note that the mentioned calibration steps are carried out with an empty DSC cell. Hence, no crucibles are placed on the platforms. The measured irradiances are displayed on the screen of the DSC in real-time, so that they can be adjusted to the desired value by changing the iris setting of the OmniCure[®] S2000 curing system. Moreover, the vertical alignment screws allow for the balancing of slight deviations between the displayed values of the irradiance on the reference and sample platforms.

2.2.3 Crosslinking

The characteristic shape of a crosslinking measurement by means of photo-DSC is depicted in Fig. 2.6. Each photo-DSC measurement comprises two subsequent runs. In the first run, the specimen is cured by the incident radiation, which yields the orange curve in Fig. 2.6. Afterward, the cured sample is irradiated a second time using the same measurement procedure to measure the specific heat flow generated by the incident radiation (grey curve).

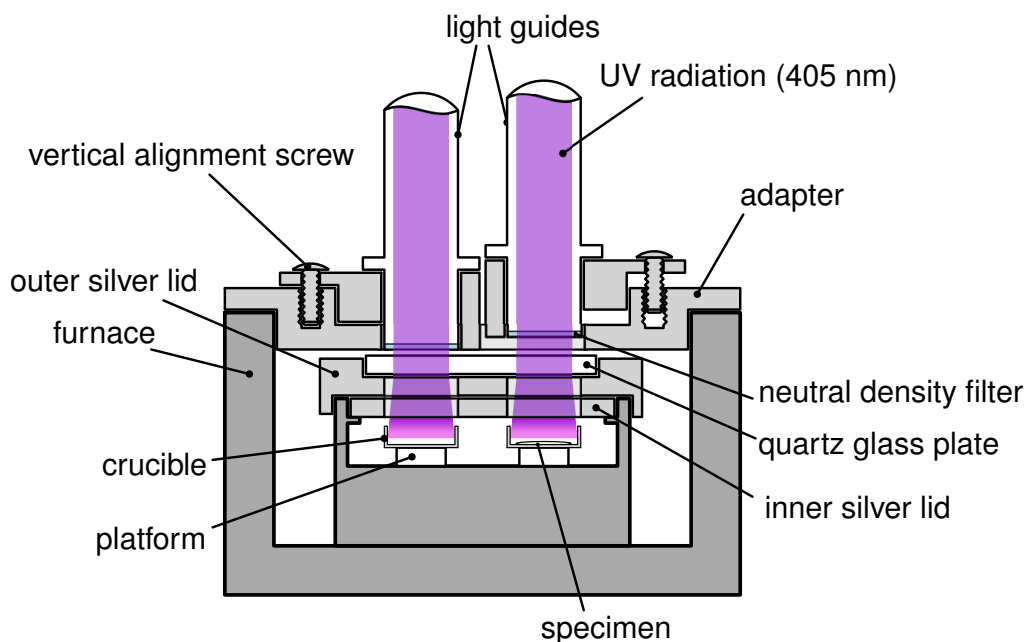


Figure 2.5. Schematic cross-sectional view of the DSC measurement cell with installed photo-DSC extension and vertically aligned light guides

Upon opening the shutter, a steep increase of the exothermic specific heat flow is visible in the first seconds. After reaching the peak value \dot{q}_{\max} , the crosslinking speed strongly decelerates, and the signal of the specific heat flow tends towards the baseline generated by the second measurement.

Particular attention should be paid to the enlarged section in fig. 2.6. Theoretically, the measurements of the first and the second run perfectly overlap after all reacting molecules of the photopolymer have been crosslinked. Since this is only a hypothetical scenario, a slight deviation is visible between the two runs.

Principally, a strong dependency on the temperature of the photopolymer resin can be expected. This dependency considerably influences the overall conversion rate and the amount of released specific heat at the end of the exposure. Thus, the resulting measurement procedure is split into three segments and reads as follows:

1. Equilibrate the specimen at a constant temperature and maintain the temperature for the predefined duration t_1 .
2. Open the shutter and irradiate both crucibles at a constant and precalibrated irradiance for the predefined duration t_2 . The crosslinking reaction starts and the DSC measures the exothermic signal generated by the crosslinking specimen.

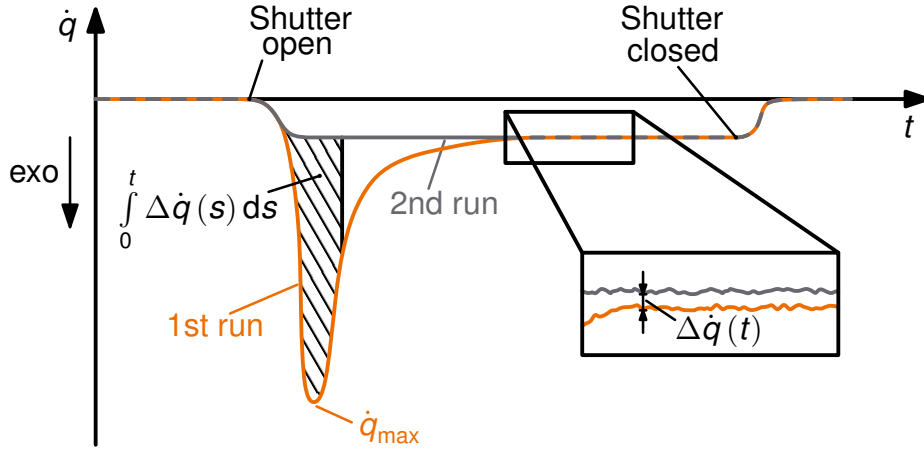


Figure 2.6. Schematic diagram of a typical photo-DSC measurement using two subsequent runs (inspired by [Menczel and Prime, 2009])

3. Close the shutter and maintain the constant temperature for the predefined duration t_3 .

This procedure is applied to both runs of each measurement. After finishing the second run, the signal of the specific differential heat flow of the second run is subtracted from the first run to evaluate the exothermic specific differential heat flow corresponding to the crosslinking reaction of the photopolymer:

$$\Delta \dot{q}(t) = \dot{q}_1(t) - \dot{q}_2(t) . \quad (2.5)$$

The slight deviation between the first and the second run at the end of the irradiation may cause bias. Avoiding this, a termination criterion must be defined to evaluate the measurements. Consequently, the data are neglected when the difference of the specific differential heat flows reaches one percent of its peak value:

$$\Delta \dot{q}(t) < 0.01 \cdot (\dot{q}_{\max,1} - \dot{q}_{\max,2}) . \quad (2.6)$$

Otherwise, the small deviation between the specific heat flows of the first and the second run would significantly contribute to the computation of the degree of cure, which is not physically sound and only caused by the inaccuracy of the device. Other techniques, such as considering equal exposures for different irradiances as a termination criterion, are also proven methods [Maffezzoli and Terzi, 1998].

Eventually, the time-dependent degree of cure $c(t)$ is computed through the cumu-

lative integral of the specific differential heat flow:

$$c(t) = \frac{\int_0^t \Delta \dot{q}(s) ds}{h_{\text{tot}}} . \quad (2.7)$$

Herein, h_{tot} denotes the total specific heat of a reaction for the fully crosslinked photopolymer, i.e., $c = 1$. It must be determined independently using a non-isothermal temperature profile while simultaneously irradiating the sample.

Previous investigations show that an oxygen atmosphere decelerates the crosslinking reaction [Rusu et al., 2012]. Considering DLP, the photopolymer layer does not stay in contact with the atmosphere. Hence, the DSC measuring cell is flooded with gaseous nitrogen to prevent limiting effects caused by oxygen.

Before presenting the results of the photo-DSC measurements under the influence of different temperatures and irradiances, the influence of the specimen mass is investigated in the photo-DSC measurements.

Influence of the specimen mass and guidelines for the dosage of the photopolymer According to the BEER-LAMBERT law, see eq. (1.1), the irradiance is a function of the vertical position in the photopolymer layer and decreases. Hence, significant attention should be paid to the layer thickness of the photopolymer specimen in the crucible and its dosage.

The bottom of the chosen Tzero™ crucibles is circular and has an area of approximately 19.63 mm². Given the density of the uncured resin ($\rho = 1.1 \frac{\text{mg}}{\text{mm}^3}$), the following height-specific mass is defined:

$$\bar{m} = 21.593 \frac{\text{mg}}{\text{mm}} . \quad (2.8)$$

The specimen has a cylindrical, poker chip-like shape if a uniform distribution of the photopolymer resin is assumed. Specimen masses can be calculated using this specific mass for a predefined layer thickness in the sample crucible. The typical layer thickness in DLP is in the range of 50 μm to 100 μm , which leads to the following lower and upper boundaries for the specimen mass:

$$m(50 \mu\text{m}) = 1.07965 \text{ mg} \quad \text{and} \quad m(100 \mu\text{m}) = 2.1593 \text{ mg} . \quad (2.9)$$

Compared to standard DSC measurements of the crosslinking process of thermosetting epoxy resins or adhesives, see [Wenzel, 2005; Menzel, 2011; Liebl, 2014], the typical specimen mass in photocalorimetric measurements is significantly lower. In

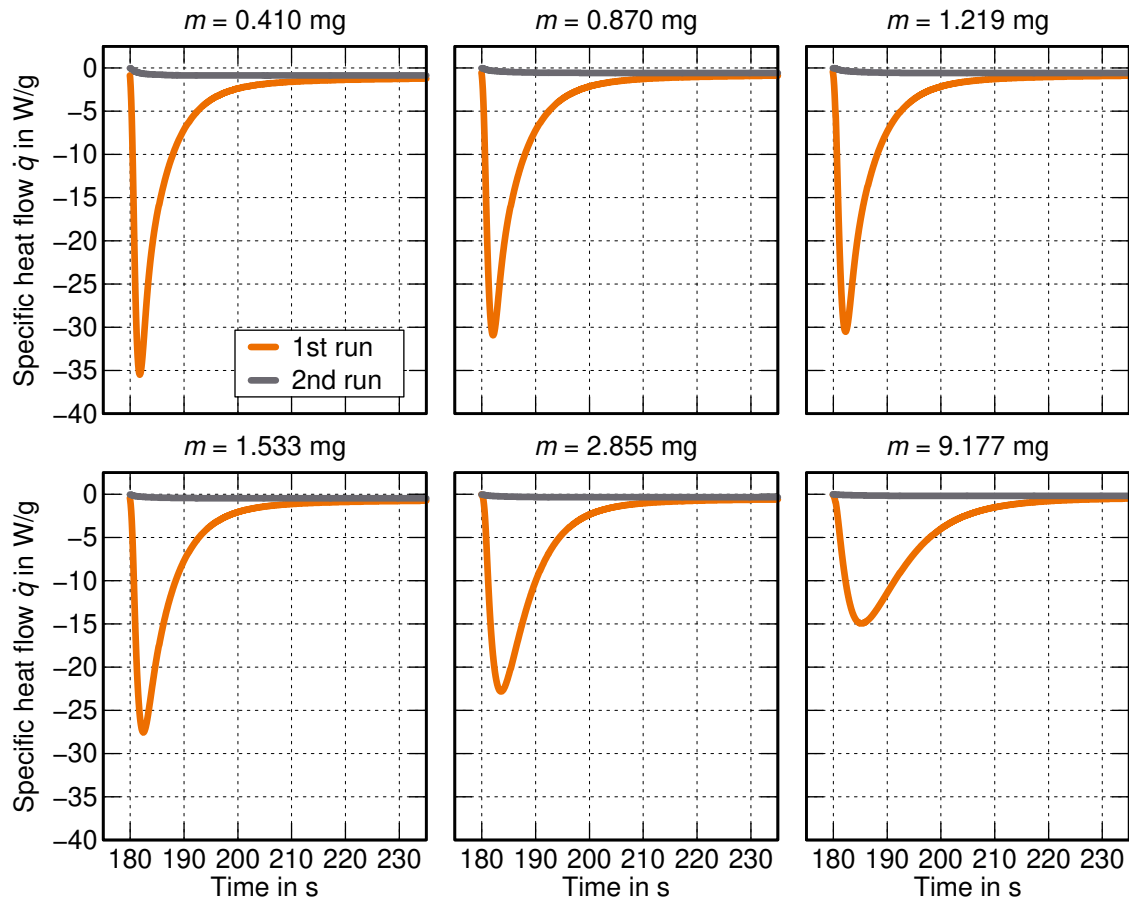


Figure 2.7. Diagrams of the specific differential heat flow depending on the specimen mass

order to investigate the influence of the specimen mass on the results of the photo-DSC measurements, several crucibles are prepared with increasing specimen mass. Six crucibles are prepared with photopolymer specimens ranging from 0.41 mg to 9.177 mg. The photopolymer is drawn up using a pipette, and a small drop is filled into the crucible. Then, using a wooden toothpick [Menczel and Prime, 2009], the photopolymer drop is distributed across the crucible's bottom area, forming a homogeneously distributed layer. Then, the crucible with the specimen is weighed using a high-precision scale. Prior to that, the mass of the empty crucible is determined to calculate the resulting specimen mass. All preparation steps are conducted with minimal room lighting. The purge gas flow rate is set to 50 ml/min. The measurements are conducted isothermally ($\theta = 20$ °C). Before opening the shutter, the DSC measuring cell is equilibrated for three minutes. The exposure time is set to ten minutes. After closing the shutter, the temperature is held constant for another three minutes, and the measurement is repeated.

Table 2.1. Evaluated specific reaction heats depending on the specimen mass

Specimen mass in mg	Specific heat of reaction in J/g	Resulting degree of cure in -
0.410	223.9	0.817
0.870	217.1	0.792
1.219	218.1	0.796
1.533	217.7	0.794
2.855	225.2	0.822
9.177	228.5	0.834

Fig. 2.7 shows the results of the measurements in the first 55 seconds after opening the shutter. Increasing the specimen mass leads to the following phenomena:

- The peak of the reaction of the first run decreases. Increasing the specimen mass from 0.41 mg to 9.177 mg reduces the reaction peak by more than 50 %.
- Additionally, the associated abscissa value of the reaction peak is slightly shifted to the right. Hence, the crosslinking is slower.
- Furthermore, the first run's heat flow signal approaches the second run's signal more slowly. However, the influence of the specimen mass on the second run is less pronounced.

Consequently, increasing the specimen mass decelerates the crosslinking reaction caused by the inhomogeneous distribution of the irradiance in the specimen.

Table 2.1 shows the specific heat of reaction of the conducted measurements and the corresponding degrees of cure. The specific heat of reaction is calculated using the numerator in eq. (2.7) for the exposure time corresponding to the termination criterion in eq. (2.6). Similarly, the degrees of cure are calculated through eq. (2.7) and $h_{\text{tot}} = 274.04 \text{ J/g}^5$.

Fortunately, the chosen specimen mass only influences the crosslinking speed and has a minor influence on the specific heat of reaction and the resulting degree of cure. The maximum relative deviation calculated between the maximum and minimum degrees of cure is approximately 5 %. Therefore, it can be considered a general deviation of the DSC device. Hence, the specimen mass is set to values between 1.0 mg and 1.5 mg for the following measurements.

⁵The total specific heat of reaction is determined in the following measurements.

Results of the crosslinking measurements The crosslinking properties of the chosen photopolymer are investigated by means of photo-DSC measurements using different irradiances and constant temperatures. According to the preparation steps mentioned above, the specimen crucibles are prepared with tiny photopolymer drops weighing between 1.0 mg and 1.5 mg. The purge gas flow rate is again set to 50 ml/min.

The constant temperatures and irradiances are set to

- 10 °C, 20 °C, 30 °C, 40 °C, 50 °C, and 60 °C and
- 5 mW/cm², 10 mW/cm², 15 mW/cm², and 20 mW/cm² .

The irradiance is calibrated before starting the individual measurement (cf. subsec. 2.2.2). Then, the specimen is held isothermally for three minutes at the selected constant temperature. In the next step, the specimen is irradiated for ten minutes to form all possible crosslinks. Finally, the specimen is again held isothermally for three minutes.

The results of the measurements are displayed in fig. 2.8. The abscissa is reduced to the first 30 seconds of the irradiation segment. Principally, the peak of the exothermic reaction, as visible in the first run of each measurement, increases with increasing temperature and irradiance. Increasing the temperature of the resin increases the molecular mobility of the photopolymer. Thus, the crosslinking speed increases and more crosslinks can form at the selected temperature. Otherwise, the number of crosslinks in the specimen is limited if the temperature is too low.

In order to calculate the degree of cure as function of the exposure time, the total specific heat of reaction must be determined. Hence, another specimen is prepared for a non-isothermal test. First, the specimen is equilibrated at $\theta = 70$ °C for three minutes and irradiated for ten minutes with $\mathcal{I} = 20$ mW/cm². Then, the DSC measuring cell temperature is increased to 130 °C with 20 °C/min while the specimen is still irradiated. Afterward, the procedure is repeated in a second run in order to detect residual crosslinking reactions.

Consequently, the crosslinking is not limited by the temperature of the measuring cell, and the fully cured state of the photopolymer is achievable. Moreover, this procedure allows for identifying the minimum required curing temperature to achieve the fully cured state.

The corresponding specific differential heat flows are visualized in fig. 2.9. Fortunately, no residual crosslinking reaction is visible in the heating segment of the irradiation. Hence, the total specific heat of reaction can be identified through this measurement. Evaluating this measurement through the numerator of eq. (2.7) and

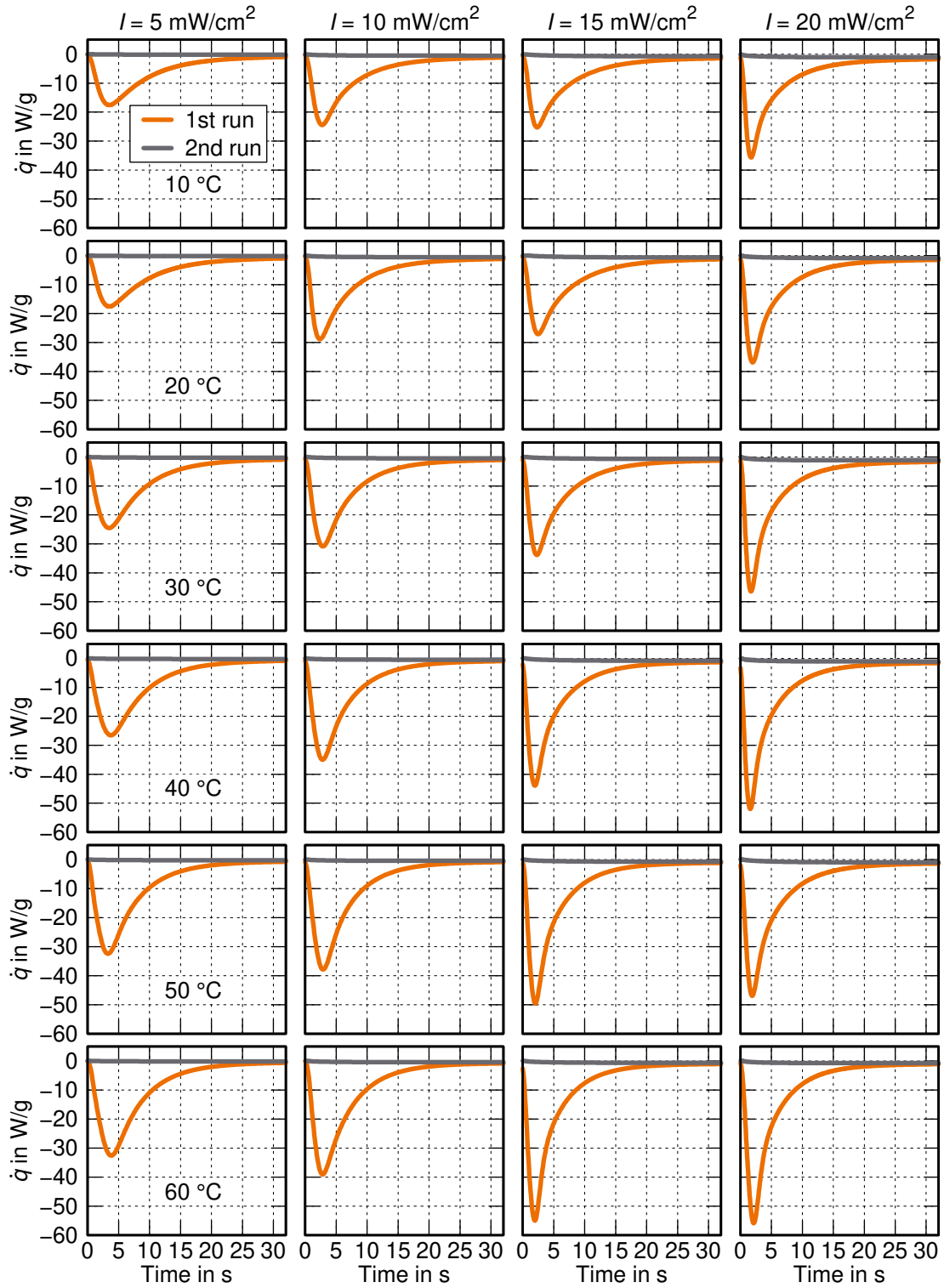


Figure 2.8. Excerpt of the measured specific differential heat flows \dot{q} of the first and second runs of each combination of temperature and irradiance. The temperature label in the first plot of each row indicates the temperature of all plots in the same row.

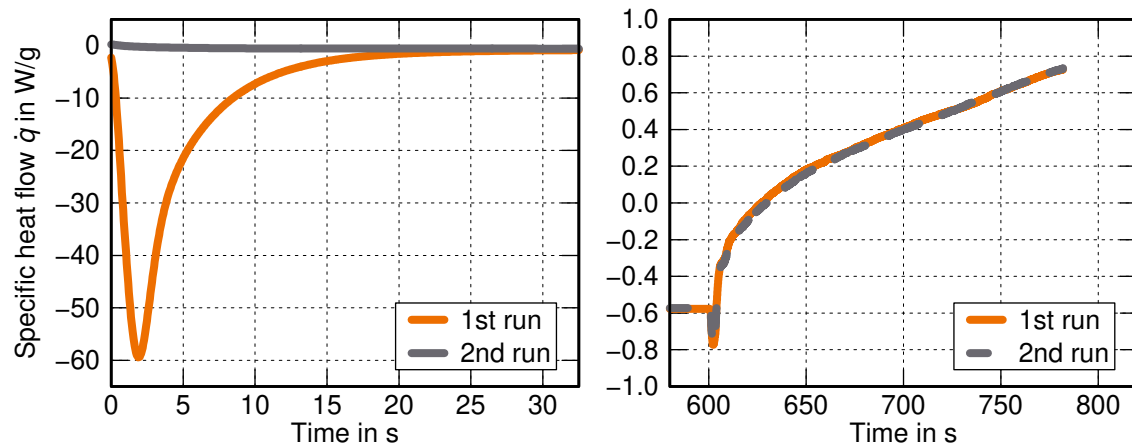


Figure 2.9. Photo-DSC measurement for the determination of the total specific heat of reaction h_{tot} . Left: exothermic peak of reaction in the first 30 seconds upon opening the shutter. Right: heating segment after ten minutes of isothermal irradiation. The slight decrease of the heat flow signal at $t = 600$ s is caused by the temperature control of the device.

eq. (2.6) leads to the total specific heat of reaction $h_{\text{tot}} = 274.04$ J/g.

Finally, fig. 2.10 shows the processed experimental data of fig. 2.8 using eq. (2.7). Apparently, the termination criterion in eq. (2.6) is reached earlier if the temperature of the specimen is increased. In summary, the temperature influences the final degree of cure at the end of the irradiation, whereas the irradiance influences the crosslinking speed.

The experimental results serve to identify the parameters of the model equation describing the degree of cure in sec. 4.1.

2.2.4 Glass transition temperature

The glass transition temperature is an essential property of every polymer. Therefore, the glass transition temperature of the chosen photopolymer in the fully cured state is determined through a modulated DSC (MDSC[®]) measurement. MDSC[®] allows for the precise determination of different phenomena [Menczel and Prime, 2009]. Compared to standard DSC measurements, the constant heating rate is superimposed by a sinusoidal temperature signal. Hence, the resulting heat flow signal is divided into reversing and non-reversing parts. Therein, the glass transition temperature can be identified in the reversing part of the heat flow signal.

For this purpose, another specimen is prepared. Initially, the specimen is irradiated in the same way as for the determination of the total specific heat of reaction to achieve its fully cured state. Then, in a second measurement, the specimen is

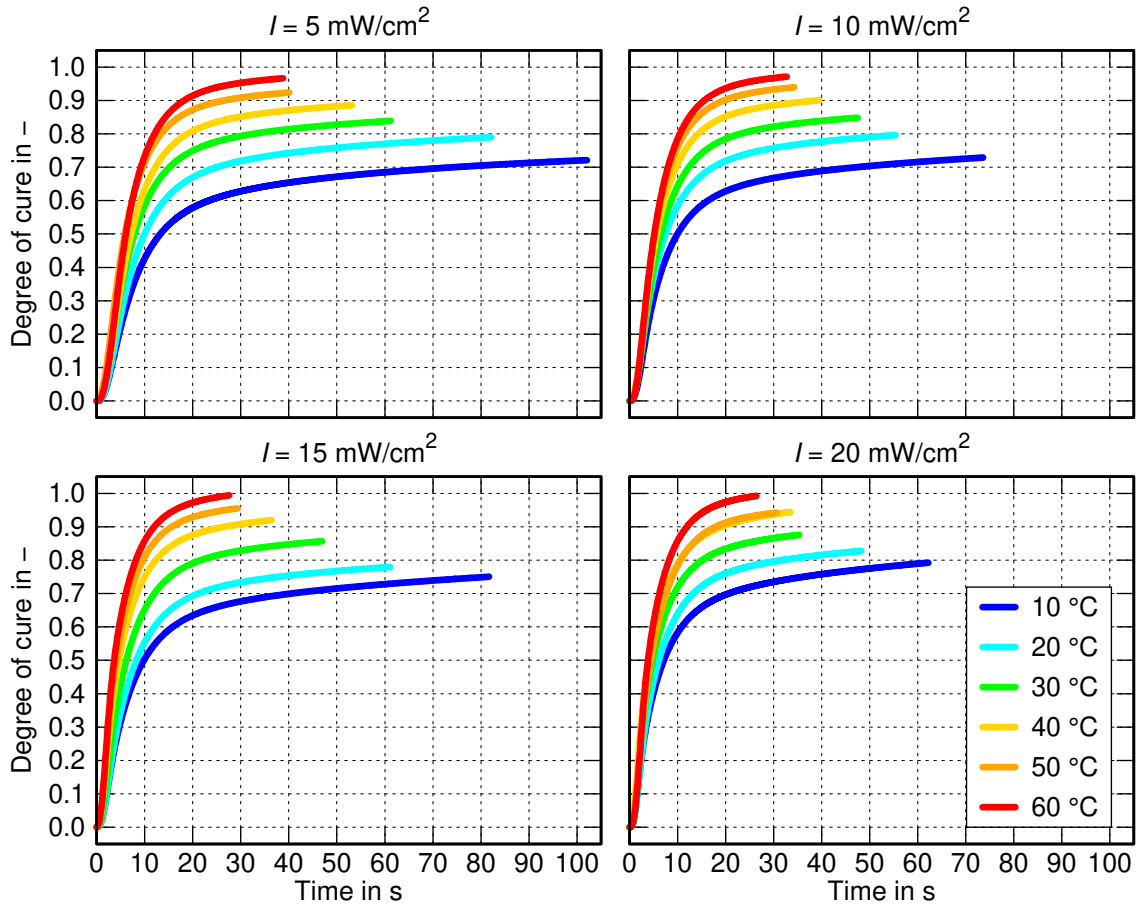


Figure 2.10. Computed curves of the degree of cure depending on temperature and irradiance

heated up from 0 °C to 120 °C with a heating rate of 2 °C/min. The temperature modulation has an amplitude of 1 °C and a period of 60 s.

Fig. 2.11 shows the measured reversing specific differential heat flow of the MDSC[®] measurement to identify the glass transition temperature in the fully cured state. The characteristic step of the glass transition is visible in the chosen temperature range. The start and endpoints of the step are set to 20 °C and 100 °C, respectively. Employing the DSC analysis software provided by TA[®] Instruments, the glass transition temperature is identified at the inflection point of the step and reads $\theta_g = 65.7$ °C. However, the glass transition does not occur at a specific temperature but rather over a broad temperature range.

Naturally, the glass transition temperature of photopolymers increases with progressing degree of cure [Ye et al., 2011]. Thus, the glass transition temperature in the fully cured state represents the ultimate value. Furthermore, KLOOSTERBOER and LIJTEN discovered that the crosslinking reaction could stop if the current glass

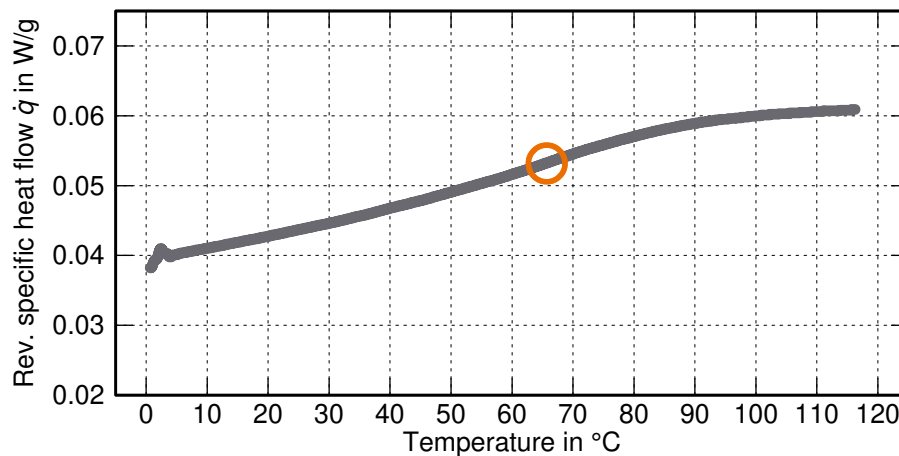


Figure 2.11. Reversing specific differential heat flow of the MDSC[®] measurement for the identification of the glass transition temperature in the fully cured state. The glass transition is indicated by the orange circle.

transition temperature exceeds the curing temperature of the photopolymer [Kloosterboer and Lijten, 1990].

Comparatively, no further crosslinking reaction is visible in the heating segment of the measurement for the determination of the total specific heat of reaction. Therefore, irradiating the specimen at 60 °C is sufficient to achieve the fully cured state.

2.2.5 Isobaric specific heat capacity

The exothermic crosslinking reaction of the photopolymer generates heat, which can substantially increase the temperature of the photopolymer. This relation is described by the isobaric specific heat capacity, which specifies the necessary amount of energy to increase the temperature of 1 g of a given substance by 1 K.

The determination of the glass transition temperature takes into account the relative change in the heat flow signal. Equivalently, the time-dependent degree of cure of the specimen is evaluated through the difference in the specific heat flows of two subsequent measurements. Thus, both evaluations do not provide any information about the absolute values of the heat flow signal. Generally, all measurements are biased by deviations caused by the DSC device, which can be neglected in qualitative measurements (determination of the glass transition) or measurements using relative changes of the heat flow signal (investigation of the crosslinking properties).

In order to determine the temperature-dependent isobaric specific heat capacity, one has to precisely evaluate the absolute values of the heat flow signal. Therefore, the following three-step procedure is applied [Höhne et al., 2003]:

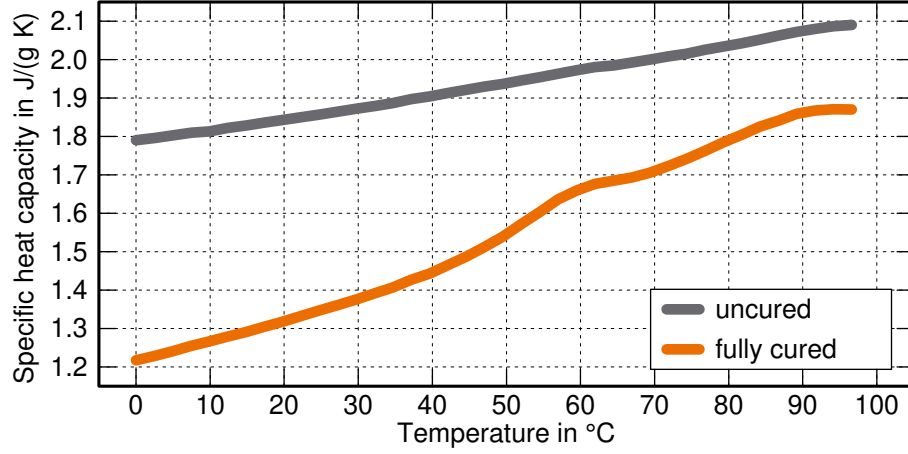


Figure 2.12. Isobaric specific heat capacity depending on the temperature for the uncured and fully cured state of the photopolymer

- The first measurement is conducted with empty crucibles. Before that, the temperature range of interest and the corresponding heating rate are defined. This measurement describes the baseline heat flow $\dot{q}_{\text{crucible}}$ and accounts for intrinsic measurement errors of the DSC device.
- Next, a substance with known values of its temperature-dependent isobaric specific heat capacity $c_{p,\text{sapphire}}(\theta)$ and mass m_{sapphire} is put into the empty specimen crucible. The measurement is conducted using the same experimental procedure. Principally, sapphire is used due to its stability over a wide temperature range.
- Finally, two measurements are conducted with uncured and fully cured specimens leading to the heat flow $\dot{q}_{\text{specimen}}$.

Hence, according to [Menczel and Prime, 2009], the temperature-dependent isobaric specific heat capacity $c_{p,\text{specimen}}(\theta)$ of the specimen is computed as

$$c_{p,\text{specimen}}(\theta) = \frac{(\dot{q}_{\text{specimen}}(\theta) - \dot{q}_{\text{crucible}}(\theta)) m_{\text{sapphire}}}{(\dot{q}_{\text{sapphire}}(\theta) - \dot{q}_{\text{crucible}}(\theta)) m_{\text{specimen}}} c_{p,\text{sapphire}}(\theta) . \quad (2.10)$$

The temperature range is set to $0 \dots 100$ °C, whereas the heating rate is 20 °C/min. Initially, the temperature is held constant for ten minutes before heating the specimen.

The evaluated results of the measurements are depicted in fig. 2.12. The heat capacity of the photopolymer in the uncured state is substantially higher than in the fully cured state and increases linearly with increasing temperature. At 0 °C, the specific heat capacity of the uncured specimen is ≈ 50 % higher than the specific heat capacity of the fully cured specimen. The difference between these two values

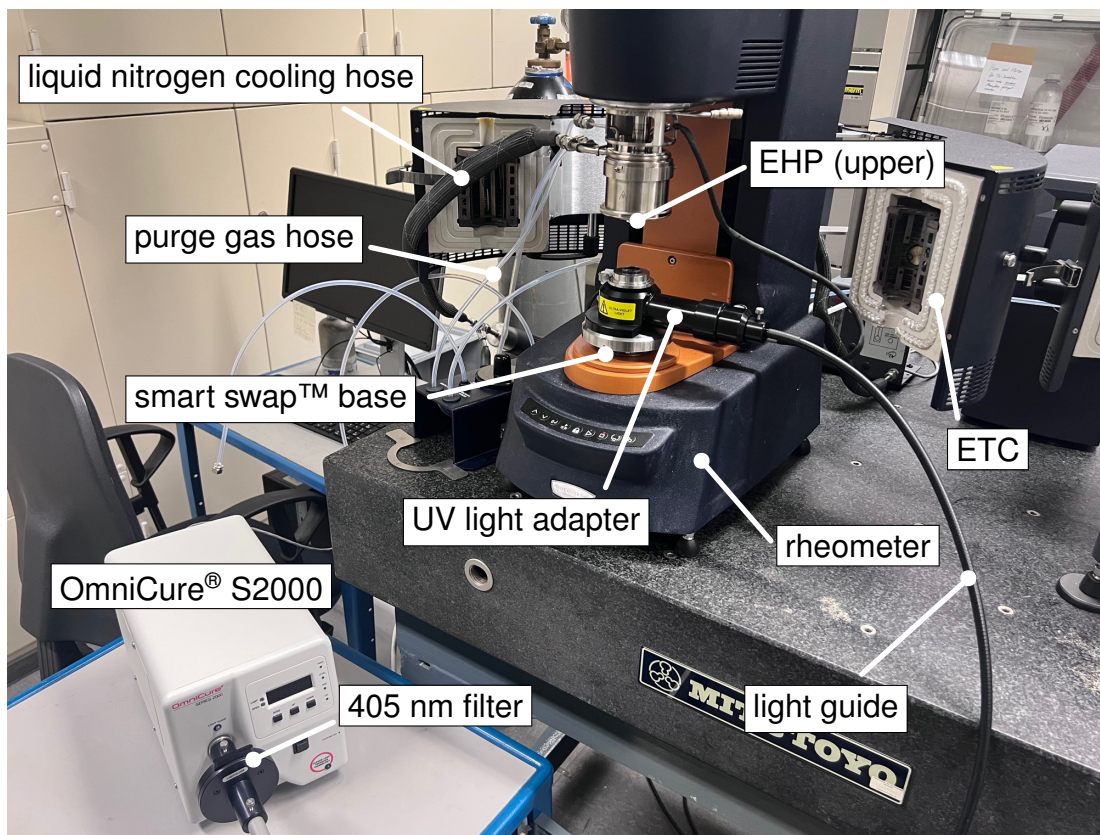


Figure 2.13. Setup of the DHR-30 rheometer incorporating the OmniCure® S2000 curing system

reduces to $\approx 12\%$ at the end of the measurement.

In the fully cured state, the specific heat capacity increases nonlinearly with increasing temperature, which is mainly caused by the glass transition located in the region $60 \dots 70\text{ }^{\circ}\text{C}$. Comparatively, the glass transition temperature of the uncured specimen must be below $0\text{ }^{\circ}\text{C}$ because no transition is visible in the chosen temperature range.

2.3 Rheometric measurements during crosslinking

After finishing the measurements of the crosslinking properties of the photopolymer by means of photo-DSC, the change in the mechanical properties is investigated during the transition from the liquid to the solid state of the photopolymer. To this end, rheometers can principally record the stiffness increase due to progressing crosslinks while oscillating the irradiated photopolymer layer. However, the experimental setup must be adapted first to apply the radiation to the photopolymer layer. In the last decades, the suitability of conventional rheometers extended by proper light sources has been successfully proven to investigate the change of the

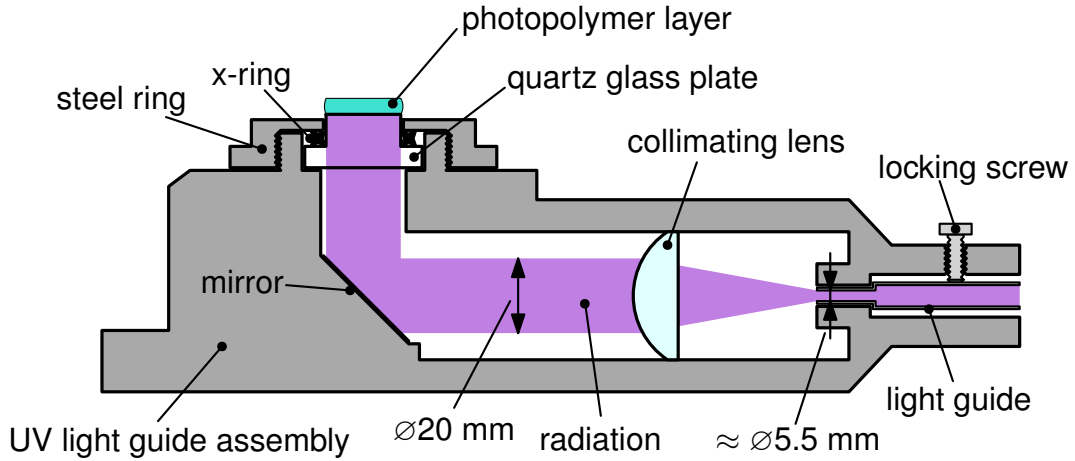


Figure 2.14. Cross-sectional view of the UV light guide assembly motivated by [TA[®] Instruments, 2021]

mechanical properties of crosslinking photopolymers [Watanabe et al., 1984; Khan et al., 1992; Lange, 1999; Lee et al., 2000; Claesson et al., 2002; Darsono et al., 2011; Higham et al., 2014].

The DHR-30 rheometer provided by TA[®] Instruments is used for the following investigations. Fig. 2.13 shows the experimental setup of the rheometer to record the change in the mechanical properties of crosslinking photopolymers. The environmental test chamber (ETC) is unnecessary for the UV rheometry measurements, but it is used for the DMA measurements following later in sec. 2.4.

The OmniCure[®] S2000 curing system generates the incoming radiation in order to compare and link the results with the photo-DSC measurements performed in the preceding section. The radiation is transported by a single liquid light guide instead of the dual fiber light guide (see fig. 2.2). Additionally, the same adapter and the 405 ± 10 nm filter as used in the photo-DSC measurements are plugged into the device. In order to better understand the experimental setup, the cross-sectional view of the UV light guide assembly and the transport of the radiation are depicted in fig. 2.14.

The end of the light guide is mounted into the UV light guide assembly and fixed with a locking screw, whereas the UV light guide assembly is magnetically fixed on the smart swap[™] base of the rheometer. Inside the assembly, the incident radiation is collimated by a lens and vertically deflected by 90° using an internal mirror system. Thus, the light beam diameter is increased from ≈ 5.5 mm to 20 mm. Then, the radiation passes through the transparent quartz glass plate and irradiates the photopolymer layer, which is applied to the top surface of the quartz glass plate. Principally, quartz glass (SiO₂) exhibits an excellent transmission (nearly 100 %)

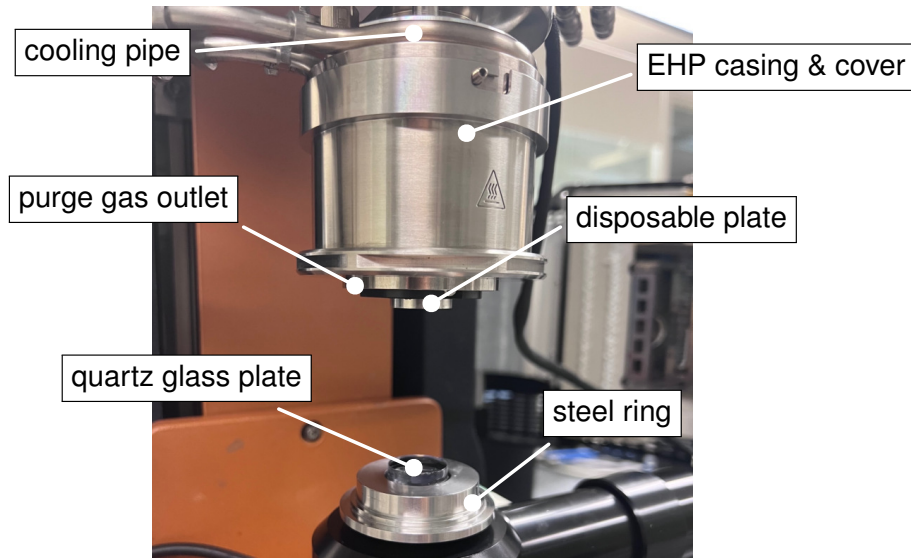


Figure 2.15. Detailed view of the UV rheometry setup

for radiation in the ultraviolet range depending on its purity and additives [Scholze, 1998]. Moreover, a steel ring is screwed onto the UV light guide assembly to keep the quartz glass plate fixed through an x-ring. In addition, the x-ring prevents the liquid photopolymer from flowing into the gap between the steel ring and the quartz glass plate.

Fig. 2.15 shows the detailed view of the UV rheometry setup. The upper disposable plate (\varnothing 20 mm) is made of aluminum and connected to the heat spreader of the electrically heated plates (EHP) accessory. In contrast, the heat spreader is connected to the rotating steel rod of the rheometer. The temperature of the casing of the EHP accessory is controlled by the internal heating coils and the cooling pipe at the top of the casing. The cooling pipe is flooded with vaporized liquid nitrogen, which flows out the storage dewar (gas cooling accessory/GCA) standing next to the rheometer. The casing surrounds the heat spreader and transfers its temperature via convection. Hence, the temperature control of the upper aluminum plate is highly accurate. Comparatively, the temperature of the quartz glass plate is not directly controlled. The EHP, in conjunction with the UV curing accessory, can control the temperature of the upper aluminum plate in the range $-70 \dots 150$ °C.

Last but not least, after establishing the desired layer thickness by lowering the upper aluminum plate, the gap between the heat spreader and the UV light guide assembly is flooded with gaseous nitrogen used as the purge gas. To this end, the cover of the EHP casing is lowered. Although only the lateral surface of the cylindrical photopolymer layer is surrounded by the oxygen in the atmosphere of

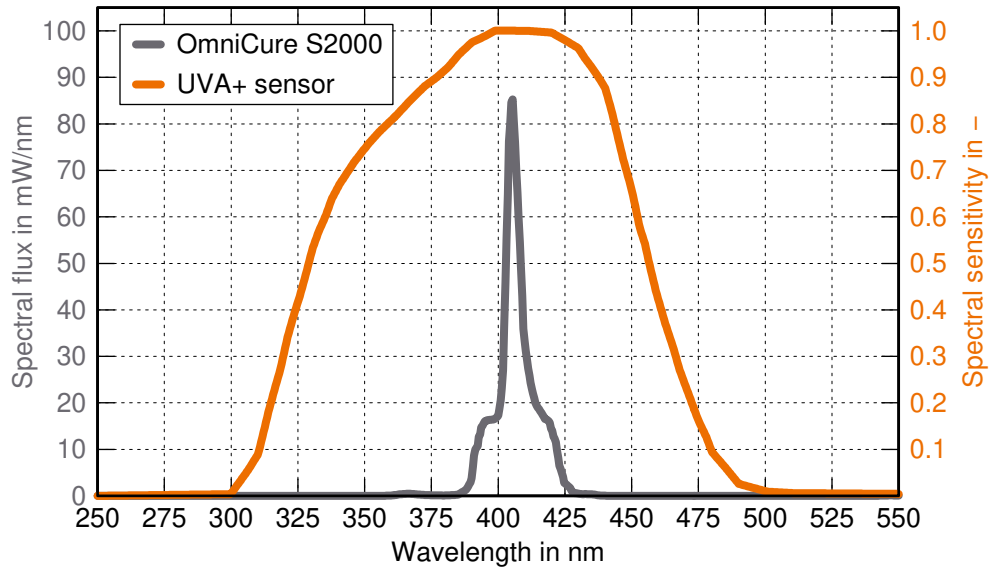


Figure 2.16. Spectral sensitivity of the UVA+ sensor and the emission spectrum of the OmniCure[®] S2000 curing system in conjunction with the 405 ± 10 nm filter

the laboratory, using purge gas is recommended to ensure comparability with the photo-DSC measurements. Additionally, lowering the EHP cover prevents direct eye contact of the radiation with the experimenter.

Irradiance calibration A critical step before using the UV curing accessory is the calibration of the irradiance of the light source on the top surface of the quartz glass plate. The iris setting of the OmniCure[®] S2000 curing system can be adjusted in steps of one percent to obtain different irradiances on the top surface of the quartz glass plate. A portable radiometer is supplied with the UV curing accessory for the DHR-30 rheometer provided by TA[®] Instruments. Unfortunately, it only allows the measurement of the irradiance on the top surface of the quartz glass plate in the wavelength range 230...410 nm. In order to correctly measure the incident irradiance on the top surface of the quartz glass plate, the RMD radiometer, in conjunction with the UVA+ sensor provided by Opsytec Dr. Gröbel GmbH, is applied for the calibration [Opsytec Dr. Gröbel GmbH, 2021]. The radiometer provides the measurement of irradiances in the range 0...10 W/cm². The sensitivity of the radiometer is $10^{-3} \mu\text{W}/\text{cm}^2$. Fig. 2.16 shows the spectral sensitivity of the UVA+ sensor and the emission spectrum of the OmniCure[®] S2000 curing system in conjunction with the 405 ± 10 nm filter. One can easily see that the UVA+ sensor can appropriately measure the radiation in the wavelength range 380...420 nm. The spectral sensitivity is reduced at wavelengths lower or higher than this range. Thus, the measured irradiance must be corrected by the reciprocal

Table 2.2. Measured irradiances of the OmniCure[®] S2000 curing system using the 405 ± 10 nm filter at the end of the light guide and on the top surface of the quartz glass plate

Iris setting in %	Irradiance in mW/cm ²		Relative loss in %
	...at the end of the light guide	...on the top surface (395...415 nm)	
1	14.6	0.662	95.5
2	28.4	1.131	96.0
3	44.0	1.790	95.9
4	58.8	2.401	95.9
5	69.2	2.849	95.9
6	79.9	3.279	95.9
7	87.6	3.766	95.7
⋮	⋮	⋮	⋮
16	229.5	10.120	95.6

of the corresponding spectral sensitivity at wavelengths lower than 380 nm or higher than 420 nm. Fortunately, this procedure does not have to be conducted for the following measurements.

Furthermore, the irradiance at the end of the light guide is measured by the OmniCure[®] R2000 radiometer, which is calibrated in the wavelength range 280...520 nm [Excelitas Technology Corp., 2014a; Bizjak-Bayer, 2021]. Table 2.2 shows the measured irradiances at the end of the light guide and on the top surface of the quartz glass plate, depending on the iris setting. In addition, the relative loss for each iris setting is calculated in the fourth column. The increase of the diameter of the radiation beam mainly causes the tremendous loss of irradiance, see fig. 2.14.

2.3.1 Mechanical properties

In order to measure the change in the mechanical properties of the photopolymer, the rheometer applies a harmonic excitation described by the twist $\varphi(t) = \varphi_0 \sin(\omega t)$ through the upper aluminum plate to the photopolymer layer while irradiated as depicted in fig. 2.17. Considering the kinematic relations between the height H and the radius R of the layer, the corresponding shear strain at $r = R$ reads as

$$\gamma(t) = \varphi(t) \frac{R}{H}. \quad (2.11)$$

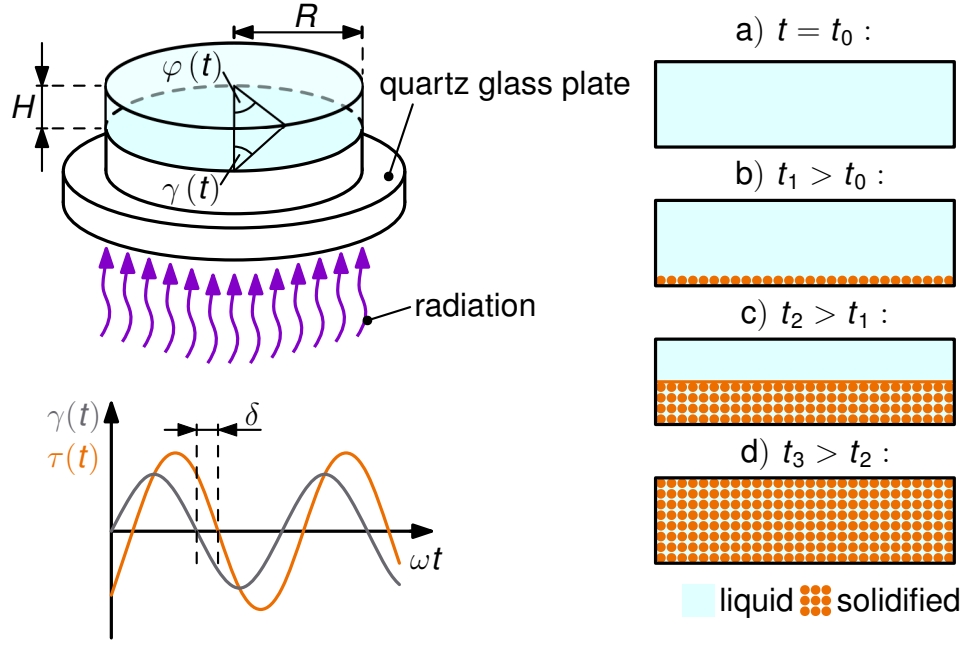


Figure 2.17. Left top: kinematic relation between the twist $\varphi(t)$ and shear strain $\gamma(t)$ of the photopolymer layer. Left bottom: graphical visualization of the phase shift between the shear strain $\gamma(t)$ and the shear stress $\tau(t)$. Right: progress of crosslinking in the photopolymer layer.

At the same time, the rheometer measures the reaction torque $M(t)$ in the photopolymer layer. Assuming small strain torsional analysis and linear elastic or linear viscoelastic material behavior, the corresponding shear stress linearly increases over the radius r and reaches its maximum value at the lateral edge of the layer. Hence, the maximum shear stress reads as

$$\tau(t) = \frac{2M(t)}{\pi R^3} . \quad (2.12)$$

Since the photopolymer principally exhibits viscoelastic material behavior, the stress response is phase-shifted by the angle δ to the harmonic shear strain, see fig. 2.17:

$$\tau(t) = \tau_0 \sin(\omega t + \delta) . \quad (2.13)$$

The rheometer continuously evaluates the shear strain and shear stress signals during the measurement. Transferring the signals into the frequency domain,

$$\gamma^* = \gamma_0 \exp(i\omega t) \quad \text{and} \quad \tau^* = \tau_0 \exp(i(\omega t + \delta)) , \quad (2.14)$$

yields the frequency-dependent complex shear modulus

$$G^* = \frac{\tau^*}{\gamma^*} = \underbrace{\frac{\tau_0}{\gamma_0} \cos(\delta)}_{G'} + i \underbrace{\frac{\tau_0}{\gamma_0} \sin(\delta)}_{G''} . \quad (2.15)$$

G' denotes the shear storage modulus, and G'' is the shear loss modulus. The measured phase shift δ generally depends on the set angular frequency and the photopolymer's current temperature and degree of cure.

As explained above, the irradiation of the photopolymer starts at the bottom of the layer. Hence, the crosslinks also start at the bottom of the layer and vertically progress with increasing time. Fig. 2.17 shows the crosslinking progress in the photopolymer layer at four different states. At the time t_0 , the shutter of the OmniCure[®] S2000 curing system has just opened, and the photopolymer is still liquid. Then, at the time t_1 , the first crosslinks form at the bottom of the layer. The crosslinks progress in the vertical direction, and the crosslinking speed depends on the chosen irradiance ($t = t_2$). Finally, at the time t_3 , the crosslinks reach the upper aluminum plate. At this point, the rheometer recognizes the stiffness increase of the photopolymer layer caused by the progressing crosslinks. At the states **a)** - **c)**, the rheometer only measures the properties of the photopolymer in the liquid state. The time t_3 mainly depends on the chosen irradiance and temperature of the photopolymer. Obviously, the time needed to reach the upper plate increases if the layer thickness increases. Since the irradiance exponentially decreases through the layer according to the BEER-LAMBERT law (see eq. (1.1)), the degree of cure is a function of the vertical location in the layer.

The following parameters are chosen to measure the change of the shear storage and loss moduli during the crosslinking of the photopolymer layer:

- Temperatures: 10 °C, 20 °C, 30 °C, 40 °C, 50 °C, and 60 °C
- Angular frequencies: 0.628 rad/s, 6.28 rad/s, 62.8 rad/s, and 628 rad/s

The iris of the OmniCure[®] S2000 curing system is set to 10 %, which corresponds to the irradiance $\mathcal{I} = 10.12 \text{ mW/cm}^2$. The layer thickness is set to $H = 500 \text{ }\mu\text{m}$ ⁶.

⁶The setting of the layer thickness is always subject to a trade-off. Since the upper aluminum plate and the lower quartz glass plate are not perfectly parallel to each other, the measurement error dramatically increases if the layer thickness is too small. Comparatively, the distribution of the degree of cure in the photopolymer layer becomes more inhomogeneous if the layer thickness is too large. Having conducted several preliminary tests with different layer thicknesses, $H = 500 \text{ }\mu\text{m}$ provided the most stable results.

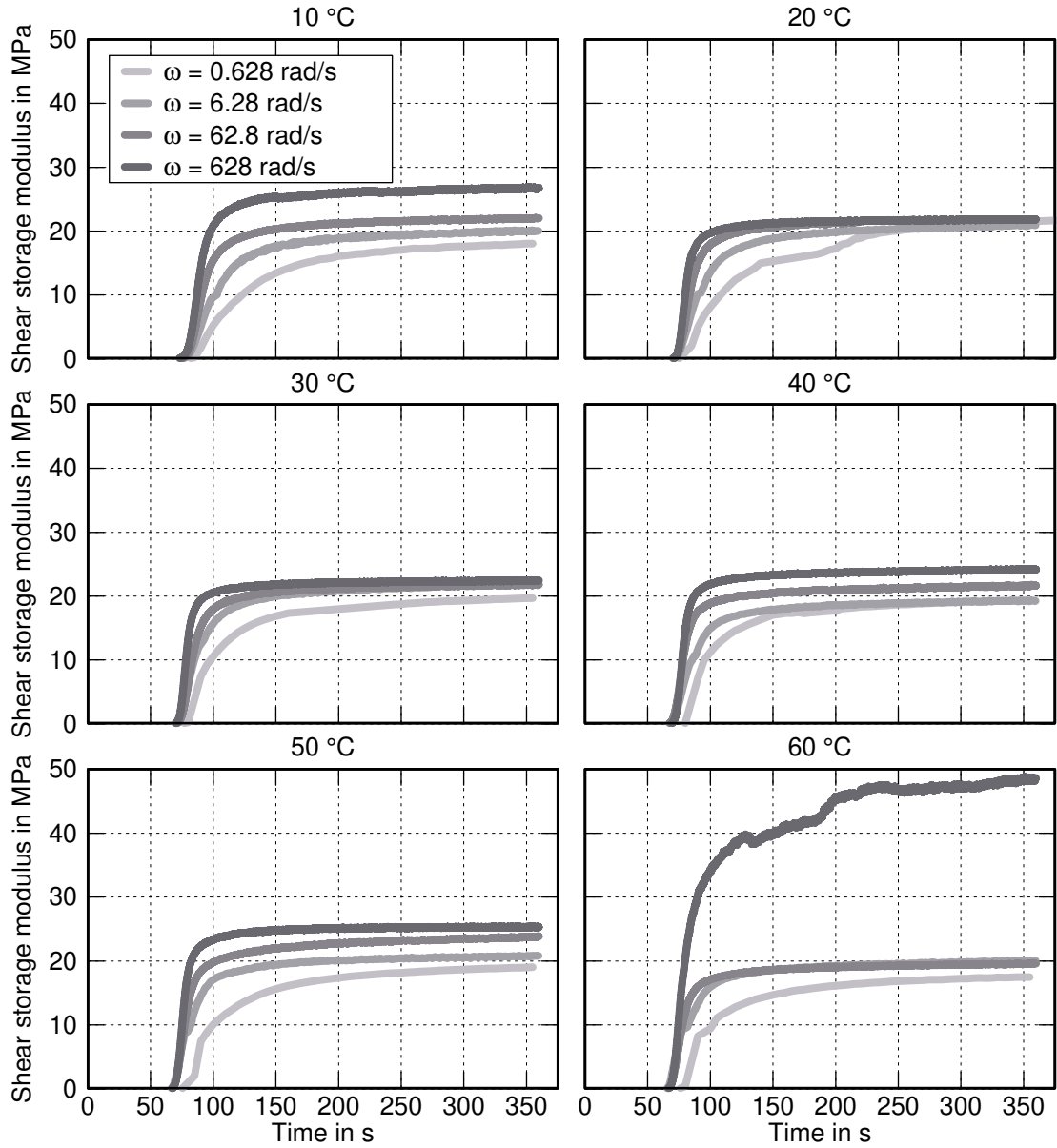


Figure 2.18. Increase of the shear storage modulus G' as a consequence of progressing crosslinks in the photopolymer layer at different constant temperatures and angular frequencies

The shear strain amplitude is dynamically adjusted in the range $10^{-3} \% \dots 10 \%$ by the rheometer and its software. If the photopolymer is in the liquid state, the amplitude must be higher to achieve a stable signal. The normal force is controlled at 0 ± 0.1 N to prevent excessive tensile stresses caused by the chemical shrinkage.

Prior to applying the photopolymer layer on the quartz glass plate, the temperature of the upper aluminum plate is set to the desired value. Then, the photopolymer is applied to the quartz glass plate using a pipette, and contact is established be-

tween the upper and lower plates. Usually, the excessive resin flows down the lateral surface of the quartz glass plate due to its low viscosity in the liquid state.

Before starting the measurement, one has to wait five minutes so that the photopolymer achieves the temperature of the upper aluminum plate. Subsequently, the EHP cover is lowered, and the purge gas cylinder valves are opened. After 60 seconds of oscillating the photopolymer layer in the liquid state, the shutter of the OmniCure® S2000 curing system is opened, and the crosslinking reaction starts. After five minutes of irradiation, the shutter is closed, and the measurement ends.

Fig. 2.18 shows the increase in the shear storage modulus of the photopolymer layer using the experimental conditions mentioned above. Evidently, the short delay is visible between the opening of the shutter and the start of the rise of the shear storage modulus. Apparently, the delays of the individual measurements do not show any deviation from each other, which can be concluded as good repeatability. All measurements show a strong dependency on the chosen angular frequency. Higher angular frequencies lead to a steeper increase and higher final values of the shear storage modulus at the end of the irradiation.

Increasing the temperature of the photopolymer layer leads to two contrary phenomena. On the one hand, increasing the temperature accelerates the crosslinking process of the photopolymer and allows for a higher degree of cure at the end of the irradiation. As a result, the photopolymer layer achieves a higher shear storage modulus at the end of the measurement. On the other hand, the photopolymer becomes softer if the temperature increases along with a lower shear storage modulus. These two mechanisms take place in parallel and cannot be separated from each other. Comparing the measurements at 10 °C and 20 °C, the stiffness reduction has a more substantial impact than the higher final value of the degree of cure caused by the higher temperature.

The frequency dependency of the measurements increases at higher temperatures. Moreover, especially at the highest angular frequency, the final value of the shear storage modulus increases accordingly. However, the measurement at 60 °C with $\omega = 628 \text{ rad/s}$ seems to show a non-physical behavior.

Overall, the conducted measurements serve to model and identify the associated parameters of the degree of cure-dependent viscoelastic properties in sec. 3.5 and subsec. 4.2.2, respectively.

2.3.2 A new method to determine temperature-dependent working curves

The photocalorimetric measurements conducted in the previous section exhibit one important fact. The temperature of the resin is an essential parameter during the crosslinking of the resin. Higher temperatures lead to faster resin conversion even if the irradiance is constant. Thus, besides photocalorimetric measurements, the feasibility of experiments to determine temperature-dependent working curves seems to be an interesting question.

Generating working curves is a fast and versatile tool for the correct setting of the exposure times in the printing process. Additionally, due to the faster conversion of the resin at elevated temperatures, a significant reduction of the printing time per layer can be achieved. In the following, a new method is presented for determining temperature-dependent working curves using the rheometer above.

The rheometer at hand cannot be only employed for oscillating measurements but also axial measurements. If the normal force of the upper plate is controlled at 0 N, the rheometer can measure the change in the thickness of the photopolymer layer caused by the crosslinking upon irradiation.

Upon opening the shutter of the light source, the crosslinking progresses to the upper side of the layer. When the curing front reaches the upper aluminum plate, the curing resin drags the upper aluminum plate downwards due to the chemical shrinkage. The upper aluminum plate follows the curing resin because the normal force is controlled at 0 ± 0.1 N.

At this point, the difference between conventional working curve measurements and this new method becomes clear. Instead of measuring the cured depth of a photopolymer layer for a given exposure time, more specifically, exposure dose, the time needed for the curing front to reach the upper aluminum plate is measured for a given layer thickness. Previous investigations show that choosing the right instrument to measure the cured depth of a photopolymer layer is not trivial, as shown in Bennett [2017]. Again, the temperature of the photopolymer layer is controlled by the EHP accessory and the additional usage of liquid nitrogen.

Fig. 2.19 shows a schematic of the measurement to determine temperature-dependent working curves. Additionally, the change in the photopolymer layer is depicted in a cross-sectional view. Generally, the measurement is divided into three different steps labeled by the numerals ① - ③. Prior to the first step, the photopolymer resin is applied to the top surface of the quartz glass plate, and the thickness of the layer is set to the chosen value C_d , which represents the curing depth. Subsequently, the upper aluminum plate is heated or cooled to achieve the predefined temperature and

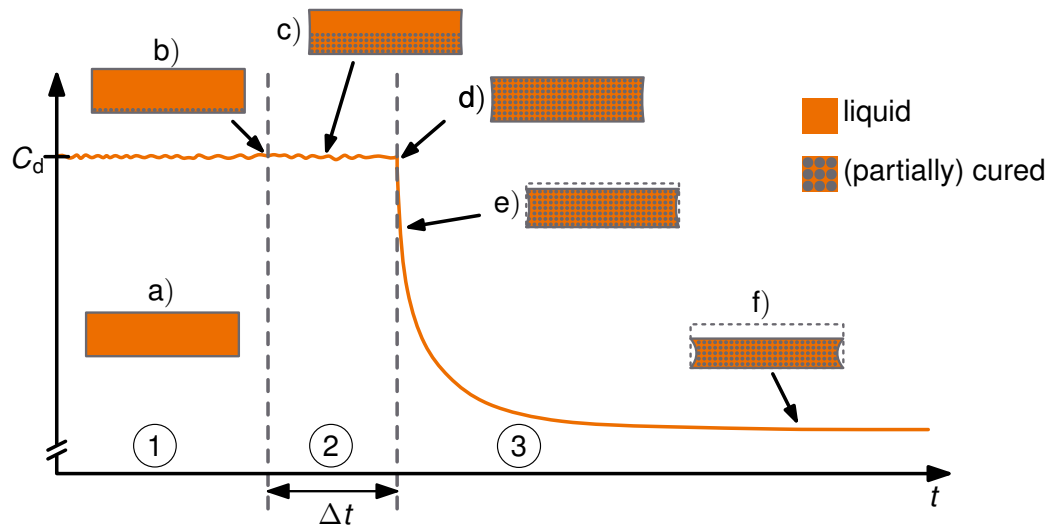


Figure 2.19. Schematic of the measurement for the determination of temperature-dependent working curves and the different states of the photopolymer layer

kept constant for five minutes to establish a homogeneous temperature distribution in the photopolymer layer.

In step ①, which acts as additional conditioning for one minute, the photopolymer layer remains liquid (a). Furthermore, minor deviations from the layer thickness are visible. These deviations are generally caused by the normal force control of the rheometer and are a few hundredths of a micrometer. Thus, they can be neglected because the geometrical change caused by the chemical shrinkage is in the range of several micrometers.

The shutter of the light source opens at the beginning of step ② and irradiates the bottom of the photopolymer layer leading to the first crosslinks indicated as the grey bullets (b). As the irradiation progresses, more crosslinks form up and cause a shrinkage strain in the radial direction because the movement in the radial direction of the photopolymer layer is not restricted ((c)). The duration for the progressing crosslinks to reach the top of the photopolymer layer is specified as Δt . Eventually, multiplied by the given irradiance, it results in the exposure dose for a specific curing depth and temperature of the resin.

The described method allows for the determination of temperature-dependent working curves and the analysis of the chemical shrinkage during the curing process of a photopolymer layer, which is elaborated in subsec. 2.3.3.

Results In order to determine the temperature-dependent working curves, three measurements are conducted for each temperature and curing depth leading to a

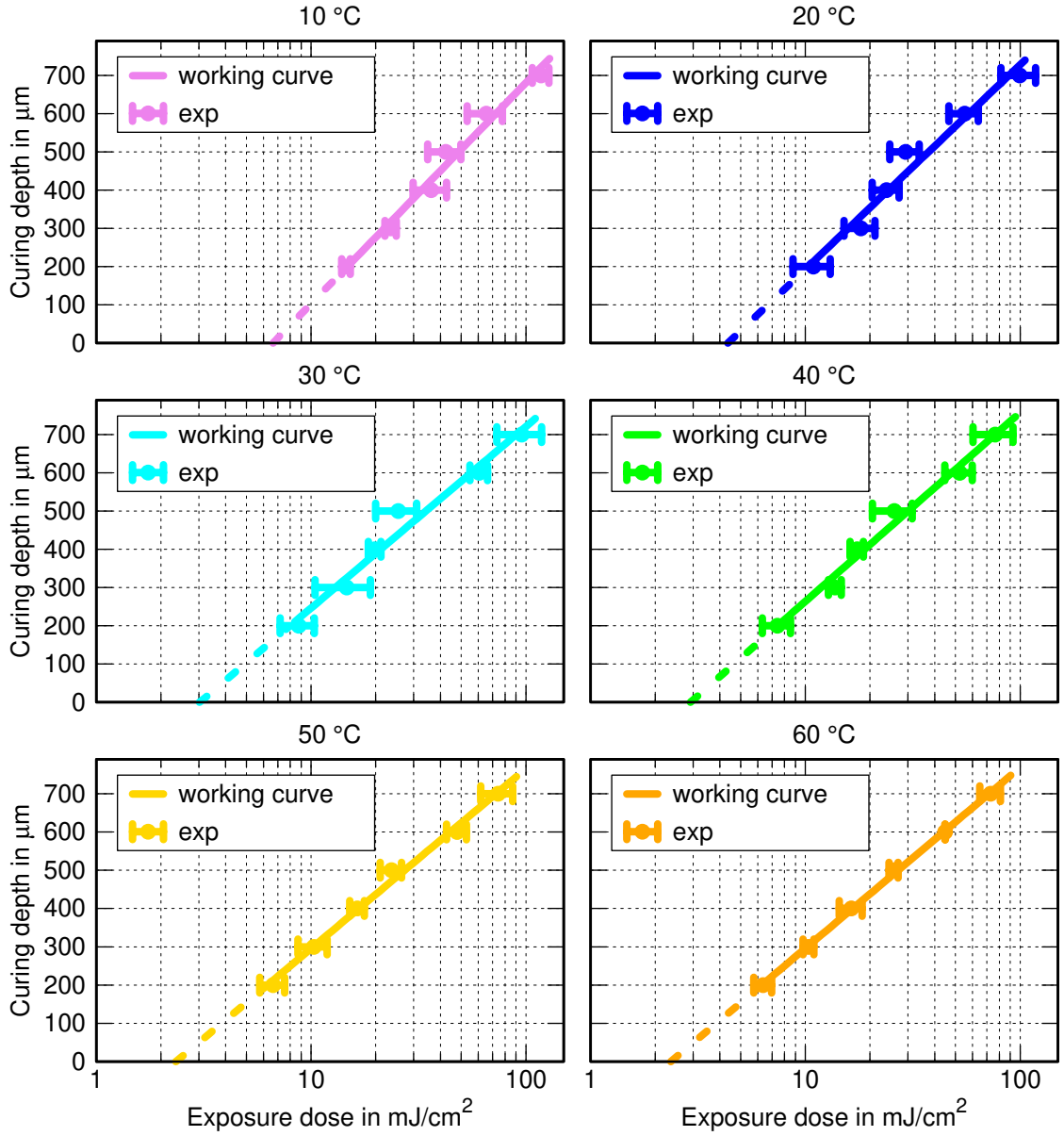


Figure 2.20. Experimentally determined exposure doses and identified working curves. The critical exposure doses are identified by the intersection of the extrapolations (dotted lines) with the abscissa.

total of 108 measurements. The photopolymer layers with curing depths of $200 \mu\text{m} \leq C_d \leq 400 \mu\text{m}$ are irradiated with 1 % iris setting, whereas the layers with curing depths of $500 \mu\text{m} \leq C_d \leq 700 \mu\text{m}$ are irradiated with 2 % iris setting.

Fig. 2.20 shows the results of the measurements. The mean value of the three measurements and the resulting standard error are calculated at each curing depth C_d , which is depicted as the horizontal bar at each curing depth. In addition, the identified working curves for each temperature are also displayed in each subfigure

Table 2.3. Parameters of the identified working curves in fig. 2.20 including standard errors

	10 °C	20 °C	30 °C
D_p in μm	250.973 ± 17.47	232.351 ± 20.46	206.186 ± 18.26
E_c in mJ/cm^2	6.642 ± 0.886	4.357 ± 0.794	3.029 ± 0.625
	40 °C	50 °C	60 °C
D_p in μm	214.397 ± 13.35	203.994 ± 8.544	205.139 ± 2.957
E_c in mJ/cm^2	2.923 ± 0.4085	2.34891 ± 0.2321	2.263 ± 0.079

as straight lines⁷.

Two main conclusions can be derived from the working curves in fig. 2.20 and the associated parameters in table 2.3:

- Higher temperatures of the resin yield a lower critical exposure dose E_c . Therefore, significant efficiency gains regarding the printing time can be obtained by increasing the resin temperature before irradiation. In this study, a reduction of $\sim 65.9\%$ regarding the critical exposure dose E_c is achieved by increasing the resin temperature from 10 °C to 60 °C.
- The identification of the second parameter of the working curve equation, the penetration depth D_p , shows a less significant decrease with increasing temperature. Lower penetration depths lead to a more substantial incident irradiance decrease when the light passes through the photopolymer layer. One possible explanation is the faster conversion of the liquid resin in the vicinity of the quartz glass plate at elevated temperatures, which yields in a stronger gradient in the degree of cure between the (partially) cured part and the still liquid part of the photopolymer layer.

Nonetheless, this assumption remains hypothetical and must be validated by further experiments.

It should be noted that the degree of cure is inhomogeneously distributed across the vertical direction of the photopolymer layer because the irradiance decreases exponentially according to the BEER-LAMBERT law. Calculating an effective degree of cure depending on the vertical location in the photopolymer layer allows for the precise determination of the degree of cure of the photopolymer layer. This method is applied in sec. 4.2.2 for the analysis of the viscoelastic properties of the photopolymer during curing.

⁷The identification of the working curve parameters E_c and C_d is conducted by the program gnuplot and its built-in LEVENBERG-MARQUARDT algorithm.

2.3.3 Chemical shrinkage

The rheometric measurements using the UV accessory give insight into the viscoelastic properties and the curing speed, but they can also quantify the curing induced shrinkage of the photopolymer.

Recalling fig. 2.19, the curing front reaches the upper aluminum plate at the beginning of step ③. After that point, the resin also begins to shrink in the vertical direction. The rapid formation of new crosslinks causes a decrease in the layer thickness due to the chemical shrinkage (d).

Taking into account the predefined layer thickness C_d , the linearized chemical shrinkage strain in the vertical direction of the photopolymer layer is defined by

$$\varepsilon_{\text{ch}}(t) = -\frac{C_d(t) - C_d(0)}{C_d(0)}. \quad (2.16)$$

Therein, $C_d(t)$ denotes the temporal evolution of the layer thickness. Although the chemical shrinkage reduces the volume of the photopolymer layer, the chemical shrinkage strain is considered as a positive value. This is mainly motivated by introducing the multiplicative decomposition of the deformation gradient in sec. 3.3. Therein, the maximum attainable chemical shrinkage is considered as a model parameter with a positive value.

In order to track the temporal evolution of the chemical shrinkage, the measurements for the determination of the temperature-dependent working curves in the preceding section are not stopped after the curing front has reached the upper plate. Thus, the following figures are associated with step ③ in fig. 2.19.

Fig. 2.21 shows the temporal evolution of the chemical shrinkage strain depending on the temperature of the photopolymer for $C_d(0) = 200 \mu\text{m}$. Higher temperatures of the photopolymer lead to a faster increase in the shrinkage strain. The shrinkage strain reaches its highest value for $\theta = 60^\circ\text{C}$, which corresponds to the findings of the photo-DSC measurements that too low temperatures limit the curing of the photopolymer. Unfortunately, several measurements fail due to the axial force control of the rheometer. The rapid conversion of the photopolymer impedes the rheometer from adjusting the axial force to 0 N. For example, at $\theta = 50^\circ\text{C}$, two measurements failed at $t \approx 190 \text{ s}$ and $t \approx 300 \text{ s}$, respectively. Nonetheless, all measurements of the same temperature show similar behavior. Therefore, sufficient repeatability can be assumed.

If the initial layer thickness is increased to higher values, see figs. 2.22 - 2.26, the same phenomena are observable as in the measurements with $C_d(0) = 200 \mu\text{m}$.

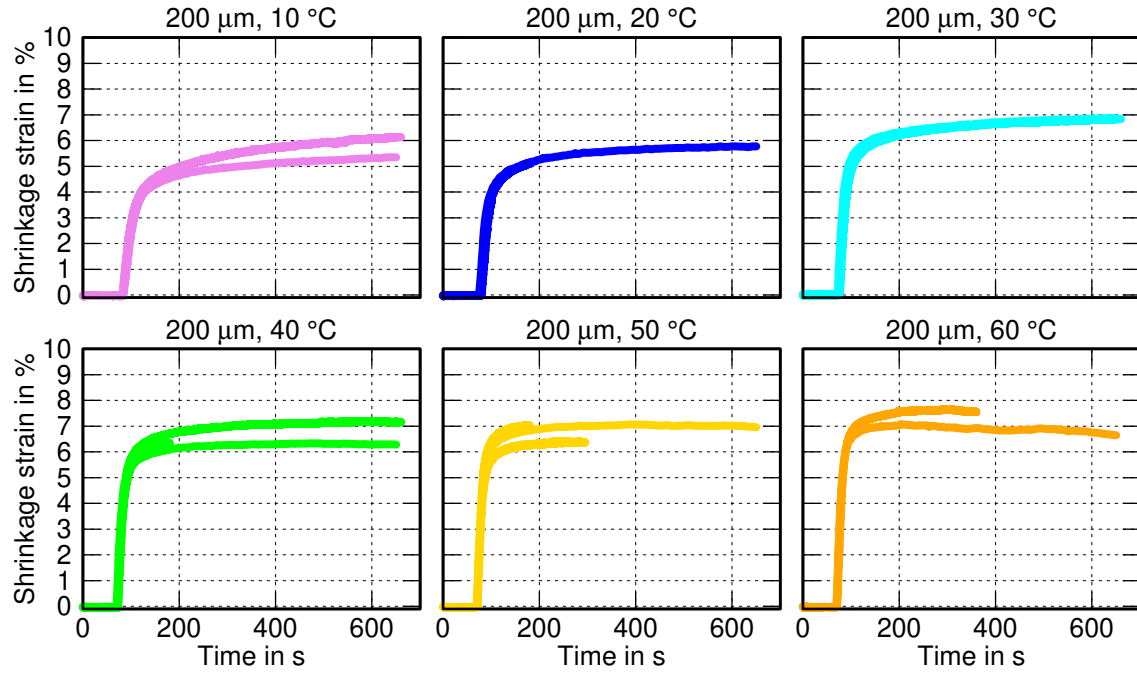


Figure 2.21. Experimentally determined chemical shrinkage strain for $C_d(0) = 200 \mu\text{m}$

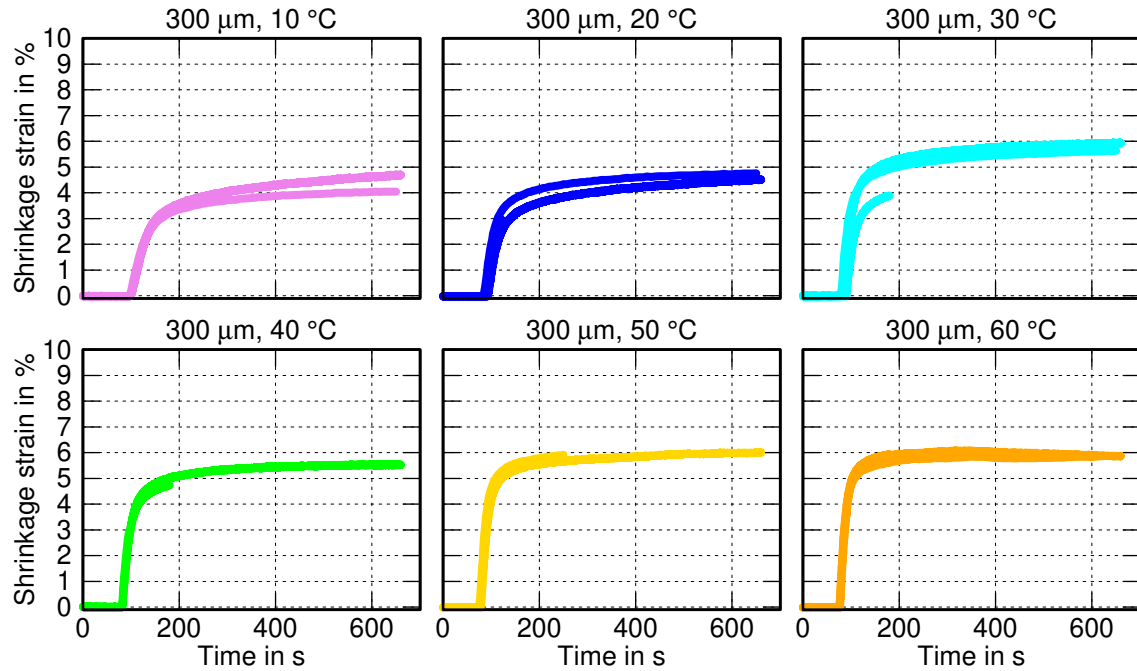


Figure 2.22. Experimentally determined chemical shrinkage strain for $C_d(0) = 300 \mu\text{m}$

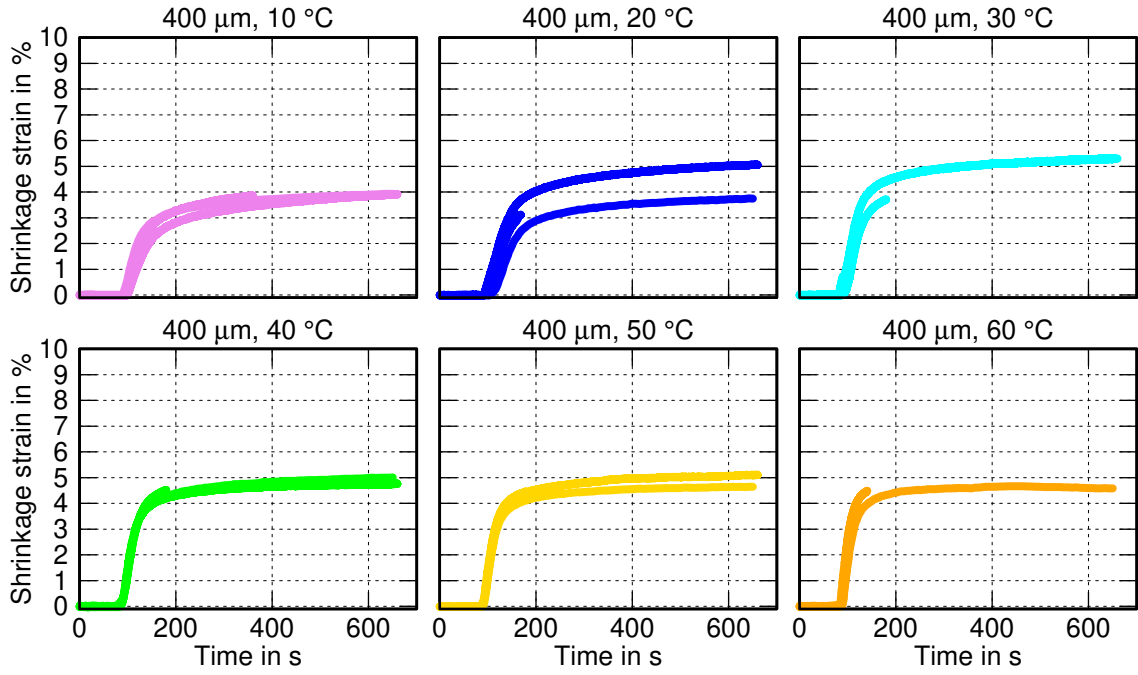


Figure 2.23. Experimentally determined chemical shrinkage strain for $C_d(0) = 400 \mu\text{m}$

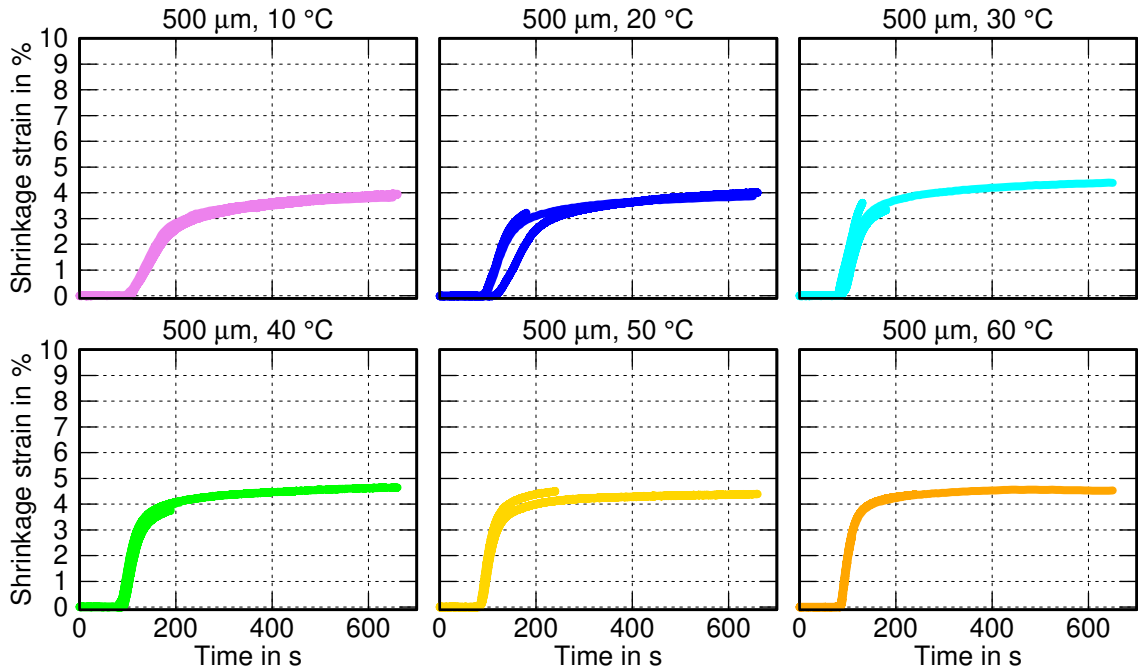


Figure 2.24. Experimentally determined chemical shrinkage strain for $C_d(0) = 500 \mu\text{m}$

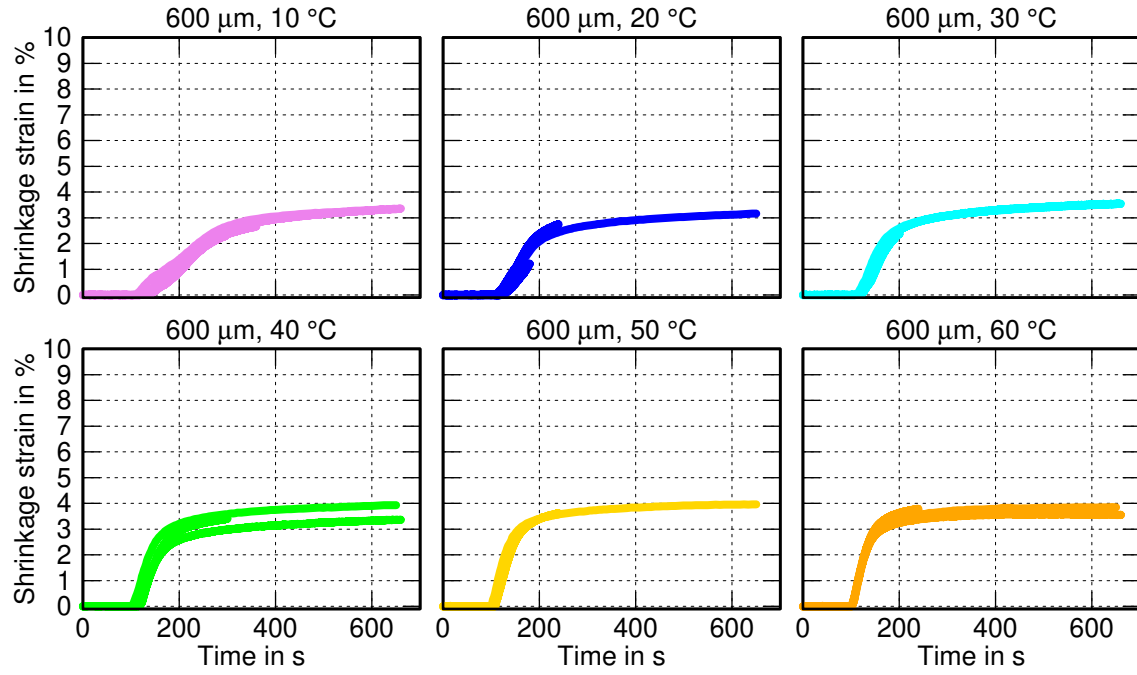


Figure 2.25. Experimentally determined chemical shrinkage strain for $C_d(0) = 600 \mu\text{m}$

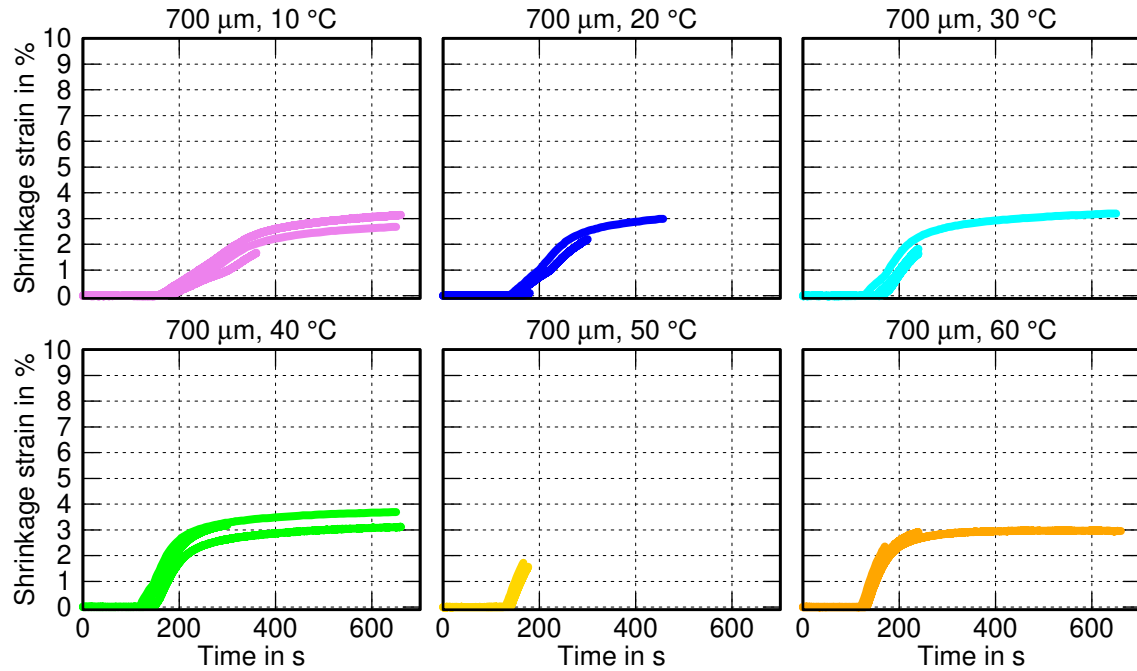


Figure 2.26. Experimentally determined chemical shrinkage strain for $C_d(0) = 700 \mu\text{m}$

Again, higher temperatures lead to a faster conversion of the photopolymer, but it takes more time for the chemical shrinkage to emerge after the shutter opening. Additionally, the shrinkage strain reaches its highest value for $\theta = 60^\circ\text{C}$, but this value decreases with increasing initial layer thickness. This phenomenon is caused by the transverse strain in the radial direction of the cylindrical-shaped photopolymer layer. Hence, the chemical shrinkage strain cannot be considered one-dimensional if the layer thickness increases. Even though several measurements fail again, repeatability is proven in principle.

As a result, the chemical shrinkage in the vertical direction strongly depends on the chosen initial layer thickness and temperature:

- Higher temperatures lead to a higher chemical shrinkage at the end of the measurement. This phenomenon is caused by the limiting effects of too low curing temperatures.
- Smaller layer thicknesses also lead to a higher chemical shrinkage at the end of the measurement. Even in the fully cured state, the upper aluminum plate and the lower quartz glass plate are much stiffer than the photopolymer. Thus, if the layer thickness is small enough, the chemical shrinkage in the radial direction is hindered because the curing front reaches the upper plate immediately upon opening the shutter.

2.4 Dynamic-mechanical analysis of printed specimens

Dynamic-mechanical analysis (DMA) is a well-established experimental method to analyze the temperature-dependent viscoelastic properties of polymers and has been applied for the experimental characterization of polymers for decades [Schwarzl, 1990; Jones, 2001; Menard and Menard, 2020]. Instead of performing tensile or relaxation tests, one can minimize the required time for experiments by determining the viscoelastic properties in the frequency domain. For this purpose, the specimen is excited by an oscillation within a fixed experimental angular frequency range $\omega_{\text{exp}} = [\omega_{\text{exp}}^{\min}, \omega_{\text{exp}}^{\max}]$ at constant temperatures. Then, by applying time-temperature superposition, the experimental angular frequency range can be extended to a more extensive shifted angular frequency range $\omega_{\text{shift}} = [\omega_{\text{shift}}^{\min}, \omega_{\text{shift}}^{\max}]$.

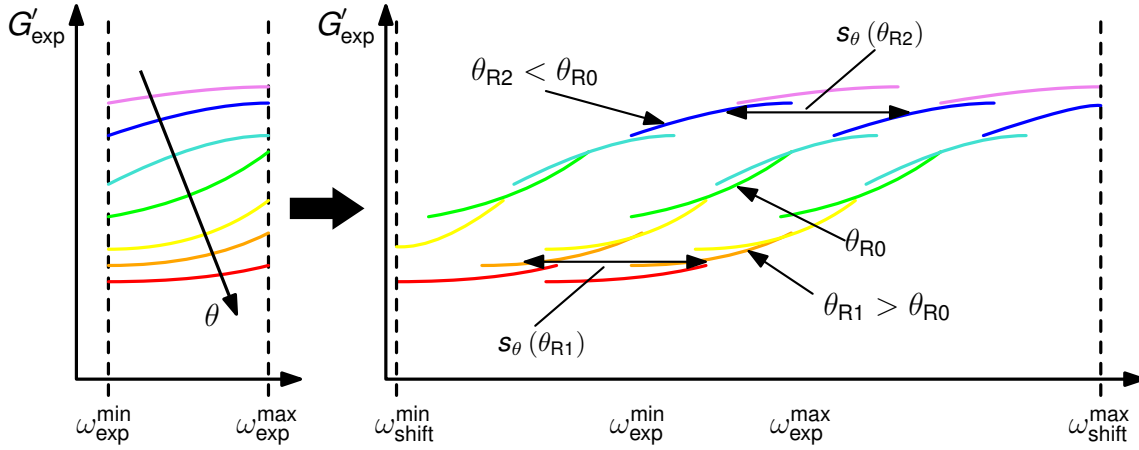


Figure 2.27. Schematic visualization of the time-temperature superposition

Fig. 2.27 shows the general principle of the time-temperature superposition principle by considering the experimentally derived shear storage modulus G' of an arbitrary polymer. If the temperature increases, the specimen becomes softer, which results in a decreasing shear storage modulus. The frequency dependency is less pronounced at low and high temperatures. Particular attention should be paid to the fact that the vertical distances between the individual isothermal curves are not too large. Otherwise, the superposition procedure may not be accomplished because the individual isothermal curves do not overlap. To apply the shift principle, the frequency axis has to be logarithmically scaled.

After choosing a reference temperature θ_R , the isothermal curves with constant temperatures $\theta < \theta_R$ are shifted to higher angular frequencies, whereas the isothermal curves with constant temperatures $\theta > \theta_R$ are shifted to lower angular frequencies. The shift factors s_θ generally range over several decades. Hence, they are usually visualized on a logarithmic scale. The rheometer employed in the preceding sections is used in conjunction with steel clamps for the torsional DMA tests of rectangular specimens. Compared to cylindrical specimens, rectangular-shaped specimens offer an enormous benefit. Since the thickness of the rectangular specimen is principally much smaller than its length and width, a temperature gradient is less likely to arise in the specimen. Moreover, better comparability to the tensile tests performed afterward is possible. The same print orientation, layer thickness, and exposure times can be used for the fabrication of the tensile specimens.

Fig. 2.28 shows the schematic representation of the rectangular specimen with length l , width w , and thickness t . The lower end is kept fixed by the steel clamps, whereas the steel clamps at the upper end apply the harmonic twist $\varphi(t) = \varphi_0 \sin(\omega t)$ to the specimen. Additionally, the rheometer applies a self-adjusting ten-

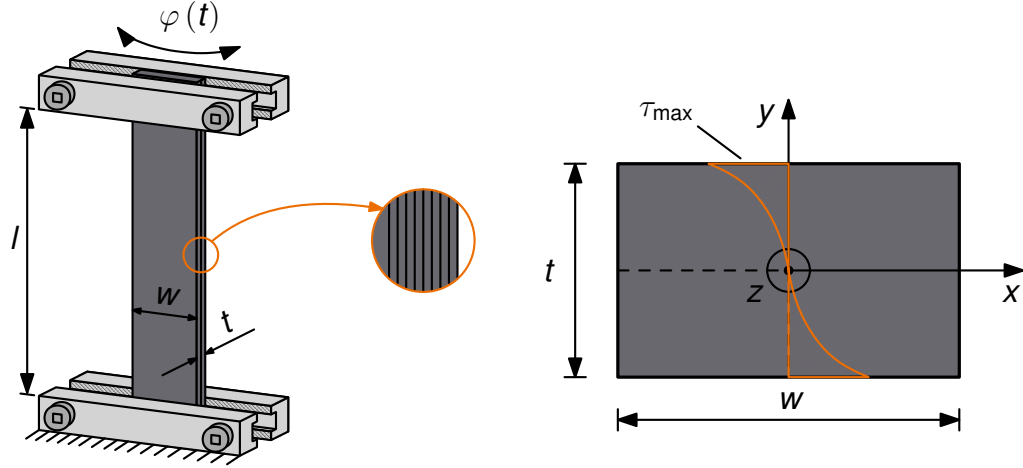


Figure 2.28. Left: schematic representation of the rectangular specimen used in the DMA tests and its boundary conditions applied by the steel clamps. Right: shear stress distribution in the cross-section of the specimen (inspired by [Szabo, 2001]).

sile force to the specimen to keep the specimen straight during the measurement. Otherwise, due to the thermal expansion and contraction of the material when passing through a broad temperature range, the specimen would bend, or excessive tensile forces would arise.

In contrast to the torsion of a cylindrical specimen, the cross-sectional warping is not generally hindered. In [Szabo, 2001], SZABO deducts the fundamental equations for the stress analysis of rectangular bodies with arbitrary aspect ratios $a = \frac{w}{t}$ subjected to torsion based on the considerations of DE SAINT-VÉNANT, see also [Diani and Gilormini, 2017]. Thereby, in contrast to cylindrical specimens subjected to torsion, the shear stresses do not linearly increase with increasing distance from the axis of rotation. The maximum shear stress, which is utilized to calculate the complex shear modulus, is found in the middle of the long edge ($x = 0, y = \frac{t}{2}$), cf. fig. 2.28.

2.4.1 Specimen fabrication

Several rectangular specimens with $t = 2$ mm, $w = 10$ mm, and $l = 40$ mm are fabricated using different exposure times and post-curing treatments to achieve different degrees of cure in the specimen. Due to the printing process, all specimens have a layer thickness of $50 \mu\text{m}$ leading to 40 layers in total. The first two layers are considered as initial layers to achieve sufficient adhesion to the build plate. Hence, the initial layers receive a higher exposure (16 s per layer). The subsequent default

layers are exposed for 1 s, 2 s, and 8 s. Additionally, some specimens irradiated for 2 s are subsequently post-cured for 15 minutes per side to achieve the material's fully cured state. The irradiance of the projector is set to $\mathcal{I} = 15 \text{ mW/cm}^2$ for all print jobs. The irradiance of the post-curing chamber is set to $\mathcal{I} = 205 \text{ mW/cm}^2$, which is the maximum irradiance of the post-curing chamber.

Using orientation ①, see fig. 2.35, all layers are printed parallelly to the build plate and resin tray. In order to further investigate the state of the material prior to the DMA test, the degree of cure of the specimens is determined in the following section.

2.4.2 Determination of the degree of cure

One big challenge arises from printing the DMA specimens parallel to the build plate. Although the number of layers to be printed is reduced to the minimum by printing in the xzy-orientation, a gradient regarding the degree of cure could develop along the z -axis during the printing process. Photo-DSC measurements may give an insight into this possible gradient formation by using poker chip-shaped specimens with varying heights h_i . Consequently, individual values c_i for the degree of cure of each specimen are determined by measuring the residual specific heat of reaction $h_{\text{res},i}$ in the photo-DSC measurement:

$$c_i = 1 - \frac{h_{\text{res},i}}{h_{\text{tot}}} . \quad (2.17)$$

Again, h_{tot} denotes the total heat of reaction for the fully cured material ($c = 1$) as previously determined in subsec. 2.2.3. However, one needs to calculate an effective degree of cure to assign an individual value for each combination of the printing parameters:

$$c_{\text{eff}} = \frac{1}{H} \int_0^H c(z) \, dz . \quad (2.18)$$

Since only distinct values c_i are determined for each individual height of the specimen, one has to approximate eq. (2.18), for example, by the trapezoidal rule

$$c_{\text{eff}} \approx \frac{1}{H} \left(h_1 c_1 + \sum_{i=2}^N (h_i - h_{i-1}) \frac{c_{i-1} + c_i}{2} \right) . \quad (2.19)$$

The parameter N stands for the number of specimens considered for the measurements. Moreover, the value c_1 is only taken into account by the rectangular rule because no specimen can be printed for $h = 0 \text{ mm}$. Generally speaking, an increase

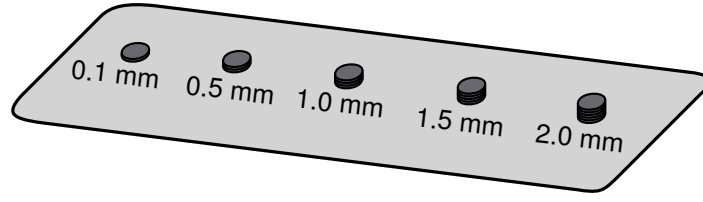


Figure 2.29. Poker chip-shaped specimens with different heights for the determination of the degree of cure of the specimens used in the DMA tests. The hatching in each specimen indicates the individual layers.

in the number of specimens will lead to a better resolution of the gradient formation. Comparatively, it will cause a higher effort by conducting more measurements, which will probably show only a slight deviation from each other.

Fig. 2.29 shows the chosen specimen heights for the photo-DSC measurements. Five different heights are chosen, ranging from nearly zero thickness to the overall thickness $H = 2$ mm of the DMA specimens. The diameter of the specimens was set to $d = 3.5$ mm to fit perfectly into the Tzero crucibles, with $\delta = 50$ μ m chosen as the layer thickness. The exposure time of the two initial layers was 16 s. For the subsequent default layers, various exposure times are chosen in accordance with the exposure times of the specimens for the DMA tests.

After finishing the print job, the specimens are cleaned for two minutes in a hyper-sonic isopropanol bath to remove excessive resin on the surface of the specimens. In the next step, the specimens are dried using pressurized air. Then, each specimen is placed into the Tzero crucible to start the photo-DSC measurement. Prior to that, the irradiance of the OmniCure[®] S2000 curing system is calibrated to $\mathcal{I} = 20$ mW/cm². In order to measure the necessary residual specific heat of reaction to achieve a fully cured specimen and avoid limiting effects, the specimens are equilibrated at $\theta = 70$ °C for three minutes.

Subsequently, the shutter opens, and the specimen is exposed to the incoming irradiation. The DSC registrates the crosslinking of the residual molecules in the (partly cured) specimen leading to the well-known exothermic peak as a phenomenon of crosslinking processes. Since only a small amount of unreacted molecules is left in the specimen, the exothermic peak is much smaller than the peaks of the photo-DSC measurements using the uncured resin in sec. 2.2.3. Then, after ten minutes of exposure, the shutter closes, and the specimen is again kept isothermally at 70 °C for three minutes.

The results of the conducted photo-DSC measurements are visualized in fig. 2.30 for each exposure time of the default layers (columns) and each specimen height

(rows). As expected, the measured specific heat flows of the two initial layers are nearly independent of the chosen exposure time for the default layers (first row). Only a slight deviation is visible, which can be addressed to the general inaccuracy of the DSC device.

For the subsequent specimens ($h = 0.5$ mm), the exothermic peaks are more significant for the exposure times $t = 1$ s and $t = 2$ s of the default layers. Considering the exposure time $t = 8$ s, the exothermic peak is smaller. All subsequent measurements exhibit a decreasing exothermic peak with increasing specimen height. The increasing number of layers leads to a higher overall exposure dose for the specimen. Hence, the residual heat of reaction turns out smaller.

After subtracting the signal of the second run from that of the first run for each specimen, one can calculate the residual heat of reaction h_{res} for each specimen by integrating the subtracted curve over time. Then, the individual values for h_{res} are employed to calculate the degree of cure of each specimen and for the overall effective degree of cure according to the eqs. (2.18) and (2.19). The resulting values of the degree of cure of each specimen and the corresponding effective degrees of cure for each combination of exposure times are listed in table 2.4. As expected, higher exposure times of the default layers lead to higher degrees of cure of each specimen and a higher effective degree of cure. Furthermore, the mean squared deviation calculated between each degree of cure and the effective degree of cure for a combination of exposure times is not very pronounced. Thus, employing an overall effective degree of cure for each specimen is an appropriate method.

The individual effective degree of cure for each combination of exposure time is then assigned to the specimens for the torsional DMA tests, which are presented in the next section.

2.4.3 Results of the torsional DMA tests

After finishing the print jobs for the rectangular specimens with the chosen combinations of exposure times, the specimens are subsequently cleaned in a hypersonic isopropanol bath and then dried with pressurized air to remove excessive resin on the surface of the specimens. Then, each specimen is clamped into the lower fixture of the rheometer one by one. In the next step, the upper fixture is lowered to the upper edge of the specimen. In order to avoid buckling or excessive tensile forces in the specimen, the normal force control of the rheometer is activated before the screws of the upper fixture are tightened. According to the user guidelines of the rheometer for stiff thermoplastic materials whose glass transition temperature θ_g is higher than room temperature, the normal force control is set to 2 ± 1.75 N. Applying the normal force guarantees that the specimen is kept straight at any time

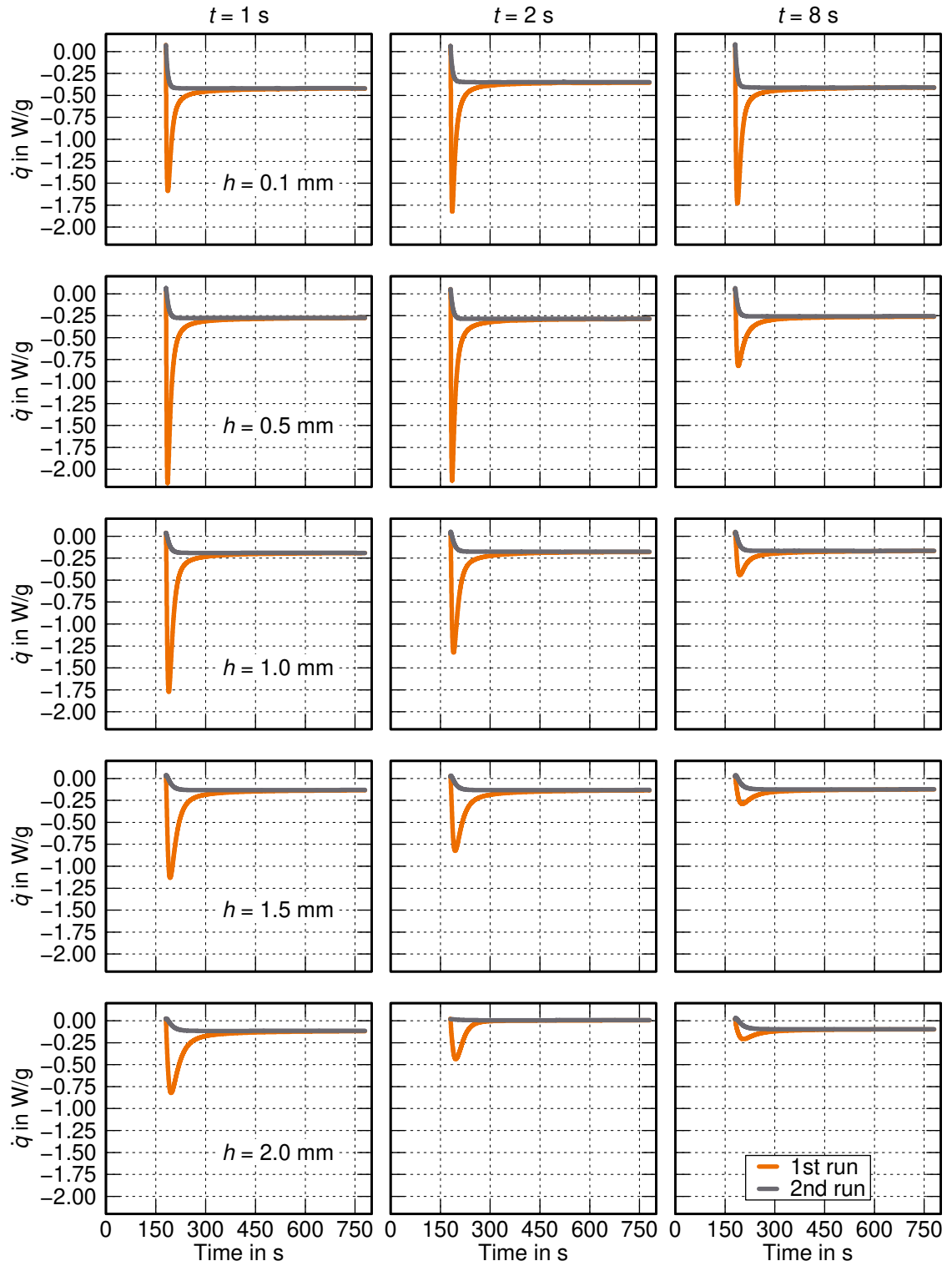


Figure 2.30. Measured specific heat flows \dot{q} of the poker chip-shaped specimens

Table 2.4. Resulting degrees of cure of the pokerchip-specimens depending on the individual exposure time

Exposure time: 1/16 s					
Height h_i in mm	0.1	0.5	1.0	1.5	2.0
Degree of cure c_i in -	0.8687	0.8365	0.8221	0.8310	0.8433
Effective degree of cure c_{eff} in -	0.8372				
Mean squared deviation in -	$2.59 \cdot 10^{-4}$				
Exposure time: 2/16 s					
Height h_i in mm	0.1	0.5	1.0	1.5	2.0
Degree of cure c_i in -	0.8568	0.8430	0.8464	0.8592	0.9277
Effective degree of cure c_{eff} in -	0.8606				
Mean squared deviation in -	$1.01 \cdot 10^{-3}$				
Exposure time: 8/16 s					
Height h_i in mm	0.1	0.5	1.0	1.5	2.0
Degree of cure c_i in -	0.8620	0.8980	0.9333	0.9422	0.9521
Effective degree of cure c_{eff} in -	0.9193				
Mean squared deviation in -	$1.11 \cdot 10^{-3}$				

of the measurement. The specimen becomes stiffer at low temperatures and softer at high temperatures. Hence, at low temperatures, the normal force is controlled at the upper limit and vice versa. On the one hand, the specimen most probably does not start to bend. On the other hand, the applied normal force does not damage the specimen while being tested at high temperatures. The screws of the lower and upper fixture of the rheometer are tightened to 0.6 Nm using a torque wrench while the normal force control is active.

Then, the environmental test chamber of the rheometer is closed. Subsequently, liquid nitrogen is vaporized and streamed into the test chamber to cool down the specimen to the desired temperature, which is set to $\theta_{\text{low}} = -100$ °C. The specimen is kept at this constant temperature for five minutes to avoid temperature gradients in it. Since the specimen contracts due to the cooling, the screws might be loosened. To avoid insufficient contact pressure between the clamps and the specimen, the test chamber is opened, and the screws are retightened. When the torque in the screws reaches the desired value, the test chamber is closed, the specimen is again cooled down, and the temperature is kept constant for five minutes before the actual measurement starts.

Starting at the lowest temperature $\theta_{\text{low}} = -100$ °C, the twist $\varphi(t)$ is set such that

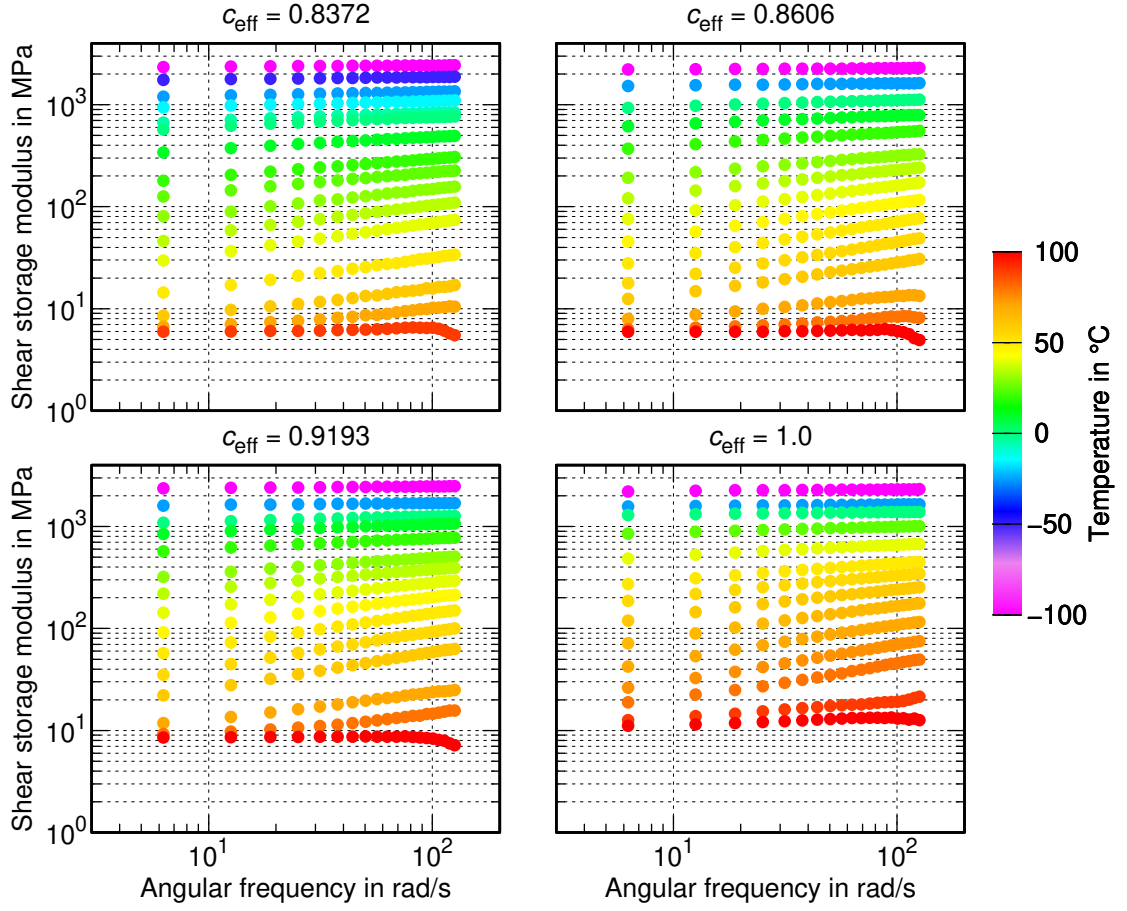


Figure 2.31. Excerpt of the isothermal curves of the DMA tests of the investigated specimens

the harmonic shear oscillation

$$\gamma(t) = \gamma_0 \sin(\omega t) \quad (2.20)$$

is applied to the specimen. During the measurement, the amplitude γ_0 is dynamically adjusted in the range $\gamma_0 = [10^{-3} \%, 10^{-1} \%]$. The following challenges arise from choosing either a too small or too large amplitude for the shear oscillation:

1. If the amplitude γ_0 is too large, the specimen will likely leave the admissible region of linear-viscoelastic behavior. Since the principle of time-temperature superposition is only admissible in the linear-viscoelastic region of thermorheological simple materials, avoiding the nonlinear-viscoelastic response of the material is essential.
2. If the amplitude γ_0 is too small, the torque measured by the rheometer to sustain the shear oscillation will be in the range of the general inaccuracy of the rheometer device. Hence, the measured torque and the computed output

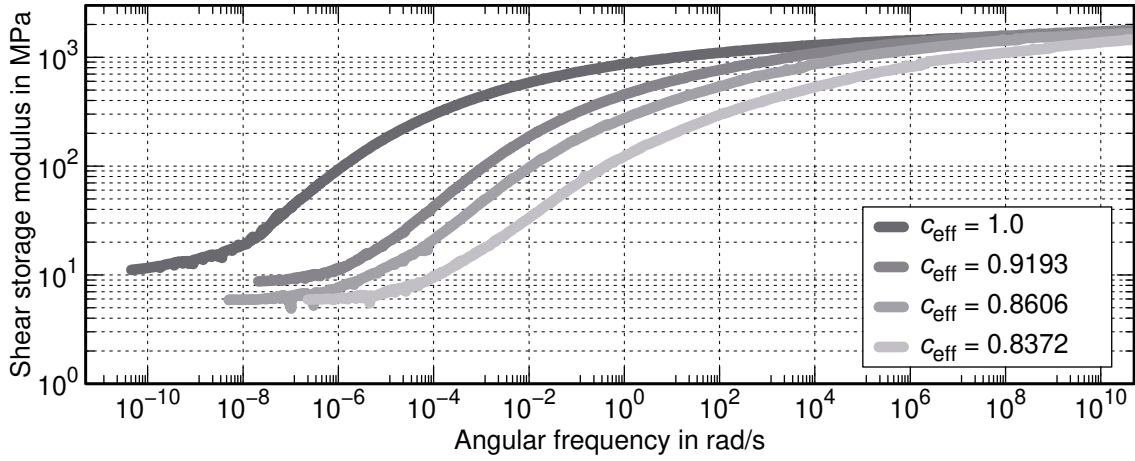


Figure 2.32. Resulting master curves of the DMA tests of the investigated specimens

signals may be too noisy.

The specimen first leaves the linear-viscoelastic region earliest at the lowest temperature and highest measurement frequency because the specimen is stiffest under this combination. With increasing temperature, the specimen becomes softer and, thus, leaves the linear-viscoelastic region at a larger amplitude. Several pretests of the specimens have shown that the upper limit ($\gamma_0 = 10^{-1} \%$) should not be exceeded. Therefore, keeping the shear oscillation amplitude in the above range seems reasonable. The chosen experimental angular frequency range is $\omega_{\text{exp}} = [2\pi \text{ s}^{-1}, 40\pi \text{ s}^{-1}]$, linearly divided into 20 frequency points. The specimen is conditioned for five cycles at each frequency, and the signals are evaluated over the following five cycles. Afterward, the harmonic shear oscillation frequency increases until the upper limit is reached.

Subsequently, the temperature of the test chamber is increased by 5°C and again kept constant for five minutes to equilibrate the specimen. The frequency sweep is again applied to the specimen, and the output signals are saved. This procedure is repeated until the temperature reaches the upper limit, which is set to 100°C for the measurements in this thesis. The rheometer calculates the shear storage and loss moduli G' and G'' based on the measured torque and applied shear oscillation amplitude for each constant temperature.

Fig. 2.31 shows individual excerpts⁸ of the isothermal curves of the shear storage modulus G' as a function of the experimental angular frequency for all tested specimens with the corresponding effective degree of cure. At low temperatures, all specimens exhibit nearly the same value. At high temperatures, the shear storage

⁸Plotting all isothermal curves would be too confusing.

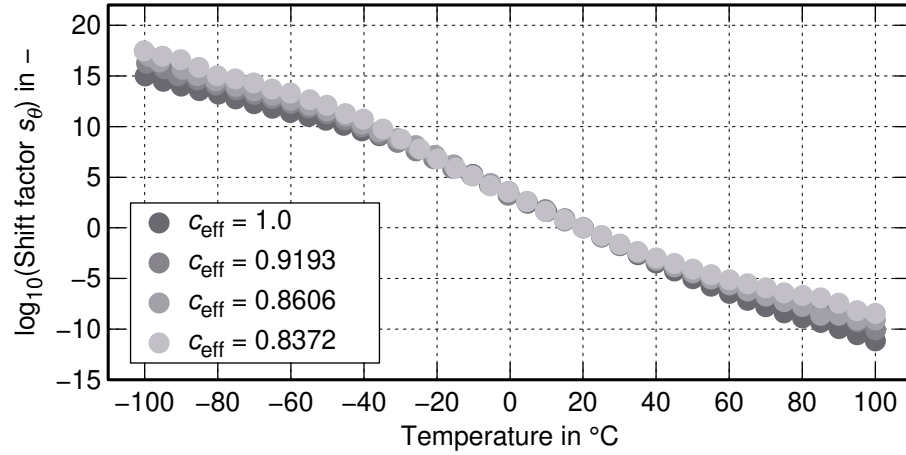


Figure 2.33. Shift factors s_θ for the generation of the master curves in fig. 2.32

modulus decreases more rapidly with decreasing degree of cure. Additionally, the equilibrium modulus at the highest temperature ($\theta_{\text{up}} = 100^\circ\text{C}$) decreases as well. Moreover, all measurements exhibit indistinct softening behavior at high temperatures and angular frequencies $\omega > 100\text{ s}^{-1}$. This phenomenon could be caused by actual damage in the specimen, or the upper limit of the chosen shear oscillation amplitude range is too small at high temperatures. However, since this phenomenon only arises at the highest temperature, no further attention is paid.

The isothermal curves at $\theta_R = 20^\circ\text{C}$ are chosen as the reference for the subsequent master curve generation. Isothermal curves at higher temperatures are shifted to lower angular frequencies and vice versa. The master curve generation is automatically performed by the analysis software of the rheometer, taking into account only the curves of the shear storage modulus.

The resulting master curves of all specimens are visualized in fig. 2.32 for the reference temperature $\theta_R = 20^\circ\text{C}$. As expected, the values of the master curve of the most compliant specimen ($c_{\text{eff}} = 0.8372$) are significantly lower than the values of the master curve of the fully cured specimen. Furthermore, the equilibrium shear storage modulus, which is identified at low angular frequencies, decreases with decreasing degrees of cure. Fortunately, all master curves are smooth and thus represent a reasonable basis for the parameter identification in ch. 4.

The corresponding shift factors for the generation of the master curves are depicted in fig. 2.33. Interestingly, no explicit dependency on the effective degree of cure is visible, which allows for the separation of temperature and degree of cure in the modeling of the shifting mechanisms.

2.5 Tensile tests

The DMA tests in the preceding section 2.4 exhibit a strong influence of the degree of cure on the viscoelastic properties of the specimens. Since only the viscoelastic properties of the deviatoric response of the material can be determined by torsional DMA tests incorporating the one-dimensional approach, cf. section 3.5, other tests are required for the complete experimental characterization of the mechanical properties of the material.

To this end, tensile tests are performed to identify the model parameters that cannot be directly identified by means of the previously introduced measurements and simplifications by using one-dimensional and homogeneously distributed deformation states. Hence, using several temperatures, strain rates, and degrees of cure, a broad range is created covering the response of the material as force-displacement curves at different states.

The following experimental design was chosen according to the previously described phenomena and the DMA tests of printed specimens in section 2.4:

- Temperatures: 10 °C, 20 °C, 30 °C, 40 °C
- Strain rates: 10^{-6} s^{-1} , 10^{-5} s^{-1} , 10^{-4} s^{-1} , 10^{-3} s^{-1}

The exposure times are set to the same values as for the specimens for the DMA tests, see subsec. 2.4.1⁹. Again, the irradiance of the DLP projector is set to $\mathcal{I} = 15 \text{ mW/cm}^2$. The specimen geometry is depicted in fig. 2.34 and is chosen with respect to the type 1 BA of [DIN EN ISO 527-2:2012, 2012]. Fig. 2.35 shows the possible orientations of the printed specimens aligned to the build head, including the global and local coordinate systems. Since the loading direction of the tensile

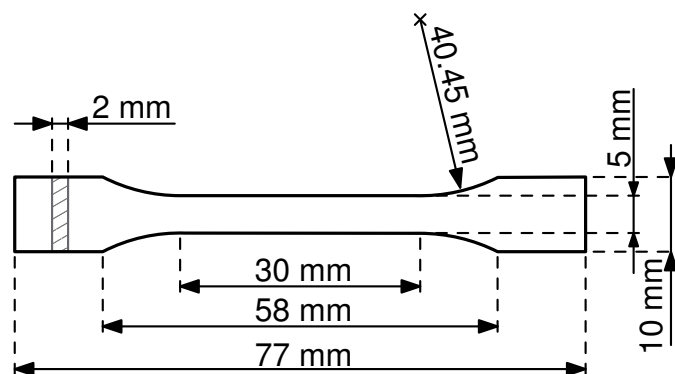


Figure 2.34. Geometry of the printed tensile specimens according to [DIN EN ISO 527-2:2012, 2012]

⁹The specimens whose default layers are irradiated for 1 s are omitted.

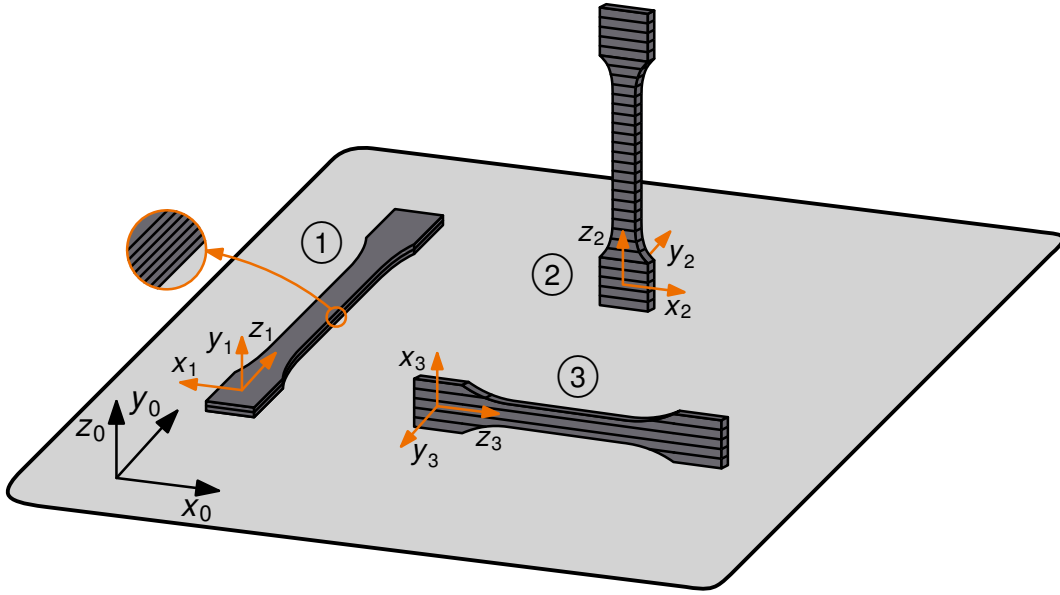


Figure 2.35. Schematic of the orientation of the printed specimens on the build plate. The individual hatching indicates the layer orientation in each individual specimen.

specimen is generally denoted as the z -direction, whereas the same applies to the normal direction of the build plate, different definitions arise from the possible specimen orientations. The definitions of the specimen orientation are deduced from the mapping of the individual local coordinates on the global ones. For example, by looking at specimen orientation ①, the specimen is printed in the xzy -orientation with respect to the global coordinate system of the build plate. On the other hand, considering specimen orientations ② and ③, the specimen is printed in the xyz - and zyx -orientation, respectively.

Considering the tensile specimen's dimensions and the chosen layer thickness ($\delta = 50 \mu\text{m}$), the slicing process results in 40 layers for orientation ①, 1540 layers for orientation ②, and 200 layers for orientation ③.

In order to reduce the printing time and the number of layers to be printed, specimen orientation ① is chosen for the fabrication of the tensile specimens. Furthermore, consistency with the DMA tests in sec. 2.4 is guaranteed. Additionally, the specimens are rotated by 90° and 45° around the global z_0 -axis after each print job to prevent the non-stick coating from damaging. Changing the contact area of the current layer after each print job leads to a more homogeneously distributed abrasion of the non-stick coating.

The tensile tests are performed on the tensile testing machine Z020 equipped with the XForce HP 2.5 kN load cell, both provided by ZwickRoell GmbH & Co. KG. In

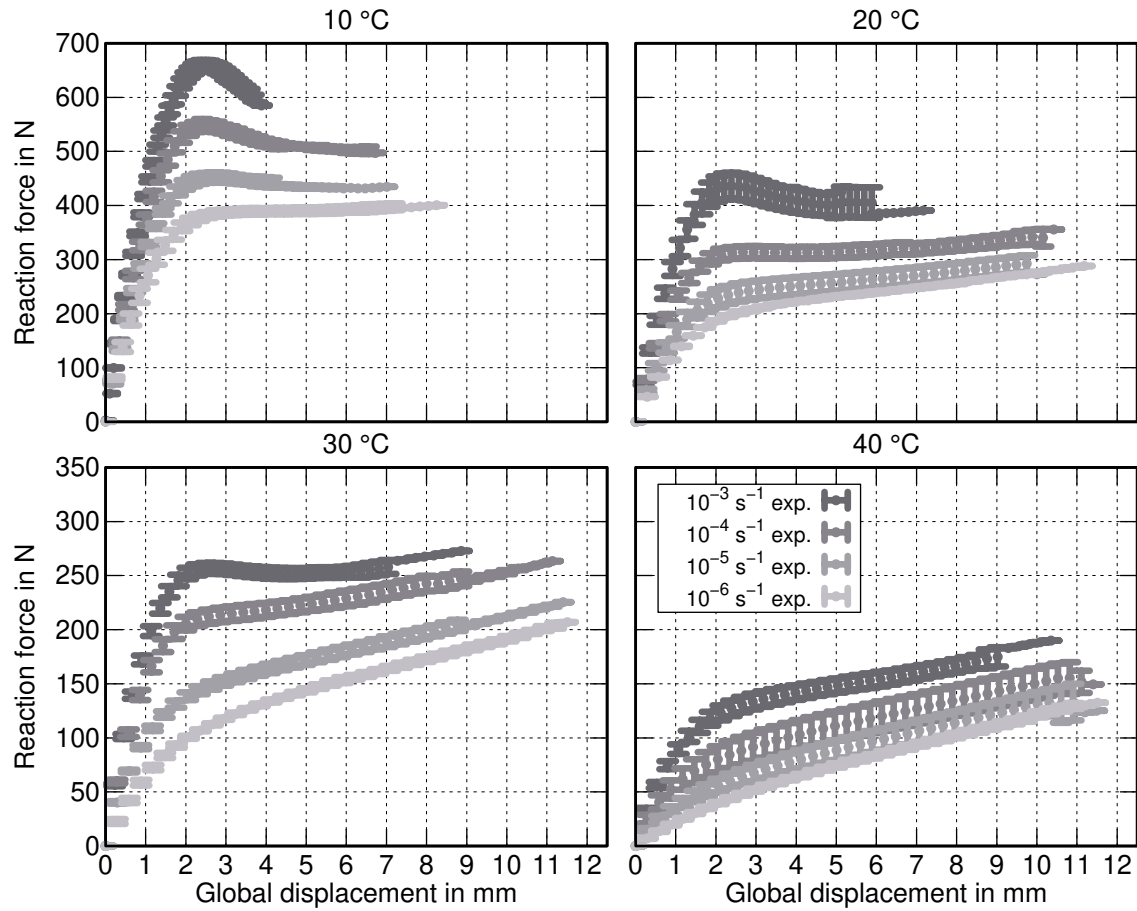


Figure 2.36. Experimental force-displacement curves of the tensile specimens with $c_{\text{eff}} = 1.0$ subjected to monotonic loading. The ordinate values are bisected in the plots of the second row.

addition, a temperature chamber is mounted to the testing machine to control the temperature during the measurement. Considering fig. 2.34, the lower and upper rectangular ends of the specimen are mounted to the clamps of the machine, but only the upper clamp is tightened. Then, the temperature is set to the desired value, and the chamber is closed. After ten minutes of equilibrating the specimen at the predefined temperature, the temperature chamber is opened, and both clamps are tightened. At the same time, the measured reaction force is controlled to 0 N by the testing machine. Otherwise, the specimen would bend while fastening the clamps. The traverse of the testing machine measures the deflection of the specimen. The following subsections discuss the results of the tensile tests subjected to monotonic loading and cyclic loading and unloading.

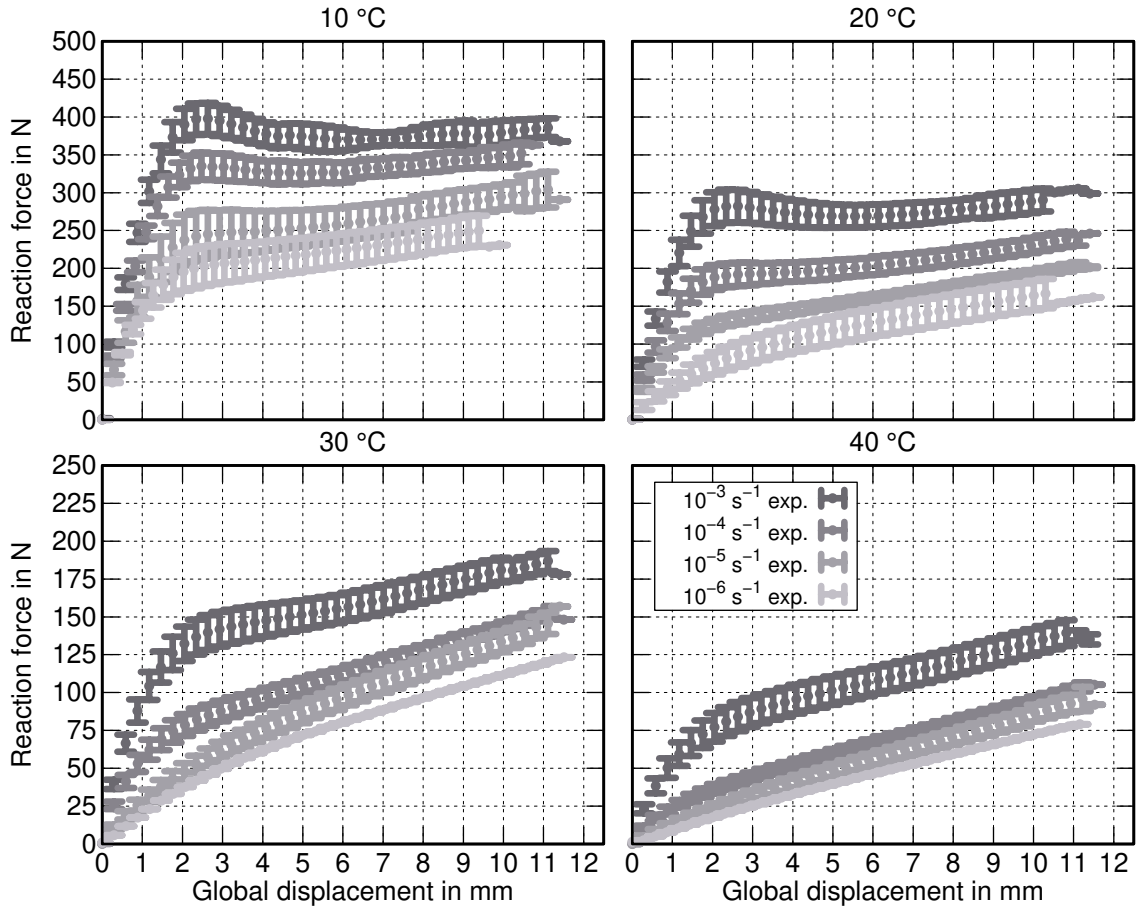


Figure 2.37. Experimental force-displacement curves of the tensile specimens with $c_{\text{eff}} = 0.9193$ subjected to monotonic loading. The ordinate values are bisected in the plots of the second row.

2.5.1 Monotonic loading

The tensile tests subjected to monotonic loading are conducted using the parameters above (temperature, strain rate) and conversion states. The velocity of the traverse is set to a constant value that corresponds to the predefined global strain rate. The tensile test is conducted five times for the two highest strain rates, whereas the measurements for the lowest strain rates are performed four times and three times, respectively. The maximum strain calculated by the deflection of the traverse and the initial length of the specimen is set to 20 %. This value is chosen in order to capture potential plastic deformations. At the same time, even when applying the lowest strain rate, the measuring time is acceptable.

Fig. 2.36 shows the results of the tensile tests performed using the specimens with a degree of cure of $c_{\text{eff}} = 1.0$. The mean value of the measured reaction force of all conducted measurements is plotted versus the global displacement of the traverse.

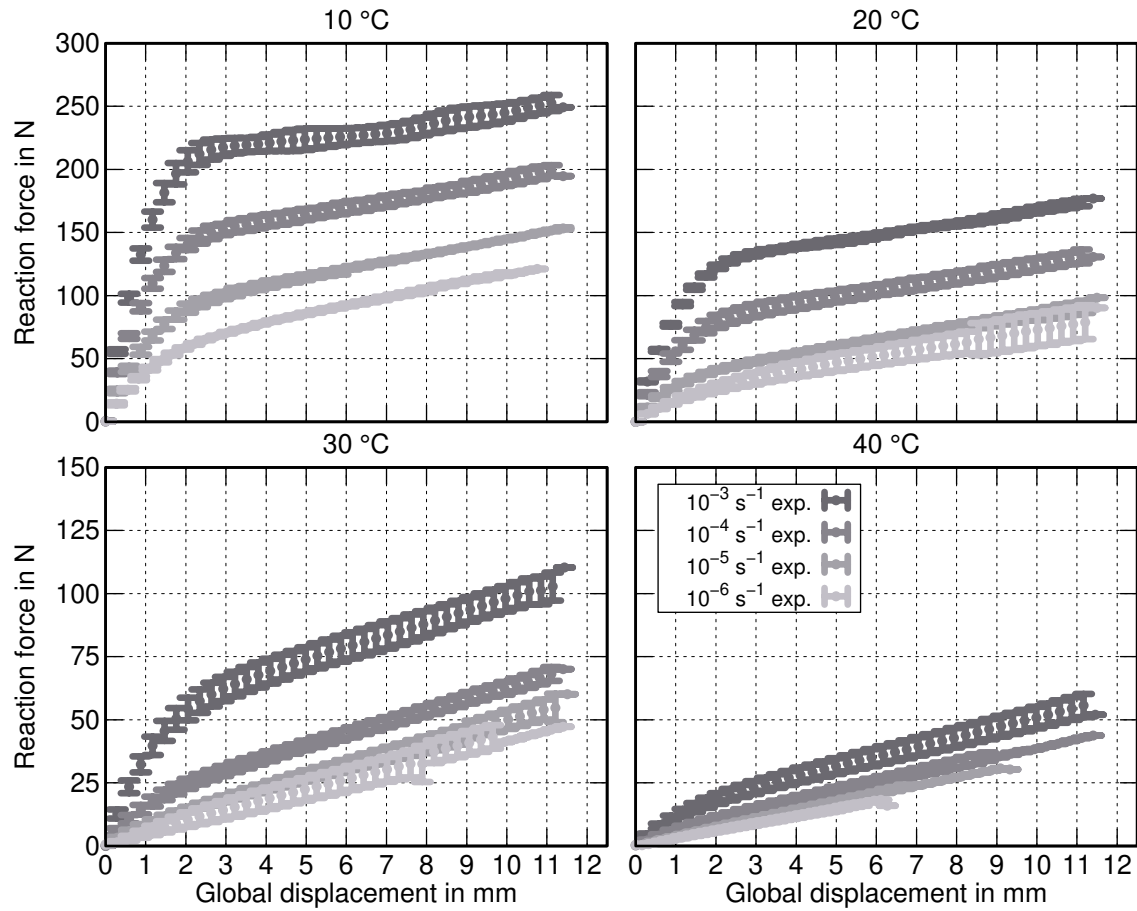


Figure 2.38. Experimental force-displacement curves of the tensile specimens with $c_{\text{eff}} = 0.8606$ subjected to monotonic loading. The ordinate values are bisected in the plots of the second row.

Additionally, the standard deviations are displayed as vertical bars. Especially in the measurements at 10 °C, softening behavior is observable at displacements greater than 2 mm, which is most pronounced at the highest strain rate. At the lowest strain rate, no softening is visible. Considering the measurements at the higher temperatures, the amount of softening decreases, and the specimens presumably show viscoelastic-viscoplastic behavior.

The tensile tests conducted using the specimens with $c_{\text{eff}} = 0.9193$ are displayed in fig. 2.37. Since the lower degree of cure leads to softer material behavior, the measured reaction forces are significantly lower than in fig. 2.36. Furthermore, the repeatability of the measurements is worse, as indicated by the higher standard deviations. However, the softening behavior is less pronounced at 10 °C and 20 °C. The same conclusions apply to the tensile tests using the specimens with $c_{\text{eff}} = 0.8606$, see fig. 2.38. Even though the degree of cure is only ≈ 14 % lower than the fully cured

state, the measured reaction forces are more than 50 % lower. Moreover, the repeatability of the measurements is better than that of the measurements in fig. 2.37.

Overall, the tensile behavior of the investigated photopolymer is strongly influenced by the chosen strain rate, temperature, and the degree of cure of the material. Therefore, the conducted measurements allow for the development of suitable model equations in ch. 3 and the identification of the corresponding parameters in ch. 4.

2.5.2 Cyclic loading and unloading

As previously discussed, the tensile tests under monotonic loading presumably show viscoplastic deformations. In order to further investigate potentially arising residual strains that are not only induced by viscoelasticity, tensile tests are performed subjected to cyclic loading and unloading. These tests are carried out by means of the global strain rate $\dot{\epsilon}_{\text{global}} = 10^{-4} \text{ s}^{-1}$ because they only serve for the validation of the proposed constitutive model and identified parameters following later. In addition, the assumption of viscoplastic deformations can be confirmed if residual strains are visible. The temperatures of the specimens are the same as those of the specimens subjected to monotonic loading. Each configuration is only tested once.

Again, the deflection of the specimen is controlled by the traverse with a constant strain rate. The strain rate is calculated by the ratio between the velocity of the traverse and the initial length of the specimen between the upper and lower clamps. The total strain of 10 % is applied to the specimen step by step. After each increase in strain by 1 %, the specimen is unloaded until the reaction force reaches 0 N while the strain rate is held constant.

The results of the measurements are visualized in figs. 2.39 - 2.41. The diagrams show the measured reaction force plotted versus the global displacement of the specimen and the global displacement plotted versus the time of the measurement. Unfortunately, the specimen at 10 °C in fig. 2.39 fails at the end of the eighth loading cycle. The other measurements show similar phenomena compared to the specimens subjected to monotonic loading:

- The specimen becomes softer if the temperature increases or the degree of cure decreases. Additionally, the hardening behavior of the material is more pronounced at higher temperatures.
- The measurements clearly show hysteresis loops caused by the viscoelastic or

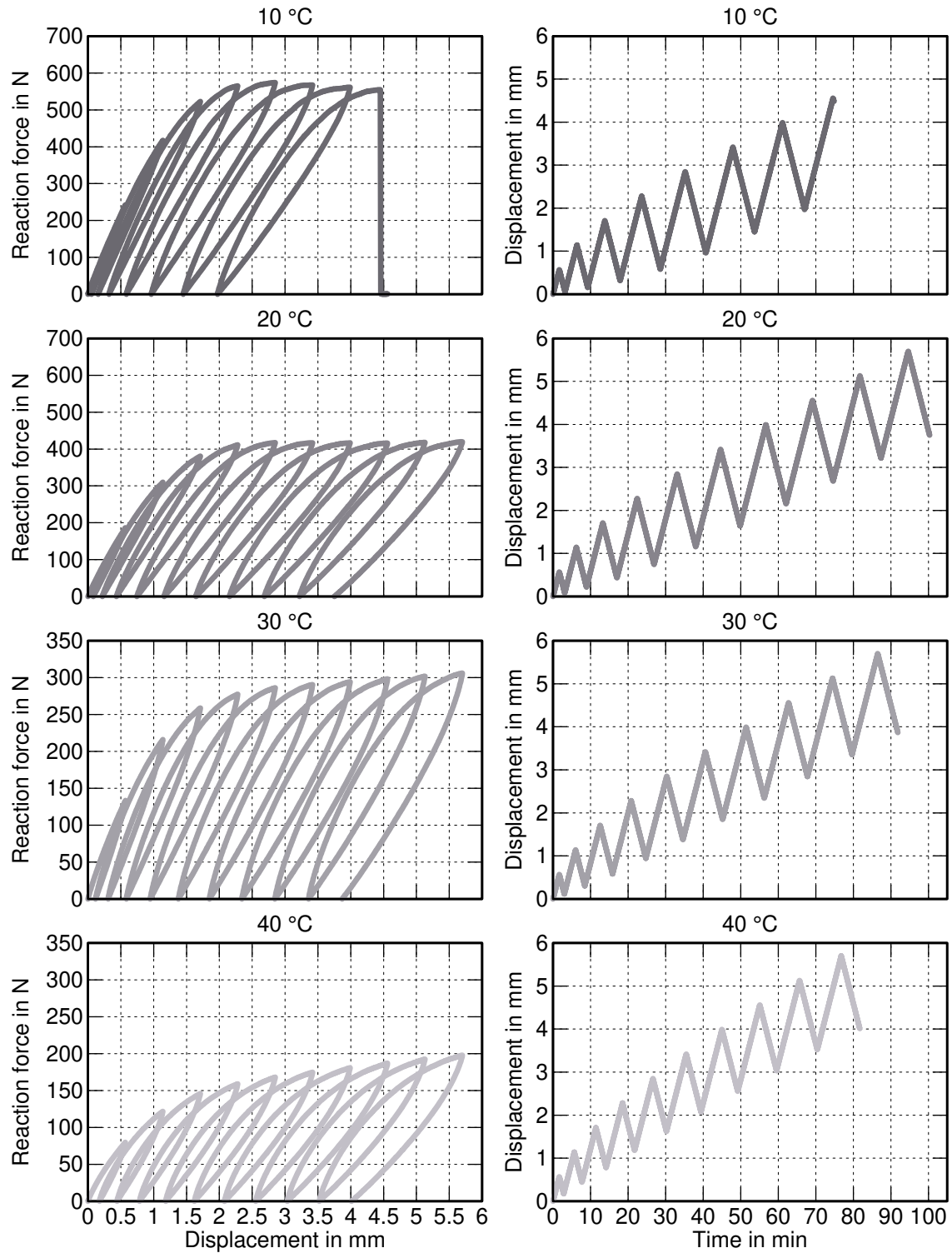


Figure 2.39. Left column: experimental force-displacement curves of the tensile specimens with $c_{\text{eff}} = 1.0$ subjected to cyclic loading and unloading ($\dot{\epsilon}_{\text{global}} = 10^{-4} \text{ s}^{-1}$). Right column: corresponding global displacement plotted versus time. The ordinate values of the plots in the left column are bisected in the lower two rows.

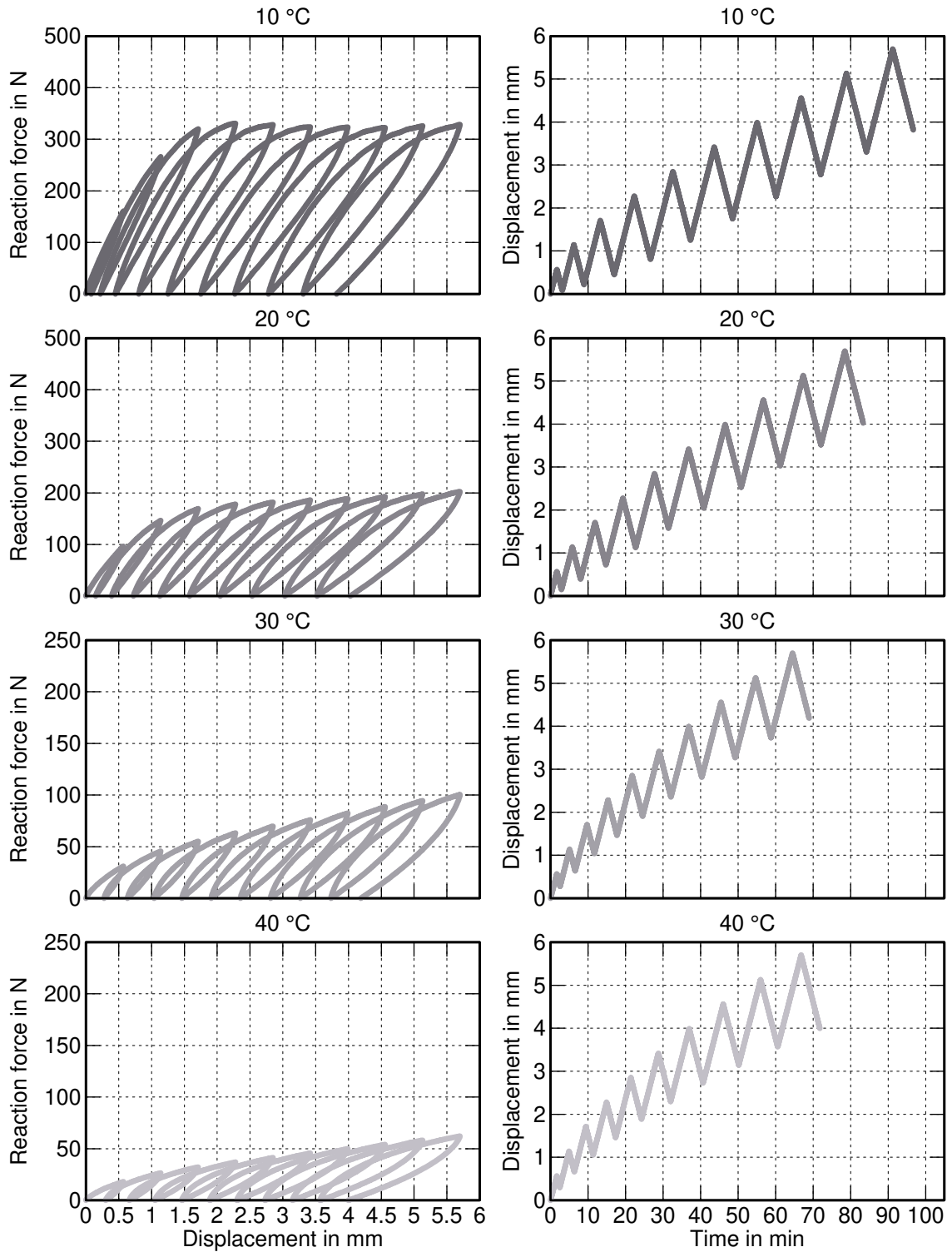


Figure 2.40. Left column: experimental force-displacement curves of the tensile specimens with $c_{\text{eff}} = 0.9193$ subjected to cyclic loading and unloading ($\dot{\epsilon}_{\text{global}} = 10^{-4} \text{ s}^{-1}$). Right column: corresponding global displacement plotted versus time. The ordinate values of the plots in the left column are bisected in the lower two rows.

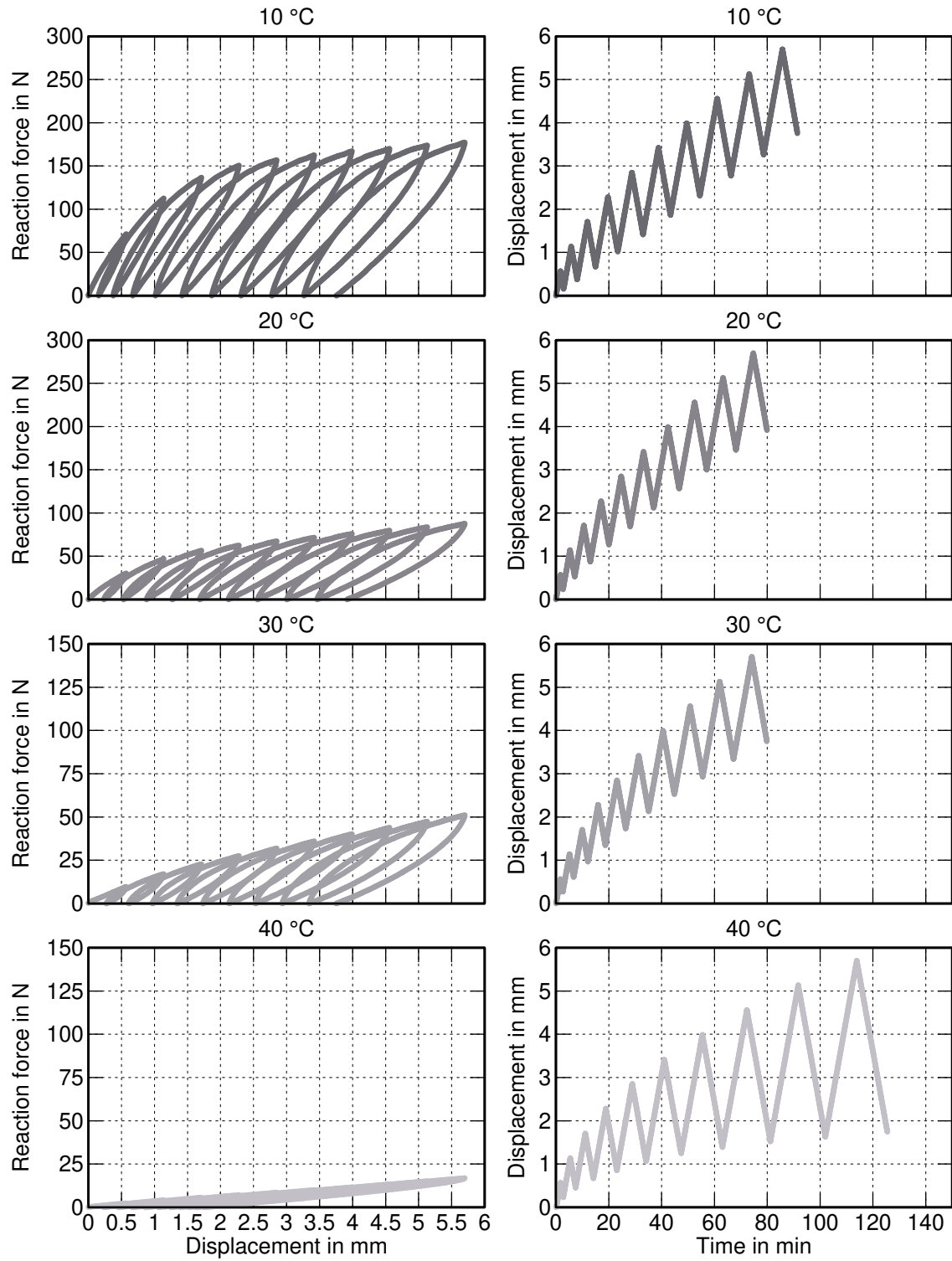


Figure 2.41. Left column: experimental force-displacement curves of the tensile specimens with $c_{\text{eff}} = 0.8606$ subjected to cyclic loading and unloading ($\dot{\epsilon}_{\text{global}} = 10^{-4} \text{ s}^{-1}$). Right column: corresponding global displacement plotted versus time. The ordinate values of the plots in the left column are bisected in the lower two rows.

viscoplastic properties of the material.

- The residual displacements at the end of each unloading cycle proportionally increase in fig. 2.39. Comparatively, the measurements at 30 °C and 40 °C in figs. 2.40 and 2.41 do not exhibit the same proportional increase of the residual displacement. For example, considering the measurement at 40 °C in fig. 2.41, the residual displacement nearly remains constant after the seventh unloading cycle, which indicates that (visco-)plastic deformations do not cause the residual displacement.

As a result, the assumption of viscoplastic deformations based on the tensile tests subjected to monotonic loading is verified by the tensile tests subjected to cyclic load and unloading.

3 Material Modeling

In general, the main objective of material modeling is the description of the experimentally observable material behavior through mathematical equations. These model equations are developed concerning the investigated material properties in ch. 2. Although the modeling approaches are based on the measurements for the Loctite® 3818 resin, the general applicability is given for other photopolymer resins. Additionally, wavelengths deviating from 405 nm can be considered. In that case, all measurement devices incorporating the OmniCure® S2000 curing system have to be equipped with an appropriate filter, and the parameters have to be identified again.

Being the critical parameter for the overall material properties of photopolymer resins, special attention is paid to the modeling of the degree of cure. The correct representation of the experimental data in sec. 2.2.3, which are influenced by the resin temperature, irradiance, and exposure time, is essential for the modeling of the mechanical properties, chemical shrinkage, and thermal expansion and contraction, respectively.

Afterward, using the fundamentals of continuum mechanics, a suitable material model is formulated representing the following phenomena identified in the experimental investigations of ch. 2:

- viscoelasticity for the rate-dependent reversible domain,
- viscoplasticity with isotropic hardening for the rate-dependent irreversible domain, and
- isotropic deformations for the chemical shrinkage as well as the thermal expansion and contraction.

For this purpose, the theoretical framework of continuum mechanics is applied in this thesis. Since the associated methods and principles are employed only as a tool, detailed derivations are omitted. Therefore, reference is made to the established textbooks [Malvern, 1969; Holzapfel, 2001; Haupt, 2002; Truesdell and Noll, 2004].

3.1 Degree of cure

3.1.1 Internal variable

In this thesis, curing is synonymously used with the crosslinking reaction of polymers. The crosslinking reaction of polymer systems causes the transition of the liquid material into a solid. In order to describe this process, the scalar, dimensionless state variable c is introduced, which is referred to as the degree of cure. Thereby, the uncured and fully cured states correspond to $c = 0$ and $c = 1$, respectively. The variable describing the degree of cure is introduced as an internal variable [Haupt, 2002].

Modeling the curing process of polymers has been the subject of research for several decades. In particular, the modeling of the curing of adhesive joints is of great interest because the prediction of the curing process as function of varying process parameters (temperature, curing time) is indispensable for the reliability of the adhesive joint.

A frequently used approach is the model equation proposed in [Kamal, 1974] for the description of the crosslinking of thermosets¹:

$$\dot{c} = (k_1 + k_2 c^n) (1 - c)^p . \quad (3.1)$$

This model equation exhibits the following properties:

- The rate of conversion \dot{c} is a function of the degree of cure itself, which is expressed by an ordinary, nonlinear, and non-homogeneous differential equation of first order.
- The rate of conversion increases with increasing degree of cure, which is denoted as autocatalytic. However, the rate of conversion starts to decrease at the inflection point of the diagram representing the degree of cure versus time. Thus, the rate of conversion tends towards zero.
- The autocatalytic behavior and the deceleration of the crosslinking reaction are controlled by the parameters n and p .

In addition, the parameters k_1 and k_2 are temperature-dependent and are described

¹A comprehensive discussion of several models describing the crosslinking reaction of polymers is given in [Hossain, 2010].

by ARRHENIUS equations:

$$k_i = A_i \exp\left(-\frac{E_i}{RT}\right) \quad , \quad i = 1, 2 . \quad (3.2)$$

Therein, A_1 and A_2 are pre-exponential factors ($[A_i] = \text{s}^{-1}$) and the parameters E_1 and E_2 are denoted as activation energies ($[E_i] = \text{J/mol}$). $R = 8.314 \text{ J/(mol K)}$ is the universal gas constant.

In general, the photo-DSC measurements conducted for the characterization of the crosslinking reaction in fig. 2.10 show the characteristics of eq. (3.1) mentioned above. As previously discussed in subsec. 2.2.3, the maximum attainable degree of cure strongly depends on the surrounding temperature of the photopolymer resin. The model eq. (3.1) always leads to $c = 1$ for $t \rightarrow \infty$, regardless which temperature program is imposed on the crosslinking substance. Thus, the influence of the surrounding temperature on the photopolymer resin and its maximum attainable degree of cure must be considered.

Therefore, eq. (3.1) is extended by the additional, temperature-dependent function $c_{\max}(T)$ for the maximum attainable degree of cure:

$$c_{\max}(T) = \frac{1}{1 + \exp(-c_0(T - T_{c_{\max}}))} . \quad (3.3)$$

This function depends on the thermodynamic temperature T in order to be consistent with the ARRHENIUS equations, see eq. (3.2). The parameters c_0 and $T_{c_{\max}}$ are adapted to the experimentally determined ultimate values of the degree of cure depending on the surrounding temperature, see sec. 4.1. Considering sufficiently high surrounding temperatures, the maximum attainable degree of cure tends towards its ultimate value $c_{\max} = 1$.

FOURNIER et al. [Fournier et al., 1996] introduced the function

$$f_D(c_{\max}(T)) = \frac{2}{1 + \exp(c - c_{\max}(T))} - 1 \quad (3.4)$$

based on [Cole, 1991] to capture diffusion controlled mechanisms during the crosslinking process of epoxide-amine polymer systems, which decelerate the reaction. For $c \rightarrow c_{\max}(T)$, the diffusion function f_D tends towards zero, and thus stops the reaction ($\dot{c} = 0$). The reaction cannot continue until the surrounding temperature of the photopolymer resin is increased. Hence, eq. (3.4) is suitable to describe the limiting effects of too low temperatures in the photo-DSC measurements.

Taking into account eq. (3.4), the modified differential equation describing the evolution of the degree of cure reads as

$$\dot{c} = (k_1 + k_2 c^n) (1 - c)^p f_D(c_{\max}(T)) . \quad (3.5)$$

The equations introduced so far can only describe the crosslinking of polymers induced by heat. In order to describe crosslinking reactions induced by radiation as present in additive manufacturing processes using photopolymerization, the irradiance \mathcal{I} must be integrated into the eq. (3.5). Therefore, the following assumptions are made being based on the crosslinking in the additive manufacturing processes of photopolymers:

- In order to start the crosslinking reaction, the photopolymeric layer must be irradiated. According to this, the rate of conversion is equal to zero if the irradiance vanishes.
- The crosslinking reaction is stopped if the light source of the additive manufacturing device is turned off. The crosslinking reaction progresses upon continuing the irradiation.

By looking at eq. (3.5) one can easily conclude that the two assumptions mentioned above are ensured if the ARRHENIUS factors k_1 and k_2 are equal to zero for $\mathcal{I} = 0$. Hence, these are extended by the consideration of incoming irradiation \mathcal{I} following the approach in [Maffezzoli and Terzi, 1998]:

$$k_i = A_i \exp\left(-\frac{E_i}{RT}\right) \left(\frac{\mathcal{I}}{\mathcal{I}_{\text{ref}}}\right)^{b_i}, \quad i = 1, 2 . \quad (3.6)$$

The reference value $\mathcal{I}_{\text{ref}} = 1 \text{ mW/cm}^2$ is only introduced to guarantee unit consistency. Moreover, the dimensionless parameters b_1 and b_2 allow for the consideration of a nonlinear dependency on the chosen irradiance during the crosslinking reaction. Furthermore, by introducing two exponents instead of one, the influence of the irradiance is separated and individually contributed to the start and the autocatalytic acceleration of the crosslinking reaction. Compared to previous works [Tryson and Shultz, 1979; da Silva Bartolo, 2007], using two individual exponents is a new approach to capture the dependency on the irradiance of the crosslinking reaction. Additionally, TRYSON and SHULTZ assumed that the rate of conversion is proportional to the square root of the incident irradiance.

In total, the model for the description of the degree of cure has eight parameters. The identification of the parameters by means of the experimental results in subsec. 2.2.3 is conducted in sec. 4.1.

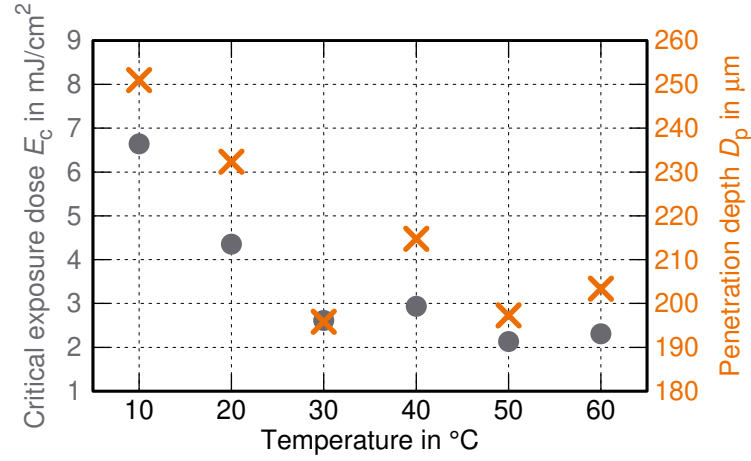


Figure 3.1. Identified critical exposure doses and penetration depths of the working curves as shown in table 2.3

3.1.2 Modified working curve model

As already seen in fig. 2.20, the curing behavior of the photopolymer is highly temperature-dependent in the working curve measurement. Hence, a modification of the working curve model given by eq. (1.2) should be applied taking into account the dependency on the temperature of the penetration depth and critical exposure dose:

$$C_d(\theta) = D_p(\theta) \ln \left(\frac{E_0}{E_c(\theta)} \right). \quad (3.7)$$

Fig. 3.1 shows the previously identified critical exposure doses and penetration depths as a function of temperature (cf. table 2.3). A strong decrease in both parameters with increasing temperature is visible, which can be represented by the following exponential approaches:

$$E_c(\theta) = E_{c0} \exp(-E_{c1}\theta) \quad (3.8)$$

$$\text{and } D_p(\theta) = D_{p0} \exp(-D_{p1}\theta). \quad (3.9)$$

Therein, the parameters E_{c0} and D_{p0} describe the critical exposure dose and the penetration depth at $\theta = 0$ °C. The scaling parameters E_{c1} and D_{p1} are introduced to guarantee unit consistency and to ensure enough flexibility in the identification process following later.

3.2 Kinematic and kinetic quantities

The modeling of the material properties of the crosslinking photopolymer based on the methods of continuum mechanics requires the introduction of several kinematic and kinetic quantities. Hence, the quantities required for the formulation of the material model are introduced in the following based on the textbooks [Malvern, 1969; Holzapfel, 2001; Haupt, 2002; Truesdell and Noll, 2004].

The crosslinking photopolymer is considered as a material body \mathcal{B} . Principally, the material body consists of an uncountable set of material points P , which are connected to each other and cannot be located at two positions simultaneously. Additionally, physical properties are assigned to the material points.

In order to describe the motion of the material body, the reference configuration and the current configuration are introduced at the beginning of ($t = t_0$) and during the movement ($t > t_0$), respectively. Fig. 3.2 shows the motion of the material body going from the reference to the current configuration. The corresponding states of the material body are referred to as \mathcal{B}_0 and \mathcal{B}_t , respectively. The individual positions of an arbitrary material point are defined by the vectors \mathbf{X} in the reference configuration and \mathbf{x} in the current configuration. Taking into account the LAGRANGIAN description, the relation between the positions of the material point in the reference and current configuration is described by the vector field ϕ :

$$\mathbf{x} = \phi(\mathbf{X}, t) . \quad (3.10)$$

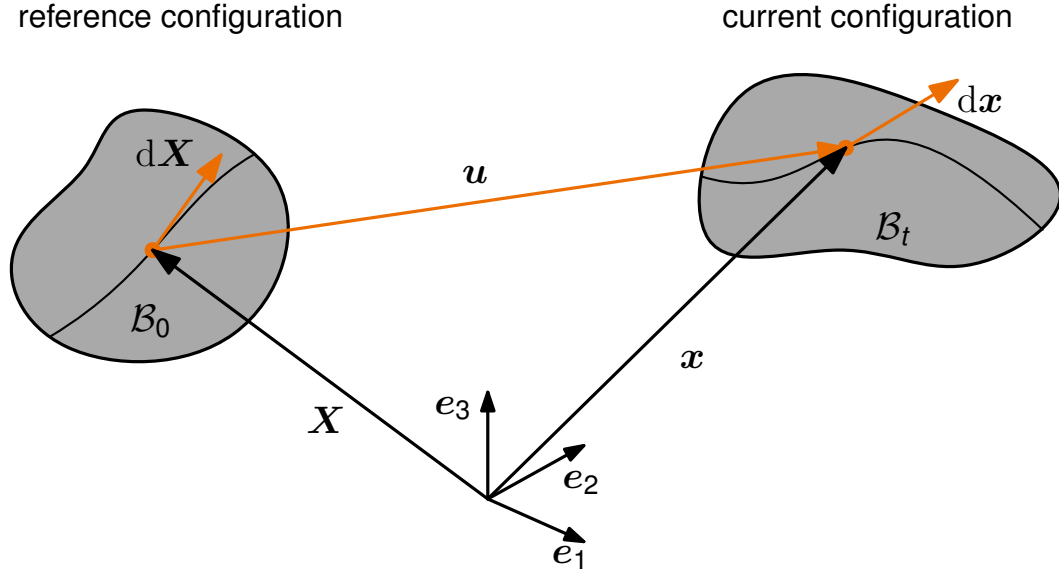
Thus, the motion of the material body is expressed by the positions of the material points in the reference configuration. Following this, the displacement vector \mathbf{u} is given by

$$\mathbf{u}(\mathbf{X}, t) = \mathbf{x}(\mathbf{X}, t) - \mathbf{X} . \quad (3.11)$$

In order to describe the deformation of the material body, the deformation gradient \mathbf{F} is introduced:

$$\mathbf{F} = \frac{\partial \phi(\mathbf{X}, t)}{\partial \mathbf{X}} = \frac{\partial \mathbf{x}}{\partial \mathbf{X}} . \quad (3.12)$$

The deformation gradient and its derived quantities allow for the transformation of line, surface, and volume elements from the reference into the current configuration. For example, reconsidering fig. 3.2, the deformation gradient directly communicates between the line elements in the corresponding configurations described by


 Figure 3.2. Motion of the material body \mathcal{B}

the tangential vectors $d\mathbf{X}$ and $d\mathbf{x}$:

$$d\mathbf{x} = \mathbf{F}d\mathbf{X} . \quad (3.13)$$

Moreover, the transition of volume elements from the reference to the current configuration is described by

$$dv = \det \mathbf{F} dV . \quad (3.14)$$

The determinant of the deformation gradient is also called the Jacobian J ($\det \mathbf{F} = J$). Equivalently, combining eqs. (3.11) and (3.12) leads to the representation

$$\mathbf{F} = \mathbf{1} + \frac{\partial \mathbf{u}(\mathbf{X}, t)}{\partial \mathbf{X}} . \quad (3.15)$$

Therein, the partial derivative of \mathbf{u} with respect to \mathbf{X} is denoted as the displacement gradient \mathbf{H} :

$$\mathbf{H} = \frac{\partial \mathbf{u}(\mathbf{X}, t)}{\partial \mathbf{X}} = \text{Grad}(\mathbf{u}(\mathbf{X}, t)) . \quad (3.16)$$

In the following section, the spatial velocity gradient is also required for the formulation of the material model. Therefore, the spatial velocity gradient is defined by

$$\mathbf{L} = \frac{\partial \mathbf{v}(\mathbf{x}, t)}{\partial \mathbf{x}} = \dot{\mathbf{F}}\mathbf{F}^{-1} , \quad (3.17)$$

whereas $\mathbf{v}(\mathbf{x}, t)$ is the spatial velocity field. The spatial velocity gradient can be additively decomposed into

$$\mathbf{L} = \mathbf{d} + \mathbf{w} . \quad (3.18)$$

Herein, \mathbf{d} is the symmetric strain rate tensor and defined by

$$\mathbf{d} = \frac{1}{2} (\mathbf{L} + \mathbf{L}^\top) . \quad (3.19)$$

Comparatively, \mathbf{w} is the skew-symmetric spin tensor and accounts for rotations:

$$\mathbf{w} = \frac{1}{2} (\mathbf{L} - \mathbf{L}^\top) . \quad (3.20)$$

In order to calculate the stresses of the material body that arise from the acting internal and external forces, the CAUCHY stress \mathbf{T} is introduced by the CAUCHY theorem

$$\mathbf{t} = \mathbf{T}\mathbf{n} . \quad (3.21)$$

Herein, \mathbf{t} is the traction vector acting on the surface element in the current configuration and \mathbf{n} is the corresponding normal vector. Hence, the CAUCHY stress operates on the current configuration and is denoted as the true stress. Moreover, the CAUCHY stress tensor is symmetric ($\mathbf{T} = \mathbf{T}^\top$).

Correspondingly, the first PIOLA-KIRCHHOFF stress \mathbf{T}_R given by

$$\mathbf{T}_R = \det(\mathbf{F}) \mathbf{T} \mathbf{F}^{-1} \quad (3.22)$$

relates the resultant force in the current configuration to the surface element in the reference configuration. Commonly speaking, the first PIOLA-KIRCHHOFF stress is denoted as the engineering stress.

3.3 Multiplicative decomposition of the deformation gradient

Material models based on a hypoelastic approach allow for the simulation of the stress-free conversion of crosslinking polymers. Both small [Hossain et al., 2009b] and finite strains [Hossain et al., 2009a, 2010] can be considered using this type of stress rate formulation. The original formulation relates any type of objective rate of the CAUCHY stress $\dot{\mathbf{T}}$ with the present stress \mathbf{T} and the elastic part of the strain

rate tensor \mathbf{d}_{el} [Truesdell and Noll, 2004; Belytschko et al., 2014]:

$$\dot{\mathbf{T}} = \mathbf{f}(\mathbf{T}, \mathbf{d}_{\text{el}}) . \quad (3.23)$$

The most simple approach is given by

$$\mathbf{T}^\nabla = \mathbf{C}_{\text{el}} \cdot \mathbf{d}_{\text{el}} . \quad (3.24)$$

Therein, \mathbf{C}_{el} is the fourth-order elasticity tensor, \mathbf{T}^∇ denotes the JAUMANN rate of the CAUCHY stress

$$\mathbf{T}^\nabla = \dot{\mathbf{T}} - \mathbf{w}\mathbf{T} + \mathbf{T}\mathbf{w} , \quad (3.25)$$

and \mathbf{w} is the spin tensor.

In order to model the curing progress of photopolymers and calculate the corresponding stresses given by the rate formulation in eq. (3.24), one has to comprehensively analyze the deformation mechanisms that influence the transition of the photopolymer from the liquid state to the solid state. In detail, the following phenomena generally accompany the transition of the photopolymer resin:

- Chemical shrinkage due to progressing crosslinks
- Thermal expansion or contraction induced by temperature variations
- Viscoelastic deformations depending on the current transition state and temperature
- Viscoplastic deformations in case of exceeding the yield condition

A milestone for the continuum mechanical modeling of curing processes of polymers in general was presented by Lion and Höfer by introducing the multiplicative split of the deformation gradient \mathbf{F} into mechanical, thermal, and chemical parts [Lion and Höfer, 2007]:

$$\mathbf{F} = \mathbf{F}_{\text{m}}\mathbf{F}_{\text{th}}\mathbf{F}_{\text{ch}} . \quad (3.26)$$

Considering adhesives that cure by heat, it should be noted that the parts representing the chemical shrinkage and thermal expansion or contraction are often summarized as one thermochemical part $\mathbf{F}_{\theta c}$ [Yagimli, 2013; Landgraf, 2015; Kolmeder, 2016]. This approach is mainly motivated by the idea that the crosslinking polymer's chemical shrinkage and thermal expansion influence each other.

Taking into account the assumptions given by the theory of hypoelasticity, one needs to compute the spatial velocity gradient \mathbf{L} by means of the multiplicative decomposition of the deformation gradient presented in eq. (3.26). First, the material time derivative of the deformation gradient is calculated:

$$\dot{\mathbf{F}} = \dot{\mathbf{F}}_{\text{m}} \mathbf{F}_{\text{th}} \mathbf{F}_{\text{ch}} + \mathbf{F}_{\text{m}} \dot{\mathbf{F}}_{\text{th}} \mathbf{F}_{\text{ch}} + \mathbf{F}_{\text{m}} \mathbf{F}_{\text{th}} \dot{\mathbf{F}}_{\text{ch}} . \quad (3.27)$$

Second, the inverse of the multiplicative decomposition of the deformation gradient reads as

$$\mathbf{F}^{-1} = \mathbf{F}_{\text{ch}}^{-1} \mathbf{F}_{\text{th}}^{-1} \mathbf{F}_{\text{m}}^{-1} . \quad (3.28)$$

Combining eq. (3.27) with eq. (3.28) leads to the following equation for the spatial velocity gradient:

$$\begin{aligned} \mathbf{L} &= \dot{\mathbf{F}} \mathbf{F}^{-1} \\ &= \left(\dot{\mathbf{F}}_{\text{m}} \mathbf{F}_{\text{th}} \mathbf{F}_{\text{ch}} + \mathbf{F}_{\text{m}} \dot{\mathbf{F}}_{\text{th}} \mathbf{F}_{\text{ch}} + \mathbf{F}_{\text{m}} \mathbf{F}_{\text{th}} \dot{\mathbf{F}}_{\text{ch}} \right) \left(\mathbf{F}_{\text{ch}}^{-1} \mathbf{F}_{\text{th}}^{-1} \mathbf{F}_{\text{m}}^{-1} \right) \\ &= \dot{\mathbf{F}}_{\text{m}} \mathbf{F}_{\text{th}} \mathbf{F}_{\text{ch}} \mathbf{F}_{\text{ch}}^{-1} \mathbf{F}_{\text{th}}^{-1} \mathbf{F}_{\text{m}}^{-1} + \mathbf{F}_{\text{m}} \dot{\mathbf{F}}_{\text{th}} \mathbf{F}_{\text{ch}} \mathbf{F}_{\text{ch}}^{-1} \mathbf{F}_{\text{th}}^{-1} \mathbf{F}_{\text{m}}^{-1} + \mathbf{F}_{\text{m}} \mathbf{F}_{\text{th}} \dot{\mathbf{F}}_{\text{ch}} \mathbf{F}_{\text{ch}}^{-1} \mathbf{F}_{\text{th}}^{-1} \mathbf{F}_{\text{m}}^{-1} \\ &= \mathbf{L}_{\text{m}} + \mathbf{F}_{\text{m}} \mathbf{L}_{\text{th}} \mathbf{F}_{\text{m}}^{-1} + \mathbf{F}_{\text{m}} \mathbf{F}_{\text{th}} \mathbf{L}_{\text{ch}} \mathbf{F}_{\text{th}}^{-1} \mathbf{F}_{\text{m}}^{-1} . \end{aligned} \quad (3.29)$$

For further simplifications, isotropic thermal expansion/contraction as well as isotropic chemical shrinkage have to be assumed depending on the temperature θ and degree of cure c :

$$\mathbf{F}_{\text{th}} = (\varphi_{\text{th}}(\theta))^{\frac{1}{3}} \mathbf{1} \quad (3.30)$$

$$\text{and } \mathbf{F}_{\text{ch}} = (\varphi_{\text{ch}}(c))^{\frac{1}{3}} \mathbf{1} . \quad (3.31)$$

Herein, $\varphi_{\text{th}}(\theta)$ and $\varphi_{\text{ch}}(c)$ are scalar-valued functions describing the thermal expansion/contraction and the chemical shrinkage, respectively. Since the experimental observations could only be performed for the fully cured state of the photopolymer, no coupling between the temperature θ and degree of cure c is assumed in the function φ_{th} . Likewise, this additional phenomenon, i.e., a thermal expansion/contraction behavior depending on the degree of cure, could easily be introduced [Lion and Höfer, 2007; Yagimli, 2013; Kolmeder, 2016].

To further evaluate eq. (3.29), one has to compute spatial velocity gradients \mathbf{L}_{th} and \mathbf{L}_{ch} . To this end, the material time derivative of the thermal and chemical parts

of the deformation gradient given by the eqs. (3.30) and (3.31) read as

$$\dot{\mathbf{F}}_{\text{th}} = \frac{1}{3} (\varphi_{\text{th}}(\theta))^{-\frac{2}{3}} \frac{\partial \varphi_{\text{th}}}{\partial \theta} \dot{\theta} \mathbf{1} \quad (3.32)$$

$$\text{and } \dot{\mathbf{F}}_{\text{ch}} = \frac{1}{3} (\varphi_{\text{ch}}(c))^{-\frac{2}{3}} \frac{\partial \varphi_{\text{ch}}}{\partial c} \dot{c} \mathbf{1} . \quad (3.33)$$

Analogously, the inverses of the thermal and shrinkage parts of the deformation gradient are given by

$$\mathbf{F}_{\text{th}}^{-1} = (\varphi_{\text{th}}(\theta))^{-\frac{1}{3}} \mathbf{1} \quad (3.34)$$

$$\text{and } \mathbf{F}_{\text{ch}}^{-1} = (\varphi_{\text{ch}}(c))^{-\frac{1}{3}} \mathbf{1} . \quad (3.35)$$

As a result, combining eqs. (3.32) and (3.33) with eqs. (3.34) and (3.35) lead to thermal and chemical parts of the spatial velocity gradient:

$$\mathbf{L}_{\text{th}} = \dot{\mathbf{F}}_{\text{th}} \mathbf{F}_{\text{th}}^{-1} = \frac{1}{3 \varphi_{\text{th}}(\theta)} \frac{\partial \varphi_{\text{th}}}{\partial \theta} \dot{\theta} \mathbf{1} \quad (3.36)$$

$$\text{and } \mathbf{L}_{\text{ch}} = \dot{\mathbf{F}}_{\text{ch}} \mathbf{F}_{\text{ch}}^{-1} = \frac{1}{3 \varphi_{\text{ch}}(c)} \frac{\partial \varphi_{\text{ch}}}{\partial c} \dot{c} \mathbf{1} . \quad (3.37)$$

Since the thermal and chemical parts of the spatial velocity gradient are assumed to be isotropic, they are also symmetric. Therefore,

$$\mathbf{L}_{\text{th}} = \mathbf{d}_{\text{th}} \quad (3.38)$$

$$\text{and } \mathbf{L}_{\text{ch}} = \mathbf{d}_{\text{ch}} \quad (3.39)$$

hold.

The most simple approaches for the functions $\varphi_{\text{th}}(\theta)$ and $\varphi_{\text{ch}}(c)$ are given by linear thermal expansion/contraction and linear chemical shrinkage, respectively:

$$\varphi_{\text{th}}(\theta) = 1 + \alpha_{\text{th}}(\theta - \theta_0) \quad (3.40)$$

$$\text{and } \varphi_{\text{ch}}(c) = 1 - \alpha_{\text{ch}}c . \quad (3.41)$$

Therein, α_{th} and α_{ch} are model parameters representing the coefficient of thermal expansion and the chemical shrinkage constant, respectively. Accordingly, the corresponding parts of the strain rate tensor are governed by

$$\mathbf{d}_{\text{th}} = \frac{\alpha_{\text{th}} \dot{\theta}}{3(1 + \alpha_{\text{th}}(\theta - \theta_0))} \mathbf{1} \quad (3.42)$$

$$\text{and } \mathbf{d}_{\text{ch}} = -\frac{\alpha_{\text{ch}} \dot{c}}{3(1 - \alpha_{\text{ch}}c)} \mathbf{1} . \quad (3.43)$$

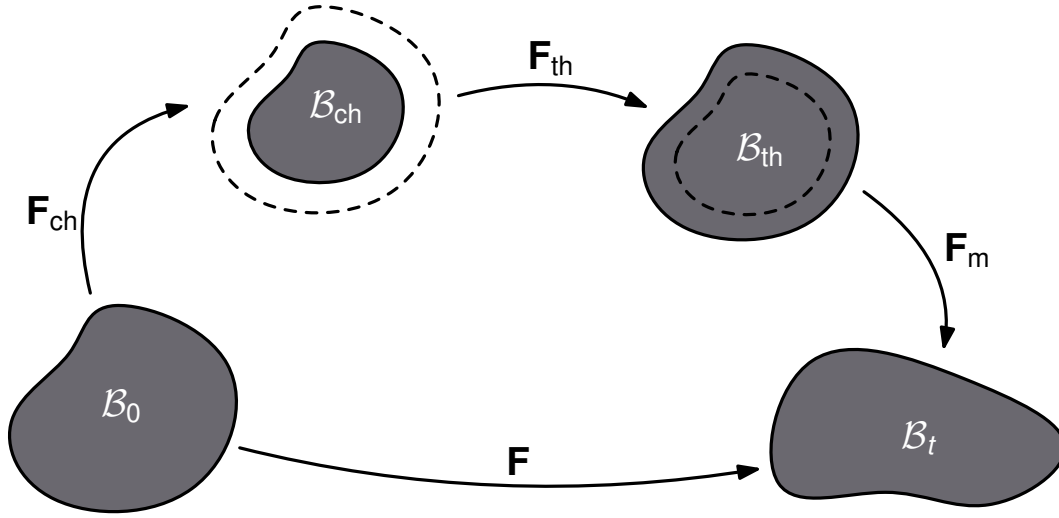


Figure 3.3. Graphical representation of the configurations corresponding to the multiplicative decomposition of the deformation gradient in eq. (3.26)

In fig. 3.3, the graphical representation of the configurations is shown corresponding to the introduced multiplicative split of eq. (3.26). Starting at the reference configuration (\mathcal{B}_0), the material body initially goes into the intermediate configuration related to the chemical shrinkage (\mathcal{B}_{ch}), which is visualized by the isotropic shrinkage (dotted lines). In the next step, the material body transforms into the intermediate configuration related to the thermal expansion/contraction. Again, this deformation is visualized as an isotropic expansion. In the last step, the material body goes into the current configuration by applying the mechanical part of the deformation gradient \mathbf{F}_m .

Reduction to small viscoelastic and large viscoplastic deformations In the last step, all derived relations lead to the additive decomposition of the spatial velocity gradient:

$$\mathbf{L} = \mathbf{L}_m + \mathbf{L}_{th} + \mathbf{L}_{ch} . \quad (3.44)$$

Equivalently, the following relations result from eq. (3.44):

$$\mathbf{d} = \mathbf{d}_m + \mathbf{d}_{th} + \mathbf{d}_{ch} \quad (3.45)$$

$$\text{and } \mathbf{w} = \mathbf{w}_m + \mathbf{w}_{th} + \mathbf{w}_{ch} . \quad (3.46)$$

In the following, the mechanical part of the spatial velocity gradient \mathbf{L}_m is analyzed. Before that, further multiplicative decompositions are introduced.

First, accounting for viscoelastic and viscoplastic deformations, the multiplicative

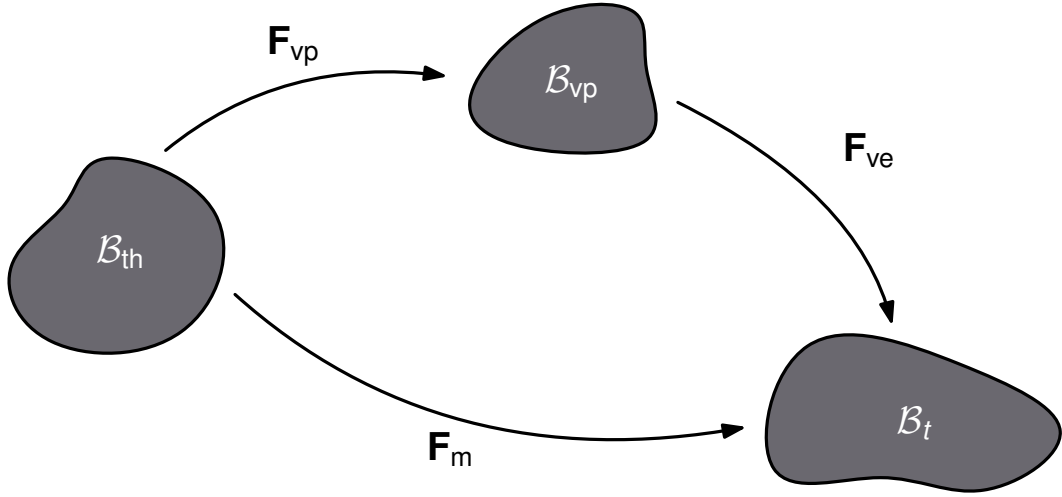


Figure 3.4. Graphical representation of the configurations corresponding to the multiplicative decomposition of the deformation gradient in eq. (3.47)

decomposition of the mechanical part of the deformation gradient \mathbf{F}_m into viscoelastic and viscoplastic parts is employed based on the proposal in [Lee, 1969]:

$$\mathbf{F}_m = \mathbf{F}_{ve} \mathbf{F}_{vp} . \quad (3.47)$$

Fig. 3.4 shows a schematic of the transition of the material body going from the thermal intermediate configuration \mathcal{B}_{th} over the viscoplastic intermediate configuration \mathcal{B}_{vp} to the current configuration \mathcal{B}_t .

Usually, in the case of modeling metals, viscoelastic deformations are excluded. Hence, the multiplicative decomposition is reduced to the elastic-viscoplastic case ($\mathbf{F}_m = \mathbf{F}_e \mathbf{F}_{vp}$). Unlike metals, polymers generally exhibit viscoelastic behavior, which is also strongly temperature-dependent. Additionally, viscoplastic deformations should not be omitted. Consequently, the viscoelastic-viscoplastic decomposition comprises all possible phenomena. Certainly, based on the experimental investigations and the specific application, this generalization can be further reduced to a simplified representation.

Experimental investigations have shown that the volumetric response of polymers is much stiffer than their deviatoric response. Hence, separating these two mechanisms and accounting viscoelastic behavior only for the deviatoric response is a well-established procedure, which can lead to a good representation of experimental data. Moreover, one can significantly reduce the amount of model parameters that are necessary to describe the viscoelastic deviatoric response and the purely elastic volumetric response.

To accurately model this behavior by means of intermediate configurations, the

volumetric-isochoric decomposition of the viscoelastic part of the deformation gradient \mathbf{F}_{ve} is introduced, see [Flory, 1961]:

$$\mathbf{F}_{\text{ve}} = \hat{\mathbf{F}}_{\text{ve}} \bar{\mathbf{F}}_{\text{ve}} . \quad (3.48)$$

Therein, $\hat{\mathbf{F}}_{\text{ve}}$ stands for the volumetric part and $\bar{\mathbf{F}}_{\text{ve}}$ represents the isochoric part. The volumetric part $\hat{\mathbf{F}}_{\text{ve}}$ is given by

$$\hat{\mathbf{F}}_{\text{ve}} = (\det \mathbf{F}_{\text{ve}})^{\frac{1}{3}} \mathbf{1} = J_{\text{ve}}^{\frac{1}{3}} \mathbf{1} \quad (3.49)$$

and the isochoric part reads as

$$\bar{\mathbf{F}}_{\text{ve}} = (\det \mathbf{F}_{\text{ve}})^{-\frac{1}{3}} \mathbf{F}_{\text{ve}} = J_{\text{ve}}^{-\frac{1}{3}} \mathbf{F}_{\text{ve}} . \quad (3.50)$$

Motivated by the one-dimensional generalized MAXWELL model, applying elastic and inelastic intermediate configurations seems to be useful. In general, Thus, the isochoric part of the viscoelastic part of the deformation gradient $\bar{\mathbf{F}}_{\text{ve}}$ is multiplicatively split into elastic and inelastic parts [Lubliner, 1985; Lion, 2000]. Taking into account the number of individual MAXWELL elementss, this procedure is carried out N times [Hartmann, 2003]:

$$\bar{\mathbf{F}}_{\text{ve}} = \bar{\mathbf{F}}_{\text{el}k} \bar{\mathbf{F}}_{\text{in}k} \quad \text{with} \quad k = 1, \dots, N . \quad (3.51)$$

For a better understanding, the transition of the material body from the viscoplastic intermediate configuration \mathcal{B}_{vp} to the current configuration \mathcal{B}_t is depicted in fig. 3.5. Depending on the individual MAXWELL element, i.e., the ratio between elastic and inelastic deformations, the corresponding part of the material body initially goes into the inelastic intermediate configuration $\hat{\mathcal{B}}_{\text{in}k}$. Then, after applying the isochoric elastic part of the viscoelastic part of the deformation gradient $\bar{\mathbf{F}}_{\text{el}k}$, the corresponding part of the material body goes into the isochoric viscoelastic intermediate configuration. The volume remains constant during these two transitions. Finally, by means of the volumetric part of the viscoelastic part of the deformation gradient $\hat{\mathbf{F}}_{\text{ve}}$, the volume of the material body istropically changes, which is indicated by the white dashed border of the material body in the current configuration \mathcal{B}_t .

After introducing all necessary decompositions of the deformation gradient, one has to evaluate the mechanical part of the spatial velocity gradient \mathbf{L}_{m} . Therefore, the material time derivative and the inverse of the mechanical part of the deforma-

tion gradient \mathbf{F}_m are calculated as

$$\begin{aligned}\dot{\mathbf{F}}_m &= \dot{\mathbf{F}}_{ve} \mathbf{F}_{vp} + \mathbf{F}_{ve} \dot{\mathbf{F}}_{vp} \\ &= \dot{\hat{\mathbf{F}}}_{ve} \bar{\mathbf{F}}_{elk} \bar{\mathbf{F}}_{ink} \mathbf{F}_{vp} + \hat{\mathbf{F}}_{ve} \dot{\bar{\mathbf{F}}}_{elk} \bar{\mathbf{F}}_{ink} \mathbf{F}_{vp} \\ &\quad + \hat{\mathbf{F}}_{ve} \bar{\mathbf{F}}_{elk} \dot{\bar{\mathbf{F}}}_{ink} \mathbf{F}_{vp} + \hat{\mathbf{F}}_{ve} \bar{\mathbf{F}}_{elk} \bar{\mathbf{F}}_{ink} \dot{\mathbf{F}}_{vp} \quad , \quad k = 1, \dots, N\end{aligned}\quad (3.52)$$

and as

$$\begin{aligned}\mathbf{F}_m^{-1} &= \mathbf{F}_{vp}^{-1} \mathbf{F}_{ve}^{-1} \\ &= \mathbf{F}_{vp}^{-1} \bar{\mathbf{F}}_{ink}^{-1} \bar{\mathbf{F}}_{elk}^{-1} \hat{\mathbf{F}}_{ve}^{-1} \quad , \quad k = 1, \dots, N,\end{aligned}\quad (3.53)$$

respectively. Combining eqs. (3.52) and (3.53) leads to the mechanical part of the spatial velocity gradient

$$\begin{aligned}\mathbf{L}_m &= \dot{\mathbf{F}}_m \mathbf{F}_m^{-1} \\ &= \dot{\hat{\mathbf{F}}}_{ve} \hat{\mathbf{F}}_{ve}^{-1} + \hat{\mathbf{F}}_{ve} \dot{\bar{\mathbf{F}}}_{elk} \bar{\mathbf{F}}_{elk}^{-1} \hat{\mathbf{F}}_{ve}^{-1} + \hat{\mathbf{F}}_{ve} \bar{\mathbf{F}}_{elk} \dot{\bar{\mathbf{F}}}_{ink} \bar{\mathbf{F}}_{ink}^{-1} \bar{\mathbf{F}}_{elk}^{-1} \hat{\mathbf{F}}_{ve}^{-1} \\ &\quad + \hat{\mathbf{F}}_{ve} \bar{\mathbf{F}}_{elk} \bar{\mathbf{F}}_{ink} \dot{\mathbf{F}}_{vp} \mathbf{F}_{vp}^{-1} \bar{\mathbf{F}}_{ink}^{-1} \bar{\mathbf{F}}_{elk}^{-1} \hat{\mathbf{F}}_{ve}^{-1} \quad , \quad k = 1, \dots, N \\ &= \hat{\mathbf{L}}_{ve} + \hat{\mathbf{F}}_{ve} \bar{\mathbf{L}}_{elk} \hat{\mathbf{F}}_{ve}^{-1} + \hat{\mathbf{F}}_{ve} \bar{\mathbf{F}}_{elk} \bar{\mathbf{L}}_{ink} \bar{\mathbf{F}}_{elk}^{-1} \hat{\mathbf{F}}_{ve}^{-1} \\ &\quad + \hat{\mathbf{F}}_{ve} \bar{\mathbf{F}}_{elk} \bar{\mathbf{F}}_{ink} \mathbf{L}_{vp} \bar{\mathbf{F}}_{ink}^{-1} \bar{\mathbf{F}}_{elk}^{-1} \hat{\mathbf{F}}_{ve}^{-1} \quad , \quad k = 1, \dots, N.\end{aligned}\quad (3.54)$$

According to eq. (3.49), the volumetric part of the viscoelastic part of the deformation gradient is isotropic. Hence, eq. (3.54) can be simplified to

$$\begin{aligned}\mathbf{L}_m &= \hat{\mathbf{L}}_{ve} + \bar{\mathbf{L}}_{elk} + \bar{\mathbf{F}}_{elk} \bar{\mathbf{L}}_{ink} \bar{\mathbf{F}}_{elk}^{-1} \\ &\quad + \bar{\mathbf{F}}_{elk} \bar{\mathbf{F}}_{ink} \mathbf{L}_{vp} \bar{\mathbf{F}}_{ink}^{-1} \bar{\mathbf{F}}_{elk}^{-1} \quad , \quad k = 1, \dots, N.\end{aligned}\quad (3.55)$$

At this point, the individual deformations mutually influence each other. Consequently, no additive decomposition of the mechanical part of the spatial velocity gradient is explicitly possible.

As previously discussed in sec. 2.5.1, the tensile tests of the specimens subjected to monotonic loading predominantly exhibit brittle fracture at small strains. Moreover, since the individual yield stresses are apparently low, the tensile behavior of the photopolymer is mainly dominated by the viscoplastic deformations. Following this, and using the linearization of the deformation gradient, the assumptions

$$\begin{aligned}\bar{\mathbf{F}}_{elk} &= \mathbf{1} + \bar{\mathbf{H}}_{elk} \approx \mathbf{1} \quad , \quad k = 1, \dots, N \quad , \quad \|\bar{\mathbf{H}}_{elk}\| \ll 1 \\ \bar{\mathbf{F}}_{ink} &= \mathbf{1} + \bar{\mathbf{H}}_{ink} \approx \mathbf{1} \quad , \quad k = 1, \dots, N \quad , \quad \|\bar{\mathbf{H}}_{ink}\| \ll 1\end{aligned}\quad (3.56)$$

for the elastic and inelastic parts of the deformation gradient are valid.

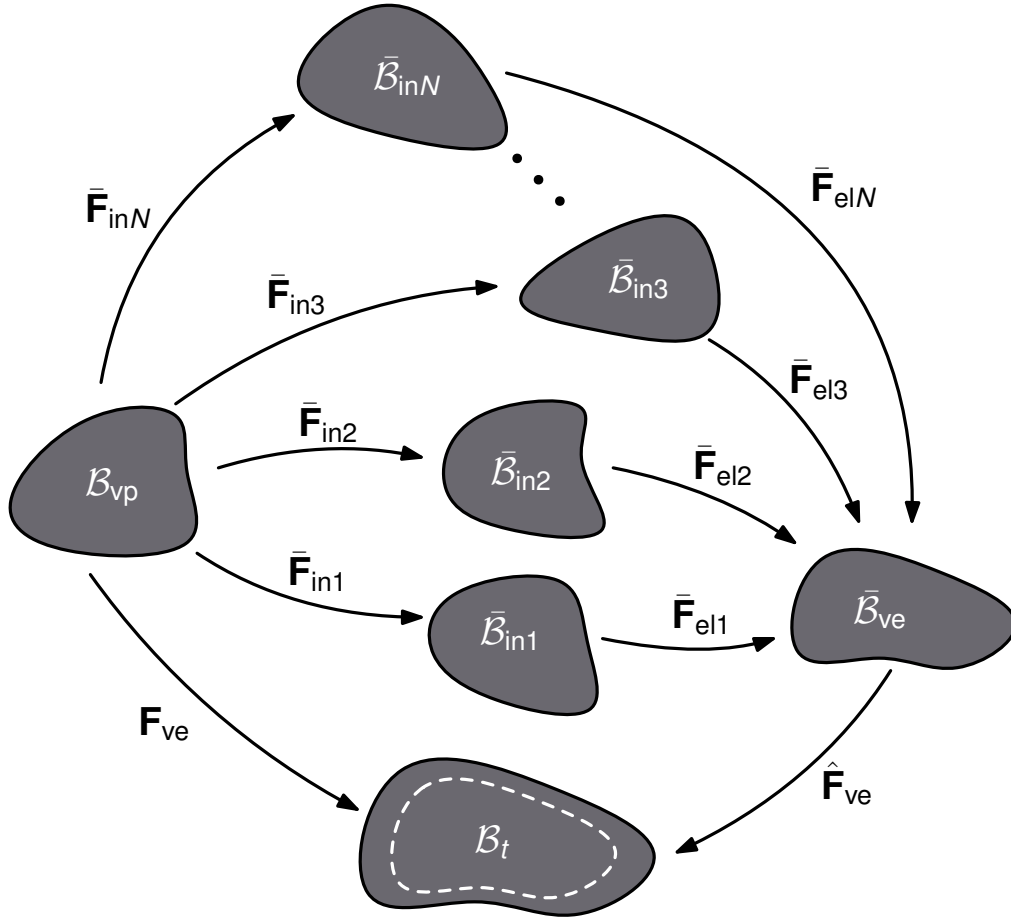


Figure 3.5. Graphical representation of the configurations corresponding to the multiplicative decomposition of the deformation gradient in eq. (3.48)

Finally, inserting the assumptions in eq. (3.56) in eq. (3.54) provides the additive decomposition of the mechanical part of the spatial velocity gradient

$$\mathbf{L}_{m,add} = \hat{\mathbf{L}}_{ve} + \bar{\mathbf{L}}_{elk} + \bar{\mathbf{L}}_{ink} + \mathbf{L}_{vp} \quad , \quad k = 1, \dots, N \quad , \quad (3.57)$$

and naturally

$$\mathbf{d}_{m,add} = \hat{\mathbf{d}}_{ve} + \bar{\mathbf{d}}_{elk} + \bar{\mathbf{d}}_{ink} + \mathbf{d}_{vp} \quad , \quad k = 1, \dots, N \quad (3.58)$$

$$\text{and } \mathbf{w}_{m,add} = \hat{\mathbf{w}}_{ve} + \bar{\mathbf{w}}_{elk} + \bar{\mathbf{w}}_{ink} + \mathbf{w}_{vp} \quad , \quad k = 1, \dots, N \quad . \quad (3.59)$$

As a result, the additive decomposition of the mechanical part of the spatial velocity gradient \mathbf{L}_m is permissible for small viscoelastic and large viscoplastic deformations. Since the thermal expansion/contraction and the chemical shrinkage are assumed to be isotropic, no limitations are imposed on these deformations.

The method mentioned above was developed for hypoelastic-plastic material models in [Healy and Dodds, 1992] and successfully applied in, for example, [Bröcker, 2013]

and [Burbulla, 2015] for the modeling and simulation of metal forming processes and for the crash analysis of structural adhesive joints, respectively. Now, as a modification, the combination of viscoelastic and viscoplastic deformations and the consideration of thermal expansion/contraction and chemical shrinkage is possible.

The increment of the mechanical part of the strain measure defined by

$$d\chi_m = \mathbf{d}_{m,\text{add}} dt \quad (3.60)$$

is identical to the true strain increment and is frequently referred to as the natural strain increment [Gross and Seelig, 2011; Betten, 2001]. Correspondingly, the mechanical part of the total strain at the time t is computed by

$$\chi_m(t) = \int_0^t \mathbf{d}_{m,\text{add}}(\tau) d\tau. \quad (3.61)$$

Additionally, each part of the total deformation contributes to the mechanical part of the strain measure:

$$\begin{aligned} \chi_m(t) &= \int_0^t \hat{\mathbf{d}}_{\text{ve}}(\tau) d\tau + \int_0^t \bar{\mathbf{d}}_{\text{elk}}(\tau) d\tau + \int_0^t \bar{\mathbf{d}}_{\text{ink}}(\tau) d\tau + \int_0^t \mathbf{d}_{\text{vp}}(\tau) d\tau \\ &= \hat{\chi}_{\text{ve}}(t) + \bar{\chi}_{\text{elk}}(t) + \bar{\chi}_{\text{ink}}(t) + \chi_{\text{vp}}(t) \quad , \quad k = 1, \dots, N . \end{aligned} \quad (3.62)$$

In the following, the structure of the volumetric and isochoric parts of the viscoelastic part of the spatial velocity gradient are analyzed. The material time derivative of the Jacobian J is given by²

$$\dot{J} = J \operatorname{tr}(\mathbf{L}) = J \operatorname{tr}(\mathbf{d}) \quad , \quad (3.63)$$

see [Holzapfel, 2001], which leads to the material time derivative of the volumetric part of the viscoelastic part of the deformation gradient:

$$\dot{\hat{\mathbf{F}}}_{\text{ve}} = \frac{d}{dt} \left(J_{\text{ve}}^{\frac{1}{3}} \mathbf{1} \right) = \frac{1}{3} J_{\text{ve}}^{-\frac{2}{3}} \dot{J}_{\text{ve}} \mathbf{1} = \frac{1}{3} J_{\text{ve}}^{\frac{1}{3}} \operatorname{tr}(\mathbf{d}_{\text{ve}}) \quad . \quad (3.64)$$

Again, multiplying eq. (3.64) with the inverse of the volumetric part of the viscoelastic part of the deformation gradient leads to the volumetric part of the viscoelastic

²The diagonal elements of a skew-symmetric tensor are zero. Hence, $\operatorname{tr}(\mathbf{w}) = 0$ holds.

part of the spatial velocity gradient:

$$\hat{\mathbf{L}}_{\text{ve}} = \dot{\hat{\mathbf{F}}}_{\text{ve}} \hat{\mathbf{F}}_{\text{ve}}^{-1} = \frac{1}{3} \text{tr}(\mathbf{d}_{\text{ve}}) \mathbf{1} . \quad (3.65)$$

Furthermore, the restriction to small viscoelastic deformations provides the additive decomposition of the viscoelastic part of the spatial velocity gradient. Thus,

$$\bar{\mathbf{L}}_{\text{ve}} = \mathbf{L}_{\text{ve}} - \hat{\mathbf{L}}_{\text{ve}} = \mathbf{L}_{\text{ve}} - \frac{1}{3} \text{tr}(\mathbf{d}_{\text{ve}}) \mathbf{1} \quad (3.66)$$

holds and is equivalent to the deviator operator $(\bullet)^{\text{D}} = (\bullet) - \frac{1}{3} \text{tr}(\bullet) \mathbf{1}$ of a second order tensor. In conclusion, it is also possible to apply the deviator operator on the isochoric and volumetric parts of the viscoelastic part of the introduced strain measure:

$$\bar{\boldsymbol{\chi}}_{\text{ve}} = \boldsymbol{\chi}_{\text{ve}} - \frac{1}{3} \text{tr}(\boldsymbol{\chi}_{\text{ve}}) \mathbf{1} \quad (3.67)$$

$$\hat{\boldsymbol{\chi}}_{\text{ve}} = \frac{1}{3} \text{tr}(\boldsymbol{\chi}_{\text{ve}}) \mathbf{1} . \quad (3.68)$$

Employing the same approach as in eq. (3.62), the parts of the strain measure describing thermal expansion/contraction and chemical shrinkage are defined by

$$\boldsymbol{\chi}_{\text{th}} = \int_0^t \mathbf{d}_{\text{th}}(\tau) \, \text{d}\tau \quad (3.69)$$

$$\text{and } \boldsymbol{\chi}_{\text{ch}} = \int_0^t \mathbf{d}_{\text{ch}}(\tau) \, \text{d}\tau \quad (3.70)$$

by means of the eqs. (3.42) and (3.43).

3.4 Representation by rheological elements

Since the derived equations describing the individual parts of the deformation are not easy to imagine, a graphical representation of the parts of the deformation would be beneficial. Hence, one has to find a framework to put the set of equations into a graphical representation.

Therefore, rheological networks are widely used to better understand and illustrate developed material models. The introduced decomposition of the overall deformation into viscoelastic, viscoplastic, thermal, and chemical parts is visualized in fig. 3.6. The total strain $\boldsymbol{\chi}$ spans over all single parts of the rheological network. As presented in the preceding section, the mechanical, thermal, and chemical parts are

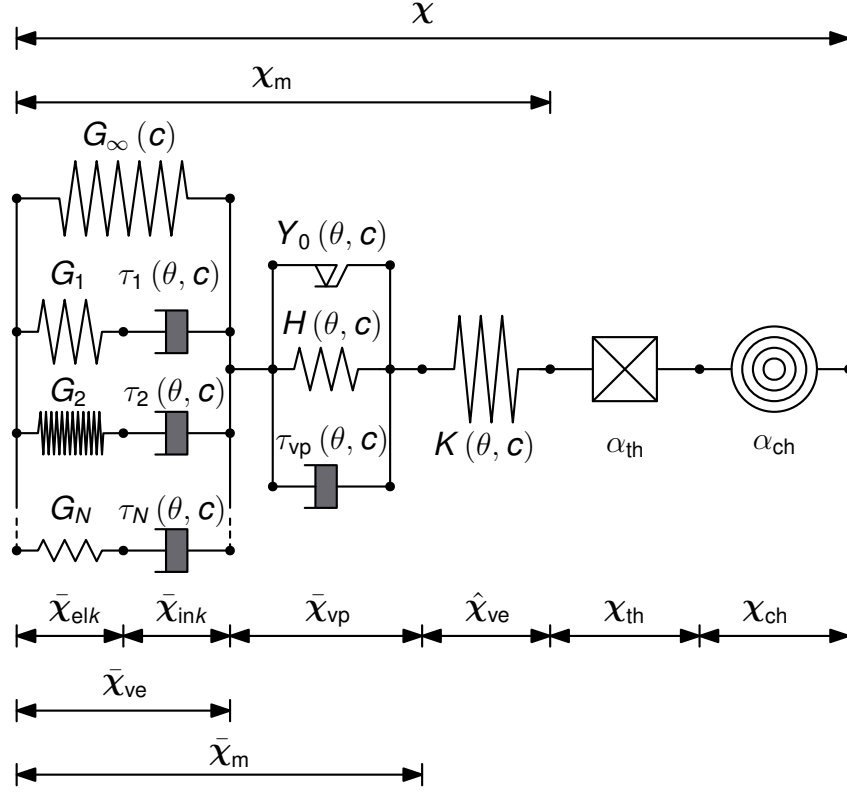


Figure 3.6. Rheological network of the proposed decomposition considering viscoelastic and viscoplastic deformations as well as thermal expansion/-contraction and chemical shrinkage

connected in series since they are additively decomposed. Starting with the viscoelastic part on the left side, several elements individually consisting of a spring and a dashpot connected in series are parallelly arranged. These elements are denoted as MAXWELL elements ($k = 1, \dots, N$) and represent fluid-like behavior. The viscoelastic part of the strain measure divides into elastic and inelastic parts, whose individual contributions are determined by the ratio between the shear moduli G_k and the relaxation times τ_k . Only with the extension of the equilibrium stiffness represented by the single spring above the MAXWELL elements does the viscoelastic part of the rheological network become a viscoelastic solid.

The viscoplastic part consists of a friction element, a spring, and a dashpot, which are parallelly connected. The friction element describes the onset of plastic yielding. After reaching the initial yield stress Y_0 , the yield stress increases with growing plastic strains. This hardening behavior is characterized by the spring positioned below the friction element. In order to capture viscoplastic behavior, the dashpot with the relaxation time τ_{vp} is introduced.

The viscoelastic and viscoplastic parts only describe the isochoric deformations. Thus, the spring with the bulk modulus K is introduced and connected in series to

the viscoelastic and viscoplastic parts to describe the purely elastic and volumetric bulk response. Additionally, since they are also volumetric, the thermal and chemical parts are connected in series to the spring representing the bulk response.

The stress-strain relationship corresponding to the introduced rheological network is presented and discretized in the following sections.

3.5 Viscoelasticity

In order to develop the stress-strain relationship corresponding to the viscoelastic part of the introduced rheological network, one has to analyze the dependencies between the individual parts of the deformation as introduced in the preceding section. Since the stress is the same in both the spring and the dashpot of the individual MAXWELL element, the following equation describes the relation between the isochoric elastic part of the total strain and the isochoric inelastic part of the strain rate tensor in the three-dimensional case:

$$\bar{\mathbf{T}} = 2G_k \bar{\boldsymbol{\chi}}_{\text{elk}} = \eta_k \bar{\mathbf{d}}_{\text{ink}} \quad , \quad k = 1, \dots, N \quad . \quad (3.71)$$

G_k are the shear moduli of the MAXWELL elements and η_k are the viscosities of the corresponding dashpots. Furthermore, the additive decomposition of the total viscoelastic strain in each MAXWELL element holds:

$$\bar{\boldsymbol{\chi}}_{\text{ve}} = \bar{\boldsymbol{\chi}}_{\text{elk}} + \bar{\boldsymbol{\chi}}_{\text{ink}} \quad , \quad k = 1, \dots, N \quad . \quad (3.72)$$

Combining eqs. (3.71) and (3.72) leads to the well-known evolution equation for the inelastic strain in each MAXWELL element:

$$\bar{\mathbf{d}}_{\text{ink}} = \frac{2G_k}{\eta_k} (\bar{\boldsymbol{\chi}}_{\text{ve}} - \bar{\boldsymbol{\chi}}_{\text{ink}}) \quad , \quad k = 1, \dots, N \quad . \quad (3.73)$$

In order to simplify this equation, the relaxation time $\tau_k = \frac{\eta_k}{2G_k}$ is introduced for each MAXWELL element. The relaxation times depend on the degree of cure and the temperature. These dependencies are expressed by the shift functions $s_\theta(\theta)$ and $s_c(c)$:

$$\tau_k(\theta, c) = \tau_{kR} s_\theta(\theta) s_c(c) \quad , \quad k = 1, \dots, N \quad . \quad (3.74)$$

The relaxation times τ_{kR} are defined for the reference degree of cure c_R and the reference temperature θ_R , respectively. Lower temperatures than the reference temperature increase the relaxation times. Analogously, lower degrees of cure than the

reference degree of cure decrease the relaxation times. Hence, $s_\theta > 1$ for $\theta < \theta_R$ and $s_c < 1$ for $c < c_R$. It should be noted that the two shifting mechanisms are independent from each other.

The evolution equations (3.73) must be individually solved for each MAXWELL element. Several integration schemes are suitable to accomplish this task. TAYLOR et al. proposed an integration scheme based on the integrating factor $\exp\left(\frac{t}{\tau_k}\right)$ so that

$$\frac{d}{dt} \left(\exp\left(\frac{t}{\tau_k(\theta, c)}\right) \bar{\chi}_{ink} \right) = \frac{1}{\tau_k(\theta, c)} \exp\left(\frac{t}{\tau_k(\theta, c)}\right) \bar{\chi}_{ve} \quad , \quad k = 1, \dots, N \quad , \quad (3.75)$$

which is second order accurate [Taylor et al., 1970]. Since the derivation of the algorithm presented by TAYLOR et al. is more elaborate, the EULER backward scheme is applied to solve the evolution equations for the inelastic strains of each MAXWELL element. Hence, the discretized inelastic part of the total viscoelastic strain at time ^{n+1}t reads as

$$\begin{aligned} ^{n+1}\bar{\chi}_{ink} &= ^n\bar{\chi}_{ink} + \Delta t \cdot ^{n+1}\bar{\mathbf{d}}_{ink} \\ &= ^n\bar{\chi}_{ink} + \frac{\Delta t}{\tau_k(\theta, c)} \left(^{n+1}\bar{\chi}_{ve} - ^{n+1}\bar{\chi}_{ink} \right) \quad , \quad k = 1, \dots, N \quad . \end{aligned} \quad (3.76)$$

This equation is directly solved for $^{n+1}\bar{\chi}_{ink}$:

$$^{n+1}\bar{\chi}_{ink} = \frac{\tau_k(\theta, c)}{\tau_k(\theta, c) + \Delta t} ^n\bar{\chi}_{ink} + \frac{\Delta t}{\tau_k(\theta, c) + \Delta t} ^{n+1}\bar{\chi}_{ve} \quad , \quad k = 1, \dots, N \quad . \quad (3.77)$$

For small relaxation times in comparison with the time scale of the process, the inelastic strain of the MAXWELL element k tends towards the total viscoelastic strain³:

$$^{n+1}\bar{\chi}_{ink} \rightarrow ^{n+1}\bar{\chi}_{ve} \quad \text{for} \quad \Delta t \gg \tau_k \quad , \quad k = 1, \dots, N \quad . \quad (3.78)$$

Given that case and taking into account eqs. (3.71) and (3.72) yields the result that no stress is contributed by the individual MAXWELL element k . Figuratively speaking, the dashpot does not block and the spring remains in the reference configuration in the rheological network.

Employing the general definitions for combining rheological elements, see [Krawietz,

³In order to accurately capture the response of the specific MAXWELL element k , the time step size should be significantly lower than the corresponding relaxation time τ_k .

1986], the contribution of the generalized MAXWELL model to the overall stress is computed by

$$\begin{aligned} {}^{n+1}\bar{\mathbf{T}} &= 2G_\infty {}^{n+1}\bar{\boldsymbol{\chi}}_{\text{ve}} + \sum_{k=1}^N 2G_k \left({}^{n+1}\bar{\boldsymbol{\chi}}_{\text{ve}} - {}^{n+1}\bar{\boldsymbol{\chi}}_{\text{ink}} \right) \\ &= 2G_\infty {}^{n+1}\bar{\boldsymbol{\chi}}_{\text{ve}} + \sum_{k=1}^N 2G_k \left(\frac{\tau_k(\theta, c)}{\tau_k(\theta, c) + \Delta t} \right) \left({}^{n+1}\bar{\boldsymbol{\chi}}_{\text{ve}} - {}^n\bar{\boldsymbol{\chi}}_{\text{ink}} \right) . \end{aligned} \quad (3.79)$$

As previously discussed, the volumetric part of the viscoelastic part of the rheological network is purely elastic and is computed by

$${}^{n+1}\hat{\mathbf{T}} = K(\theta, c) {}^{n+1}\hat{\boldsymbol{\chi}}_{\text{ve}} . \quad (3.80)$$

One-dimensional model for small shear deformations in the frequency domain

In order to identify the relaxation times and shear moduli of the generalized MAXWELL model, the three-dimensional model must be reduced to the one-dimensional case. Hence, simplifications are assumed based on one-dimensional stress and deformation states to analyze the DMA test data, see [Findley et al., 1976]. For this purpose, the resulting CAUCHY stress tensor reduces to

$$\bar{\mathbf{T}} = \begin{pmatrix} 0 & \tau & 0 \\ \tau & 0 & 0 \\ 0 & 0 & 0 \end{pmatrix} . \quad (3.81)$$

Analogously, considering the MAXWELL element k , the corresponding elastic part of the total viscoelastic strain $\bar{\boldsymbol{\chi}}_{\text{elk}}$ and the inelastic part of the viscoelastic strain rate tensor of eq. (3.71) are defined by

$$\bar{\boldsymbol{\chi}}_{\text{elk}} = \begin{pmatrix} 0 & \frac{\gamma_{\text{elk}}}{2} & 0 \\ \frac{\gamma_{\text{elk}}}{2} & 0 & 0 \\ 0 & 0 & 0 \end{pmatrix} \quad \text{and} \quad \bar{\mathbf{d}}_{\text{ink}} = \begin{pmatrix} 0 & \dot{\gamma}_{\text{ink}} & 0 \\ \dot{\gamma}_{\text{ink}} & 0 & 0 \\ 0 & 0 & 0 \end{pmatrix} . \quad (3.82)$$

In the torsional DMA tests in sec. 2.4, the harmonic shear excitation $\gamma(t)$ with angular frequency ω and shear strain amplitude γ_0 is applied to rectangular specimens:

$$\gamma(t) = \gamma_0 \exp(i\omega t) \quad \text{and} \quad \dot{\gamma}(t) = \gamma_0 i\omega \exp(i\omega t) . \quad (3.83)$$

Depending on the viscoelastic properties, i.e., whether the considered material is more solid-like or fluid-like, the stress response also exhibits harmonic behavior but

is delayed with the phase shift angle δ :

$$\tau(t) = \tau_0 \exp(i(\omega t + \delta)) \quad \text{and} \quad \dot{\tau}(t) = \tau_0 i \omega \exp(i(\omega t + \delta)) . \quad (3.84)$$

At this point, the main objective is to find suitable model equations consisting of an arrangement of rheological elements capable of representing the experimental data. Among the well-established compositions of rheological elements covering a broad range of particular phenomena, such as creep and relaxation, the generalized MAXWELL model can capture the material response in the DMA test over a wide frequency range.

Recalling the constitutive equations of a linear-elastic spring and a newtonian fluid represented by a damper for the shear stress τ as a function of one-dimensional shear deformation (cf. eqs. (3.81) and (3.82)), i.e.

$$\tau(t) = G\gamma_{\text{el}}(t) \quad \text{and} \quad \tau = \eta\dot{\gamma}_{\text{in}}(t) , \quad (3.85)$$

and applying the additive composition of elastic and inelastic shear deformations

$$\gamma(t) = \gamma_{\text{el}}(t) + \gamma_{\text{in}}(t) , \quad (3.86)$$

the composed differential equation for one MAXWELL element consisting of a spring and a damper connected in series reads as

$$\dot{\tau}(t) + \frac{G}{\eta}\tau(t) = G\dot{\gamma}(t) . \quad (3.87)$$

Inserting of eqs. (3.83) and (3.84) into the differential eq. (3.87) yields to the algebraic equation

$$\tau_0 i \omega \exp(i(\omega t + \delta)) + \frac{G}{\eta}\tau_0 \exp(i(\omega t + \delta)) = G\gamma_0 i \omega \exp(i\omega t) , \quad (3.88)$$

which can be further simplified to

$$\frac{\tau_0}{\gamma_0} \exp(i\delta) = G \frac{i\omega}{i\omega + \frac{G}{\eta}} . \quad (3.89)$$

By introducing the relaxation time $\tau = \frac{G}{\eta}$ as a replacement for the shear stress, the complex shear modulus is defined as

$$G^* := G \frac{i\omega}{i\omega + \frac{1}{\tau}} = G \left(\frac{(\omega\tau)^2}{1 + (\omega\tau)^2} + i \frac{\omega\tau}{1 + (\omega\tau)^2} \right) . \quad (3.90)$$

Herein, the real part is the storage modulus, whereas the imaginary part is the loss modulus. For the best accordance between the experimental data and the model equation based on the MAXWELL element, identifying the shear modulus G and the relaxation time τ is a challenging task. In general, one MAXWELL element is not sufficient to cover the whole experimental data set. Furthermore, because the MAXWELL element only represents a fluid and infinitely deforms when loaded with a constant shear stress $\tau(t) = \text{const.}$, an additional spring characterized by the equilibrial shear modulus G_∞ is added to represent the stationary (equilibrium) response. Thus, the overall shear storage G' and loss moduli G'' are given by

$$G'(\omega, G_\infty, G_1, \dots, G_N, \tau_1, \dots, \tau_N) = G_\infty + \sum_{k=1}^N G_k \frac{(\omega\tau_k)^2}{1 + (\omega\tau_k)^2} \quad (3.91)$$

and

$$G''(\omega, G_1, \dots, G_N, \tau_1, \dots, \tau_N) = \sum_{k=1}^N G_k \frac{\omega\tau_k}{1 + (\omega\tau_k)^2} . \quad (3.92)$$

The combination of an arbitrary number of individual MAXWELL elements in conjunction with one additional equilibrium spring is also referred to as the generalized MAXWELL model. Subsequently, the main objective is to find the best values for the shear moduli G_1, \dots, G_N and relaxation times τ_1, \dots, τ_N of the individual MAXWELL elements. As a result, by measuring the mean squared error, the best parameter set will reduce the deviation between the experimental data and the governed equations of the generalized MAXWELL model. Hence, sophisticated optimization algorithms and modifications are applied to accomplish this task in sec. 4.2.

3.6 Plasticity

Based on the observable residual plastic strains in the cyclic tensile tests, the VON MISES yield criterion is applied:

$$f(J_2, \zeta) = \sqrt{2J_2} - \sqrt{\frac{2}{3}} (Y_0(\theta, c) + H(\zeta, \theta, c)) = 0. \quad (3.93)$$

With the definition of the second invariant of the isochoric part of the CAUCHY stress tensor [Lubliner, 2008], i.e.⁴,

$$J_2 = \frac{1}{2} \bar{\mathbf{T}} \cdot \bar{\mathbf{T}}, \quad (3.94)$$

the yield criterion in eq. (3.93) can be visualized in the I_1 - $\sqrt{J_2}$ space as displayed in fig. 3.7 for a material without hardening effects. Since the plastic yielding only depends on the isochoric part of the CAUCHY stress, the yield surface is a horizontal line and intersects the ordinate at $\sqrt{J_2} = \frac{Y_0}{\sqrt{3}}$. Given that case, hydrostatic compression and dilatation are purely elastic.

The onset of plastic yielding is defined by the function $Y_0(\theta, c)$, which describes the initial yield stress and depends on the temperature θ and degree of cure c . Additionally, the isotropic hardening function $H(\zeta, \theta, c)$ is introduced to cover hardening effects of the material and to ensure enough flexibility in the parameter identification process following later.

For the description of the temporal evolution of the plastic strains, the associated flow rule

$$\bar{\mathbf{d}}_{\text{pl}} = \lambda \frac{\partial f}{\partial \bar{\mathbf{T}}} = \lambda \frac{\bar{\mathbf{T}}}{\|\bar{\mathbf{T}}\|} \quad (3.95)$$

is chosen, whose direction is defined by the normal

$$\mathbf{N} = \frac{\bar{\mathbf{T}}}{\|\bar{\mathbf{T}}\|} \quad (3.96)$$

of the yield surface. Therein, the plastic part of the strain rate tensor $\bar{\mathbf{d}}_{\text{pl}}$ is isochoric. The scalar plastic multiplier λ , $[\lambda] = \text{s}^{-1}$, specifies the rate of plastic yielding during plastic loading, which is always equal to or greater than zero in the case of plastic yielding.

The isotropic hardening function $H(\zeta, \theta, c)$, which characterizes the uniform expan-

⁴The operator $(.) \cdot (.)$ defines the double scalar contraction between two second order tensors $(.)$ and $(.)$ (e.g., $\mathbf{A} \cdot \mathbf{B} = A_{ij} B_{ij}$).

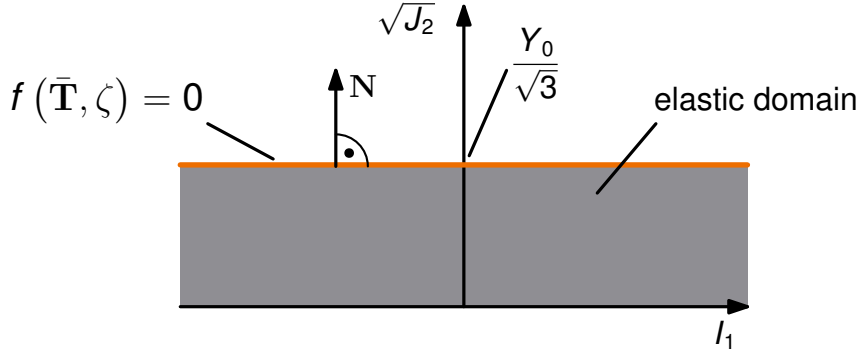


Figure 3.7. Schematic representation of the VON MISES yield criterion in the I_1 - $\sqrt{J_2}$ space without hardening effects. I_1 is the trace (first invariant) of the CAUCHY stress tensor \mathbf{T} .

sion of the yield surface in the stress space, is assumed to be nonlinear based on the following exponential saturation [Simo and Hughes, 1998]:

$$H(\zeta, \theta, c) = H_0(\theta, c)\zeta + \kappa_0(\theta, c)(1 - \exp(-\kappa_1(\theta, c)\zeta)) . \quad (3.97)$$

Considering the representation in the I_1 - $\sqrt{J_2}$ space, the yield surface vertically translates with increasing plastic deformations. The exponential saturation part in the second summand declines with increasing accumulated plastic strain ζ . κ_0 is a stress-like value describing the additional amount of yield stress during the transition to the purely linear hardening behavior characterized by the slope H_0 . κ_1 is a strain-like parameter introduced to ensure enough flexibility during the parameter identification process. All of the introduced parameters can depend on the degree of cure c as well as on the temperature θ . Suitable equations describing these dependencies are introduced in the following chapter based on the results of the parameter identification process.

The accumulated plastic strain ζ is the driving force for the isotropic hardening function and evolves with increasing plastic deformations. Thus, the evolution equation

$$\dot{\zeta} = \sqrt{\frac{2}{3}}\lambda = \sqrt{\frac{2}{3}}\|\bar{\mathbf{d}}_{\text{pl}}\| . \quad (3.98)$$

is appropriate to represent this behavior in accordance to the yield function in eq. (3.93). Additionally, the integral representation

$$\zeta(t) = \int_0^t \sqrt{\frac{2}{3}}\|\bar{\mathbf{d}}_{\text{pl}}(\tau)\|d\tau \quad (3.99)$$

holds.

The introduced equations for the consideration of plastic material behavior represent a system of algebraic and differential equations. In order to employ these model equations for finite element analyses, one has to consistently integrate this system of equations taking into account the model equations for the viscoelastic part of the material model in the preceding section. Before that, however, the model equations mentioned above are extended to cover viscoplastic behavior.

3.6.1 Consideration of viscoplastic effects

As previously discussed, the experimental force-displacement curves in sec. 2.5 exhibit a strain-rate dependency in the yielding domain. Higher strain rates lead to an offset of the reaction force in the plastic domain with increasing displacement, which cannot be modeled by the nonlinear saturation term in eq. (3.97). One established approach is the definition of a flow rule whose increment is not determined by the yield condition $f = 0$. These models are denoted as viscoplastic and allow for stress states that leave the yield condition $f = 0$, i.e., $f \geq 0$ is possible.

A common approach is based on the proposal in [Perzyna, 1963] and has the following structure [Haupt, 2002]:

$$\bar{\mathbf{d}}_{\text{vp}} = \frac{1}{\tau_{\text{vp}}(\theta, c)} \left\langle \frac{f}{f_0} \right\rangle^{m_{\text{vp}}(\theta, c)} \mathbf{N}. \quad (3.100)$$

In contrast to eq. (3.95), $\bar{\mathbf{d}}_{\text{vp}}$ is now the viscoplastic strain rate tensor and is also assumed to be purely isochoric. The direction of the viscoplastic flow is again determined by the normal of the yield surface \mathbf{N} via an associative flow rule. The time constant $\tau_{\text{vp}}(\theta, c)$ accounts for strain-rate effects and leads to similar behavior as the relaxation times of the viscoelastic part of the model. Ensuring unit-consistency, the constant $f_0 = 1 \text{ MPa}$ is introduced. The parameter $m_{\text{vp}}(\theta, c)$ is introduced to ensure enough flexibility during the parameter identification process. The MACAULAY brackets $\langle \cdot \rangle$ ensure that the viscoplastic strains can only remain constant or increase. The accumulated viscoplastic strain is now defined by the evolution equation

$$\dot{\zeta} = \sqrt{\frac{2}{3}} \frac{1}{\tau_{\text{vp}}} \left\langle \frac{f}{f_0} \right\rangle^{m_{\text{vp}}}. \quad (3.101)$$

Viscoplastic material models are usually applied to simulate forming processes of metals because the material behavior of metals exhibits a strong strain-rate dependency in the inelastic domain at high temperatures [Lührs, 1997; Bröcker, 2013].

Considering polymers, one may also identify the same strain-rate dependency in the inelastic domain. Other than metals, this phenomenon is more pronounced because slight temperature changes give rise to changes in the material behavior even in the vicinity of room temperature.

3.6.2 Consistent discretization

The introduced model equations represent a system of tensor and scalar valued differential and algebraic equations. In order to put them into the framework given by the finite element method, these equations must be consistently discretized [Belytschko et al., 2014].

The commercial program LS-DYNA[®] and its programming interface for user defined material models are employed for the finite element simulations in this thesis⁵. Therein, the stress update is computed by the JAUMANN stress rate given by eq. (3.24) [Livermore Software Technology Corp., 2017].

The strain increment

$${}^{n+1}\Delta\boldsymbol{\chi} = \left({}^{n+1}\mathbf{d}_m + {}^{n+1}\mathbf{d}_{th} + {}^{n+1}\mathbf{d}_{ch} \right) \Delta t \quad (3.102)$$

is the input variable for the computation of the stress update. Thus, considering the presented material model, one has to compute the stress increment based on

$$\begin{aligned} {}^{n+1}\Delta\mathbf{T} &= \mathbf{C}_{ve} \cdot {}^{n+1}\Delta\boldsymbol{\chi}_{ve} \\ &= \mathbf{C}_{ve} \cdot \left({}^{n+1}\Delta\boldsymbol{\chi} - {}^{n+1}\Delta\boldsymbol{\chi}_{vp} - {}^{n+1}\Delta\boldsymbol{\chi}_{th} - {}^{n+1}\Delta\boldsymbol{\chi}_{ch} \right), \end{aligned} \quad (3.103)$$

whereas \mathbf{C}_{ve} is the fourth order constitutive tensor describing viscoelastic material behavior⁶. Algorithms based on elastic predictor-plastic corrector procedures are an established method to solve this system of equations [Simo and Hughes, 1998; Wriggers, 2008; de Souza Neto et al., 2008]. In the following, the general procedure is presented for the viscoelastic-plastic case ($\bar{\boldsymbol{\chi}}_{vp} = \bar{\boldsymbol{\chi}}_{pl}$). In a second step, the consistent discretization is derived for the viscoplastic material behavior. For the sake of clarity, all quantities that depend on the time-dependent temperature ${}^{n+1}\theta$ and degree of cure ${}^{n+1}c$ are abbreviated. For example, the hardening function at the time ${}^{n+1}t$ is abbreviated as ${}^{n+1}H({}^{n+1}\theta, {}^{n+1}c) \Rightarrow {}^{n+1}H$.

Considering eqs. (3.42) and (3.43), the strain increments ${}^{n+1}\Delta\boldsymbol{\chi}_{th}$ and ${}^{n+1}\Delta\boldsymbol{\chi}_{ch}$ are

⁵See [Belytschko et al., 2014; Zienkiewicz et al., 2013] for a comprehensive overview of the finite element method.

⁶Again, the operator $(.) \cdot (.)$ defines the double scalar contraction between a fourth order tensor $(.)$ and a second order tensor $(.)$ (e.g., $\mathbf{A} \cdot \mathbf{B} = A_{ijkl}B_{kl}$).

computed as

$${}^{n+1}\Delta\boldsymbol{\chi}_{\text{th}} = \frac{{}^{n+1}\alpha_{\text{th}}\Delta\theta}{3\left(1 + \alpha_{\text{th}}\left({}^{n+1}\theta - \theta_0\right)\right)}\mathbf{1} \quad (3.104)$$

$$\text{and } {}^{n+1}\Delta\boldsymbol{\chi}_{\text{ch}} = -\frac{\alpha_{\text{ch}}{}^{n+1}\Delta c}{3(1 - \alpha_{\text{ch}}{}^{n+1}c)}\mathbf{1} . \quad (3.105)$$

The quantities in these equations are required for the computation of the mechanical part of the strain increment. In order to calculate the stress increment, the necessary derivations can be reduced to the purely mechanical case. Thus, the thermal and chemical parts of the strain increment are omitted.

First, at the time ${}^{n+1}t$, the stress state is assumed to be purely viscoelastic (${}^{n+1}\bar{\boldsymbol{\chi}}_{\text{pl}} = {}^n\bar{\boldsymbol{\chi}}_{\text{pl}}$). Therefore, the individual parts of the mechanical part of the total strain and the accumulated plastic strain at time ${}^{n+1}t$ are governed by

$$\begin{aligned} {}^{n+1}\boldsymbol{\chi}_{\text{m}} &= {}^{n+1}\bar{\boldsymbol{\chi}}_{\text{ve}} + {}^{n+1}\hat{\boldsymbol{\chi}}_{\text{ve}} + {}^n\bar{\boldsymbol{\chi}}_{\text{pl}} \\ {}^{n+1}\bar{\boldsymbol{\chi}}_{\text{ve}} &= {}^n\bar{\boldsymbol{\chi}}_{\text{ve}} + {}^{n+1}\Delta\bar{\boldsymbol{\chi}}_{\text{ve}} \\ {}^{n+1}\hat{\boldsymbol{\chi}}_{\text{ve}} &= {}^n\hat{\boldsymbol{\chi}}_{\text{ve}} + {}^{n+1}\Delta\hat{\boldsymbol{\chi}}_{\text{ve}} \\ {}^{n+1}\bar{\boldsymbol{\chi}}_{\text{ink,tr}} &= \frac{{}^{n+1}\tau_k}{{}^{n+1}\tau_k + \Delta t} {}^n\bar{\boldsymbol{\chi}}_{\text{ink}} + \frac{\Delta t}{{}^{n+1}\tau_k + \Delta t} \left({}^{n+1}\bar{\boldsymbol{\chi}}_{\text{m}} - {}^n\bar{\boldsymbol{\chi}}_{\text{pl}}\right) \\ {}^{n+1}\zeta_{\text{tr}} &= {}^n\zeta . \end{aligned} \quad (3.106)$$

The volumetric part of the CAUCHY stress does not influence the plastic yielding. Hence, it is updated by

$${}^{n+1}\hat{\mathbf{T}} = {}^n\hat{\mathbf{T}} + {}^{n+1}K {}^{n+1}\Delta\hat{\boldsymbol{\chi}}_{\text{ve}} . \quad (3.107)$$

Using the updated isochoric part of the viscoelastic part of the total strain, the isochoric part of the trial state of the CAUCHY stress at the time ${}^{n+1}t$ is incrementally calculated with respect to eqs. (3.79) and (3.106) as

$$\begin{aligned} {}^{n+1}\bar{\mathbf{T}}_{\text{tr}} &= {}^n\bar{\mathbf{T}} + {}^{n+1}\Delta\bar{\mathbf{T}}_{\text{tr}} \\ &= {}^n\bar{\mathbf{T}}_{\infty} + 2{}^{n+1}G_{\infty} \left({}^{n+1}\Delta\bar{\boldsymbol{\chi}}_{\text{m}} - {}^n\Delta\bar{\boldsymbol{\chi}}_{\text{pl}}\right) \\ &\quad + \sum_{k=1}^N 2G_k \left({}^{n+1}\bar{\boldsymbol{\chi}}_{\text{m}} - {}^{n+1}\bar{\boldsymbol{\chi}}_{\text{ink,tr}} - {}^n\bar{\boldsymbol{\chi}}_{\text{pl}}\right) . \end{aligned} \quad (3.108)$$

The corresponding trial state of second invariant of the isochoric part of the CAUCHY stress is governed by

$${}^{n+1}J_{2,\text{tr}} = \frac{1}{2} {}^{n+1}\bar{\mathbf{T}}_{\text{tr}} \cdot {}^{n+1}\bar{\mathbf{T}}_{\text{tr}} . \quad (3.109)$$

Inserting the trial state of the second invariant given by eq. (3.109) leads to the corresponding yield function of the trial state at the time ${}^{n+1}t$:

$$\begin{aligned} {}^{n+1}f_{\text{tr}} \left({}^{n+1}J_{2,\text{tr}}, {}^{n+1}\zeta_{\text{tr}} \right) &= \sqrt{2} {}^{n+1}J_{2,\text{tr}} - \sqrt{\frac{2}{3}} \left({}^{n+1}Y_0 + {}^{n+1}H_{\text{tr}} \right) \\ {}^{n+1}H_{\text{tr}} &= {}^{n+1}H \left({}^{n+1}\zeta_{\text{tr}}, {}^{n+1}\theta, {}^{n+1}c \right) \end{aligned} \quad (3.110)$$

The timestep is considered as viscoelastic or plastic depending on the following differentiation:

$${}^{n+1}f_{\text{tr}} \begin{cases} \leq 0 & \rightarrow \text{viscoelastic timestep} \\ > 0 & \rightarrow \text{plastic timestep} \end{cases} . \quad (3.111)$$

If the timestep is viscoelastic, all quantities are determined by the trial state and saved for the next timestep.

If the yield condition is violated by ${}^{n+1}f_{\text{tr}} > 0$, the plastic part of the total strain has to be calculated to satisfy the yield condition. Therefore, considering the flow rule given by eq. (3.95), the plastic part of the total strain at the time ${}^{n+1}t$ is numerically integrated by the backward EULER method:

$${}^{n+1}\bar{\boldsymbol{\chi}}_{\text{pl}} = {}^n\bar{\boldsymbol{\chi}}_{\text{pl}} + \Delta t \cdot {}^{n+1}\bar{\mathbf{d}}_{\text{pl}} = {}^n\bar{\boldsymbol{\chi}}_{\text{pl}} + {}^{n+1}\Delta\lambda {}^{n+1}\mathbf{N} . \quad (3.112)$$

The increment of the plastic multiplier ${}^{n+1}\Delta\lambda$ characterizes the amount of plastic yielding in the timestep. Equivalently, the accumulated plastic strain is numerically integrated by the backward EULER method, too:

$${}^{n+1}\zeta \left({}^{n+1}\Delta\lambda \right) = {}^n\zeta + \Delta t \cdot {}^{n+1}\dot{\zeta} = {}^n\zeta + \sqrt{\frac{2}{3}} {}^{n+1}\Delta\lambda . \quad (3.113)$$

Without showing the proof, the normals of the yield surface ${}^{n+1}\mathbf{N}$ and ${}^{n+1}\mathbf{N}_{\text{tr}} = \frac{{}^{n+1}\bar{\mathbf{T}}_{\text{tr}}}{\|{}^{n+1}\bar{\mathbf{T}}_{\text{tr}}\|}$ point in the same direction⁷. Thus, ${}^{n+1}\mathbf{N} = {}^{n+1}\mathbf{N}_{\text{tr}}$ holds. Accordingly,

⁷See [Simo and Hughes, 1998; Wriggers, 2008] for the proof of this relation.

the inelastic strain in each of the MAXWELL elements now reads as (cf. eq. (3.77))

$${}^{n+1}\bar{\chi}_{\text{ink}} = {}^{n+1}\bar{\chi}_{\text{ink, tr}} - \frac{\Delta t}{{}^{n+1}\tau_k + \Delta t} {}^{n+1}\Delta\lambda {}^{n+1}\mathbf{N}_{\text{tr}} . \quad (3.114)$$

Now, employing the trial stress state in eq. (3.108) and the updates of the inelastic and plastic strains in eqs. (3.112) and (3.114), the isochoric part of the CAUCHY stress reads as

$${}^{n+1}\bar{\mathbf{T}} = {}^{n+1}\bar{\mathbf{T}}_{\text{tr}} - \left(2 {}^{n+1}G_{\infty} + \sum_{k=1}^N 2G_k \left(1 - \frac{\Delta t}{{}^{n+1}\tau_k + \Delta t} \right) \right) {}^{n+1}\Delta\lambda {}^{n+1}\mathbf{N}_{\text{tr}} \quad (3.115)$$

and subsequently, by taking the scalar product on both sides with ${}^{n+1}\mathbf{N}_{\text{tr}} = {}^{n+1}\mathbf{N}$,

$$\sqrt{2 {}^{n+1}J_2} = \sqrt{2 {}^{n+1}J_{2, \text{tr}}} - \left(2 {}^{n+1}G_{\infty} + \sum_{k=1}^N 2G_k \left(1 - \frac{\Delta t}{{}^{n+1}\tau_k + \Delta t} \right) \right) {}^{n+1}\Delta\lambda . \quad (3.116)$$

Next, the isotropic hardening function must also be updated:

$${}^{n+1}H = {}^{n+1}H_0 {}^{n+1}\zeta + {}^{n+1}\kappa_0 \left(1 - \exp \left(- {}^{n+1}\kappa_1 {}^{n+1}\zeta \right) \right) . \quad (3.117)$$

Inserting eqs. (3.116) and (3.117) into the yield condition eq. (3.93) gives the equation for the determination of the increment of the plastic multiplier ${}^{n+1}\Delta\lambda$:

$$\begin{aligned} {}^{n+1}f &= \sqrt{2 {}^{n+1}J_{2, \text{tr}}} - \left(2 {}^{n+1}G_{\infty} + \sum_{k=1}^N 2G_k \left(1 + \frac{\Delta t}{{}^{n+1}\tau_k + \Delta t} \right) \right) {}^{n+1}\Delta\lambda \\ &\quad - \sqrt{\frac{2}{3}} \left({}^{n+1}Y_0 + {}^{n+1}H \right) \stackrel{!}{=} 0 . \end{aligned} \quad (3.118)$$

This equation cannot be directly solved for ${}^{n+1}\Delta\lambda$. For this purpose, the NEWTON-RAPHSON scheme

$$\begin{aligned} {}^{n+1}_{j+1}\Delta\lambda &= {}^{n+1}_j\Delta\lambda + {}^{n+1}_{j+1}\Delta\Delta\lambda \\ {}^{n+1}_{j+1}\Delta\Delta\lambda &= - \left(\frac{\partial {}^{n+1}f}{\partial {}^{n+1}\Delta\lambda} \Big|_j \right)^{-1} {}^{n+1}_j f \\ \frac{\partial {}^{n+1}f}{\partial {}^{n+1}\Delta\lambda} \Big|_j &= -2 {}^{n+1}G_{\infty} - \sum_{k=1}^N 2G_k \left(1 + \frac{\Delta t}{{}^{n+1}\tau_k + \Delta t} \right) \\ &\quad - \frac{2}{3} \left({}^{n+1}H_0 + {}^{n+1}\kappa_0 {}^{n+1}\kappa_1 \exp \left(- {}^{n+1}\kappa_1 \zeta \left({}^{n+1}_j\Delta\lambda \right) \right) \right) \end{aligned} \quad (3.119)$$

is applied. The local iteration is performed at every integration point of the finite element model in the current timestep. In each iteration step, the convergence criterion $|_{j+1}^{n+1}f \left({}_{j+1}^{n+1}\Delta\lambda \right)| < 10^{-8}$ is checked. If the convergence is achieved, the local iteration is stopped and the increment of the plastic multiplier is determined.

Finally, all variables depending on the increment of the plastic multiplier according to the eqs. (3.112) - (3.115) can be updated for the next timestep.

Viscoelastic-viscoplastic material behavior Based on the presented procedure for the determination of the increment of the plastic multiplier in the viscoelastic-plastic case, the computation of the CAUCHY stress is executed in the viscoelastic-viscoplastic case. In order to ensure a better clarity in the following derivations, the time-dependent shear modulus at time ${}^{n+1}t$ is abbreviated as

$${}^{n+1}G = 2 {}^{n+1}G_{\infty} + \sum_{k=1}^N 2G_k \left(1 - \frac{\Delta t}{{}^{n+1}\tau_k + \Delta t} \right) . \quad (3.120)$$

As previously discussed, the yield condition $f = 0$ is violated in the viscoelastic-viscoplastic case allowing for stress states with $f > 0$. Thus, the increment of the plastic multiplier is not the variable searched anymore. Recalling the viscoplastic flow rule of eq. (3.100), the discretized form of the viscoplastic strain now reads as

$$\begin{aligned} {}^{n+1}\bar{\boldsymbol{\chi}}_{\text{vp}} &= {}^n\bar{\boldsymbol{\chi}}_{\text{vp}} + \Delta t \cdot {}^{n+1}\bar{\mathbf{d}}_{\text{vp}} \\ &= {}^n\bar{\boldsymbol{\chi}}_{\text{vp}} + \frac{\Delta t}{{}^{n+1}\tau_{\text{vp}}} \left\langle \frac{{}^{n+1}f}{f_0} \right\rangle {}^{n+1}m_{\text{vp}} {}^{n+1}\mathbf{N}_{\text{tr}} . \end{aligned} \quad (3.121)$$

One can easily identify the apparent value of the yield function ${}^{n+1}f$ as the searched variable for the determination of the viscoplastic flow. Again, one has to check the yield condition employing the quantities of the trial step:

$${}^{n+1}f_{\text{tr}} \begin{cases} \leq 0 & \rightarrow \text{viscoelastic timestep} \\ > 0 & \rightarrow \text{viscoplastic timestep} \end{cases} . \quad (3.122)$$

Again, if the timestep is viscoelastic, all quantities are already determined by the trial state. In the case of viscoplastic yielding, one has to find the right value for ${}^{n+1}f$. For this purpose, the accumulated viscoplastic strain is now governed by

$${}^{n+1}\zeta_{\text{vp}} \left({}^{n+1}f \right) = {}^n\zeta_{\text{vp}} + \frac{\Delta t}{{}^{n+1}\tau_{\text{vp}}} \left\langle \frac{{}^{n+1}f}{f_0} \right\rangle {}^{n+1}m_{\text{vp}} , \quad (3.123)$$

which modifies the isotropic hardening function at time ^{n+1}t , cf. eq. (3.117).

Equivalently, the updated inelastic strain in each MAXWELL element (cf. eq. (3.114)), the updated isochoric part of the CAUCHY stress (cf. eq. (3.115)), and the updated second invariant of the isochoric part of CAUCHY stress (cf. eq. (3.116)) are expressed by means of the discretized viscoplastic flow rule in eq. (3.121):

$$^{n+1}\bar{\chi}_{ink} = ^{n+1}\bar{\chi}_{ink, \text{tr}} - \frac{\Delta t}{^{n+1}\tau_k + \Delta t} \frac{\Delta t}{^{n+1}\tau_{vp}} \left\langle \frac{^{n+1}f}{f_0} \right\rangle^{^{n+1}m_{vp}} ^{n+1}\mathbf{N}_{\text{tr}} \quad (3.124)$$

$$^{n+1}\bar{\mathbf{T}} = ^{n+1}\bar{\mathbf{T}}_{\text{tr}} - ^{n+1}G \frac{\Delta t}{^{n+1}\tau_{vp}} \left\langle \frac{^{n+1}f}{f_0} \right\rangle^{^{n+1}m_{vp}} ^{n+1}\mathbf{N}_{\text{tr}} \quad (3.125)$$

$$\sqrt{2^{n+1}J_2} = \sqrt{2^{n+1}J_{2, \text{tr}}} - ^{n+1}G \frac{\Delta t}{^{n+1}\tau_{vp}} \left\langle \frac{^{n+1}f}{f_0} \right\rangle^{^{n+1}m_{vp}} \quad (3.126)$$

Inserting eq. (3.126) into eq. (3.93) and taking into account the isotropic hardening function modified by the viscoplastic flow rule leads to the equation for the determination of ^{n+1}f :

$$^{n+1}f = \sqrt{2^{n+1}J_{2, \text{tr}}} - ^{n+1}G \frac{\Delta t}{^{n+1}\tau_{vp}} \left\langle \frac{^{n+1}f}{f_0} \right\rangle^{^{n+1}m_{vp}} - \sqrt{\frac{2}{3}} \left(^{n+1}Y_0 + ^{n+1}H \right) . \quad (3.127)$$

Again, as in the viscoelastic-plastic case, this equation cannot be directly solved for ^{n+1}f due to the nonlinear isotropic hardening function. Rearranging of eq. (3.127) yields

$$\begin{aligned} F\left(^{n+1}f\right) &= \sqrt{2^{n+1}J_{2, \text{tr}}} - ^{n+1}G \frac{\Delta t}{^{n+1}\tau_{vp}} \left\langle \frac{^{n+1}f}{f_0} \right\rangle^{^{n+1}m_{vp}} \\ &\quad - \sqrt{\frac{2}{3}} \left(^{n+1}Y_0 + ^{n+1}H \right) - ^{n+1}f \\ &\stackrel{!}{=} 0 , \end{aligned} \quad (3.128)$$

whose zero is the searched value for ^{n+1}f .

Similarly to the viscoelastic-plastic case, the function $F\left(^{n+1}f\right)$ is iteratively solved

for ${}^{n+1}f$ by a local NEWTON-RAPHSON scheme, which reads as

$$\begin{aligned}
{}^{n+1}f &= {}^{n+1}f + {}^{n+1}\Delta f \\
{}^{n+1}\Delta f &= - \left(\frac{\partial {}^{n+1}F}{\partial {}^{n+1}f} \Big|_j \right)^{-1} \cdot {}^{n+1}F({}^{n+1}f) \\
\frac{\partial {}^{n+1}F}{\partial {}^{n+1}f} \Big|_j &= \left(- {}^{n+1}G - \frac{2}{3} ({}^{n+1}H_0 \right. \\
&\quad \left. + {}^{n+1}\kappa_0 {}^{n+1}\kappa_1 \exp \left(- {}^{n+1}\kappa_1 {}^{n+1}\zeta \left({}^{n+1}f \right) \right) \right) \\
&\quad \cdot \frac{{}^{n+1}m_{vp}\Delta t}{{}^{n+1}\tau_{vp}f_0} \left\langle \frac{{}^{n+1}f}{f_0} \right\rangle^{n+1m_{vp}-1} - 1 .
\end{aligned} \tag{3.129}$$

This NEWTON-RAPHSON procedure is executed until $\left| {}^{n+1}F({}^{n+1}f) \right| < 10^{-8}$ holds. As a result, all quantities depending on the non-zero value of ${}^{n+1}f$ can be updated according to eqs. (3.121) - (3.125).

A summary of the consistent discretization of the stress computation in case of viscoelastic-viscoplastic material behavior is provided in fig. 3.8. Therein, the main steps for the correct calculation of the stress update depending on the input variables are described for a straightforward implementation.

Consistent tangent modulus In order to guarantee the best convergence in the implicit finite element simulations, the correct derivation of the consistent tangent modulus is necessary with respect to the previously introduced viscoelastic predictor-viscoplastic corrector procedure. In the following, the derivations are carried out for the viscoelastic-viscoplastic case as it is the most general form. Naturally, the derived equations can be reduced to the viscoelastic-plastic case by neglecting the viscoplastic contribution of the material model. Principally, using the temporal discretization of the hypoelastic relation between the Jaumann rate of the Cauchy stress tensor and the elastic part of the strain rate tensor, the discretized consistent tangent modulus at time ${}^{n+1}t$ is additively split into isochoric and volumetric parts:

$${}^{n+1}\mathbf{C} = \frac{\partial {}^{n+1}\Delta \mathbf{T}}{\partial {}^{n+1}\Delta \boldsymbol{\chi}} = \frac{\partial {}^{n+1}\Delta \bar{\mathbf{T}}}{\partial {}^{n+1}\Delta \boldsymbol{\chi}} + \frac{\partial {}^{n+1}\Delta \hat{\mathbf{T}}}{\partial {}^{n+1}\Delta \boldsymbol{\chi}} . \tag{3.130}$$

The following calculations are performed employing the basics of tensor analysis⁸. The volumetric part, which is assumed to be purely viscoelastic, is easily derived by

⁸See [Itskov, 2015] for a comprehensive overview of tensor algebra and tensor analysis.

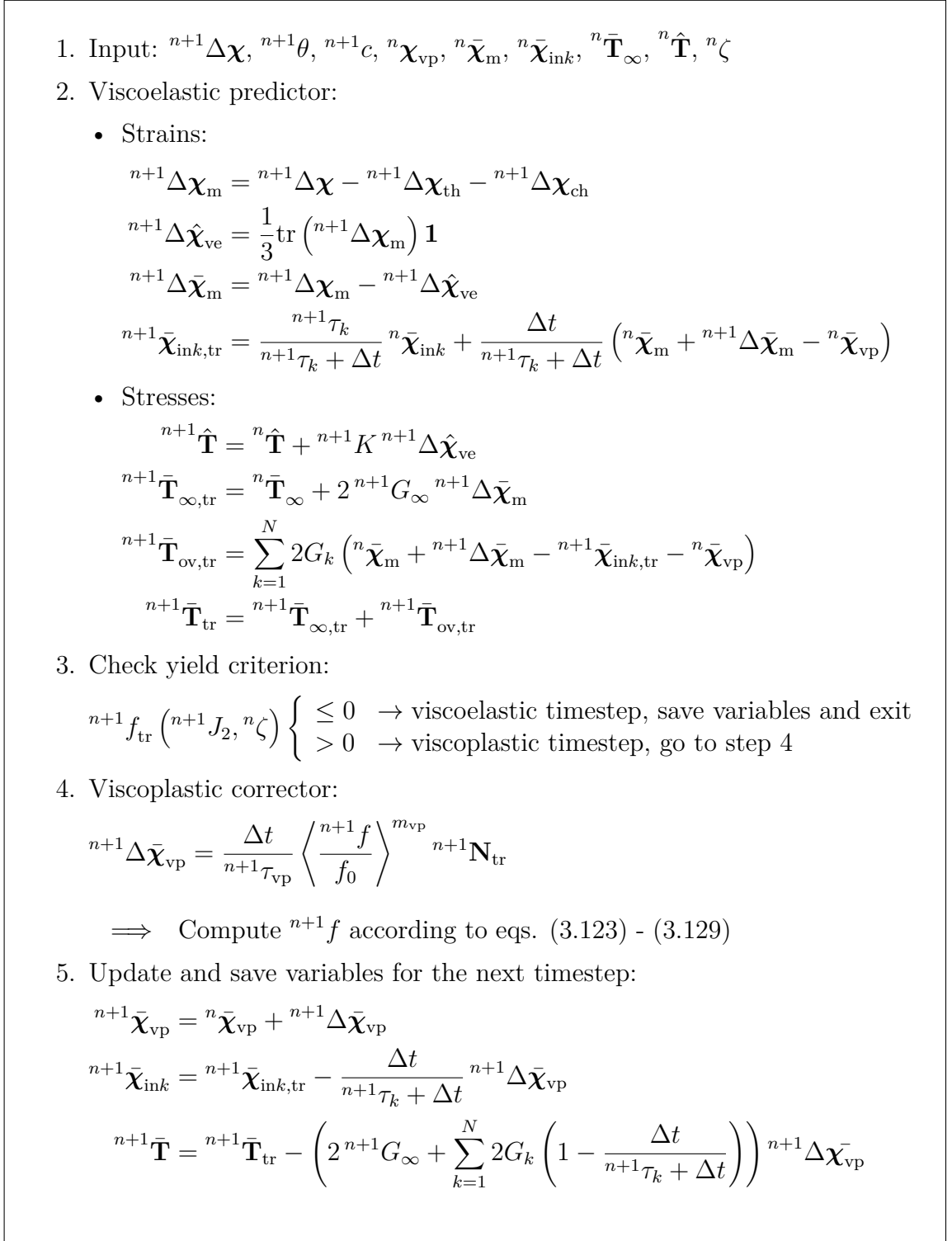


Figure 3.8. Summary of the algorithm for the computation of the viscoelastic-viscoplastic material model

the following expression:

$$\begin{aligned}\frac{\partial^{n+1}\Delta\hat{\mathbf{T}}}{\partial^{n+1}\Delta\boldsymbol{\chi}} &= \frac{1}{3} {}^{n+1}K \frac{\partial \operatorname{tr} \left({}^{n+1}\Delta\boldsymbol{\chi} - {}^{n+1}\Delta\boldsymbol{\chi}_{\text{th}} - {}^{n+1}\Delta\boldsymbol{\chi}_{\text{ch}} \right)}{\partial^{n+1}\Delta\boldsymbol{\chi}} \\ &= \frac{1}{3} {}^{n+1}K \mathbf{1} \otimes \mathbf{1} .\end{aligned}\tag{3.131}$$

The derivation of the deviatoric part, on the other hand, seems to require more effort, which is mainly caused by the consideration of the viscoelastic and viscoplastic effects. Analogously to the volumetric part, the general derivation of the deviatoric part of the consistent tangent modulus is⁹

$$\begin{aligned}\frac{\partial^{n+1}\Delta\bar{\mathbf{T}}}{\partial^{n+1}\Delta\boldsymbol{\chi}} &= \frac{\partial^{n+1}\Delta\bar{\mathbf{T}}_{\text{tr}}}{\partial^{n+1}\Delta\boldsymbol{\chi}} - \frac{{}^{n+1}G\Delta t}{{}^{n+1}\tau_{\text{vp}}} \frac{\partial}{\partial^{n+1}\Delta\boldsymbol{\chi}} \left(\left\langle \frac{{}^{n+1}f({}^{n+1}\Delta\boldsymbol{\chi})}{f_0} \right\rangle^{n+1m_{\text{vp}}} {}^{n+1}\mathbf{N}_{\text{tr}} \right) \\ &= \frac{\partial^{n+1}\Delta\bar{\mathbf{T}}_{\text{tr}}}{\partial^{n+1}\Delta\boldsymbol{\chi}} - \frac{{}^{n+1}G\Delta t}{{}^{n+1}\tau_{\text{vp}}} \left({}^{n+1}\mathbf{N}_{\text{tr}} \otimes \frac{{}^{n+1}m_{\text{vp}}}{f_0} \left\langle \frac{{}^{n+1}f}{f_0} \right\rangle^{n+1m_{\text{vp}}-1} \right. \\ &\quad \cdot \left. \frac{\partial^{n+1}f}{\partial^{n+1}\Delta\boldsymbol{\chi}} + \left\langle \frac{{}^{n+1}f}{f_0} \right\rangle^{n+1m_{\text{vp}}} \frac{\partial^{n+1}\mathbf{N}_{\text{tr}}}{\partial^{n+1}\Delta\boldsymbol{\chi}} \right) .\end{aligned}\tag{3.132}$$

Herein, the first summand describes the purely elastic behavior given by the viscoelastic trial stress state (cf. eq. (3.108)):

$$\frac{\partial^{n+1}\Delta\bar{\mathbf{T}}_{\text{tr}}}{\partial^{n+1}\Delta\boldsymbol{\chi}} = {}^{n+1}G \left(\boldsymbol{\mathcal{I}} - \frac{1}{3} \mathbf{1} \otimes \mathbf{1} \right) .\tag{3.133}$$

$\boldsymbol{\mathcal{I}}$ and $\mathbf{1}$ are the fourth order and second order identity tensors, respectively. Using the implicit function theorem, see [Binmore and Davies, 2001], the following expression holds for the partial derivative of the yield function ${}^{n+1}f$ with respect to the strain increment ${}^{n+1}\Delta\boldsymbol{\chi}$:

$$\frac{\partial^{n+1}F}{\partial^{n+1}\Delta\boldsymbol{\chi}} + \frac{\partial^{n+1}F}{\partial^{n+1}f} \frac{\partial^{n+1}f}{\partial^{n+1}\Delta\boldsymbol{\chi}} = \mathbf{0} .\tag{3.134}$$

Rearranging this equation leads to

$$\frac{\partial^{n+1}f}{\partial^{n+1}\Delta\boldsymbol{\chi}} = - \left(\frac{\partial^{n+1}F}{\partial^{n+1}f} \right)^{-1} \frac{\partial^{n+1}F}{\partial^{n+1}\Delta\boldsymbol{\chi}}\tag{3.135}$$

⁹The operator $(.) \otimes (.)$ defines the dyadic product between two second order tensors $(.)$ and $(.)$ (e.g., $\mathbf{A} \otimes \mathbf{B} = A_{ij}B_{kl}$).

in which the partial derivative of ${}^{n+1}F$ with respect to ${}^{n+1}f$ is given by eq. (3.129) and the partial derivative of ${}^{n+1}F$ with respect to ${}^{n+1}\Delta\chi$ reads as

$$\begin{aligned}
 \frac{\partial {}^{n+1}F}{\partial {}^{n+1}\Delta\chi} &= \frac{\partial \sqrt{2 {}^{n+1}J_{2,\text{tr}}}}{\partial {}^{n+1}\Delta\chi} = \frac{\partial}{\partial {}^{n+1}\Delta\chi} \left({}^{n+1}\bar{\mathbf{T}}_{\text{tr}} \cdot {}^{n+1}\bar{\mathbf{T}}_{\text{tr}} \right)^{\frac{1}{2}} \\
 &= \frac{\partial {}^{n+1}\bar{\mathbf{T}}_{\text{tr}}}{\partial {}^{n+1}\Delta\chi} \cdot \frac{{}^{n+1}\bar{\mathbf{T}}_{\text{tr}}}{\sqrt{2 {}^{n+1}J_{2,\text{tr}}}} \\
 &= {}^{n+1}G \left(\mathcal{I} - \frac{1}{3} \mathbf{1} \otimes \mathbf{1} \right) {}^{n+1}\mathbf{N}_{\text{tr}} \\
 &= {}^{n+1}G {}^{n+1}\mathbf{N}_{\text{tr}} .
 \end{aligned} \tag{3.136}$$

In a last step, one has to derive ${}^{n+1}\mathbf{N}_{\text{tr}}$ with respect to ${}^{n+1}\Delta\chi$ by means of the eqs. (3.133) and (3.136):

$$\begin{aligned}
 \frac{\partial {}^{n+1}\mathbf{N}_{\text{tr}}}{\partial {}^{n+1}\Delta\chi} &= \frac{1}{2 {}^{n+1}J_{2,\text{tr}}} \left(\frac{\partial {}^{n+1}\bar{\mathbf{T}}_{\text{tr}}}{\partial {}^{n+1}\Delta\chi} \sqrt{2 {}^{n+1}J_{2,\text{tr}}} - {}^{n+1}\bar{\mathbf{T}}_{\text{tr}} \otimes \frac{\partial \sqrt{2 {}^{n+1}J_{2,\text{tr}}}}{\partial {}^{n+1}\Delta\chi} \right) \\
 &= \frac{{}^{n+1}G}{\sqrt{2 {}^{n+1}J_{2,\text{tr}}}} \left(\mathcal{I} - \mathbf{1} \otimes \mathbf{1} - {}^{n+1}\mathbf{N}_{\text{tr}} \otimes {}^{n+1}\mathbf{N}_{\text{tr}} \right) .
 \end{aligned} \tag{3.137}$$

If the timestep is considered as viscoelastic, ${}^{n+1}f_{\text{tr}} \leq 0$ holds and the consistent tangent modulus is reduced to the viscoelastic tangent modulus:

$${}^{n+1}\mathbf{C} = {}^{n+1}G \left(\mathcal{I} - \frac{1}{3} \mathbf{1} \otimes \mathbf{1} \right) + \frac{1}{3} {}^{n+1}K \mathbf{1} \otimes \mathbf{1} \quad \text{if} \quad {}^{n+1}f_{\text{tr}} \leq 0 . \tag{3.138}$$

The set of the derived equations mentioned above represents the framework for the computation of the stress update and its consistent tangent modulus in every timestep. They are implemented as user subroutines into the commercial finite element program LS-DYNA[®] for the finite element analyses following in the next chapter. For this purpose, the tensor-valued quantities are transferred into the VOIGT notation. Hence, all second order tensors become column vectors $\in \mathbb{R}^6$ and the consistent tangent modulus becomes a matrix $\in \mathbb{R}^{6 \times 6}$.

4 Parameter Identification and Validation

This chapter connects the experimental results of ch. 2 with the modeling approaches of ch. 3 in order to show the suitability of the proposed equations. To this end, nonlinear optimization programs and the according algorithms are applied. The identified parameter sets serve for the calibration of the temperature- and degree of cure-dependent equations of the material model.

The commercial optimization program LS-OPT[®] employs the sequential response surface methodology (SRSM), which is well-suited for conducting parameter identifications in continuum mechanical problems. Since this method is neither investigated nor is part of the research in this thesis, reference is made to [Myers et al., 2016; Kok and Stander, 1999] for a better understanding of this method and its application.

Additionally, the open-source program gnuplot can fit the parameters of algebraic equations to experimental data using the LEVENBERG-MARQUARDT algorithm. Hence, in the following sections, gnuplot is applied to identify the parameters of the algebraic model equations following later.

After finishing the parameter identification, the identified parameters are used for the validation of tensile specimens subjected to cyclic loading and unloading.

4.1 Crosslinking

Identifying the parameters of the one-dimensional evolution equation of the degree of cure c is performed first because all subsequent properties of the photopolymer strongly depend on this variable. Hence, the identification is accomplished through the SRSM implemented in the commercial optimization program LS-OPT[®]. Moreover, the evolution equation of the degree of cure c is solved by the ode45 solver implemented in MATLAB[®].

Finishing the optimization process after twelve iterations yields the parameters listed in table 4.1. Before conducting the optimization process, the parameters c_0 and $T_{c_{\max}}$ of eq. (3.3) are adapted to the mean values of the degrees of cure at the end of the

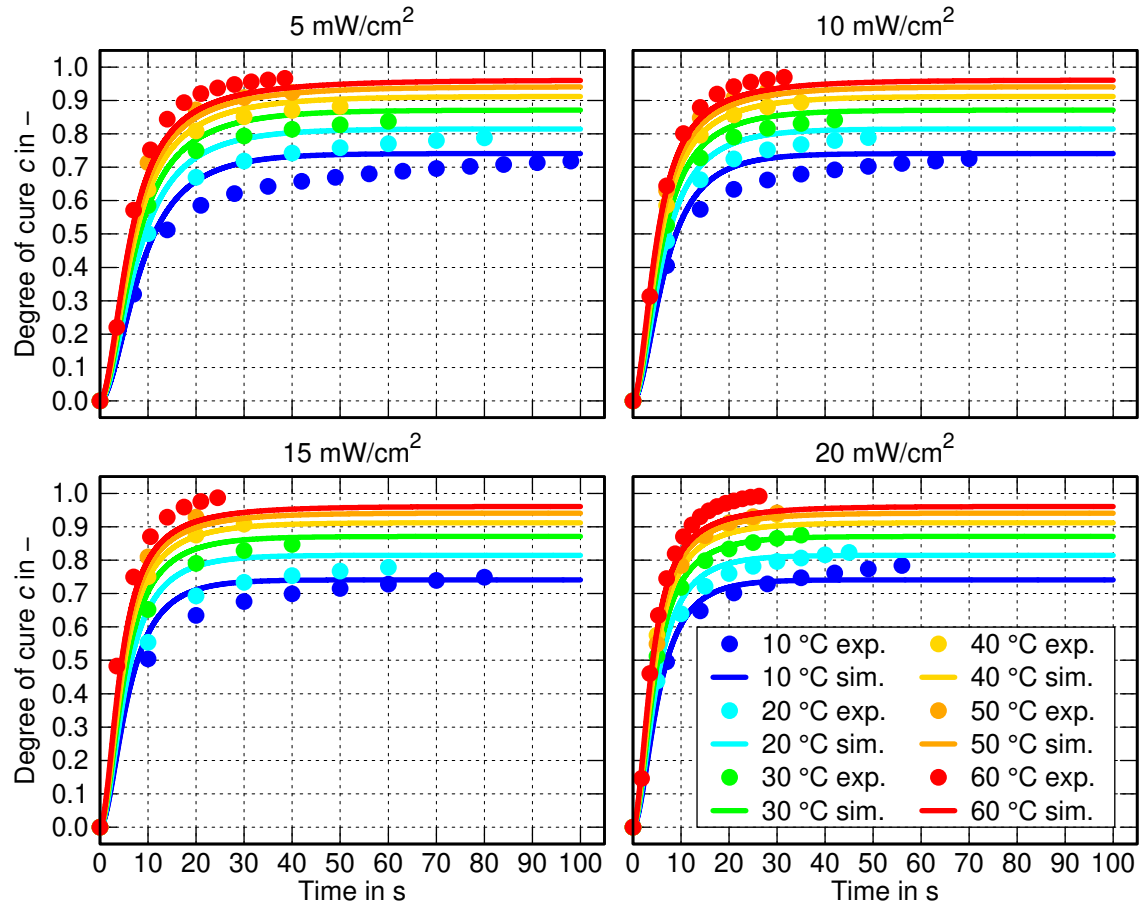


Figure 4.1. Comparison between experimental curves generated by photo-DSC measurements and simulated curves by means of eq. (3.5) and the parameters enlisted in table 4.1

irradiation for each temperature. The comparison between the experimental results of the photo-DSC measurements and the proposed model equation is shown in fig. 4.1. Generally, good accordance is achieved between the experimental results and the proposed model equation.

Since the number of parameters used for this model equation is high, further improvements on the identification strategy can yield a better representation of the

Table 4.1. Parameters of the model equation of the degree of cure identified by means of the experimental data of sec. 2.2.3

A_1	A_2	E_1	E_2	n
0.3 s^{-1}	1.0008 s^{-1}	$17.58 \frac{\text{kJ}}{\text{mol}}$	$2.75 \frac{\text{kJ}}{\text{mol}}$	0.4632
p	b_1	b_2	c_0	$T_{c_{\max}}$
0.585	0.05664	0.3354	$4.29 \cdot 10^{-2} \text{ K}^{-1}$	258.67 K

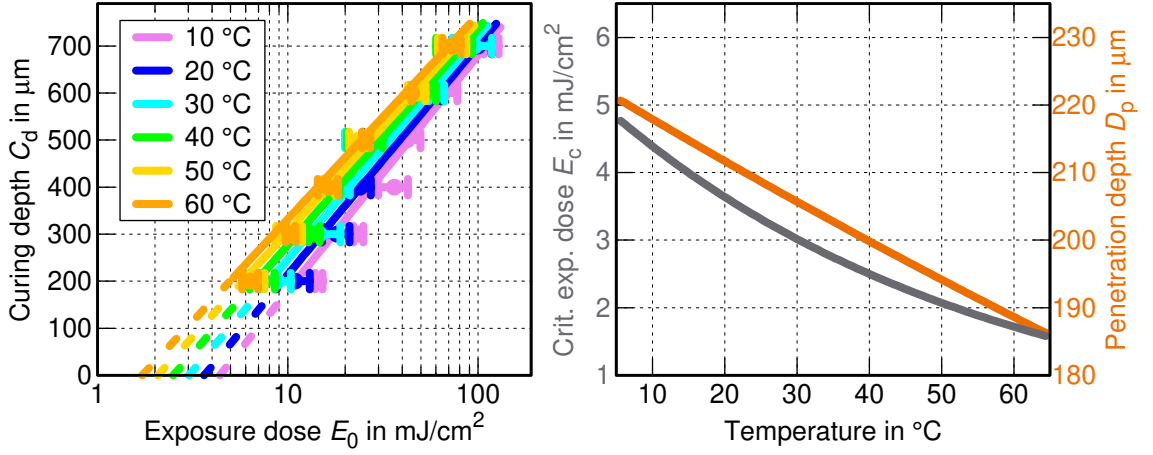


Figure 4.2. Left: modified working curve model based on eq. (3.7). Right: temperature-dependent critical exposure dose and penetration depth based on eqs. (3.8) and (3.9).

experimental data. Furthermore, a more sophisticated analysis of the model equation, e.g., the direct identification of the ARRHENIUS coefficients k_1 and k_2 , can lead to better results and a reduced parameter set.

The identification of the parameters of the modified working curve model, see eqs. (3.7) - (3.9), is also conducted using LS-OPT[®] in conjunction with SRSM. To do this, the parameters of the modified working curve model are adapted so that the error between the experimentally determined exposure doses for the considered curing depths and the evaluated working curves is minimized. Fig. 4.2 shows the evaluations of the modified working curve model for the investigated temperatures in subsec. 2.3.2 and the temperature-dependent functions for the critical exposure dose and the penetration depth. The identified and applied values of the parameters are listed in table 4.2. Using these values leads to an apparently linear relationship between the penetration depth and the temperature of the photopolymer resin. Comparatively, the function describing the critical exposure dose rather exponentially decreases with increasing temperature.

Compared to the individual working curves in fig. 2.20, the resulting critical exposure doses are smaller using the modified working curve model. Furthermore, the deviation between the modified working curve model and the experimental data seems to be larger than in fig. 2.20.

Table 4.2. Identified values of the parameters of the modified working curve model

Parameter	E_{c0} in mJ/cm^2	E_{c1} in $^{\circ}\text{C}^{-1}$	D_{p0} in μm	D_{p1} in $^{\circ}\text{C}^{-1}$
Value	5.297	$1.877 \cdot 10^{-2}$	224.278	$2.884 \cdot 10^{-3}$

4.2 Viscoelastic properties

First of all, the parameters representing the viscoelastic properties are identified. Since the resulting master curves cover a broad range of angular frequencies, the identification procedure cannot be directly conducted. In general, assuming linear viscoelastic behavior, the resulting number of MAXWELL chains is double-digit to reduce the error between the experimental and simulated master curves to a sufficient minimum [Jalocha et al., 2015].

4.2.1 Viscoelastic properties of printed specimens

The master curves of the storage moduli generated by the experimental data from DMA tests in sec. 2.4 generally show an increase over several orders of magnitude with increasing angular frequency. Hence, the main objective in the parameter identification process for the relaxation times and shear moduli is to find suitable parameter combinations that do not overweight large absolute differences between the experimental and simulated values in the error measure. For example, standard error measure such as the mean squared error (MSE) show that undesired behavior. In contrast, error measures such as the mean squared logarithmic error that focus more on relative differences between experimental and simulated values may be the better choice in such cases.

In the case of the experimentally derived shear storage modulus G'_{exp} as the objective value, the MSLE reads as follows:

$$\text{MSLE} = \frac{1}{P} \sum_{i=1}^P \left(\log_{10} G'_{i,\text{sim}} (G_{\infty}(c), \mathbf{G}, \boldsymbol{\tau}_{\text{R}}) - \log_{10} G'_{i,\text{exp}} \right)^2. \quad (4.1)$$

The vectors \mathbf{G} and $\boldsymbol{\tau}_{\text{R}}$ include the shear moduli G_k and relaxation times $\tau_{k\text{R}}$ at the reference temperature θ_{R} and reference degree of cure c_{R} , respectively. The error between the simulated and experimental values is computed at each regression point i with a total number of P regression points. Especially in the identification process of the parameters of viscoelastic material models on data sets based on master curves obtained from DMA tests, the usage of error measures that focus more on relative than absolute changes is preferable. By looking at the master curve of the DMA test, the increase of the shear storage modulus over several orders of magnitude is visible thus leading to the reasonable usage of the MSLE.

Fig. 4.3 shows a schematic comparison between the MSLE and MSE for logarithmically distributed experimental values y_{exp} and simulated values y_{sim} . According to typical test data of DMA measurements of thermosetting or thermoplastic polymers, the range of the chosen simulated and experimental values is set to

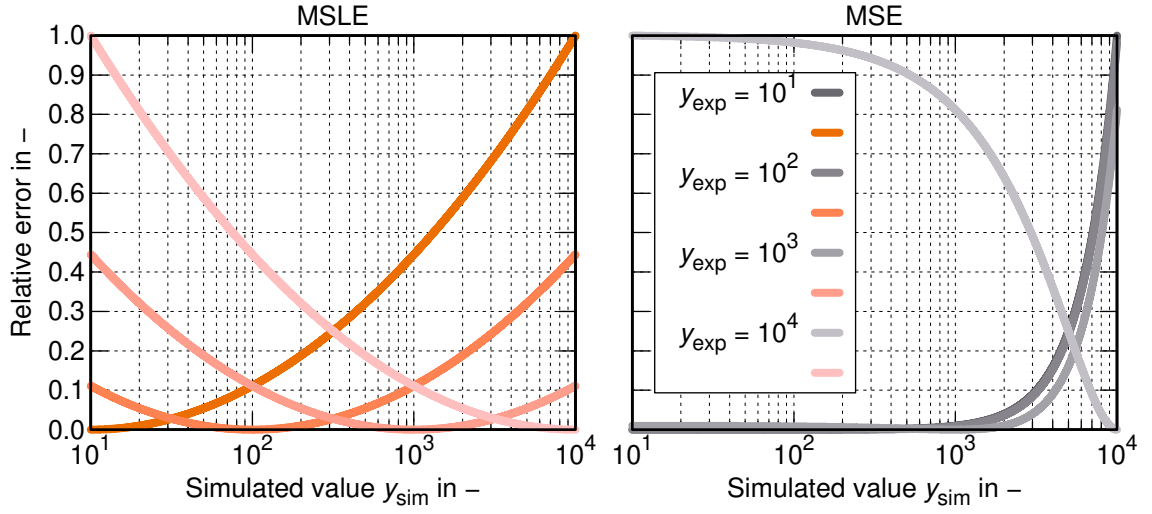


Figure 4.3. Schematic comparison between the mean squared logarithmic error (MSLE) and the mean squared error (MSE) for random, logarithmically distributed simulated values y_{sim} and fixed experimental values $y_{\text{exp}} = 10^1 \dots 10^4$. For a better comparison, the absolute MSE and MSLE values are divided by the maximum values $\text{MSE}_{\text{max}} = 9990^2$ and $\text{MSLE}_{\text{max}} = 9$.

$y_{\text{sim}} = y_{\text{exp}} = [10^1, 10^4]$. For a better comparability, the error measures are normalized. To do this, the individual MSE and MSLE values are divided by each each maximum value $\text{MSE}_{\text{max}} = 9990^2$ and $\text{MSLE}_{\text{max}} = 9$, respectively. It is obvious that using the MSLE leads to a more appropriate error for logarithmically distributed ordinate values. The relative error nearly tends towards a linear relationship depending on the deviation between the simulated value y_{sim} and the experimental value y_{exp} . Considering the usage of the MSE, the relative error is more nonlinear and overestimates the error between the simulated and experimental values if they are high. Thus, large relative deviations between simulated and experimental values would be underestimated if the values are small.

Using the MSLE for the identification of relaxation times and moduli of viscoelastic material models is successfully conducted in [Rehbein and Matzenmiller, 2018] and [Rehbein et al., 2021] and leads to satisfying results. Therefore, the MSLE is preferred over the MSE for the following identification.

After implementing the MSLE into the optimization process of SRSIM, the identification of the shear moduli G_k and relaxation times τ_k can be conducted. To define a suitable starting set of parameters, the shifted angular frequency range as visible in fig. 2.32 is divided into 30 subdomains. Hence, the total number of MAXWELL chains is set to $N = 30$. At first, the optimization procedure is conducted for the master curve belonging to the reference point ($\theta_R = 20^\circ\text{C}$, $c_R = c_{\text{eff}} = 1.0$). The

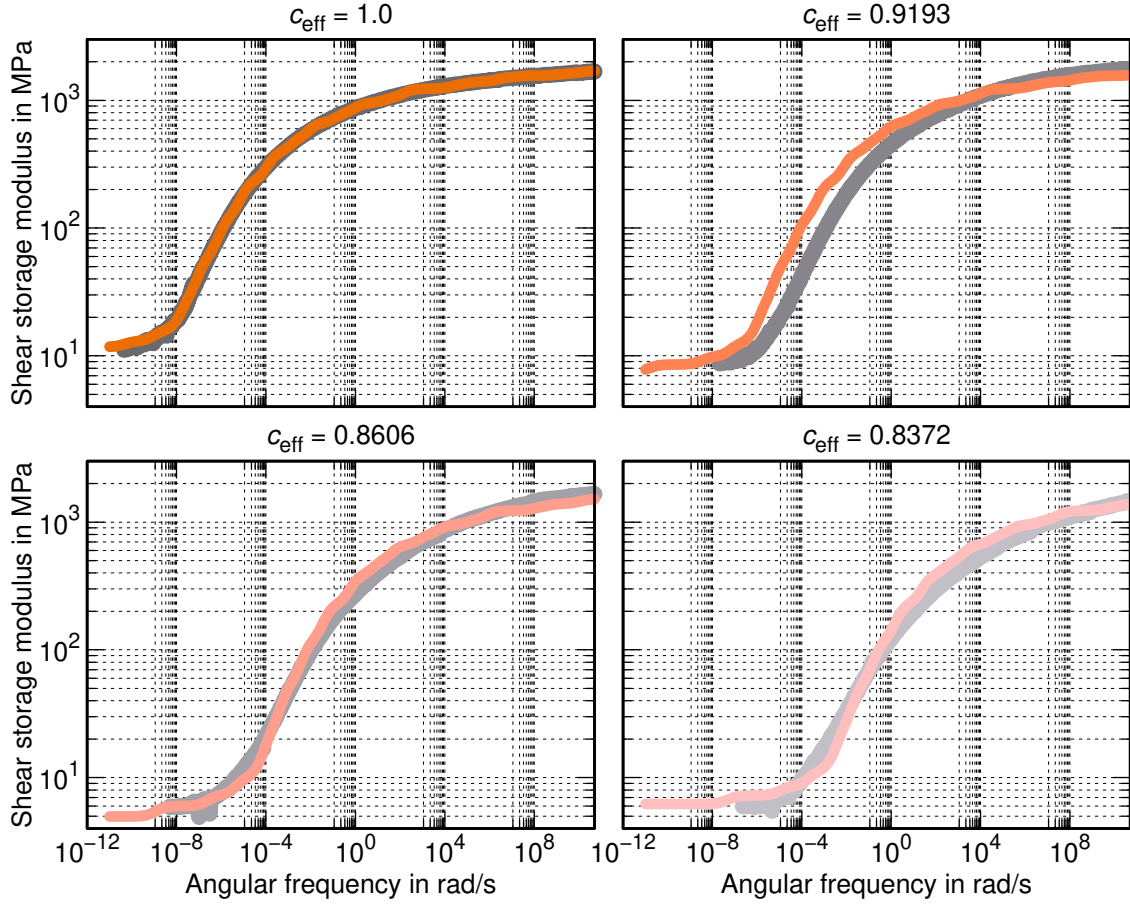


Figure 4.4. Comparison between the experimentally derived shear storage moduli G'_{exp} and the simulated shear storage moduli G'_{sim} by means of the parameters enlisted in table A.1

individual relaxation times are initially set to a value corresponding to the reciprocal of the mean angular frequency of the subdomain. The bounds of the relaxation time are set to overlap the upper and lower bounds of each neighboring relaxation time. All shear moduli are initially set to 10 MPa, whereas the lower bound is set to 1 MPa and the upper bound is set to 1000 MPa. The equilibrium shear modulus G_{∞} is also set to 10 MPa, and the bounds are set to 5 MPa and 15 MPa, respectively. The identification procedure leads to the values enlisted in table A.1 for the shear moduli and relaxation times at the reference temperature and reference degree of cure.

In order to represent the master curves at lower effective degrees of cure, the relaxation times assigned to the reference degree of cure are equally shifted to find the best accordance with the corresponding master curve. Additionally, since the material becomes softer at low angular frequencies with decreasing degree of cure,

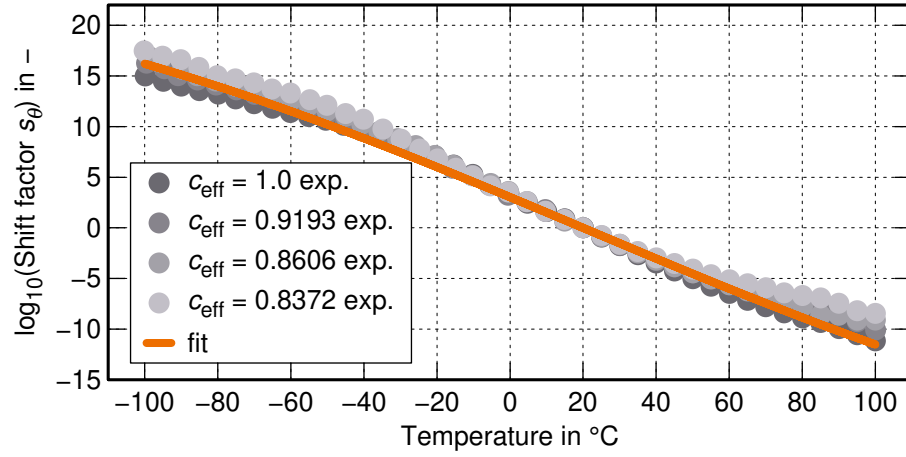


Figure 4.5. Shift factors of the time-temperature superposition (cf. fig. 2.33) and fit function according to eq. (4.2)

the equilibrium shear modulus is readjusted, too. This identification procedure is performed for each master curve leading to individual shift factors and equilibrium shear moduli for each effective degree of cure, see table 4.3. However, the shear moduli G_k remain independent on the temperature and the degree of cure. Fig. 4.4

Table 4.3. Identified shift factors $s_c(c)$ and equilibrium shear moduli $G_\infty(c)$

Effective degree of cure c_{eff} in -	1.0	0.9193	0.8606	0.8372
Shift factor $s_c(c)$ in -	1.0	$1.5 \cdot 10^{-2}$	$1.99 \cdot 10^{-4}$	$4.73 \cdot 10^{-6}$
Equilibrium shear modulus G_∞ in -	10.72	7.53	4.97	6.22

shows the comparison between the experimental and the simulated master curves. In summary, a good accordance is achieved by means of the identified parameters.

If the temperature of the specimen deviates from the reference temperature $\theta_R = 20^\circ\text{C}$, the relaxation times must be shifted. Consequently, a continuous function has to be defined for the temperature-dependent shift factors in fig. 2.33. A suitable approach is governed by

$$\log_{10}(s_\theta(\theta)) = s_{\theta 0} \tanh(-s_{\theta 1}(\theta - \theta_R)) , \quad (4.2)$$

which can describe the temperature-dependent shift factors over a broad temperature range with the two parameters $s_{\theta 0} = 29.14$ and $s_{\theta 1} = 5.22 \cdot 10^{-3} \text{ }^\circ\text{C}^{-1}$. Other functions like the well-known WLF-equation [Williams et al., 1955] would also lead to a satisfying result. Fig. 4.5 shows the comparison between the experimentally determined shift factors of sec. 2.4.3 and the interpolation function given by eq. (4.2).

As previously discussed, the shift factors do not exhibit a strong dependency on the degree of cure. Hence, the approach proposed in eq. (4.2) seems to be reasonable.

4.2.2 Viscoelastic properties during crosslinking

The identification in the previous subsec. 4.2.1 only covers conversion states near the fully cured state. In order to describe the change in the viscoelastic properties over the whole transition of the photopolymer, the experimental results of the rheometric measurements during crosslinking in sec. 2.3 must be taken into account. The following procedure is inspired by [Eom et al., 2000] and is successfully applied in [Rehbein et al., 2021] with regard to photopolymers. Therein, a novel approach is presented using time-cure superposition to describe the change in the mechanical properties of crosslinking polymers through rheometric measurements.

Recalling that the irradiance decreases exponentially with the layer thickness while the radiation passes through the photopolymer layer, the degree of cure is inhomogeneously distributed in the photopolymer layer. Different from the photocalorimetric measurements in sec. 2.2.3, the dimensions of the layer must be taken into account. Given the model equation of the degree of cure (eq. (3.5)), the effective degree of cure in the photopolymer layer is computed by

$$c_{\text{eff}}(t) = \frac{1}{h_0} \int_0^{h_0} \int_0^t \dot{c}(\tau, z) d\tau dz . \quad (4.3)$$

The decrease of the irradiance is described by the BEER-LAMBERT law in eq. (1.1) and included in the ARRHENIUS factors in eq. (3.6). The attenuation factor α is given by the reciprocal of the identified penetration depths D_p , see table 2.3. According to the measurements in subsec. 2.3.1, the layer thickness is set to $h_0 = 500 \mu\text{m}$ and the incident irradiance is $\mathcal{I} = 10.12 \text{ mW/cm}^2$. The integral over the layer thickness is approximated by the trapezoidal rule, whereas the evolution equation describing the degree of cure is integrated by means of the ode45 solver implemented in MATLAB®.

Fig. 4.6 shows the development of the effective degree of cure computed by eq. (4.3) for the conducted measurements in subsec. 2.3.1. Compared to the computed degrees of cure reproducing the photo-DSC measurements with $\mathcal{I} = 10 \text{ mW/cm}^2$, see fig. 4.1, the degree of cure increases more slowly for all temperatures. This behavior is caused by the decrease of the irradiance over the layer thickness.

In the next step, the experimental curves of the storage modulus in fig. 2.18 are

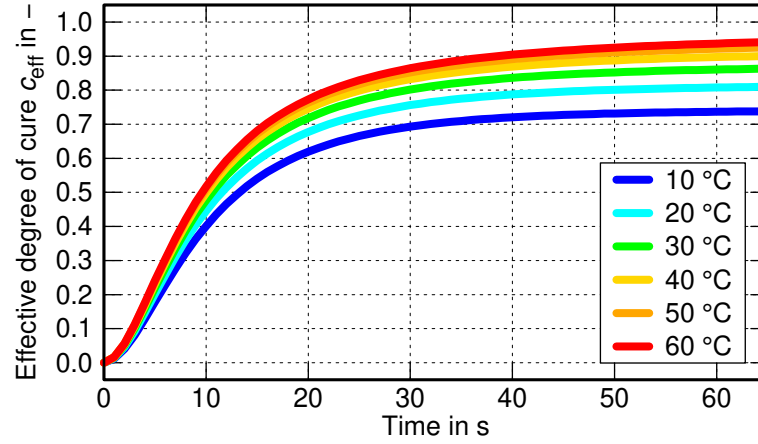


Figure 4.6. Development of the effective degree of cure c_{eff} in the rheometry measurements during crosslinking calculated by eq. (4.3)

plotted versus the computed effective degree of cure in fig. 4.6 for each temperature. Subsequently, the shear storage modulus is extracted for selected degrees of cure and plotted in the frequency domain. This representation is equivalent to the isothermal curves of the shear storage modulus in fig. 2.31.

The corresponding data points are visualized in fig. 4.7 for all considered temperatures. Consequently, the shear storage modulus is defined for conversion states lower than $c = 0.8372$ (cf. fig. 4.4). In order to identify the missing shift factors for these conversion states, a continuous master curve is generated using the data points at $\theta = 10\text{ °C}$. The maximum degree of cure $c = 0.7408$ in this data set is taken as the reference degree of cure. Hence, all data points exhibiting a degree of cure lower than the reference degree of cure are manually shifted to lower angular frequencies. The corresponding shift factors are displayed in fig. 4.8 (right) as light gray dots. Since these shift factors are determined for the reference degree of cure $c = 0.7408$, the shift factors must be shifted vertically to account for the reference degree of cure $c = 1.0$. Hence, the shift factors are equally shifted by 10^{-9} in the vertical direction. In conclusion, the composed shift factors form the continuous line in fig. 4.8 (right) indicated as dark grey dots.

Finally, suitable equations must be formulated in order to describe the degree of cure-dependent equilibrium shear modulus and shift factors for the time-cure superposition. For this purpose, ADOLF and MARTIN [Adolf and Martin, 1996] as well as EOM et al. [Eom et al., 2000] presented suitable model approaches taking into account the degree of cure at the gel point. Thus, in the following, the gel point of the photopolymer is evaluated.

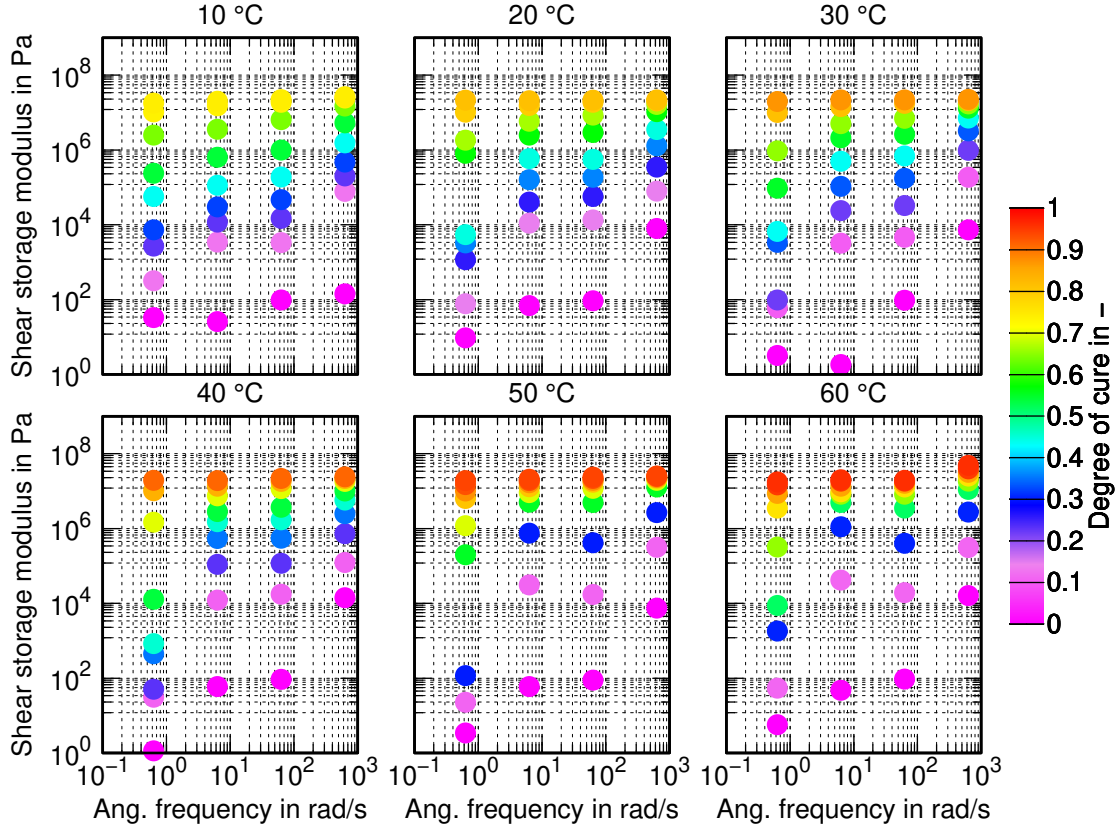


Figure 4.7. Experimentally derived shear storage modulus depending on the degree of cure, temperature, and angular frequency

Determination of the gel point According to [Winter and Chambon, 1986], the gel point is characterized as the state at which the crosslinking polymer transitions from the liquid to the solid state. The degree of cure-dependent equilibrium shear modulus $G_\infty(c)$ in fig. 3.6 describes this transition by

$$G_\infty(c) \begin{cases} = 0 & , \quad c < c_{\text{gel}} \\ > 0 & , \quad c \geq c_{\text{gel}} \end{cases} . \quad (4.4)$$

As already discussed in sec. 1.2, the necessary exposure dose to reach the gel point of a photopolymer layer with layer thickness C_d is given by the incident exposure dose E_0 , which is calculated by

$$E_0 = E_c \exp\left(\frac{C_d}{D_p}\right) . \quad (4.5)$$

Given the parameters of the critical exposure dose E_c and penetration depth D_p for the different temperatures (cf. table 2.3), one can calculate the incident exposure dose for each temperature and $C_d = 500 \mu\text{m}$, whereas the exposure time is given by

Table 4.4. Calculated effective degrees of cure $c_{\text{eff,gel}}$ at the gel point depending on the temperature

Temperature θ in °C	10	20	30	40	50	60
Eff. degree of cure $c_{\text{eff,gel}}$ in -	0.169	0.131	0.123	0.106	0.092	0.088

$t_0 = \frac{E_0}{\mathcal{I}_0}$. Afterward, the effective degree of cure at the gel point is determined by the calculated exposure times and the curves in fig. 4.6 for each temperature. The determined effective degrees of cure corresponding to the gel point are shown in table 4.5. If the temperature of the photopolymer resin increases, the effective degree of cure decreases, i.e., the photopolymer reaches its gel point faster. This result seems to be unphysical because the effective degree of cure at the gel point should be independent on the temperature of the photopolymer during the crosslinking process. However, one possible explanation is the nonlinear dependency on the irradiance of the differential equation for the degree of cure.

In order to circumvent this deficiency, the mean value of the listed values is used. Hence, the effective degree of cure at the gel point of the photopolymer reads as $c_{\text{eff,gel}} = 0.118$, which is also considered as the degree of cure at the gel point c_{gel} . The value is significantly lower than the degree of cure at the gel point of curing adhesives [Liebl, 2014] or other crosslinking polymers.

Degree of cure-dependent equilibrium shear modulus and shift factors The function for the degree of cure-dependent equilibrium shear modulus reads as

$$G_{\infty}(c) = \begin{cases} 0 & , \quad c < c_{\text{gel}} \\ G_{\infty 1} \left(\frac{c - c_{\text{gel}}}{1 - c_{\text{gel}}} \right)^{G_{\infty 2}} & , \quad c \geq c_{\text{gel}} \end{cases} \quad (4.6)$$

and follows the approach presented in [Adolf and Martin, 1996]¹. The additional parameter $G_{\infty 2}$ is introduced in order to allow for a better reproduction of the experimental data. The parameter $G_{\infty 1}$ describes the equilibrium shear modulus at the fully cured state.

Fig. 4.8 (left) shows the identified values of the equilibrium shear modulus (cf. table 4.3) and the fit function given by eq. (4.6) for conversion states above the gel point. Unfortunately, the suitability of eq. (4.6) cannot be assessed for $0.118 < c < 0.8372$ due to missing data points. However, eq. (4.6) yields a good accordance with the given data points. The corresponding identified parameters are listed in table 4.5.

¹The parameter $G_{\infty 2}$ was initially set to $\frac{8}{3}$.

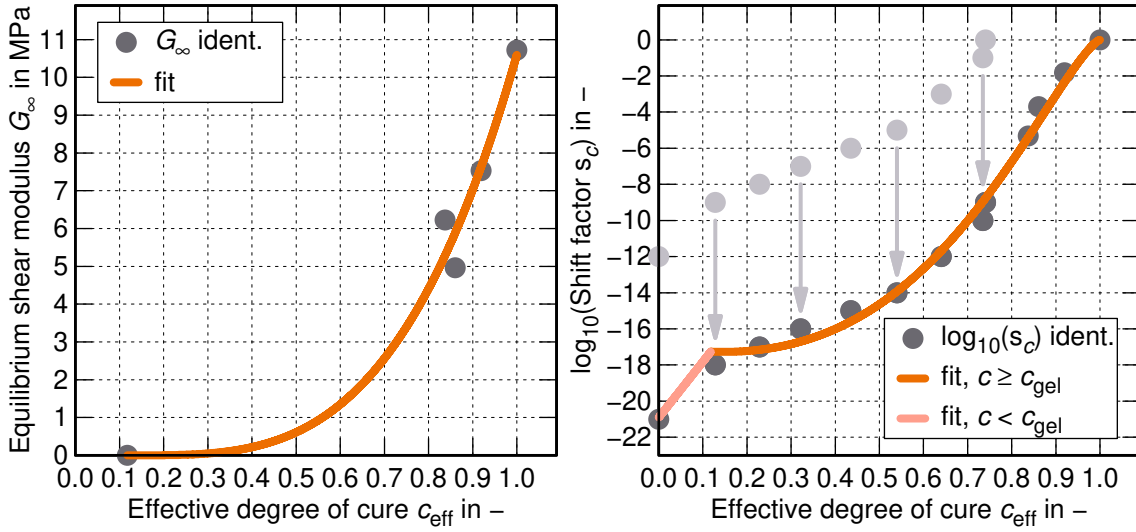


Figure 4.8. Left: degree of cure-dependent equilibrium shear modulus $G_\infty(c)$. Right: shift factors $s_c(c)$ for the time-cure superposition.

The function describing the shift factors of the time-cure superposition reads as

$$\log_{10}(s_c(c)) = \begin{cases} s_{c1}c + s_{c2} & , \quad c < c_{\text{gel}} \\ s_{c_{\text{gel}}}s_{c3}^{c-c_{\text{gel}}} \left(\frac{1-c}{1-c_{\text{gel}}} \right)^{s_{c4}} & , \quad c \geq c_{\text{gel}} \end{cases} \quad (4.7)$$

and is based on the proposal in [Eom et al., 2000]. The shift factors are interpolated by a linear function for conversion states below the gel point. Moreover, the nonlinear function describing the shift factors for conversion states beyond the gel point intersects the linear function at $c = c_{\text{gel}}$. The parameter $s_{c_{\text{gel}}}$ represents the shift factor corresponding to the degree of cure at the gel point.

The shift factors and the corresponding shift function are depicted in fig. 4.8 (right). The values of the parameters of eq. (4.7) are given in table 4.5. Principally, a good accordance is achieved between the identified shift factors and the model approach given by eq. (4.7). It should be noted that the vertical shift of the shift factors below $c = 0.8372$ is performed before the identification of the parameters of eq. (4.7).

Employing the shift functions $s_\theta(\theta)$ and $s_c(c)$ as well as the function for the equilibrium shear modulus $G_\infty(c)$, the deviatoric response of the material model is

Table 4.5. Identified values of the parameters of the eqs. (4.6) and (4.7)

Parameter	$G_{\infty 1}$	$G_{\infty 2}$	s_{c1}	s_{c2}	s_{c3}	s_{c4}	$s_{c_{\text{gel}}}$
Value	10.59 MPa	3.41	27.77	-20.95	4.99	1.37	-17.67

completely defined.

In the next step, the missing model equations representing the volumetric response of the material model are presented by means of the tensile tests in subsec. 2.5.1.

4.3 Tensile properties

4.3.1 Finite element model of the tensile specimen

The finite element model of the tensile specimen is depicted in fig. 4.9. The specimen geometry is discretized by 6 elements over the width and 4 elements over the thickness of the specimen leading to a total of 1248 hexahedral elements (element formulation 2). Furthermore, the simulations are conducted using the implicit time integration. Thus, the global equilibrium is established in every timestep.

The lower end, indicated by the blue coloring, is modeled as a rigid body to represent the fixed clamp of the tensile testing machine whereas the upper end (highlighted in green), which is also modeled as a rigid body, exhibits translational degrees of freedom to apply the displacement boundary condition $u(t)$. Considering the velocity $\dot{u}(t)$ of the movable clamp of the tensile testing machine, the global strain rate

$$\dot{\varepsilon}_{\text{global}} = \frac{\dot{u}(t)}{l_0} \quad (4.8)$$

is set in the tensile specimen with l_0 denoting the distance between both clamps. Since the displacement of the rigid body at the upper part of the specimen is given by the boundary condition of the movable clamp, the displacement in x -direction of the middle node in the transition line between the deformable part (red) and the rigid part (green) is selected to calculate the global true strain of the specimen:

$$\varepsilon_{\text{true,global}} = \ln \left(1 + \frac{u_x^0}{l_0} \right) . \quad (4.9)$$

The reaction force in x -direction, which is compared with the measured reaction force of the testing machine, is evaluated as the accumulated forces in x -direction of the nodes located in the cross-section between the deformable (red) and rigid (green) parts. Although the force sensor of the tensile testing machine is located at the lower end of the steel rod of the lower clamp, the simulated and measured reaction forces are comparable because the steel rod connected to the lower clamp shows a significantly higher stiffness compared to the specimen. Thus, including

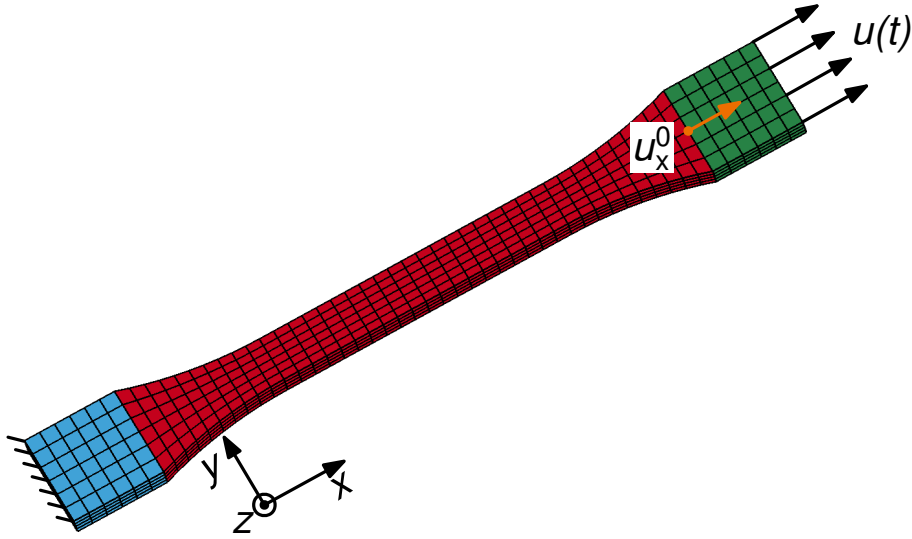


Figure 4.9. Finite element model of the tensile specimen

the clamps and the connected steel rods would not increase the precision of the simulations, but it would tremendously increase the simulation time.

4.3.2 Temperature- and degree of cure-dependent bulk modulus

As explained in sec. 3.5, the bulk behavior is assumed to show only elasticity. Consequently, no strain rate dependency is assumed in purely dilatational deformation states. Nonetheless, as visible in the experimental data of sec. 2.5, different temperatures and degrees of cure of the printed specimens may also influence the bulk modulus. Although the stress state in the tensile specimen is dominated by the deviatoric contributions, the small influence of the bulk modulus on the overall reaction force cannot be neglected. Hence, in the following, the bulk modulus is individually identified for each data set defined by a specific temperature and degree of cure.

The procedure for the identification reads as follows:

1. The experimental force-displacement curves are limited to a maximum displacement of 0.6 mm, which is equal to a global true strain of $\varepsilon_{\text{true,global}} \approx 1.05\%$. This limitation provides two benefits. First, as an assumption, no plastic deformations are visible in this region, and second, a reasonable number of data points is available for the identification.
2. Using finite element simulations of the tensile specimen in the aforementioned limited strain region, the simulated force-displacements curves are created corresponding to the data set depending on the specific temperature and degree

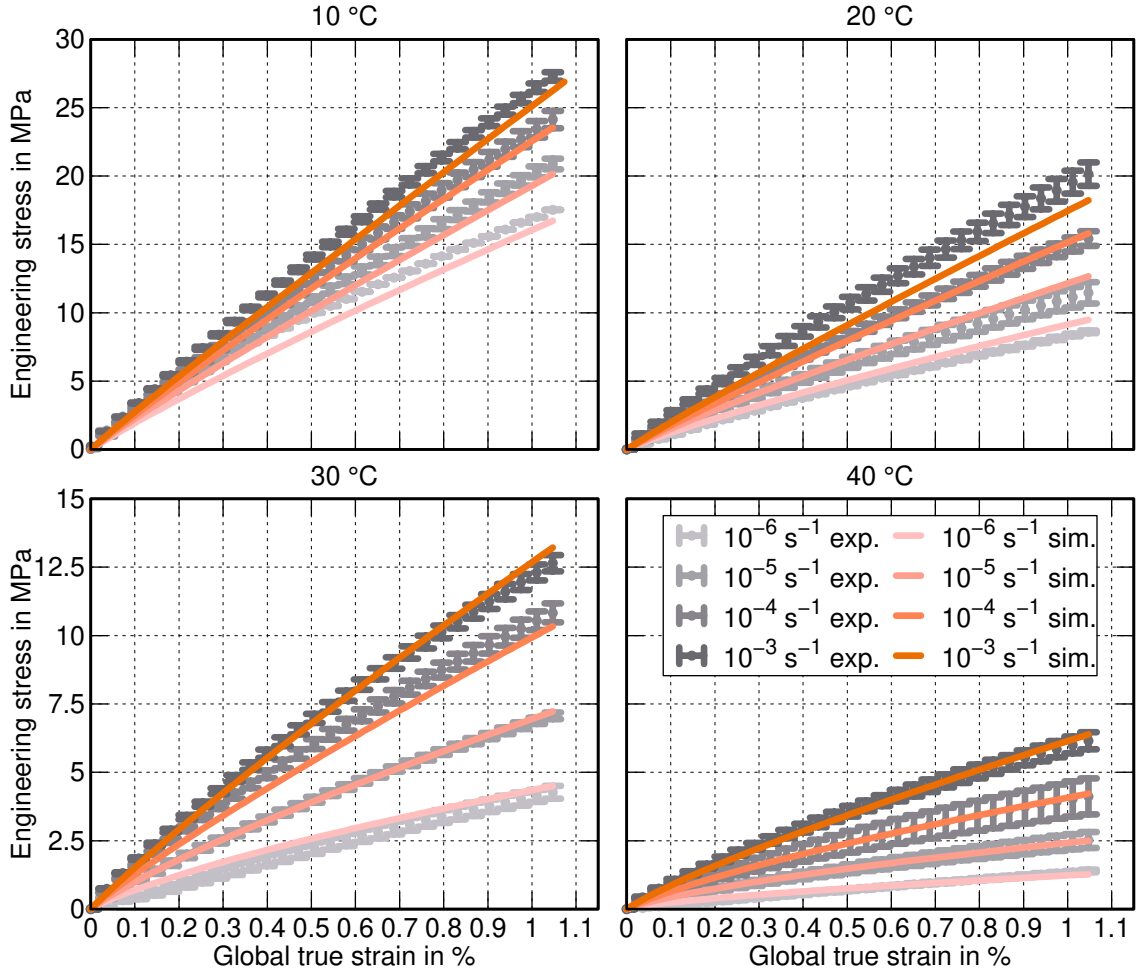


Figure 4.10. Comparison between the experimental and simulated curves of the tensile tests in the reversible domain for $c = 1.0$. The ordinate values are bisected in the plots of the second row.

of cure. All four considered strain rates are taken into account for each data set.

3. Then, by using LS-OPT[®] and SRSIM as optimization tool, the bulk modulus is individually identified for each data set by means of minimizing the sum of the mean squared errors calculated between the simulated and experimental curves. All individual mean squared errors contribute by the same weight factors.

As a result, this procedure yields different values for the bulk modulus depending on the chosen temperatures and degrees of cure. Afterwards, a suitable equation representing these dependencies has to be developed and its parameters must be identified by minimizing the error between the identified bulk moduli and the developed equation describing the aforementioned dependencies.

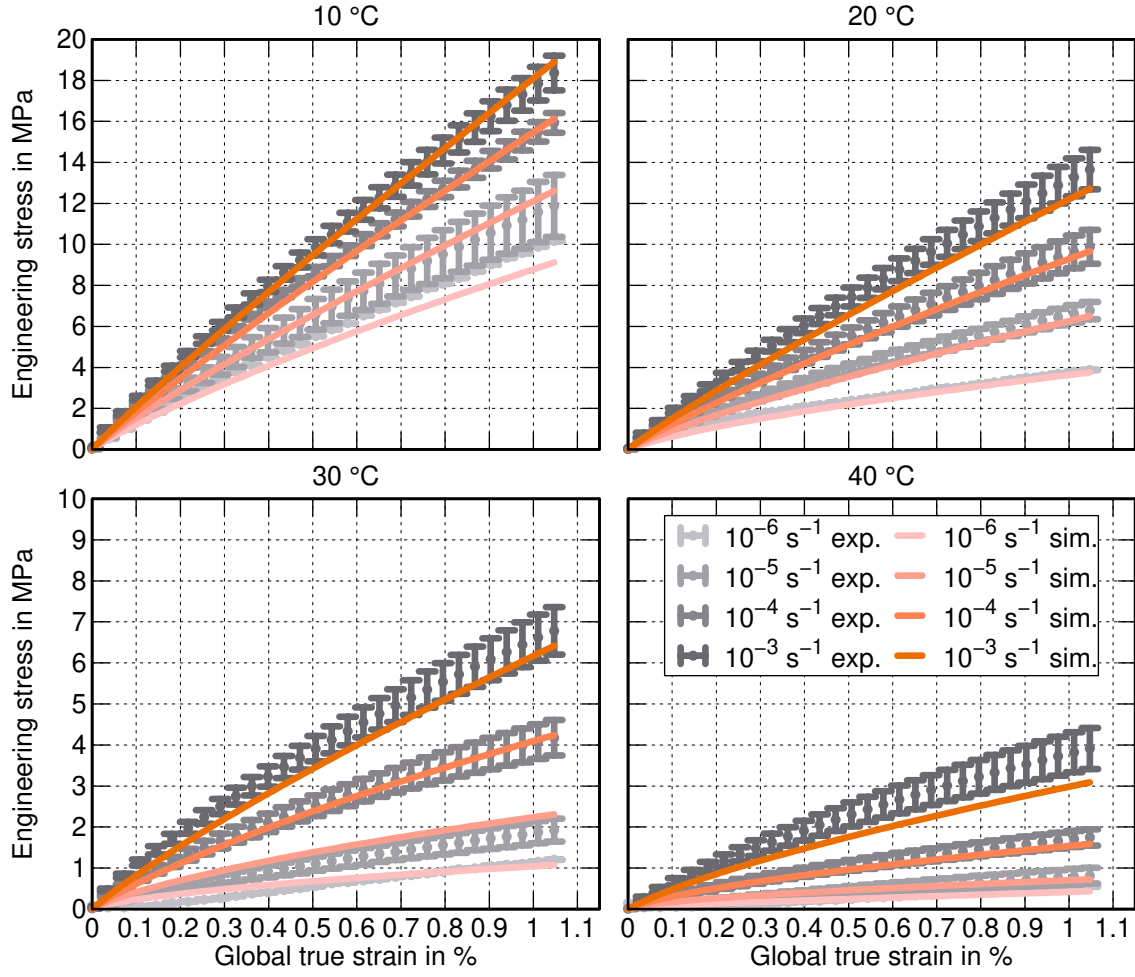


Figure 4.11. Comparison between the experimental and simulated curves of the tensile tests in the reversible domain for $c = 0.9193$. The ordinate values are bisected in the plots of the second row.

The identified values of the bulk modulus are visualized in fig. 4.13 for each chosen temperature and degree of cure. Additionally, figs. 4.10 - 4.12 show a good accordance between the experimental and simulated stress-strain curves.

A suitable constitutive equation to describe the bulk modulus depending on the temperature and the degree of cure is given by

$$K(\theta, c) = (K_0 \tanh(-K_1(\theta - \theta_R)) + K_2) s_{c, \text{bulk}}(c) . \quad (4.10)$$

Herein, K_0 , K_1 , and K_2 are model parameters. The function $s_{c, \text{bulk}}(c)$ represents the dependency on the degree of cure. The reference temperature is set to $\theta_R = 20$ °C. First, the parameters K_0 , K_1 , and K_2 are identified by means of the identified bulk moduli for $c_{\text{eff}} = 1.0$. Then, the parameters K_0 , K_1 , and K_2 are kept constant

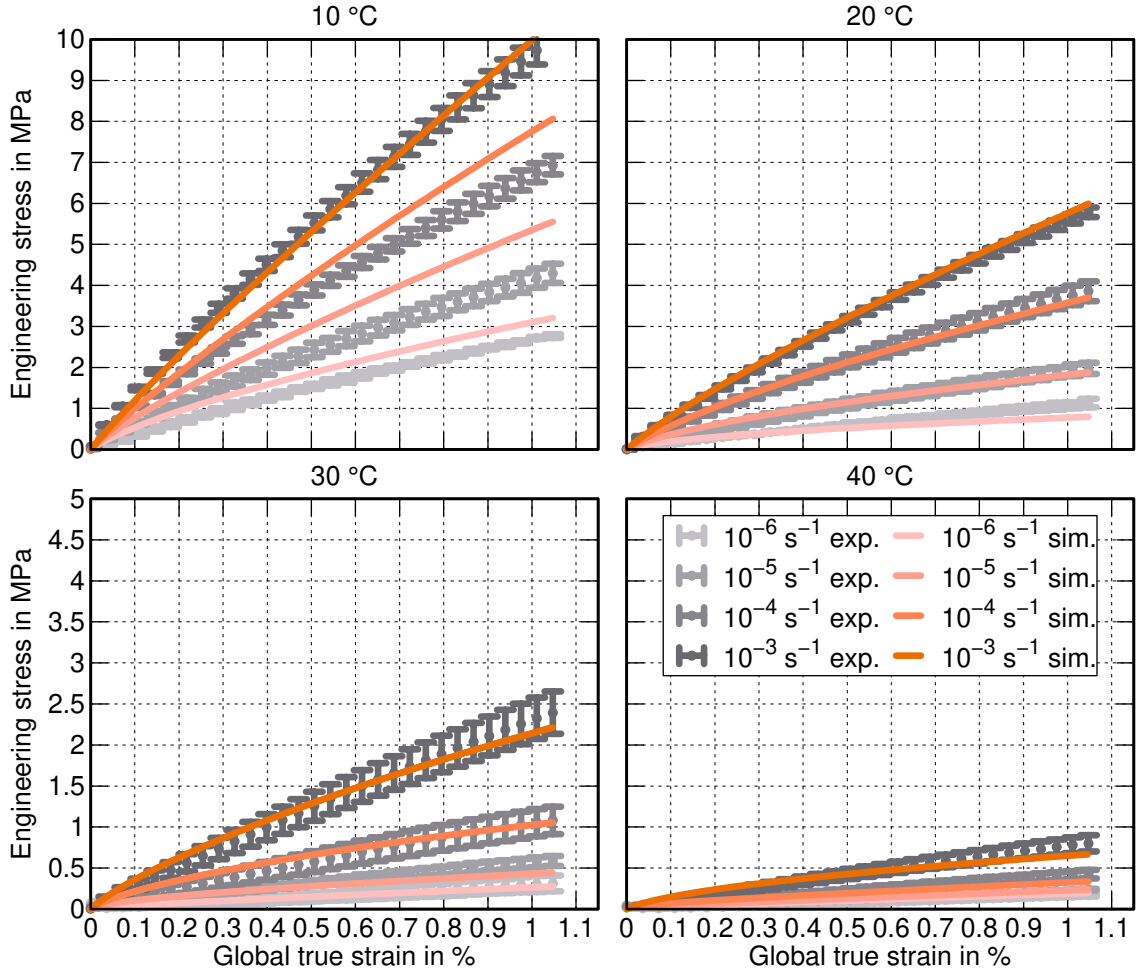


Figure 4.12. Comparison between the experimental and simulated curves of the tensile tests in the reversible domain for $c = 0.8606$. The ordinate values are bisected in the plots of the second row.

and the shift factors are identified for $c_{\text{eff}} = 0.9193$ and $c_{\text{eff}} = 0.8606$, respectively. The identified parameters and shift factors are listed in table 4.6. Fig. 4.13 shows the comparison between the identified values of the bulk moduli and the fit function according to eq. (4.10). The tensile properties of only three different crosslinking

Table 4.6. Parameters of the function of the temperature- and degree of cure-dependent bulk modulus and corresponding shift factors

Parameter	K_0	K_1	K_2
Value	1414.04 MPa	$0.102801 \text{ } ^\circ\text{C}^{-1}$	2420.25 MPa
Degree of cure c_{eff} in -	1.0	0.9193	0.8606
Shift factor $s_{c,\text{bulk}}$ in -	1.0	0.662814	0.290974

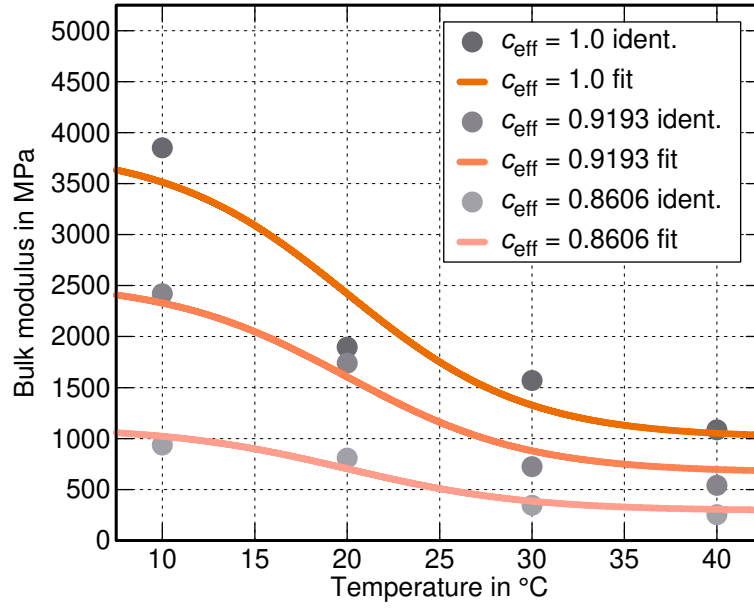


Figure 4.13. Comparison between the identified values of the bulk moduli for each temperature and degree of cure and the fit function eq. (4.10) by means of the parameters of table 4.6

states are investigated in this thesis, which complicates the derivation of a suitable function $s_{c,\text{bulk}}(c)$. Hence, the individual shift factors in the last row of table 4.6 are used for the identification of the viscoplastic parameters in sec. 4.3.3 and for the validation in sec. 4.4.

4.3.3 Parameters of the viscoplastic part of the material model

After finishing the identification procedure for the temperature- and degree of cure-dependent bulk modulus, the parameters of the viscoplastic part of the material model must be identified.

For the sake of simplicity, the isotropic hardening function in eq. (3.97) is restricted to the linear case. Hence, the parameters κ_0 and κ_1 representing the saturation yield stress do not influence the hardening behavior. Restricting the isotropic hardening function to the linear case significantly reduces the number of the parameters of the viscoplastic part of the material model and allows for a better interpretation of the identified values. LS-OPT[®], in conjunction with the SRSSM, is applied again to identify the parameters of the viscoplastic part of the material model by means of simulated tensile tests. The parameter set comprises

- the initial yield stress $Y_0(\theta, c)$,
- the hardening modulus $H_0(\theta, c)$,

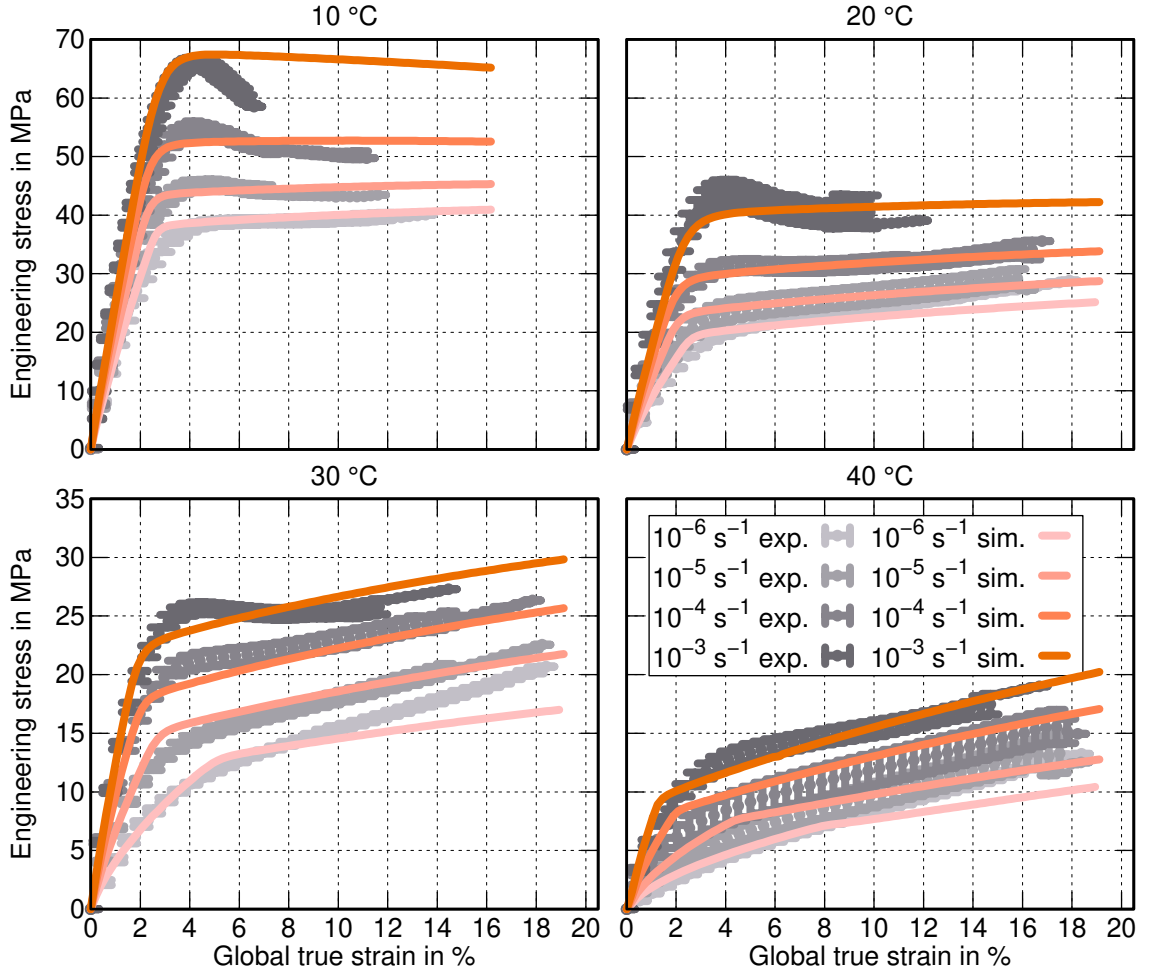


Figure 4.14. Comparison between the experimental and simulated results of the tensile tests for $c_{\text{eff}} = 1.0$. The ordinate values are bisected in the plots of the second row.

- the viscoplastic relaxation time $\tau_{\text{vp}}(\theta, c)$, and
- the exponent $m_{\text{vp}}(\theta, c)$.

The same finite element model as in sec. 4.3.1 is used for the simulations. During the identification process, all measurements with the same temperature and degree of cure are taken into account, which results in four objectives for each identification. At first, since $\theta_{\text{R}} = 20 \text{ °C}$ and $c_{\text{eff,R}} = 1.0$ are considered as the reference temperature and reference degree of cure, the parameters of the list mentioned above are identified by means of the tensile tests in fig. 2.36. Next, the identified value of $m_{\text{vp}} = 3.94971$ is kept constant, and only the viscoplastic relaxation time is considered as the only temperature- and degree of cure-dependent parameter of the viscoplastic flow rule. Then, the parameters are identified by means of the tensile tests subjected to temperatures lower and higher than the reference temperature

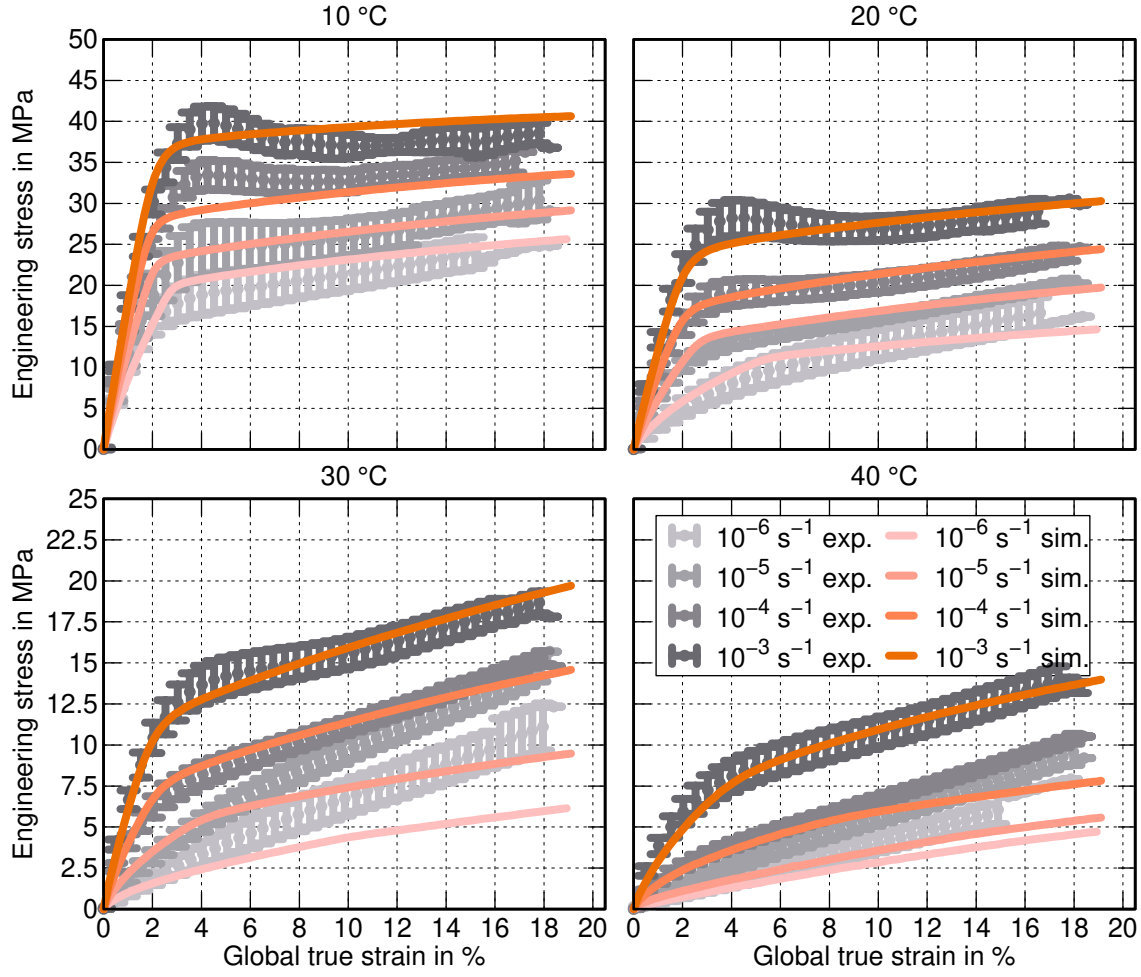


Figure 4.15. Comparison between the experimental and simulated tensile tests for $c_{\text{eff}} = 0.9193$. The ordinate values are bisected in the plots of the second row.

$$\theta_{\text{R}} = 20 \text{ }^{\circ}\text{C}.$$

Fig. 4.14 shows the comparison between the experimental and simulated results of the tensile tests subjected to monotonic loading for $c_{\text{eff}} = 1.0$. The corresponding identified values of the parameters are visualized in the figs. 4.17 - 4.19. Overall, good accordance is achieved by the viscoplastic material model and the identified parameters. Furthermore, using the interpolation of the bulk modulus by means of eq. (4.13) does not cause large deviations. Particular attention should be paid to the simulations at $\theta = 10 \text{ }^{\circ}\text{C}$ in the viscoplastic domain. One could easily interpret the slight decrease of the engineering stress as some kind of damage or softening behavior. However, this behavior is caused by the inhomogeneously distributed stresses and the localization of the plastic strains in the tensile specimen.

Subsequently, the initial yield stress, the hardening modulus, and the viscoplastic

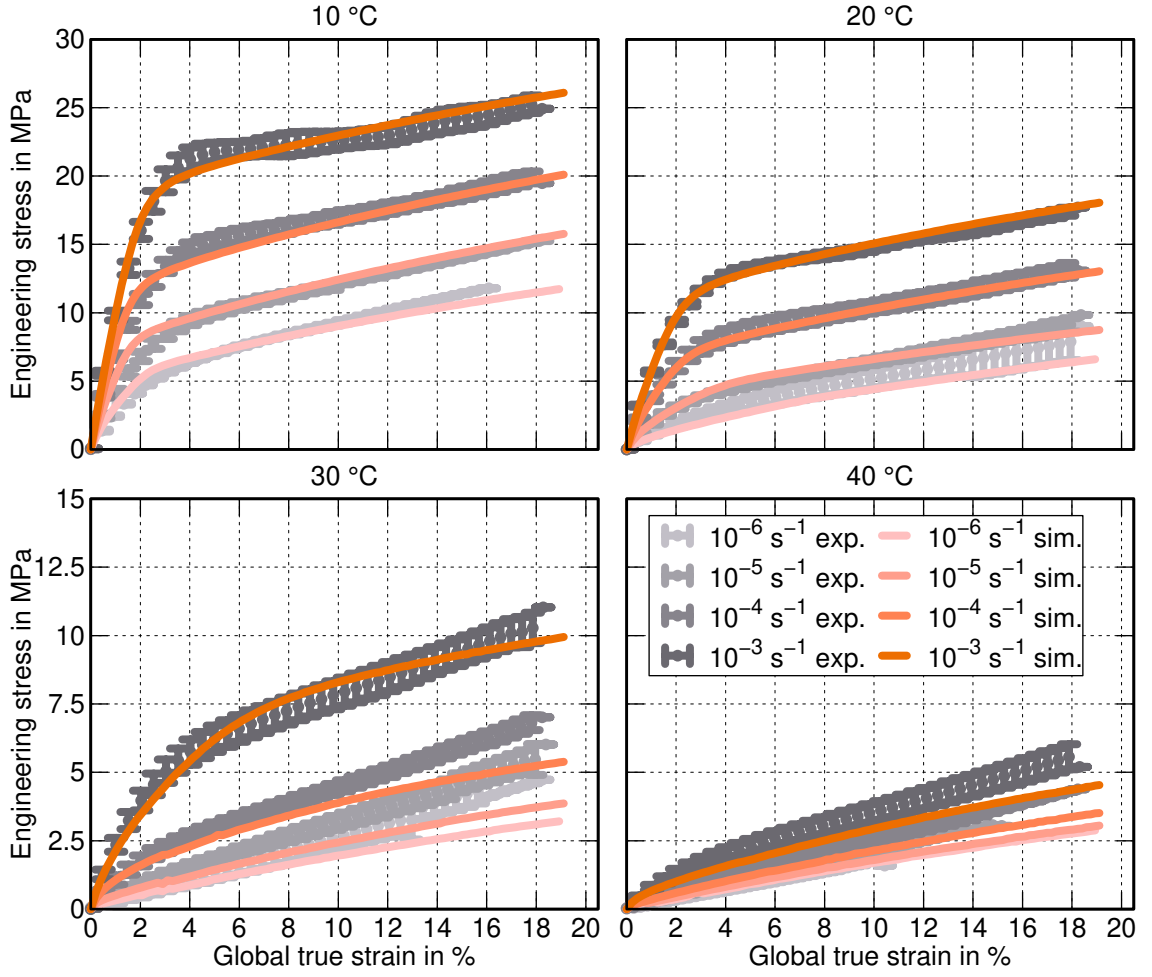


Figure 4.16. Comparison between the experimental and simulated tensile tests for $c_{\text{eff}} = 0.8606$. The ordinate values are bisected in the plots of the second row.

relaxation time are individually identified for each combination of temperature and degree of cure. The results of the simulations are displayed in the figs. 4.15 and 4.16, and the corresponding values of the material functions are shown in the figs. 4.17 - 4.19. Again, good accordance is achieved between the measurements and the simulations.

Unfortunately, considering the simulations with $\dot{\epsilon}_{\text{global}} = 10^{-6} \text{ s}^{-1}$ and $\dot{\epsilon}_{\text{global}} = 10^{-5} \text{ s}^{-1}$, the stress responses of the tensile tests at $\theta = 30 \text{ }^{\circ}\text{C}$ and $\theta = 40 \text{ }^{\circ}\text{C}$ are too soft. One possible reason is the identified value of the hardening modulus, which might be too low to accurately represent the material behavior after the onset of plastic yielding. Since the identification is conducted taking into account all four experimental tensile tests at a specific temperature and degree of cure, the identified value of the hardening modulus might be higher if only the experimental tensile tests of the two lowest strain rates would be considered. Nonetheless, the identified

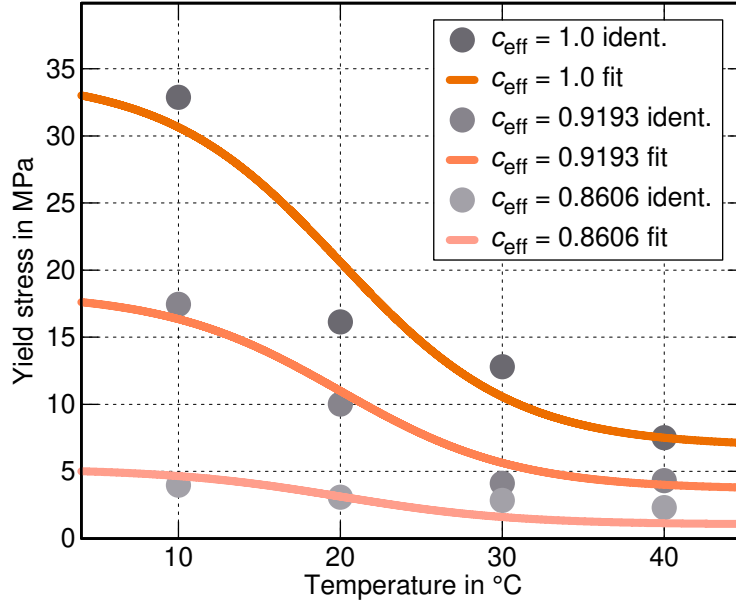


Figure 4.17. Comparison between the identified values of the initial yield stress and the fit function eq. (4.11) by means of the parameters in table 4.7

parameter set yields the lowest accumulated mean squared error. Another possible reason is the selection of the load cell for the tensile tests in sec. 2.5, whose accuracy is not high enough at low forces as measured in the tests. Thus, the measured force-displacement curve might be distorted.

After having identified distinct values for the aforementioned parameters at each chosen temperature and degree of cure, suitable model equations have to be formulated to accurately represent the dependencies on the temperature and the degree of cure. Starting with the initial yield stress $Y_0(\theta, c)$, a suitable approach is given by

$$Y_0(\theta, c) = (Y_{01} \tanh(-Y_{02}(\theta - \theta_R)) + Y_{03}) s_{c, \text{yield}}(c) . \quad (4.11)$$

This equation has the same structure as the function for the temperature- and degree of cure-dependent bulk modulus, cf. eq. (4.10). Again, the parameters Y_{01} , Y_{02} , and Y_{03} are identified by means of the values of the initial yield stress for $c_{\text{eff}} = 1.0$. Next, the shift factors $s_{c, \text{yield}}$ are individually determined through the identified values of the initial yield stress at $c_{\text{eff}} = 0.9193$ and $c_{\text{eff}} = 0.8606$, respectively.

The same procedure is applied for the interpolation function of the viscoplastic relaxation time:

$$\log_{10}(\tau_{\text{vp}}(\theta, c)) = (\tau_{\text{vp}0} \tanh(-\tau_{\text{vp}1}(\theta - \theta_R)) + \tau_{\text{vp}2}) s_{c, \text{relax}}(c) . \quad (4.12)$$

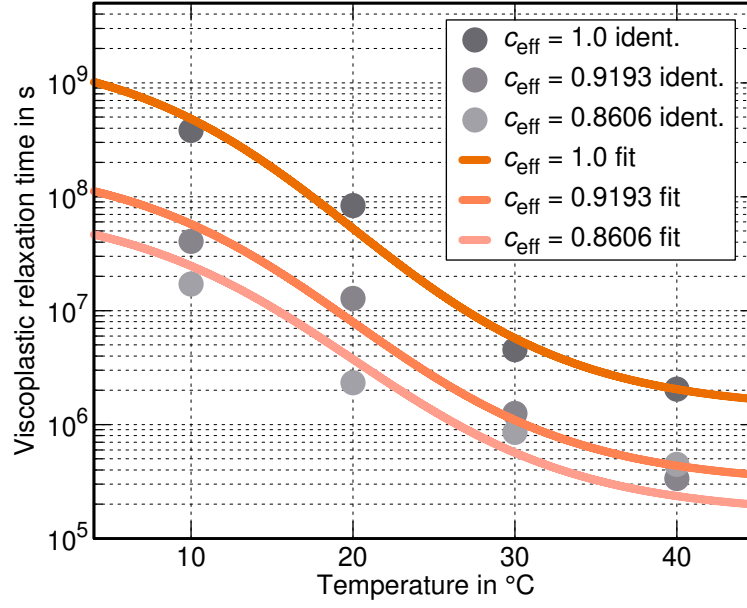


Figure 4.18. Comparison between the identified values of the viscoplastic relaxation time and the fit function eq. (4.12) by means of the parameters in table 4.7

Since the viscoplastic relaxation time rapidly decreases with increasing temperature, the identified values and the interpolation function are visualized in a semi-logarithmic plot in fig. 4.18. The corresponding parameters are also listed in table 4.7.

Last but not least, the identified values of the hardening modulus must be analyzed. Unfortunately, no clear tendency regarding the degree of cure is as visible as for the values of the initial yield stress and the viscoplastic relaxation time, see fig. 4.19.

However, the hardening modulus increases with increasing temperature. Hence, the hardening modulus is only dependent on the temperature, and the interpolation function is governed by

$$H_0(\theta) = H_{01} \tanh(-H_{02}(\theta - \theta_R)) + H_{03} . \quad (4.13)$$

The parameters H_{01} , H_{02} , and H_{03} are determined considering the mean value of the identified values of the hardening modulus at each temperature. Using the values listed in table 4.7 leads to an apparent linear progression of the hardening modulus in the considered temperature range. Although the identified value for H_{01} is negative, the function based on eq. (4.13) returns positive values starting at ≈ 60 MPa for $\theta = 10$ °C.

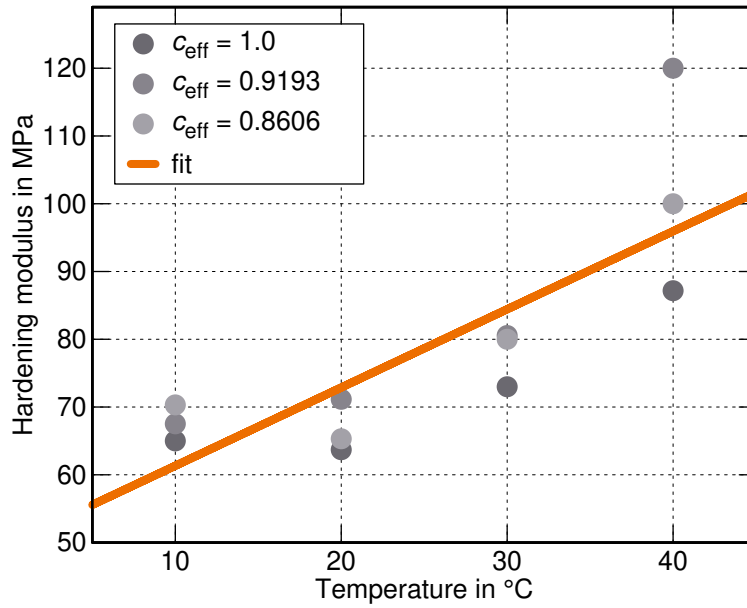


Figure 4.19. Comparison between the identified values of the hardening modulus and the fit function eq. (4.12) by means of the parameters in table 4.7

In summary, introducing the eqs. (4.11) - (4.13) fully describes the remaining parameters of ch. 3. Analogously to the bulk modulus, suitable functions are only missing for the degree of cure-dependent shift factors $s_{c,\text{yield}}$ and $s_{c,\text{relax}}$. Using the distinct values of the shift factors in table 4.7 again follows the argumentation that the material behavior is only investigated in a limited range of the degree of cure. In the following section, all introduced model equations are employed to conduct simulations of the cyclic loading and unloading tests of sec. 2.5.2. These simulations serve as a validation of the suitability of the proposed model approaches and the accuracy of the parameter identification strategy.

4.4 Validation by means of tensile specimens subjected to cyclic loading and unloading

After finishing the identification of all parameters describing the viscoelastic and viscoplastic behavior of the investigated photopolymer, the suitability of the model and the accuracy of the parameter identification strategy are assessed through simulations of the tensile tests subjected to cyclic loading and unloading. Therefore, the only input parameters of the material model are the temperature and the degree of cure of the individual specimen. As previously discussed, the individual shift factors $s_{c,\text{bulk}}$, $s_{c,\text{yield}}$, and $s_{c,\text{relax}}$ are not interpolated by additional functions.

For this purpose, the recorded displacement curves of the individual measurements

Table 4.7. Parameters of the functions of the temperature- and degree of cure-dependent initial yield stress, viscoplastic relaxation time, and hardening modulus and the corresponding shift factors

Parameter	Y_{01}	Y_{02}	Y_{03}
Value	13.751 MPa	0.09284 °C ⁻¹	20.609 MPa
Parameter	τ_{vp0}	τ_{vp1}	τ_{vp2}
Value	1.593	0.06996 °C ⁻¹	7.72
Parameter	H_{01}	H_{02}	H_{03}
Value	-294.304 MPa	0.00393 °C ⁻¹	72.875 MPa
Degree of cure c_{eff} in -	1.0	0.9193	0.8606
Shift factor $s_{c,\text{yield}}$ in -	1.0	0.5336	0.1519
Shift factor $s_{c,\text{relax}}$ in -	1.0	0.8936	0.8514

(see right columns of the figs. 2.39 - 2.41) are applied as the time-dependent boundary condition to the upper rigid part of the finite element model of the tensile specimen, see fig. 4.9. The measured reaction forces of the tensile specimens are compared with the simulations by means of the corresponding stress-strain curves. The main objectives are the accurate representation of the measured hystereses and both the minima and maxima of the reaction forces.

First, the simulation results of the tensile specimens with $c_{\text{eff}} = 1.0$ are considered in fig. 4.20. Since the tensile specimen of the measurement with $\theta = 10$ °C broke at the end of the eighth loading cycle ($\varepsilon_{\text{true,global}} \approx 7.5$ %), the corresponding simulation is stopped at the end of the eighth loading cycle.

The lower temperature $\theta = 10$ °C of the specimen compared to the reference temperature yields a stiffer response, which is captured well by the material model in the first three loading and unloading cycles. At the end of the third unloading cycle, the resulting engineering stress becomes negative, i.e., the specimen is compressed at the end of the unloading cycle. In the following cycles, the simulated hystereses are smaller than the measured ones. Moreover, the residual stresses at the end of the unloading cycles increase with progressing load. The mutual interaction of the inelastic and viscoplastic strains complicates the identification of the reason for this phenomenon. By definition, the viscoplastic strain does not increase during the unloading cycle. Therefore, the overstress represented by the dashpot in the viscoplastic part of the rheological network in fig. 3.6 relaxes. Similarly, the dashpots of the generalized MAXWELL model in the rheological network ensure that the

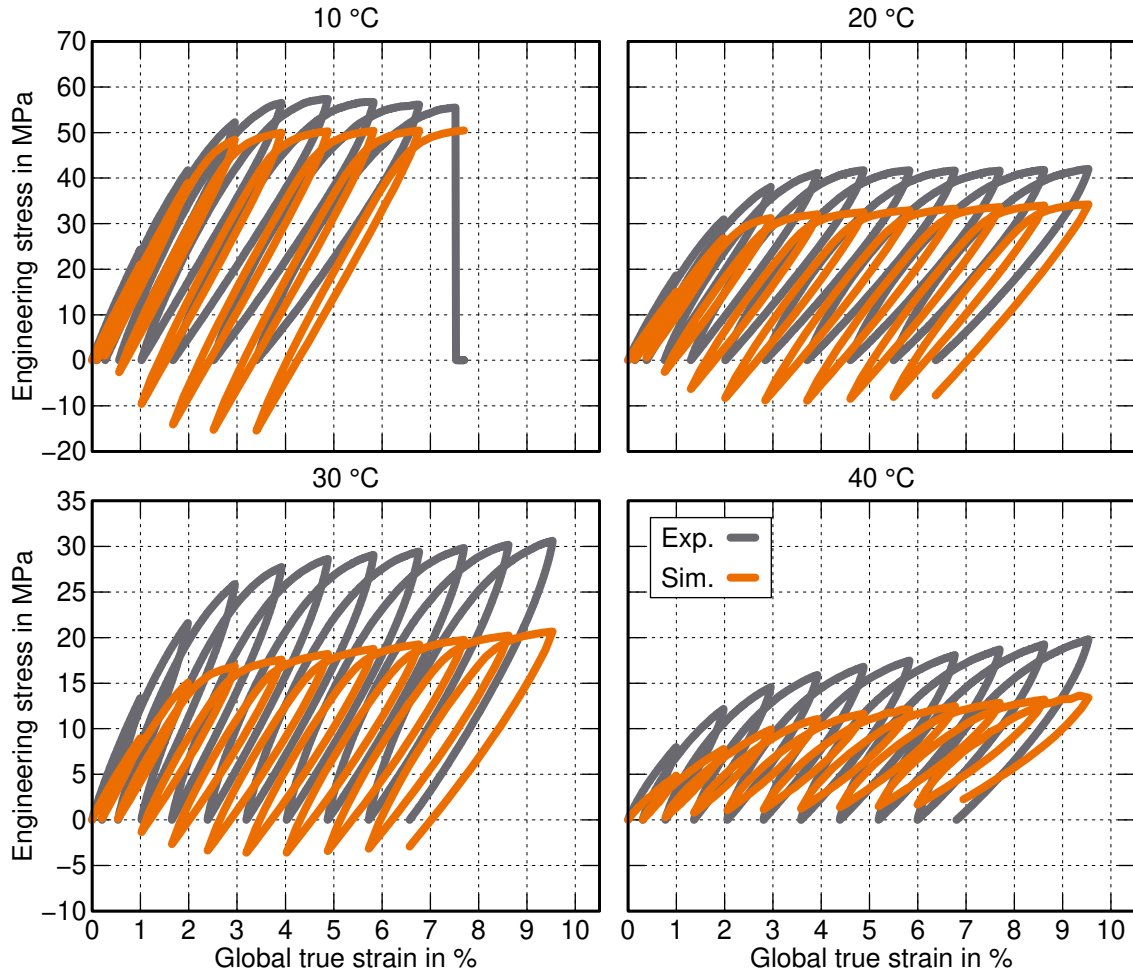


Figure 4.20. Comparison between the experimental and simulated curves of the tensile tests subjected to cyclic loading and unloading for $c_{\text{eff}} = 1.0$. The ordinate values are bisected in the plots of the second row.

stresses in the MAXWELL elements do not change proportionally to the displacement boundary condition during the unloading cycles. Thus, it is obvious that the resulting stress-strain curve is caused by the interaction of the viscoelastic and viscoplastic parts of the material model. Apart from that, the maxima at the end of the loading cycles are well captured, taking into account the general deviation of the experiments.

The same phenomena are visible in the simulations at higher temperatures. However, the maxima at the end of the loading cycles are more underestimated for $\theta = 30\text{ °C}$ and $\theta = 40\text{ °C}$. Furthermore, considering the simulation with $\theta = 40\text{ °C}$, the minima at the end of the unloading cycles are well captured.

Fig. 4.21 shows the simulation results compared to the experiments of the specimens with $c_{\text{eff}} = 0.9193$. Overall, better accordance than in fig. 4.20 is achieved by

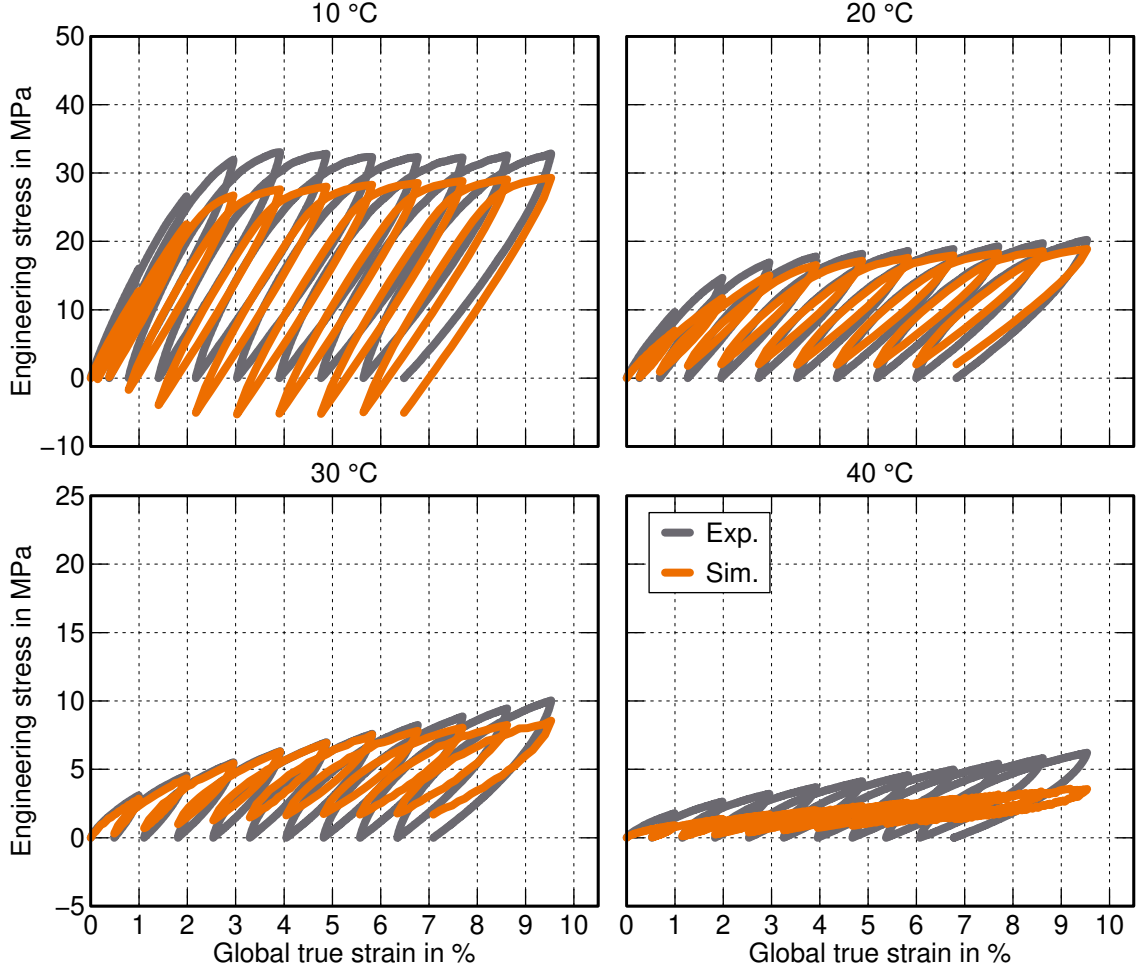


Figure 4.21. Comparison between the experimental and simulated curves of the tensile tests subjected to cyclic loading and unloading for $c_{\text{eff}} = 0.9193$. The ordinate values are bisected in the plots of the second row.

using the model approaches and identified parameters. Especially, the stress-strain curves of the measurements with $\theta = 20^\circ\text{C}$ and $\theta = 30^\circ\text{C}$ are well captured. Again, residual stresses are present at the end of each unloading cycle. Particular attention should be paid to the non-smoothness of the curves at $\theta = 30^\circ\text{C}$ and $\theta = 40^\circ\text{C}$, which is an indication of the imprecision of the backward EULER scheme for the integration of the inelastic strains, see eqs. (3.76) and (3.77). Thus, higher-order integration schemes would be more appropriate.

Last but not least, fig. 4.22 shows the comparison between the simulated and experimental results of the cyclic tensile tests for $c_{\text{eff}} = 0.8606$. Acceptable accordance is achieved for $\theta = 10^\circ\text{C}$ and $\theta = 20^\circ\text{C}$. Comparatively, the simulation at $\theta = 30^\circ\text{C}$ cannot represent the measured hystereses. The same applies to the simulation at $\theta = 40^\circ\text{C}$ whereby the measured values appear at least questionable due to the

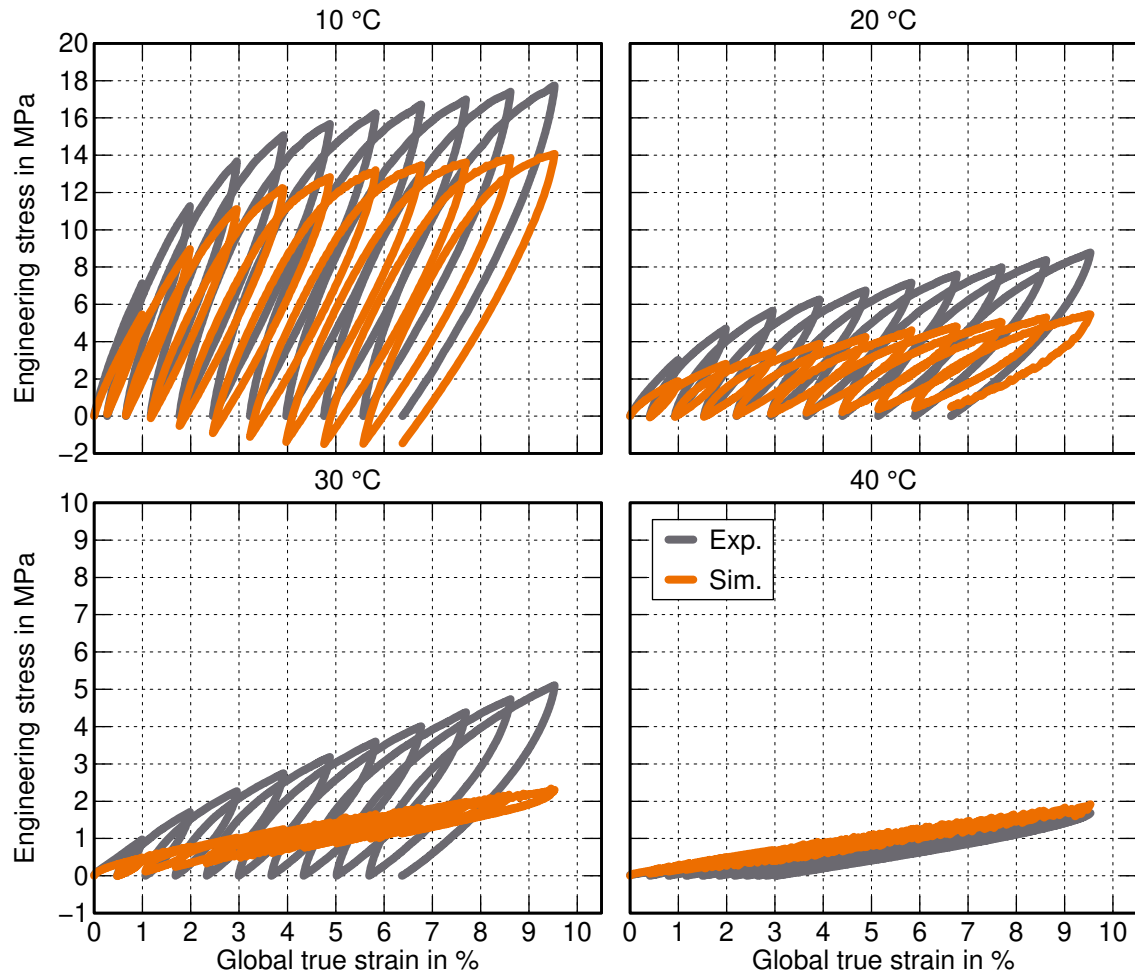


Figure 4.22. Comparison between the experimental and simulated curves of the tensile tests subjected to cyclic loading and unloading for $c_{\text{eff}} = 0.8606$. The ordinate values are bisected in the plots of the second row.

sensitivity of the employed load cell.

As a result, the conducted simulations prove the general applicability of the proposed model equations and the parameter identification strategy. Nevertheless, room for improvement always exists by considering more sophisticated model approaches, even though they may be difficult to understand.

5 Conclusion and Outlook

In the present thesis, a material model is developed for the description of the crosslinking process of photopolymers used in additive manufacturing processes. Employing the concept of continuum mechanics, the total deformation is separated into mechanical, thermal, and chemical parts. The developed model describe both the temperature- and degree of cure-dependent viscoelastic and the viscoplastic material behavior of the photopolymer at hand. For this purpose, time-temperature and time-cure superposition principles are applied.

Furthermore, the material model is discretized and implemented as a material subroutine into the commercial finite element program LS-DYNA® in order to conduct three-dimensional simulations. However, the conducted simulations are only restricted to the purely mechanical case and constant conversion states of the photopolymer. Overall, good accordance is achieved between the experiments and simulations by means of the developed model equations and the identified values for the parameters.

Photo-DSC measurements are conducted for the experimental characterization of the crosslinking progress. As a result, the temperature of the photopolymer has a more substantial influence on the crosslinking speed than the irradiance. Therefore, considerable efficiency gains regarding the print job duration can be obtained by increasing the temperature of the photopolymer. Additionally, this phenomenon is confirmed by an innovative experimental method for the determination of temperature-dependent working curves. A conventional rheometer is modified in order to record the viscoelastic properties depending on the crosslinking progress. Unfortunately, the quality of the measurements contain room for improvement. However, the measurements show the expected qualitative development of the viscoelastic properties upon irradiation.

Last but not least, the tensile tests show that the temperature and the degree of cure have a strong influence on the material properties of printed parts. Considering the tensile tests subjected to cyclic loading and unloading, viscoelastic and viscoplastic deformations overlap each other.

Naturally, the conducted investigations do not cover all of the arisen questions.

Primarily, no simulations considering the shrinkage of the photopolymer layer are conducted in this thesis. Therefore, simulations should be conducted taking into account the coupling between the mechanical, thermal, and chemical parts of the material model in order to predict the chemical shrinkage and potential residual stresses. Additionally, the heat generation caused by the exothermic crosslinking reaction could be investigated.

Furthermore, the thermomechanical consistency of the material model should be proven in order to avoid unphysical behavior of the model.

Although three different conversion states of the photopolymer are investigated in the tensile tests, the underlying database can be easily extended by testing more specimens with lower degrees of cure. For this purpose, one can also change the chosen layer thickness, exposure time, and irradiance during the printing process. This would also give insight into the dependencies of the tensile behavior on the mentioned printing parameters. Following this, the introduced equations describing the temperature- and degree of cure-dependent parameters can be extended to a broader range of possible conversion states and temperatures.

A Identified values of the shear moduli and relaxation times

Table A.1. Identified values of the shear moduli G_k and relaxation times τ_{kR}

Shear moduli G_k in MPa					
G_1 1.025	G_2 1.308	G_3 2.548	G_4 0.4937	G_5 13.13	G_6 30.39
G_7 63.74	G_8 110.9	G_9 159.2	G_{10} 165.3	G_{11} 110.7	G_{12} 17.92
G_{13} 117.7	G_{14} 149.7	G_{15} 94.7	G_{16} 183.1	G_{17} 90.99	G_{18} 75.64
G_{19} 114.2	G_{20} 3.989	G_{21} 43.69	G_{22} 50.71	G_{23} 19.17	G_{24} 70.69
G_{25} 131.3	G_{26} 30.74	G_{27} 227.4	G_{28} 86.35	G_{29} 49.87	G_{30} 135.9
Relaxation times τ_{kR} in s					
τ_{1R} $4.17 \cdot 10^{12}$	τ_{2R} $1.95 \cdot 10^{10}$	τ_{3R} $1.04 \cdot 10^9$	τ_{4R} $2.23 \cdot 10^8$	τ_{5R} $5.11 \cdot 10^7$	τ_{6R} $9.21 \cdot 10^6$
τ_{7R} $1.09 \cdot 10^6$	τ_{8R} $1.16 \cdot 10^5$	τ_{9R} $7.74 \cdot 10^3$	τ_{10R} $1.13 \cdot 10^2$	τ_{11R} $7.59 \cdot 10^2$	τ_{12R} $3.39 \cdot 10^0$
τ_{13R} $7.29 \cdot 10^0$	τ_{14R} $9.62 \cdot 10^{-1}$	τ_{15R} $5.18 \cdot 10^{-2}$	τ_{16R} $6.50 \cdot 10^{-3}$	τ_{17R} $5.36 \cdot 10^{-5}$	τ_{18R} $1.08 \cdot 10^{-5}$
τ_{19R} $4.64 \cdot 10^{-7}$	τ_{20R} $3.11 \cdot 10^{-8}$	τ_{21R} $5.70 \cdot 10^{-8}$	τ_{22R} $1.03 \cdot 10^{-9}$	τ_{23R} $2.05 \cdot 10^{-10}$	τ_{24R} $6.84 \cdot 10^{-11}$
τ_{25R} $8.27 \cdot 10^{-13}$	τ_{26R} $1.78 \cdot 10^{-13}$	τ_{27R} $1.27 \cdot 10^{-14}$	τ_{28R} $6.10 \cdot 10^{-16}$	τ_{29R} $1.98 \cdot 10^{-16}$	τ_{30R} $2.81 \cdot 10^{-17}$

Bibliography

- 3D Systems, Inc. (2017). ProX™ 950 User Guide. Manual, accessed: 2022-04-22. http://infocenter.3dsystems.com/product-library/sites/default/files/printers/prox950/guides/40-D063%20%20ProX%20950%20User%20Guide_Rev%20F.pdf. (Cited on page 4)
- Adolf, D. and Martin, J. E. (1996). Calculation of Stresses in Crosslinking Polymers. *Journal of Composite Materials*, 30(1):13–34. (Cited on pages 117 and 119)
- Agnelli, F., Constantinescu, A., and Nika, G. (2020). Design and testing of 3D-printed micro-architected polymer materials exhibiting a negative Poisson's ratio. *Continuum Mechanics and Thermodynamics*, 32(2):433–449. (Cited on page 10)
- Agnelli, F., Tricarico, M., and Constantinescu, A. (2021). Shape-shifting panel from 3D printed undulated ribbon lattice. *Extreme Mechanics Letters*, 42:101089. (Cited on page 10)
- atum3D (2022). DLP STATION 5-405. Brochure, accessed: 2022-04-22. https://www.atum3d.com/includes/pdf/products/atum3D_DLP_Station_5-405.pdf. (Cited on page 6)
- Bachmann, J., Schmölzer, S., Ruderer, M. A., Fruhmann, G., and Hinrichsen, O. (2021). Photo-differential scanning calorimetry parameter study of photopolymers used in digital light synthesis. *SPE Polymers*, 3(1):41–53. (Cited on page 9)
- Belytschko, T., Liu, W. K., Moran, B., and Elkhodary, K. I. (2014). *Nonlinear Finite Elements for Continua and Structures*. John Wiley & Sons, Ltd. (Cited on pages 79 and 98)
- Bennett, J. (2017). Measuring UV curing parameters of commercial photopolymers used in additive manufacturing. *Additive Manufacturing*, 18:203–212. (Cited on pages 9 and 41)
- Bergman, T. L. and Lavine, A. S. (2017). *Fundamentals of Heat and Mass Transfer*. John Wiley & Sons, Inc. (Cited on page 15)
- Betten, J. (2001). *Kontinuumsmechanik*. Springer Verlag Berlin Heidelberg. (Cited on page 87)
- Binmore, K. and Davies, J. (2001). *Calculus: Concepts and Methods*. Cambridge University Press, New York. (Cited on page 106)

- Bizjak-Bayer, T. (2021). Qioptiq Photonics GmbH & Co. KG. Personal communication on 2021-06-23. (Cited on page 36)
- Brennesholtz, M. S. and Stupp, E. H. (2008). *Projection Displays*. John Wiley & Sons. (Cited on page 6)
- Bröcker, C. (2013). *Materialmodellierung für die simultane Kalt-/Warmumformung auf Basis erweiterter rheologischer Modelle*. Dissertation. (Cited on pages 86 and 97)
- Burbulla, F. (2015). *Kontinuumsmechanische und bruchmechanische Modelle für Werkstoffverbunde*. Dissertation, University of Kassel. (Cited on page 87)
- Carbon, Inc. (2021). Introducing adidas 4dfwd. Accessed: 2022-04-21. <https://www.carbon3d.com/adidas-4dfwd/>. (Cited on pages 10 and 153)
- Cheah, C., Fuh, J., Nee, A., and Lu, L. (1999). Mechanical characteristics of fiber-filled photo-polymer used in stereolithography. *Rapid Prototyping Journal*, 5(3):112–119. (Cited on page 11)
- Claesson, H., Malmström, E., Johansson, M., Hult, A., Doyle, M., and Månson, J.-A. E. (2002). Rheological behaviour during UV-curing of a star-branched polyester. *Progress in Organic Coatings*, 44(1):63–67. (Cited on page 33)
- Cole, K. C. (1991). A new approach to modeling the cure kinetics of epoxy/amine thermosetting resins. 1. mathematical development. *Macromolecules*, 24(11):3093–3097. (Cited on page 73)
- da Silva Bartolo, P. J. (2007). Photo-curing modelling: direct irradiation. *The International Journal of Advanced Manufacturing Technology*, 32:480–491. (Cited on pages 10 and 74)
- Dall’Argine, C., Hochwallner, A., Klikovits, N., Liska, R., Stampf, J., and Sangermano, M. (2020). Hot-Lithography SLA-3D Printing of Epoxy Resin. *Macromolecular Materials and Engineering*, 305:2000325. (Cited on page 8)
- Danley, R. L. (2003). New heat flux DSC measurement technique. *Thermochimica Acta*, 395(1):201–208. (Cited on pages 15, 16 and 153)
- Darsono, N., Mizunuma, H., and Obara, H. (2011). Rheological study of the solidification of photopolymer and dispersed nanotube systems. *Applied Rheology*, 21(6):63566. (Cited on page 33)
- de Souza Neto, E. A., Perić, D., and Owen, D. R. J. (2008). *Computational Methods for Plasticity: Theory and Applications*. John Wiley & Sons Ltd. (Cited on page 98)
- Diani, J. and Gilormini, P. (2017). On necessary precautions when measuring solid polymer linear viscoelasticity with dynamic analysis in torsion. *Polymer Testing*, 63:275–280. (Cited on page 51)

- DIN EN ISO 527-2:2012 (2012). Kunststoffe – Bestimmung der Zugeigenschaften – Teil 2: Prüfbedingungen für Form- und Extrusionsmassen. Technical report, DIN Deutsches Institut für Normung e. V. (Cited on pages 60 and 155)
- Dr. Hönle AG (2020). UV-LED vs. konventionelle UV-Technologie. Brochure, accessed: 2020-07-29. <https://www.hoenle.de/hoenle.de/pdfs/produktbroschueren/de/uv-vs-led-d.pdf>. (Cited on page 18)
- Eom, Y., Boogh, L., Michaud, V., Sunderland, P., and Manson, J.-A. (2000). Time-Cure-Temperature Superposition for the Prediction of Instantaneous Viscoelastic Properties During Cure. *Polymer Engineering and Science*, 40(6):1281–1292. (Cited on pages 116, 117 and 120)
- Excelitas Technology Corp. (2014a). OmniCure R2000 Radiometer. Brochure, accessed: 2020-07-16. https://www.excelitas.com/de/file-download/download/public/56646?filename=OmniCure_R2000_UV_Radiometer_Brochure.pdf. (Cited on page 36)
- Excelitas Technology Corp. (2014b). OmniCure S2000. Brochure, accessed: 2020-07-16. https://www.excelitas.com/file-download/download/public/55911?filename=__OmniCure_S2000_Brochure.pdf. (Cited on pages 19 and 153)
- Findley, W. N., Lai, J. S., and Onaran, K. (1976). *Creep and Relaxation of viscoelastic materials*. Dover Publications. (Cited on page 92)
- Flory, P. J. (1961). Thermodynamic relations for high elastic materials. *Trans. Faraday Soc.*, 57:829–838. (Cited on page 84)
- Formlabs (2021). Form 3L: Large-format Low Force Stereolithography (LFS)TM 3D printer. Manual, accessed: 2022-04-22. <https://media.formlabs.com/m/5f0ed4f707037528/original/-ENUS-Form-3L-Manual.pdf>. (Cited on page 4)
- Fournier, J., Williams, G., Duch, C., and Aldrige, G. A. (1996). Changes in Molecular Dynamics during Bulk Polymerization of an Epoxide-Amine System As Studied by Dielectric Relaxation Spectroscopy. *Macromolecules*, 29:7097–7107. (Cited on page 73)
- Frick, A. and Stern, C. (2013). *DSC-Prüfung in der Anwendung*. Carl Hanser Verlag. (Cited on page 15)
- Gibson, I., Rosen, D., and Stucker, B. (2015). *Additive Manufacturing Technologies: 3D Printing, Rapid Prototyping, and Direct Digital Manufacturing*. Springer Science+Business Media New York. (Cited on pages 1 and 3)
- Gross, D. and Seelig, T. (2011). *Bruchmechanik*. Springer Verlag Berlin Heidelberg. (Cited on page 87)
- Hartmann, S. (2003). *Finite-Elemente Berechnung inelastischer Kontinua*. Habilitation, University of Kassel. (Cited on page 84)

- Haupt, P. (2002). *Continuum Mechanics and Theory of Materials*. Springer-Verlag Berlin Heidelberg. (Cited on pages 71, 72, 76 and 97)
- Healy, B. E. and Dodds, R. H. (1992). A large strain plasticity model for implicit finite element analyses. *Computational Mechanics*, 9:95–112. (Cited on page 86)
- Henkel Corp. (2019). LOCTITE® 3D 3818 Technical Data Sheet. (Cited on page 14)
- Higham, A. K., Bonino, C. A., Raghavan, S. R., and Khan, S. A. (2014). Photo-activated ionic gelation of alginate hydrogel: real-time rheological monitoring of the two-step crosslinking mechanism. *Soft Matter*, 10:4990–5002. (Cited on page 33)
- Höhne, G. W. H., Hemminger, W. F., and Flammersheim, H.-J. (2003). *Differential Scanning Calorimetry*. Springer-Verlag Berlin Heidelberg. (Cited on pages 14, 15 and 30)
- Holman, J. P. (2010). *Heat Transfer*. McGraw-Hill. (Cited on page 15)
- Holzapfel, G. (2001). *Nonlinear Solid Mechanics. A Continuum Approach for Engineering*. John Wiley & Sons. (Cited on pages 71, 76 and 87)
- Hossain, M. (2010). *Modellierung und Simulation der Aushärtung von Polymeren*. Dissertation, Friedrich-Alexander-Universität Erlangen-Nürnberg. (Cited on page 72)
- Hossain, M. and Liao, Z. (2020). An additively manufactured silicone polymer: Thermo-viscoelastic experimental study and computational modelling. *Additive Manufacturing*, 35:101395. (Cited on page 10)
- Hossain, M., Navaratne, R., and Perić, D. (2020). 3D printed elastomeric polyurethane: Viscoelastic experimental characterizations and constitutive modelling with nonlinear viscosity functions. *International Journal of Non-Linear Mechanics*, 126:103546. (Cited on page 10)
- Hossain, M., Possart, G., and Steinmann, P. (2009a). A finite strain framework for the simulation of polymer curing. Part I: elasticity. *Computational Mechanics*, 44:621–630. (Cited on page 78)
- Hossain, M., Possart, G., and Steinmann, P. (2009b). A small-strain model to simulate the curing of thermosets. *Computational Mechanics*, 43:769–779. (Cited on page 78)
- Hossain, M., Possart, G., and Steinmann, P. (2010). A finite strain framework for the simulation of polymer curing. Part II. Viscoelasticity and shrinkage. *Computational Mechanics*, 46:363–375. (Cited on page 78)
- Itskov, M. (2015). *Tensor Algebra and Tensor Analysis for Engineers*. Springer International Publishing AG Switzerland. (Cited on page 104)

- Jacobs, P. F. (1992). *Rapid Prototyping and Manufacturing: Fundamentals of Stereolithography*. Society of Manufacturing Engineers. (Cited on page 9)
- Jalocha, D., Constantinescu, A., and Nevriere, R. (2015). Revisiting the identification of generalized Maxwell models from experimental results. *International Journal of Solids and Structures*, 67-68:169–181. (Cited on page 112)
- Jones, D. I. G. (2001). *Handbook of Viscoelastic Vibration Damping*. John Wiley & Sons Ltd. (Cited on page 49)
- Kaiser, W. (2006). *Kunststoffchemie für Ingenieure*. Carl Hanser Verlag München Wien. (Cited on page 2)
- Kamal, M. R. (1974). Thermoset Characterization for Moldability Analysis. *Polymer Engineering and Science*, 14(3):231–239. (Cited on page 72)
- Khan, S. A., Plitz, I. M., and Frantz, R. A. (1992). In situ technique for monitoring the gelation of UV curable polymers. *Rheologica Acta*, 31:151–160. (Cited on page 33)
- Kim, Y. C., Hong, S., Sun, H., Kim, M. G., Choi, K., Cho, J., Choi, H. R., Koo, J. C., Moon, H., Byun, D., Kim, K. J., Suhr, J., Kim, S. H., and Nam, J.-D. (2017). UV-curing kinetics and performance development of in situ curable 3D printing materials. *European Polymer Journal*, 93:140–147. (Cited on page 9)
- Kloosterboer, J. G. and Lijten, G. F. C. M. (1990). Photopolymers exhibiting a large difference between glass transition and curing temperatures. *Polymer*, 31:95–101. (Cited on page 30)
- Kok, S. and Stander, N. (1999). Optimization of a sheet metal forming process using successive multipoint approximations. *Structural Optimization*, 18:277–295. (Cited on page 109)
- Kolmeder, S. (2016). *Thermomechanical-chemically coupled Material Modelling and Computational Fluid Dynamics Simulation of Adhesives in Medicine*. Dissertation, University of the Bundeswehr Munich. (Cited on pages 79 and 80)
- Koseki, K., Sakamaki, H., and Jeong, K.-M. (2013). In situ Measurement of Shrinkage Behavior of Photopolymers. *Journal of Photopolymer Science and Technology*, 26:567–572. (Cited on page 10)
- Krawietz, A. (1986). *Materialtheorie: mathematische Beschreibung des phänomenologischen thermomechanischen Verhaltens*. Springer-Verlag Berlin Heidelberg. (Cited on page 91)
- Krödel, S., Li, L., Constantinescu, A., and Daraio, C. (2017). Stress relaxation in polymeric microlattice materials. *Materials & Design*, 130:433–441. (Cited on page 10)
- Landgraf, R. (2015). *Modellierung und Simulation der Aushärtung polymerer Werkstoffe*. Dissertation, Technische Universität Chemnitz. (Cited on page 79)

- Lange, J. (1999). Viscoelastic properties and transitions during thermal and uv cure of a methacrylate resin. *Polymer Engineering & Science*, 39(9):1651–1660. (Cited on page 33)
- Lee, E. H. (1969). Elastic-Plastic Deformation at Finite Strains. *Journal of Applied Mechanics*, 36(1):1–6. (Cited on page 83)
- Lee, S. S., Luciani, A., and Manson, J.-A. E. (2000). A rheological characterisation technique for fast uv-curable systems. *Progress in Organic Coatings*, 38(3):193–197. (Cited on page 33)
- Liebl, C. (2014). *Viskoelastisch-Viskoplastische Modellierung von Strukturklebstoffen während der Aushärtung*. Dissertation, University of the Bundeswehr Munich. (Cited on pages 23 and 119)
- Ligon, S. C., Husár, B., Wutzel, H., Holman, R., and Liska, R. (2014). Strategies to Reduce Oxygen Inhibition in Photoinduced Polymerization. *Chemical Reviews*, 114(1):557–589. (Cited on page 8)
- Lion, A. (2000). *Thermomechanik von Elastomeren*. Habilitation, University of Kassel. (Cited on page 84)
- Lion, A. and Höfer, P. (2007). On the phenomenological representation of curing phenomena in continuum mechanics. *Arch. Mech.*, 59(1):59–89. (Cited on pages 79 and 80)
- Livermore Software Technology Corp. (2017). *LS-DYNA® Theory Manual*. Manual. (Cited on page 98)
- Lubliner, C. (2008). *Plasticity Theory*. Dover Publications Inc. (Cited on page 95)
- Lubliner, J. (1985). A model of rubber viscoelasticity. *Mechanics Research Communications*, 12(2):93 – 99. (Cited on page 84)
- Lührs, G. (1997). *Randwertaufgaben der Viskoplastizität*. Dissertation, University of Kassel. (Cited on page 97)
- Maffezzoli, A. and Terzi, R. (1998). Effect of irradiation intensity on the isothermal photopolymerization kinetics of acrylic resins for stereolithography. *Thermochimica Acta*, 321:111–121. (Cited on pages 9, 22 and 74)
- Malvern, L. E. (1969). *Introduction to the Mechanics of a Continuous Medium*. Prentice-Hall, Inc. (Cited on pages 71 and 76)
- Martin, B., Puentes, J., Wruck, L., and Osswald, T. A. (2018). Degree of cure of epoxy/acrylic photopolymers: Characterization with raman spectroscopy and a modified phenomenological model. *Polymer Engineering & Science*, 58(2):228–237. (Cited on page 9)
- Menard, K. P. and Menard, N. R. M. (2020). *Dynamic Mechanical Analysis*. CRC Press. (Cited on page 49)

- Menczel, J. D. and Prime, R. B. (2009). *Thermal Analysis of Polymers*. John Wiley & Sons, Inc. (Cited on pages 14, 22, 24, 28, 31 and 153)
- Menzel, S. (2011). *Zur Berechnung von Klebverbindungen hybrider Karosseriestrukturen beim Lacktrocknungsprozess*. Dissertation, Institut für Leichtbau und Kunststofftechnik, Technische Universität Dresden. (Cited on page 23)
- Mesago Messe Frankfurt GmbH (2021). formnext AM Field Guide compact 2021. Brochure. (Cited on pages 2, 5 and 153)
- Myers, R. H., Montgomery, D. C., and Anderson-Cook, C. M. (2016). *Response Surface Methodology*. John Wiley & Sons, Inc. (Cited on page 109)
- Nakamura, K. (2015). *Photopolymers: Photoresist Materials, Processes, and Applications*. Taylor & Francis Group. (Cited on page 2)
- Nika, G. and Constantinescu, A. (2019). Design of multi-layer materials using inverse homogenization and a level set method. *Computer Methods in Applied Mechanics and Engineering*, 346:388–409. (Cited on page 10)
- Obst, P., Riedelbauch, J., Oehlmann, P., Rietzel, D., Launhardt, M., Schmölzer, S., Osswald, T. A., and Witt, G. (2020). Investigation of the influence of exposure time on the dual-curing reaction of rpu 70 during the dls process and the resulting mechanical part properties. *Additive Manufacturing*, 32:101002. (Cited on page 9)
- OECD (2016). *OECD Science, Technology and Innovation Outlook 2016*. OECD Publishing, Paris. (Cited on page 1)
- Opsytec Dr. Gröbel GmbH (2021). Digitales Radiometer RMD Pro. Brochure, accessed: 2021-09-27. https://www.opsytec.de/fileadmin/user_upload/products/downloads/Messgeraete/D_RMD.pdf. (Cited on page 35)
- Pappas, S. P. (1992). *Radiation Curing: Science and Technology*. Springer Science+Business Media. (Cited on pages 2 and 3)
- Park, J.-W., Shim, G.-S., Back, J.-H., Kim, H.-J., Shin, S., and Hwang, T.-S. (2016). Characteristic shrinkage evaluation of photocurable materials. *Polymer Testing*, 56:344–353. (Cited on page 10)
- Pedrotti, F. L., Pedrotti, L. S., Bausch, W., and Schmidt, H. (2005). *Optik für Ingenieure*. Springer-Verlag Berlin Heidelberg. (Cited on pages 18 and 19)
- Perzyna, P. (1963). The constitutive equations for rate sensitive plastic materials. *Quarterly of Applied Mathematics*, 20(4):321–332. (Cited on page 97)
- Pfaffinger, M. (2018). Hot Lithography - New Possibilities in Polymer 3D Printing: A newly developed stereolithography-based additive manufacturing technology combines good material properties with outstanding manufacturing precision. *Laser Technik Journal*, 15:45–47. (Cited on page 8)

- Plocher, J. and Panesar, A. (2019). Review on design and structural optimisation in additive manufacturing: Towards next-generation lightweight structures. *Materials & Design*, 183:108164. (Cited on page 1)
- Rehbein, T., Lion, A., Johlitz, M., and Constantinescu, A. (2020). Experimental investigation and modelling of the curing behaviour of photopolymers. *Polymer Testing*, 83:106356. (Cited on page 9)
- Rehbein, T., Lion, A., Johlitz, M., Sekmen, K., and Constantinescu, A. (2021). Temperature- and degree of cure-dependent viscoelastic properties of photopolymer resins used in digital light processing. *Progress in Additive Manufacturing*, 6:743–756. (Cited on pages 113 and 116)
- Rehbein, T. and Matzenmiller, A. (2018). Modelling and Finite Element Analysis of Viscoelastic Adhesive Joints. *Proceedings in Applied Mathematics and Mechanics*, 18:e201800237. (Cited on page 113)
- Rusu, M. C., Block, C., Van Assche, G., and Van Mele, B. (2012). Influence of temperature and uv intensity on photo-polymerization reaction studied by photodsc. *Journal of Thermal Analysis and Calorimetry*, 110:287–294. (Cited on pages 9 and 23)
- Schlotthauer, T., Nolan, D., and Middendorf, P. (2021). Influence of short carbon and glass fibers on the curing behavior and accuracy of photopolymers used in stereolithography. *Additive Manufacturing*, 42:102005. (Cited on page 11)
- Scholze, H. (1998). *Glas - Natur, Struktur und Eigenschaften*. Springer-Verlag Berlin Heidelberg. (Cited on page 34)
- Schwarzl, F. R. (1990). *Polymermechanik: Struktur und mechanisches Verhalten von Polymeren*. Springer-Verlag Berlin Heidelberg. (Cited on page 49)
- Scranton, A. B., Bowman, C. N., and Peiffer, R. W. (1997). *Photopolymerization: Fundamentals and Application*. American Chemical Society. (Cited on page 2)
- Simo, J. and Hughes, T. (1998). *Computational Inelasticity*. Springer New York. (Cited on pages 96, 98 and 100)
- Steyrer, B., Buseti, B., Harakály, G., Liska, R., and Stampfl, J. (2018). Hot Lithography vs. room temperature DLP 3D-printing of a dimethacrylate. *Additive Manufacturing*, 21:209–214. (Cited on page 8)
- Stratasys, Ltd. (2021). Hello Origin@One, goodbye tooling lead times. Brochure, accessed: 2022-04-22. https://www.stratasys.com/siteassets/3d-printers/prINTER-catalog/p3/origin-one-prINTER/br_p3_origin-one_0421a.pdf?v=4af256. (Cited on page 6)
- Szabo, I. (2001). *Höhere Technische Mechanik*. Springer-Verlag Berlin Heidelberg. (Cited on pages 51 and 155)

- Tartaglia, G. M., Mapelli, A., Maspero, C., Santaniello, T., Serafin, M., Farronato, M., and Caprioglio, A. (2021). Direct 3d printing of clear orthodontic aligners: Current state and future possibilities. *Materials*, 14(7). (Cited on page 11)
- TA[®] Instruments (2019). Photocalorimeter Accessory for Discovery DSC Getting Started Guide. Manual. (Cited on page 20)
- TA[®] Instruments (2021). Discovery Hybrid Rheometers: Temperature Systems and Accessories. Brochure, accessed: 2022-04-04. <https://www.tainstruments.com/wp-content/uploads/BROCH-DHR-Accessories.pdf>. (Cited on pages 33 and 154)
- Taylor, R. L., Pister, K. S., and Goudreau, G. L. (1970). Thermomechanical Analysis of Viscoelastic Solids. *Int. J. for Numerical Methods in Engineering*, 2:45–49. (Cited on page 91)
- Truesdell, C. and Noll, W. (2004). *The Non-Linear Field Theories of Mechanics*. Springer-Verlag Berlin Heidelberg. (Cited on pages 71, 76 and 79)
- Tryson, G. R. and Shultz, A. R. (1979). A Calorimetric Study of Acrylate Photopolymerization. *Journal of Polymer Science Part B: Polymer Physics*, 17:2059–2075. (Cited on pages 9 and 74)
- Tumbleston, J. R., Shirvanyants, D., Ermoshkin, N., Janusziewicz, R., Johnson, A. R., Kelly, D., Chen, K., Pinschmidt, R., Rolland, J. P., Ermoshkin, A., Samulski, E. T., and DeSimone, J. M. (2015). Continuous liquid interface production of 3D objects. *Science*, 347(6228):1349–1352. (Cited on page 8)
- Watanabe, K., Amari, T., and Otsubo, Y. (1984). Dynamic viscoelastic measurements of photosensitive polymers. *Journal of Applied Polymer Science*, 29(1):57–66. (Cited on page 33)
- Weeger, O., Boddeti, N., Yeung, S.-K., Kaijima, S., and Dunn, M. (2019). Digital design and nonlinear simulation for additive manufacturing of soft lattice structures. *Additive Manufacturing*, 25:39 – 49. (Cited on page 10)
- Wenzel, M. (2005). *Spannungsbildung und Relaxationsverhalten bei der Aushärtung von Epoxidharzen*. Dissertation, Technical University of Darmstadt. (Cited on page 23)
- Westbeek, S., Remmers, J., van Dommelen, J., and Geers, M. (2020). Multi-scale process simulation for additive manufacturing through particle filled vat photopolymerization. *Computational Materials Science*, 180:109647. (Cited on page 10)
- Westbeek, S., Remmers, J., van Dommelen, J., Maalderink, H., and Geers, M. (2021). Prediction of the deformed geometry of vat photo-polymerized components using a multi-physical modeling framework. *Additive Manufacturing*, 40:101922. (Cited on page 10)

- Williams, M. L., Landel, R. F., and Ferry, J. D. (1955). The Temperature Dependence of Relaxation Mechanisms in Amorphous Polymers and Other Glass-forming Liquids. *Journal of the American Chemical Society*, 77:3701–3707. (Cited on page 115)
- Winter, H. H. and Chambon, F. (1986). Analysis of linear viscoelasticity of a crosslinking polymer at the gel point. *Journal of Rheology*, 30(2):367–382. (Cited on page 118)
- Wriggers, P. (2008). *Nonlinear Finite Element Methods*. Springer-Verlag Berlin Heidelberg. (Cited on pages 98 and 100)
- Wu, J., Zhao, Z., Hamel, C. M., Mu, X., Kuang, X., Guo, Z., and Qi, H. J. (2018). Evolution of material properties during free radical photopolymerization. *Journal of the Mechanics and Physics of Solids*, 112:25–49. (Cited on page 10)
- Xu, A., Langefeld, B., Erharder, M., and Kourkejian, V. (2020). Polymer additive manufacturing – market today and in the future. Accessed: 2022-03-09. <https://www.rolandberger.com/en/Insights/Publications/Polymer-additive-manufacturing-Market-today-and-in-the-future.html>. (Cited on page 3)
- Yagimli, B. (2013). *Kontinuumsmechanische Betrachtung von Aushärtvorgängen*. Dissertation, University of the Bundeswehr Munich. (Cited on pages 79 and 80)
- Ye, S., Cramer, N. B., and Bowman, C. N. (2011). Relationship between glass transition temperature and polymerization temperature for cross-linked photopolymers. *Macromolecules*, 44:490–494. (Cited on page 29)
- Zienkiewicz, O. C., Taylor, R. L., and Zhu, J. Z. (2013). *The Finite Element Method: Its Basis & Fundamentals*. Butterworth-Heinemann. (Cited on page 98)

List of Tables

2.1	Evaluated specific reaction heats depending on the specimen mass . .	25
2.2	Measured irradiances of the OmniCure® S2000 curing system using the 405 ± 10 nm filter at the end of the light guide and on the top surface of the quartz glass plate	36
2.3	Parameters of the identified working curves in fig. 2.20 including standard errors	44
2.4	Resulting degrees of cure of the pokerchip-specimens depending on the individual exposure time	56
4.1	Parameters of the model equation of the degree of cure identified by means of the experimental data of sec. 2.2.3	110
4.2	Identified values of the parameters of the modified working curve model	111
4.3	Identified shift factors $s_c(c)$ and equilibrium shear moduli $G_\infty(c)$. .	115
4.4	Calculated effective degrees of cure $c_{\text{eff,gel}}$ at the gel point depending on the temperature	119
4.5	Identified values of the parameters of the eqs. (4.6) and (4.7)	120
4.6	Parameters of the function of the temperature- and degree of cure- dependent bulk modulus and corresponding shift factors	125
4.7	Parameters of the functions of the temperature- and degree of cure- dependent initial yield stress, viscoplastic relaxation time, and hard- ening modulus and the corresponding shift factors	133
A.1	Identified values of the shear moduli G_k and relaxation times τ_{kR} . .	139

List of Figures

1.1	Additive manufacturing processes for the fusion of polymers in the powdery and solid state [Mesago Messe Frankfurt GmbH, 2021] . . .	2
1.2	Schematics of material jetting and stereolithography [Mesago Messe Frankfurt GmbH, 2021]	5
1.3	Cross-sectional schematic of a DLP™ additive manufacturing device .	6
1.4	Images of selected slices of the printed sphere in fig. 1.3 (support structures are neglected). The stair-like approximation of the edges is caused by the resolution of the DMD™.	7
1.5	Schematic diagram of the working curve equation	8
1.6	Adidas® 4DFWD running shoe with additively manufactured midsole [Carbon, Inc., 2021]	10
2.1	Cross-sectional view of the Tzero™ sensor of the TA® Instruments Q2000 DSC (derived from and inspired by [Danley, 2003])	16
2.2	Experimental setup of the photo-DSC	18
2.3	Diagram of the spectral flux (grey) of the high pressure mercury vapor lamp of the OmniCure® S2000 curing system without the internal 320 - 500 nm bandpass filter (derived from [Excelitas Technology Corp., 2014b]) and relative transmittance of the additional 405 ± 10 nm bandpass filter (orange)	19
2.4	Resulting diagram of the spectral flux of the high pressure mercury vapor lamp of the OmniCure® S2000 curing system using the additional 405 ± 20 nm bandpass filter	20
2.5	Schematic cross-sectional view of the DSC measurement cell with installed photo-DSC extension and vertically aligned light guides . . .	21
2.6	Schematic diagram of a typical photo-DSC measurement using two subsequent runs (inspired by [Menczel and Prime, 2009])	22
2.7	Diagrams of the specific differential heat flow depending on the specimen mass	24

2.8	Excerpt of the measured specific differential heat flows \dot{q} of the first and second runs of each combination of temperature and irradiance. The temperature label in the first plot of each row indicates the temperature of all plots in the same row.	27
2.9	Photo-DSC measurement for the determination of the total specific heat of reaction h_{tot} . Left: exothermic peak of reaction in the first 30 seconds upon opening the shutter. Right: heating segment after ten minutes of isothermal irradiation. The slight decrease of the heat flow signal at $t = 600$ s is caused by the temperature control of the device.	28
2.10	Computed curves of the degree of cure depending on temperature and irradiance	29
2.11	Reversing specific differential heat flow of the MDSC [®] measurement for the identification of the glass transition temperature in the fully cured state. The glass transition is indicated by the orange circle. . .	30
2.12	Isobaric specific heat capacity depending on the temperature for the uncured and fully cured state of the photopolymer	31
2.13	Setup of the DHR-30 rheometer incorporating the OmniCure [®] S2000 curing system	32
2.14	Cross-sectional view of the UV light guide assembly motivated by [TA [®] Instruments, 2021]	33
2.15	Detailed view of the UV rheometry setup	34
2.16	Spectral sensitivity of the UVA+ sensor and the emission spectrum of the OmniCure [®] S2000 curing system in conjunction with the 405 ± 10 nm filter	35
2.17	Left top: kinematic relation between the twist $\varphi(t)$ and shear strain $\gamma(t)$ of the photopolymer layer. Left bottom: graphical visualization of the phase shift between the shear strain $\gamma(t)$ and the shear stress $\tau(t)$. Right: progress of crosslinking in the photopolymer layer. . . .	37
2.18	Increase of the shear storage modulus G' as a consequence of progressing crosslinks in the photopolymer layer at different constant temperatures and angular frequencies	39
2.19	Schematic of the measurement for the determination of temperature-dependent working curves and the different states of the photopolymer layer	42
2.20	Experimentally determined exposure doses and identified working curves. The critical exposure doses are identified by the intersection of the extrapolations (dotted lines) with the abscissa.	43

2.21	Experimentally determined chemical shrinkage strain for $C_d(0) = 200 \mu\text{m}$	46
2.22	Experimentally determined chemical shrinkage strain for $C_d(0) = 300 \mu\text{m}$	46
2.23	Experimentally determined chemical shrinkage strain for $C_d(0) = 400 \mu\text{m}$	47
2.24	Experimentally determined chemical shrinkage strain for $C_d(0) = 500 \mu\text{m}$	47
2.25	Experimentally determined chemical shrinkage strain for $C_d(0) = 600 \mu\text{m}$	48
2.26	Experimentally determined chemical shrinkage strain for $C_d(0) = 700 \mu\text{m}$	48
2.27	Schematic visualization of the time-temperature superposition	50
2.28	Left: schematic representation of the rectangular specimen used in the DMA tests and its boundary conditions applied by the steel clamps. Right: shear stress distribution in the cross-section of the specimen (inspired by [Szabo, 2001]).	51
2.29	Poker chip-shaped specimens with different heights for the determination of the degree of cure of the specimens used in the DMA tests. The hatching in each specimen indicates the individual layers.	53
2.30	Measured specific heat flows \dot{q} of the poker chip-shaped specimens . .	55
2.31	Excerpt of the isothermal curves of the DMA tests of the investigated specimens	57
2.32	Resulting master curves of the DMA tests of the investigated specimens	58
2.33	Shift factors s_θ for the generation of the master curves in fig. 2.32 . .	59
2.34	Geometry of the printed tensile specimens according to [DIN EN ISO 527-2:2012, 2012]	60
2.35	Schematic of the orientation of the printed specimens on the build plate. The individual hatching indicates the layer orientation in each individual specimen.	61
2.36	Experimental force-displacement curves of the tensile specimens with $c_{\text{eff}} = 1.0$ subjected to monotonic loading. The ordinate values are bisected in the plots of the second row.	62
2.37	Experimental force-displacement curves of the tensile specimens with $c_{\text{eff}} = 0.9193$ subjected to monotonic loading. The ordinate values are bisected in the plots of the second row.	63

2.38	Experimental force-displacement curves of the tensile specimens with $c_{\text{eff}} = 0.8606$ subjected to monotonic loading. The ordinate values are bisected in the plots of the second row.	64
2.39	Left column: experimental force-displacement curves of the tensile specimens with $c_{\text{eff}} = 1.0$ subjected to cyclic loading and unloading ($\dot{\epsilon}_{\text{global}} = 10^{-4} \text{ s}^{-1}$). Right column: corresponding global displacement plotted versus time. The ordinate values of the plots in the left column are bisected in the lower two rows.	66
2.40	Left column: experimental force-displacement curves of the tensile specimens with $c_{\text{eff}} = 0.9193$ subjected to cyclic loading and unloading ($\dot{\epsilon}_{\text{global}} = 10^{-4} \text{ s}^{-1}$). Right column: corresponding global displacement plotted versus time. The ordinate values of the plots in the left column are bisected in the lower two rows.	67
2.41	Left column: experimental force-displacement curves of the tensile specimens with $c_{\text{eff}} = 0.8606$ subjected to cyclic loading and unloading ($\dot{\epsilon}_{\text{global}} = 10^{-4} \text{ s}^{-1}$). Right column: corresponding global displacement plotted versus time. The ordinate values of the plots in the left column are bisected in the lower two rows.	68
3.1	Identified critical exposure doses and penetration depths of the working curves as shown in table 2.3	75
3.2	Motion of the material body \mathcal{B}	77
3.3	Graphical representation of the configurations corresponding to the multiplicative decomposition of the deformation gradient in eq. (3.26)	82
3.4	Graphical representation of the configurations corresponding to the multiplicative decomposition of the deformation gradient in eq. (3.47)	83
3.5	Graphical representation of the configurations corresponding to the multiplicative decomposition of the deformation gradient in eq. (3.48)	86
3.6	Rheological network of the proposed decomposition considering viscoelastic and viscoplastic deformations as well as thermal expansion/contraction and chemical shrinkage	89
3.7	Schematic representation of the VON MISES yield criterion in the I_1 - $\sqrt{J_2}$ space without hardening effects. I_1 is the trace (first invariant) of the CAUCHY stress tensor \mathbf{T}	96
3.8	Summary of the algorithm for the computation of the viscoelastic-viscoplastic material model	105

4.1	Comparison between experimental curves generated by photo-DSC measurements and simulated curves by means of eq. (3.5) and the parameters enlisted in table 4.1	110
4.2	Left: modified working curve model based on eq. (3.7). Right: temperature-dependent critical exposure dose and penetration depth based on eqs. (3.8) and (3.9).	111
4.3	Schematic comparison between the mean squared logarithmic error (MSLE) and the mean squared error (MSE) for random, logarithmically distributed simulated values y_{sim} and fixed experimental values $y_{\text{exp}} = 10^1 \dots 10^4$. For a better comparison, the absolute MSE and MSLE values are divided by the maximum values $\text{MSE}_{\text{max}} = 9990^2$ and $\text{MSLE}_{\text{max}} = 9$	113
4.4	Comparison between the experimentally derived shear storage moduli G'_{exp} and the simulated shear storage moduli G'_{sim} by means of the parameters enlisted in table A.1	114
4.5	Shift factors of the time-temperature superposition (cf. fig. 2.33) and fit function according to eq. (4.2)	115
4.6	Development of the effective degree of cure c_{eff} in the rheometry measurements during crosslinking calculated by eq. (4.3)	117
4.7	Experimentally derived shear storage modulus depending on the degree of cure, temperature, and angular frequency	118
4.8	Left: degree of cure-dependent equilibrium shear modulus $G_{\infty}(c)$. Right: shift factors $s_c(c)$ for the time-cure superposition.	120
4.9	Finite element model of the tensile specimen	122
4.10	Comparison between the experimental and simulated curves of the tensile tests in the reversible domain for $c = 1.0$. The ordinate values are bisected in the plots of the second row.	123
4.11	Comparison between the experimental and simulated curves of the tensile tests in the reversible domain for $c = 0.9193$. The ordinate values are bisected in the plots of the second row.	124
4.12	Comparison between the experimental and simulated curves of the tensile tests in the reversible domain for $c = 0.8606$. The ordinate values are bisected in the plots of the second row.	125
4.13	Comparison between the identified values of the bulk moduli for each temperature and degree of cure and the fit function eq. (4.10) by means of the parameters of table 4.6	126

4.14	Comparison between the experimental and simulated results of the tensile tests for $c_{\text{eff}} = 1.0$. The ordinate values are bisected in the plots of the second row.	127
4.15	Comparison between the experimental and simulated tensile tests for $c_{\text{eff}} = 0.9193$. The ordinate values are bisected in the plots of the second row.	128
4.16	Comparison between the experimental and simulated tensile tests for $c_{\text{eff}} = 0.8606$. The ordinate values are bisected in the plots of the second row.	129
4.17	Comparison between the identified values of the initial yield stress and the fit function eq. (4.11) by means of the parameters in table 4.7	130
4.18	Comparison between the identified values of the viscoplastic relaxation time and the fit function eq. (4.12) by means of the parameters in table 4.7	131
4.19	Comparison between the identified values of the hardening modulus and the fit function eq. (4.12) by means of the parameters in table 4.7	132
4.20	Comparison between the experimental and simulated curves of the tensile tests subjected to cyclic loading and unloading for $c_{\text{eff}} = 1.0$. The ordinate values are bisected in the plots of the second row. . . .	134
4.21	Comparison between the experimental and simulated curves of the tensile tests subjected to cyclic loading and unloading for $c_{\text{eff}} = 0.9193$. The ordinate values are bisected in the plots of the second row.	135
4.22	Comparison between the experimental and simulated curves of the tensile tests subjected to cyclic loading and unloading for $c_{\text{eff}} = 0.8606$. The ordinate values are bisected in the plots of the second row.	136